Electrochemical and Spectroelectrochemical Studies on 2,2'-Bipyridine and Pyridine Complexes of Pt(II) and Pd(II).

Lorna Anne Jack

Ph.D Thesis

University of Edinburgh

2003

To Mum and Dad, thank you

Acknowledgements

First and foremost I would like to thank Dr. Lesley Yellowlees for her excellent supervision, input, support and boundless enthusiasm over the last three years. Thanks also to Dr. Neil Robertson for his helpful discussions on the work covered in Chapter 6 and for showing me how to use the spectrofluorimeter. Thanks also have to go to the crystallography section, that is Drs. Simon Parsons and Andy Parkin, to the technical staff, particularly Mr. Donald Roberston and to the mechanical and electronic workshops.

In the lab: thanks to members of the Yellowlees Group both past and present, particularly Dr. Marie Elliot who first taught me how to use the electrochemistry and OTTLE equipment and could always be relied on to turn up later than me for work on a Saturday morning; Dr. Ken Macnamara without whom most of the work would never have been done as I am unable to open any of the solvent bottles in the lab without assistance and for a very enjoyable trip to Italy and lastly Paul Murray for putting up with me in writing up mode.

Thanks to those in the Chapman group especially Dr. Simon Daff and Dr. Toby Ost whose help in the hundred and one little computer problems I've encountered in the last six months has been much appreciated.

Finally thanks to all of my friends in Edinburgh and beyond who have been writing up at the same time as me, (you know who you are), for biscuits, trips to the pub, silly emails and constant reminders that this doesn't last forever.

Abstract

This thesis is concerned with the synthesis, electrochemistry and spectroelectrochemistry of three different types of ligands; the 5,5'-$(X)_2$-bpys, (bpy = 2,2'-bipyridine), the bidentate di-2-pyridyls, (py)-X-(py), (where py = pyridine and X is a bridging group) and the nitro substituted bpys 4,4'-$(NO_2)_2$-bpy and 4-NO_2-bpy and 4-NO_2-py. The Pt(II) complexes of these ligands were also studied along with the Pd(II) complexes of the nitro substituted ligands.

The ligands and complexes of general type 5,5'-$(X)_2$-bpy and [Pt(5,5'-$(X)_2$-bpy)Cl_2] are shown by cyclic voltammetry to undergo two reversible, one electron reductions. Analysis of the absorption and epr spectra of the one electron reduction products reveal that the first reduction is localised on the bpy moiety although there is a small but significant (*ca.* 10 %) admixture of the Pt $5d_{yz}$ and $6p_z$ orbitals in the SOMO. Spin pairing of the two reduction electrons in the bpy π^* orbital occurs. Comparison of the gradients on a plot of the Hammett parameters σ_m and σ_p *vs.* the first reduction potentials of [Pt(5,5'-$(X)_2$-bpy)Cl_2] and [Pt(4,4'-$(X)_2$-bpy)Cl_2] indicates that the 5,5' position on bpy is electronically the more important site of substitution.

The electrochemical behaviour of 4,4'-$(NO_2)_2$-bpy, [Pt(4,4'-$(NO_2)_2$-bpy)Cl_2] and [Pd(4,4'-$(NO_2)_2$-bpy)Cl_2] can be explained in terms of a molecular orbital scheme with a low-lying LUMO and a small LUMO/LUMO-1 energy gap. For the free ligand, 4,4'-$(NO_2)_2$-bpy, the 4-NO_2-py rings lie orthogonal to one another and thus the two reduction electrons are localised on separate 4–NO_2-py moieties. On complexation the 4,4'-$(NO_2)_2$-bpy is forced to become planar and the reduction electrons are localised over the entire ligand. However, epr studies show that the di-reduced species are paramagnetic indicating that the LUMO/LUMO-1 energy gap is still less than the spin pairing energy and di-reduction of 4,4'-$(NO_2)_2$-bpy and its Pt and Pd complexes leads to the spin-triplet species.

In the case of 4-NO_2-bpy^{1-} and its mono-reduced complexes of Pt(II) and Pd(II), the reduction electron is localised on the 4-NO_2-py moiety rather than delocalised over the whole ligand. The redox chemistry of [Pt(4-NO_2-py)$_2Cl_2$], [Pd(4-NO_2-py)$_2Cl_2$] and [Pt(4-NO_2-py)$_2$(ox)], (ox = oxalate), indicates that the 4-NO_2-py ligands are reduced at very similar potentials with no communication between ligands. The single crystal X-ray structure of *trans*-[Pt(4-NO_2-py)$_2Cl_2$] is reported.

The redox behaviour of di-2-pyridyl ketone (dpk) and [Pt(dpk)Cl_2] indicates that the reduction electron enters the π^* LUMO of dpk. This promotes the addition of water to the carbonyl group and the formation of dpk.H_2O^{1-} via the intermediate dpk.H^0. From the UV/vis/nir data [Pt(dpk.H)Cl_2]^0 and [Pt(dpk.H_2O)Cl_2]$^{1-}$ appear to be the most stable species in this series of reactions.

The complexes [Pt(5,5'-(Me)$_2$-bpy)(mnt)] and [Pt(5,5'-(CO_2Et)$_2$-bpy)(mnt)] show very similar redox behaviour to their Cl analogues, indicating that the LUMO is bpy-based and unaffected by the other ligands bound to the Pt(II) centre. The lowest energy absorption band for both complexes is assigned to a mixed Pt(d)/S(p)$\rightarrow\pi^*$bpy charge transfer transition. Both complexes luminesce in solution at room temperature and at 77 K. For [Pt(5,5'-(CO_2Et)$_2$-bpy)(mnt)] the emitting state is ^{3}{(Pt)d/(S)p$\rightarrow\pi^*$(bpy)}. The emitting state(s) of [Pt(5,5'-(Me)$_2$-bpy)(mnt)] is dependent on the excitation energy; excitation above 20,000 cm^{-1} gives emission from the ^{3}{(Pt)d/(S)p$\rightarrow\pi^*$(bpy)} and ^{3}{(Pt)d/(S)p$\rightarrow\pi^*$(mnt)} emitting states. On excitation below 20,000 cm^{-1}, only emission from the ^{3}{(Pt)d/(S)p$\rightarrow\pi^*$(bpy)} state is observed. This behaviour arises because the electron donating Me substituents destabilise the bpy-based LUMO so that the LUMO/LUMO-1 (LUMO-1 is mnt-based) energy gap is small enough to allow population of both the bpy and mnt excited states.

Contents

Abbreviations

A	hyperfine coupling between unpaired e^- and the metal nucleus
a	superhyperfine coupling between unpaired e^- and the ligand nucleus
B	magnetic field
bpy	2,2,'-bipyridine
CE	counter electrode
CV	cyclic voltammogram
DCM	dichloromethane
DMF	dimethylformamide
E	potential
$E_{½}$	half-wave potential
e^-	an electron
E_{pa}	potential peak for an oxidation process
E_{pc}	potential peak for an reduction process
epr	electron paramagnetic resonance
g	epr proportionality factor
G	Gauss
HOMO	highest occupied molecular orbital
i_p	peak current
IR	infra red
LUMO	lowest unoccupied molecular orbital
MLCT	metal-to-ligand charge transfer
py	pyridine
$TBABF_4$	tetrabutylammonium tetrafluoroborate
UV	ultraviolet
vis	visible

List of Figures

List of Tables

List of Schemes

CHAPTER 1:

Introduction

Chapter 1 Introduction

1.1 Introductory Remarks

The intriguing electrochemical, photophysical and photoelectrochemical properties of transition metal complexes of 2,2'-bipyridine (bpy) have led to their use as photocatalysts[1], photosentisers[2] and luminescent probes for detecting steroids[3] and cations.[4]

This thesis is concerned with the synthesis, electrochemistry and spectroelectrochemistry of three different types of ligand: the 5,5'-$(X)_2$-2,2'-bpys, the bidentate dipyridyl groups (py)-X-(py), where X is a bridging group and the nitro substituted 2,2'-bpys and 4-NO_2-py. The Pt(II) complexes of these ligands were studied along with the Pd(II) complexes of the nitro substituted ligands. By way of introduction, a brief discussion on ligand field theory is given, followed by a short review on Pt(II) bpy complexes. Emphasis is given to the electrochemistry and spectroelectrochemistry of $[Pt(bpy)Cl_2]$. As with most chemistry, it is difficult to examine one feature in isolation.

1.2 History of Platinum and Palladium

Platinum has been known since ancient times, impure platinum being used by South American Indians to make jewellery. The metal was first introduced to Europe by Wood in 1741 although de Ulloa, a Spanish naval officer and astronomer, became the first person to publish a report on the properties of platinum in 1748. In the course of his studies on platinum, Wollaston isolated and identified palladium from the mother liquor remaining after platinum had been precipitated as $(NH_4)_2PtCl_6$, from its solution in aqua regia.[5]

1.3 2,2'-Bipyridine

2,2'-Bipyridine (bpy) and its derivatives are renowned for their ability to form co-ordination complexes with metal ions from almost all groups in the Periodic Table.[6] Bpy is a bidentate, chelating ligand that co-ordinates with metal ions by making the M^{n+} part of a stable, five membered ring. Bpy is both a σ-donor and a π-acceptor ligand. The lone pair of electrons on the nitrogen can form a σ-bond with an unoccupied σ-orbital of the metal ion and in doing this will provide both of the electrons. Occupied orbitals of the metal having appropriate symmetry, (*ie* d orbitals), can overlap with the unoccupied orbitals of the delocalised bpy π^* system. These two types of bonding reinforce each other; as the σ-donor bonding increases the electron density on the metal ion, its ability to form a π-bond with the bpy is enhanced, *ie* back bonding occurs, see Figure 1.1.

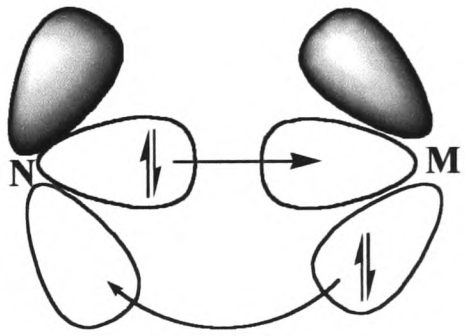

Figure 1.1 Schematic representation of σ and π-back bonding between a nitrogen atom on bpy and a metal centre.

Studies on the X-ray crystal structure of bpy indicate that the two pyridine rings are coplanar, with the nitrogen atoms *trans* to the C(1)-C(1') bond joining the two pyridine rings.[7, 8] Thus the molecule has a centre of symmetry. The unit cell is monoclinic with two molecules per unit cell. The average bond lengths in the pyridine ring are C-C 1.39 Å and C-N 1.36 Å and agree well with the same bond lengths given for pyridine and pyrazine. The C(1)-C(1') bond is 1.50 Å long. Bond angles indicate a slight distortion of the pyridine rings. As there are no short intermolecular distances in the crystal packing, the intermolecular binding must be due only to weak Van der

Waals forces. This is supported by the low melting point (69.5 °C) of bpy and also the tendency of these crystals to slowly sublime in air at room temperature.[8]

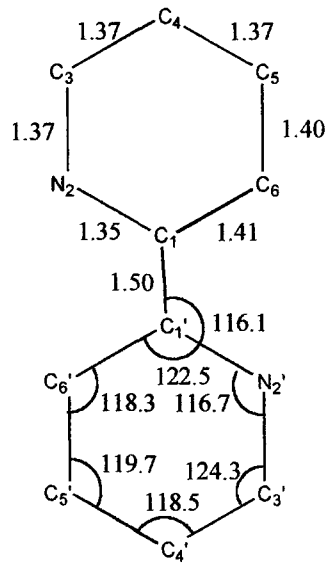

Figure 1.2 Experimental bond lengths (in Å) and bond angles (in °) for 2,2'-bpy, from Merritt.[8]

1.4 Crystal Field Theory

For an octahedral complex the d orbitals are split into two groups; the doubly degenerate e_g orbitals (d_z^2, d_x^2-$_y^2$) and the triply degenerate t_{2g} orbitals (d_{xy}, d_{xz}, d_{yz}). This model leads to an energy level diagram where the t_{2g} orbitals lie lower in energy than the e_g orbitals and the separation between the sets of orbitals is known as the ligand-field splitting parameter, Δ_o. Δ_o varies with the identity of the ligand. During studies on the series of complexes $[CoX(NH_3)_5]^{n+}$, where X = I^-, Br^-, Cl^-, H_2O and NH_3, Tsuchida noted that the colours of the complexes changed from deep purple to yellow, indicating that the energy of the lowest energy electronic transition and thus Δ_o increases as the ligands are varied along the series.[9] The series was found to be quite general and the same order of ligands was followed regardless of the metal centre. Tsuchida arranged the ligands in a spectrochemical series:

$I^- < Br^- < S^{2-} < \underline{S}CN^- < Cl^- < NO^{3-} < F^- < OH^- < C_2O_4^{2-} < H_2O < \underline{N}CS^- < CH_3CN < NH_3 < en < bpy < phen < NO_2^- < PPh_3 < \underline{C}N^- < \underline{C}O.$

where the ligands are arranged in order of the increasing energy of transitions in a complex.[9] However, the values of Δ_o also depends on the particular metal ion, the series mirrors the improved metal-ligand bonding of the more expanded 4d and 5d orbitals compared to the compact 3d orbitals. The spectrochemical series for metal ions is approximately:[10]

$$Mn^{2+} < Ni^{2+} < Co^{2+} < Fe^{3+} < Co^{3+} < Mn^{4+} < Mo^{3+} < Rh^{3+} < Ru^{3+} < Pd^{4+} < Ir^{3+} < Pt^{4+}$$

By convention the average energy of the d orbitals is zero and therefore the three t_{2g} orbitals lie $2/5\Delta_o$ below the average energy and the two e_g orbitals lie $3/5\Delta_o$ above it, see Figure 1.3. Thus the ligand-field stabilisation energy (LFSE), the overall energy of a $t_{2g}^{x}e_g^{y}$ configuration relative to the average energy of the orbitals is given by equation 1.1, below.

$$LFSE = (-0.4x + 0.6y)\ \Delta o \qquad (1.1)$$

For d^1, d^2 and d^3 complexes the low energy t_{2g} orbitals are occupied with the electrons having parallel spins. For complexes with between 4 and 7 d electrons, the possible electronic configurations become more complicated as these additional electrons can either pair with an electron in a t_{2g} orbital and experience a strong coulombic repulsion, the pairing energy P, or occupy the e_g orbitals which will avoid the pairing energy but will have a higher energy by Δ_o. In the case of Cr^{2+} (d^4), the LFSE can either be $1.6\Delta_o - P$ (t_{2g}^{4}) or $0.6\Delta_o$ ($t_{2g}^{3}e_g^{1}$). Which configuration is adopted depends on the magnitudes of P and Δ_o. If $\Delta_o < P$, a weak-field case, occupation of the e_g orbital is more favourable. If $\Delta_o > P$, a strong field case, it is energetically more favourable for the electrons to pair in the t_{2g} orbital. 4d and 5d metals have larger values of Δ_o than 3d metals and hence complexes of these metals are generally characteristic of strong ligand fields. When alternative d orbital configurations are possible, the configuration with fewer parallel electron spins (unpaired) is called a low spin configuration whereas the complex with a greater number of a parallel electron spins is called a high spin configuration. As the value of Δ_o depends on both the metal and the ligand and P

varies with the metal, it is not possible to specify the point in the spectrochemical series where the complex changes from high to low spin. Low spin complexes commonly occur for 3d metals where the ligand is high in the spectrochemical series. Low spin complexes are common for 4d and 5d ions as Δ_o is larger and P is smaller than for 3d orbitals.

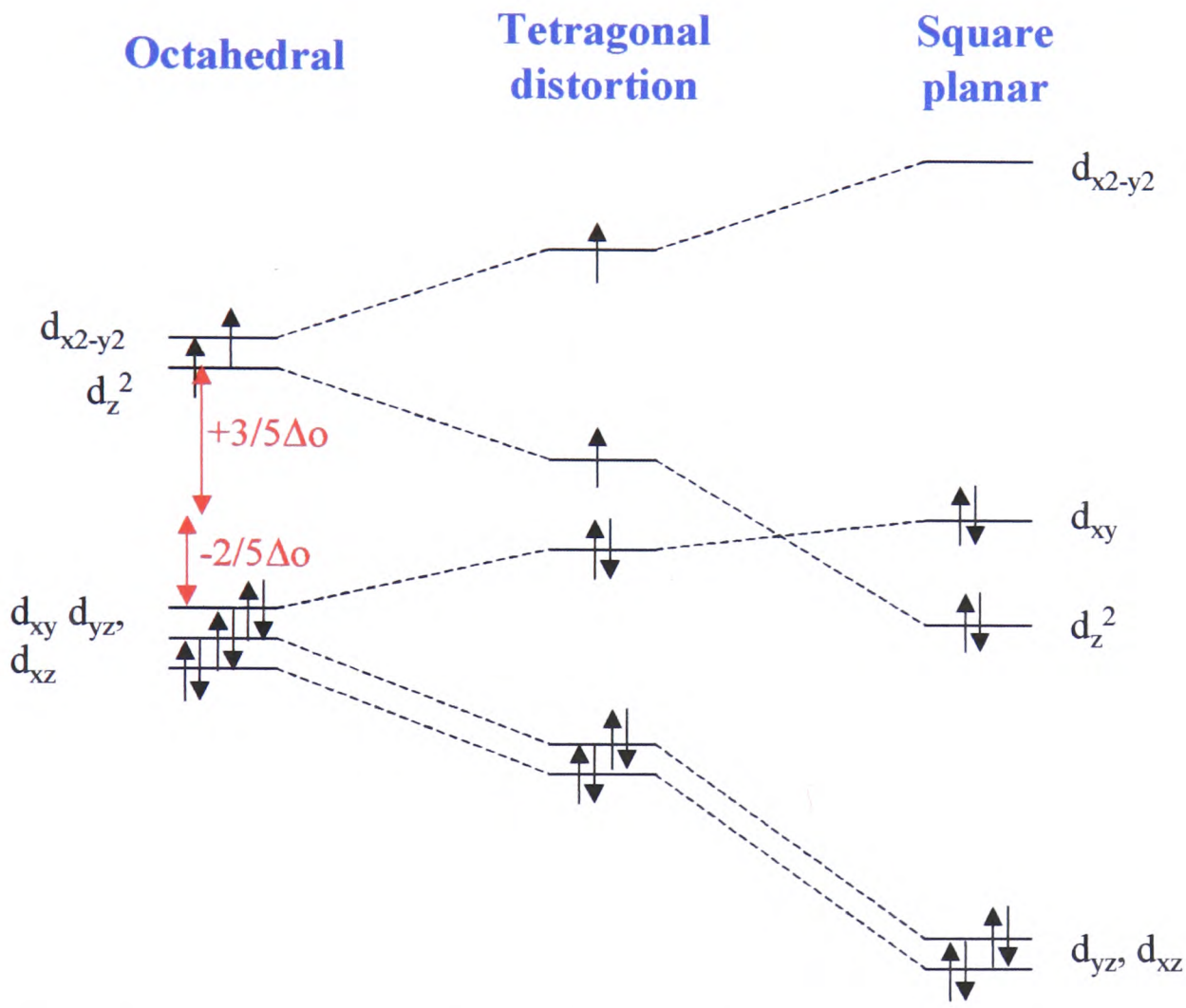

Figure 1.3 The splitting of d orbitals in fields of different geometries and the resulting electronic configuration of the d^8, Pt(II) ion.

Square planar complexes are particularly common for Pt(II) and Pd(II). Square planar complexes are best explained by first discussing tetragonally distorted six coordinate metal complexes. A tetragonal distortion is one where the M-L bonds along the z axis are extended and those along the x and y axes are compressed. This reduces the energy of the e_g (d_z^2) orbital, but increases the energy of the e_g (d_x^2-$_y^2$) orbital. Should one, two or three electrons occupy the e_g orbitals then a tetragonal distortion may be

energetically advantageous. Such tetragonal distortions represent examples of the Jahn-Teller effect that occurs when the ground electronic configuration of a non-linear molecule is degenerate and the molecule distorts to remove this degeneracy and achieve a lower energy. For a d^9 complex like Cu^{2+} such a distortion stabilises two electrons but destabilises the third, see Figure 1.3. If the distortion of d^8 complexes is large enough to encourage pairing of the two e_g electrons in the d_z^2 orbital, the ligands on the z axis may be lost altogether leading to the formation of a d^8 square planar complex, see Figure 1.3, such as those found for Rh(I)[11], Ir(I)[11], Pt(II)[12], Pd(II)[13] and Au(III).[14]

1.5 Common Oxidation States of Platinum and Palladium

Pt(IV) complexes are numerous and are both thermodynamically stable and kinetically inert. Complexes of Pt(IV) with halides and N-donor ligands are especially numerous. K_2PtCl_6 is commercially the most common compound of platinum. In contrast, Pd(IV) complexes are rare and much less stable than those than those of Pt(IV).[5]

The 2^+, (d^8), oxidation state and consequently the square planar configuration, is the most common for platinum and palladium. The complexes of Pt(II) and Pd(II) have played a major part in the development of coordination chemistry. The complexes with ammonia and amines, especially those of the types $[ML_4]^{2+}$ and $[ML_2X_2]$ are particularly abundant. The best known of these complexes is Magnus' green salt, $[Pt(NH_3)_4][PtCl_4]$. The fact that a green salt results from a colourless cation and a red anion was found to be due to the structure. The square planar anions and cations are stacked alternately to produce a linear chain of Pt atoms only 3.25 Å apart. Interaction between these metal atoms shifts the d-d absorption of the $[PtCl_4]^{2-}$ ion from the green region, (hence the normal red colour), towards the red, so producing the green colour.[5]

Interest in these apparently simple complexes was rekindled in 1969 with Rosenberg and co-workers discovery of the anti-tumour activity of *cis*-$[PtCl_2(NH_3)_2]$, cisplatin.[15] This is still one of the best treatments for some types of cancer.

1.6 [Pt(bpy)Cl$_2$] and Related Complexes

Since their initial synthesis by Morgan and Burstall[16] Pt(II) complexes of bpy have been a source of great interest for their interesting structural [17, 18] absorption and emission spectral [19-22] and electrochemical properties. [23-25].

1.6.1 Dimorphism of [Pt(bpy)Cl$_2$]

Morgan and Burstall were the first to synthesize platinum salts of bpy.[16] They found that $[Pt(bpy)Cl_2]$ exhibits dimorphism, with the complex either forming as pale yellow crystals, (Y form), or deep red crystals, (R form). Y is formed by boiling bpy and $K_2[PtCl_4]$ in water with dilute hydrochloric acid, (HCl), or by boiling $[Pt(bpy)(en)]Cl_2.2H_2O$ in water with dilute HCl. R is formed by boiling $[Pt(bpy)(en)]Cl_2.2H_2O$ in concentrated HCl, see Scheme 1.1, below.

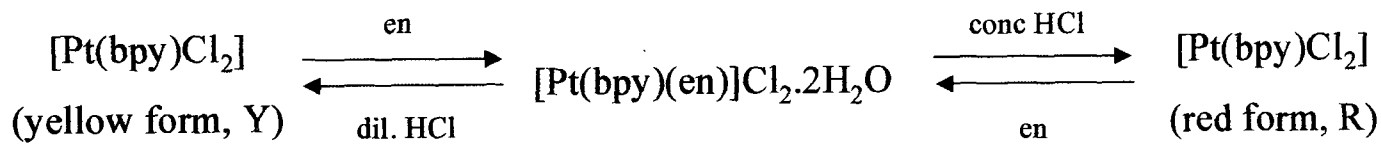

Scheme 1. 1 Scheme showing how the two forms of $[Pt(bpy)Cl_2]$ can be obtained from the same starting complex, Morgan and Burstall.[16]

The red and yellow forms give the same chemical formulations although the red form is only stable as a solid. When dissolved in solvents such as chloroform, ($CHCl_3$) or dichloromethane, (DCM), the red form converts to the yellow. From this behaviour Morgan and Burstall concluded that the "difference in colour of the two chlorides denotes some modification in the arrangement of the molecules in the crystal rather than a difference in chemical structure."[16] Futhermore, attempts to prepare two

polymorphs of $[Pt(bpy)X_2]$, (X = Br, I), $[Pt(phen)Cl_2]$, (phen = 1,10-phenanthroline) and $[Pd(bpy)Cl_2]$ have all been unsuccessful.[16, 20]

The crystal structure of the R form of $[Pt(bpy)Cl_2]$ was solved and an initial study into the crystal structure of the Y form was carried out by Osborn and Rogers.[17] The R form is orthorhombic, space group C*mcm*, with four molecules per unit cell. The complex is square planar with Pt-Cl and Pt-N distances of 2.306(2) and 2.001(6) Å respectively, see Table 1.1. The structure is shown to be a simple stacked arrangement of monomers. Subsequent monomers in a stack are related by inversion centres so that in alternating layers, the chlorine atoms of one molecule are sandwiched between the pyridine rings of those above and below and the platinum atoms are nearly superimposed, see Figure 1.4. The Pt…Pt separation is 3.45 Å. The distances between the Cl atoms and the nearest atoms in the adjacent pyridine ring are Cl…N 3.48 Å, Cl…C(1) 3.55 Å and Cl…C(5) 3.64 Å. None of these distances are shorter than the Van der Waals contact distance.[17] The separation between molecular planes is 3.40 Å.

Table 1. 1 Selected bond lengths and angles for the red form of $[Pt(bpy)Cl_2]$. Standard deviations are given in parentheses, from Osborn and Rogers.[17]

Bond lengths / Å		**Bond angles[a] / °**	
Pt-Cl	2.306(2)	Cl-Pt-Cl'	88
Pt-N	2.001(6)	Cl-Pt-N	96
N-C(1)	1.33(1)	N-Pt-N'	80
C(1)-C(2)	1.37(1)	Pt-N-C(1)	117
C(1)-C(1')	1.15(3)	N-C(1)-C(1')	113
		N-C(1)-C(2)	124
		C(1)-C(2)-C(3)	118

[a] Standard deviation for all angles is *ca* 1.0 Å

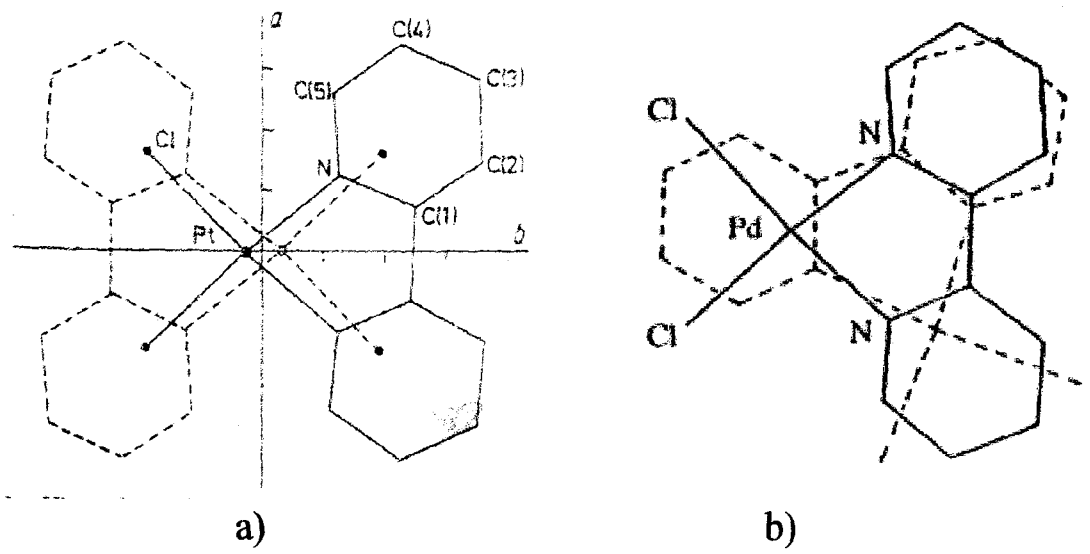

a) b)

Figure 1.4 Relationship between neighbouring molecules in columns of $[M(bpy)Cl_2]$: a) "red" form of $[Pt(bpy)Cl_2]$ viewed along c axis,[17] b) $[Pd(bpy)Cl_2]$, isomorphous with "yellow" form of $[Pt(bpy)Cl_2]$, also viewed along the c axis.[13]

Crystals of the Y form of $[Pt(bpy)Cl_2]$ are also orthorhombic, but have eight molecules per unit cell.[17] The structure is isomorphous with that of $[Pd(bpy)Cl_2]$.[13] Canty and co-workers studied the crystal structure of $[Pd(bpy)Cl_2]$ and found the crystals to be orthorhombic, space group P*cba*, with eight molecule in the unit cell.[13] The planar molecules of $[Pd(bpy)Cl_2]$ are stacked into columns along the c direction, at a separation of c/2, neighbouring molecules in stacks are related by glide planes with a Pd...Pd separation of 4.587(2) Å. Canty noted that this packing is more efficient than that of the R Pt complex as the densities of the red and "yellow" forms differ by approximately 3 %.[13]

It was not until the study by Herber and co-workers that the structural differences between the R and Y forms of $[Pt(bpy)Cl_2]$ were finally confirmed.[26] Selected bond lengths and angles of the R and Y forms of $[Pt(bpy)Cl_2]$ are shown in Table 1.2. Two major differences in the crystal structures of Y and R are immediately apparent. The Pt...Pt distances are quite different, (4.435(1) Å for Y and 3.45 Å for R), as is the arrangement of the molecules in adjacent layers. This has changed from a "staggered" arrangement of molecules in adjacent layers in the R form to the less elegant and symmetrical rotated orientation of molecules in adjacent layers in the Y form, see Figure 1.4. In the Y arrangement, (in which there is no pseudo-2-fold axis along the

metal-metal direction), there are two inequivalent Pt-Cl distances (2.281(4) and 2.300(3) Å), compared to a single value of 2.306(2) Å reported for the R form.[26] Similarly, the single Pt-N distance of 2.001(6) Å in the R form is to be compared to the 2.006 (10) and 2.011 (10) Å distances observed in the Y form, see Table 1.2. Finally, the calculated Cl-Pt-N angle of 184° in the R form is to be compared with the significantly smaller values of 175.9(3)° and 174.7(3)° in the Y form. Thus it is apparent that the red form obtained from the high temperature treatment of the yellow form accommodates a Pt…Pt stacking arrangement with significantly larger metal-metal interaction than is present in the yellow form.[26]

Table 1. 2 Comparison of selected bond lengths (Å) and angles (°) for the red and yellow forms of [Pt(bpy)Cl_2], Herber *et al.*.[26]

Compound	Pt-N[a]	C-C'[a]	N(1)-Pt-N(2)[b]	Pt-Cl[a]	Pt…Pt
[Pt(bpy)Cl_2] Y	2.006(10)	1.462(17)	80.6(4)	2.281(4)	4.435(1)
	2.011(10)			2.300(3)	
[Pt(bpy)Cl_2] R	2.001(6)	1.51(3)	80(1)	2.306(2)	3.45

a) bond lengths / Å, b) bond angles / °

Bielli *et al.* carried out electronic reflectance spectroscopy on crystals of Y and R [Pt(bpy)Cl_2] and found that the spectra are very similar except for the appearance of an additional band at 520 nm in the R form.[20] The needle shaped crystals of R exhibit marked dichroism, appearing dark red when the electric vector of the light is parallel to the c-axis, (needle-axis) and yellow when perpendicular. The 520 nm band which causes the red colour is polarised along the needle axis, *ie* perpendicular to the molecular plane.[20]

1.6.2 Electronic spectra

The electronic spectra of $[Pt(bpy)Cl_2]$, (as well as those of the Br, I and CN analogues) are strongly affected by solvent, with the bands moving to lower energy with decreasing solvent polarity.[19] Gidney and co-workers reported the UV/vis absorption spectrum of $[Pt(bpy)Cl_2]$ in methanol, identifying the bands at 30 kcm^{-1} and 32.2 kcm^{-1} as the first intraligand $\pi \rightarrow \pi^*$ transition of bpy and the band at 27.0 kcm^{-1} as a spin allowed metal-to-ligand charge transfer (MLCT, d-π^*) transition.[19] In butyronitrile solution this spin allowed MLCT transition is found at 25.4 kcm^{-1}.[21] However, Miskowski found that the lowest energy absorption feature of $[Pt(bpy)Cl_2]$ is completely insensitive to solvent and appears at 20.9 kcm^{-1} for both the R and Y forms in the solid state[19] and in butyronitrile solution.[21] Consequently, Miskowski ruled out the possibility of this absorption feature being the spin forbidden component of the MLCT transition discussed above.[21] The broad, unstructured emission at 610 nm in glassy butyronitrile at 77 K was assigned as a ligand field (d-d) transition due to its solvent insensitivity and lack of vibronic structure. As a result Miskowski assigned the weak, low energy absorption bands to ligand field transitions.[21] Interestingly they assign a similar feature at 22.4 kcm^{-1} in the absorption spectrum of $[Pt(bpy)(en)]^{2+}$ as a singlet-triplet $\pi \rightarrow \pi^*$ transition and the corresponding emission centred on 458 nm as a $^3\pi \rightarrow \pi^*$ emissive excited state due to the vibronic structure of the emission, (MeOH/EtOH glass at 77 K). Similar emissions have been observed for $[Pt(bpy)(CN)_2]$ and $[Pt(phen)(CN)_2]$.[18, 22] Consequently, Miskowski assigned the LUMO of $[Pt(bpy)L_2]$ as metal based when L = Cl but bpy π^*-based where L is a nitrogen- or carbon-donor. This was subsequently found to be incorrect after exhaustive studies by McInnes and co-workers indicated that the LUMO was based on a π^* anti-bonding orbital of bpy.[25, 27]

The absorption spectrum of $[Pt(bpy)Cl_2]$ in DMF solution is dominated by the intense intraligand $\pi \rightarrow \pi^*$ transitions of the bpy ligand at 30.8 kcm^{-1} and 32.0 kcm^{-1} and the lower energy MLCT (d-π(7)bpy) transition at 25.7 kcm^{-1}.[25, 27] The spectral changes of $[Pt(bpy)Cl_2]$ on reduction to $[Pt(bpy)Cl_2]^{1-}$ are consistent with the redox orbital being

the lowest energy unoccupied antibonding π^* orbital of the bpy ligand.[25, 27, 28] By direct comparison with the UV/vis/nir spectrum of Na^+ bpy^{1-},[29] Collison *et al.* assign the bands at 11.2 kcm^{-1}, 20.1 kcm^{-1}, 21.6 kcm^{-1} and 27.9 kcm^{-1} to intraligand transitions of co-ordinated bpy^{1-}. Thus the UV/vis/nir spectrum suggests that the one electron reduction product of $[Pt(bpy)Cl_2]$ is formulated as $[Pt(II)(bpy^{1-})Cl_2]^{1-}$.

Table 1. 3 UV/vis/nir data for $Na^+(bpy^{1-})$, $[Pt(bpy)Cl_2]$ and $[Pt(bpy)Cl_2]^{1-}$.

Complex	π(7-8,9)*	π(7-10)*	MLCT	π(6-7)*	π(6-8)*
	10^{-3} / cm^{-1}	10^{-3} / cm^{-1}	10^{-3} / cm^{-1}	10^{-3} / cm^{-1}	10^{-3} / cm^{-1}
$Na^+(bpy^{1-})$[a]	12.3	17.8, 18.8	-	26	-
$[Pt(bpy)Cl_2]$[b]	-	-	25.7	30.8	32.0
$[Pt(bpy)Cl_2]^{1-}$[c]	11.2	20.1, 21.6	23.9	27.9	-

a) in THF solution,[29] b) in 0.1 M $TBABF_4$/DMF at 293 K,[25] c) in 0.1 M $TBABF_4$/DMF at 243 K.[27]

1.6.3 Electrochemistry

A number of electrochemical studies have been performed to gain a greater insight into the electronic structure of the Pt(II) bpy complexes.[23-25, 27, 30-32]. Typically two, one-electron reductions are observed. On the basis of spectroelectrochemical (UV/vis/nir, epr) studies on $[Pt(bpy)(Ph)_2]$, $[Pt(bpy)(py)](BF_4)_2$ and $[Pt(bpy)(en)](BF_4)_2$ Braterman and co-workers assigned the LUMO as being bpy based, with the metal based LUMO-1 lying close in energy.[23, 24] These results are in agreement with the spectroelectrochemical studies on $[Pt(bpy)Cl_2]$, $[Pt(4,4'\text{-}(Ph)_2\text{-}bpy)Cl_2]$ and $[Pt(4,4'\text{-}(Me)_2\text{-}bpy)Cl_2]$.[31] Yang *et al.* attributed the first reduction to being bpy based and the second to being metal based *ie* the LUMO is bpy based and the LUMO-1 is based on the Pt metal centre.[31] The definitive spectroelectrochemical

investigation of complexes of general formula [Pt(bpy)L_2] where L is changed systematically from a π-donor, weak-field ligand (Cl) to a π-acceptor, strong-field ligand (CN) was carried out by McInnes.[25, 27, 32] Here cyclic voltammetric studies on [Pt(bpy)Cl_2] show a fully reversible, one electron reduction at –1.06 V (0.07) followed by a second reversible reduction at –1.79 V (0.110), the separation of ~700 mV between the two reductions being typical of successive reductions of bpy; *ie* spin pairing of the two added electrons in the same molecular orbital occurs.[25, 27] Thus both reductions are based on the bpy ligand, contrary to the assignments made by Yang *et al.*.

1.6.4 Extended Hückel Molecular Orbital (EHMO) Calculations

EHMO calculations indicate that the LUMO of [Pt(bpy)Cl_2] is of b_2 symmetry with 96 % bpy-π^* character (the lowest energy bpy π^* orbital $\pi(7)$), with small Pt $5d_{yz}$ and $6p_z$ admixtures of 2.0 % and 1.7 % respectively.[25, 27] These results are in general agreement with those of Eisenberg *et al.* on complexes such as [Pt(bpy)(mnt)].[34] The major contribution to the bpy-based π^* LUMO are from the two nitrogen nuclei and the C2, 2', 4 and 4' nuclei, see numbering scheme, Figure 1.5. There is no significant contribution to the LUMO from the orbitals based on the Cl ligands.[25, 27] The calculations indicate that the two highest occupied molecular orbitals (HOMOs) are very close in energy with one being predominantly the Pt $d_{x^2-y^2}$ orbital and the other the highest energy bpy based π orbital.[25]

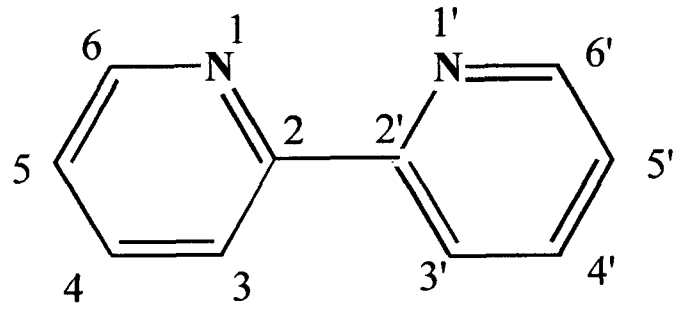

Figure 1.5 Numbering scheme for 2,2'-bpy.

1.6.5 Epr Spectroscopy

Epr studies on the one electron reduction product of $[Pt(bpy)Cl_2]$ and its derivatives have also been instrumental in probing the electronic structures of these compounds.[25, 27, 32, 33]

The solution spectra of electrogenerated or chemically reduced $[Pt(bpy)X_2]^{(n-1)+}$ complexes, (X = Cl, CN, n = 0; X = NH_3, py, PMe_3, or X_2 = en, n = 2) in DMF at room temperature are as expected for interaction of the unpaired electron with platinum, (^{195}Pt, 34 % natural abundance, I = ½), with a broad single resonance with ^{195}Pt satellites being observed.[25, 27, 32, 33] The isotropic epr signals observed show that for $[Pt(bpy)X_2]^{1-}$ the coupling of the unpaired electron is mainly to the Pt nucleus, with any coupling to ligand nuclei unresolved. Thus the coupling of the unpaired electron to any ligand nuclei must be much smaller than coupling to the Pt centre. The solution epr spectrum of $[Pt(bpy)Cl_2]^{1-}$ can be simulated with A_{iso} = -54 G and g_{iso} = 1.998, as shown in Table 1.4. Only $[Pt(bpy)(CN)_2]^{1-}$ shows superhyperfine coupling of the reduction electron to nuclei of the bpy ligand.[27, 33] The results of these combined electrochemistry, UV/vis/nir and epr experiments led McInnes and co-workers to assign the first one-electron reduction of $[Pt(bpy)Cl_2]$ as a ligand-localised process yielding $[Pt(II)(bpy^{1-})Cl_2]^{1-}$.[25, 27]

On freezing at 77 K the X-band epr spectrum exhibits rhombic g and A matrices. There is no resolution of the ^{195}Pt coupling in the high field (g_3) component, the value of A_3 quoted by McInnes *et al.* is that required to give the best fit between the experimental and simulated spectra, see Table 1.4.[27] No superhyperfine splitting could be resolved from the frozen glass spectrum. McInnes and co-workers attributed the small shift in g_{iso} from the free electron value, g_e = 2.0023, as a sign that there is only a small admixture of metal orbitals in the SOMO and that the reduction electron must therefore be localised mainly on the bpy ligand in line with the results of UV/vis/nir spectroelectrochemistry.[25, 27] From the frozen solution spectra one g value is significantly smaller than g_e = 2.0023. This indicates that the SOMO is interacting with an empty Pt-based orbital

Table 1. 4 Epr parameters for $[Pt(bpy)Cl_2]^{1-}$ from Collison *et al.*.[27]

	g_{iso} [a]	g_1 [b]	g_2	g_3	A_{iso} (Pt) [c]	A_1 [c]	A_2 [c]	A_3 [c, d]
$[Pt(bpy)Cl_2]^{1-}$	1.998	2.038	2.009	1.935	-54	-56	-95	-11

a) Isotropic data from chemically generated species in DMF. b) Anisotropic data from the electrochemically generated species, 0.1 M $TBABF_4$/DMF, spectrum recorded at 77 K.
c) 10^4 A / cm^{-1}. d) estimated value from A_{iso}, A_1 and A_2.

EHMO calculations indicate that the only metal orbitals of the correct symmetry and energy to mix with the predominantly π^* ligand based LUMO of b_2 symmetry are the $6p_z$ and $5d_{yz}$ orbitals. Using established procedures to analyse the ^{195}Pt hyperfine data, the contribution of the Pt 5d orbital to the SOMO of $[Pt(bpy)Cl_2]^{1-}$ was calculated to be *ca.* 10 %. Although this is in good agreement with EHMO calculations carried out on the other Pt(II) analogues, the same calculations indicated that contributions from the Pt $6p_z$ orbital may be of equal importance.[25, 27] The contribution of the Pt $5d_{yz}$ and $6p_z$ orbitals to the SOMO of $[Pt(bpy)Cl_2]^{1-}$ was later re-calculated to be 5.1 % and 7.5 % respectively, using the equations given by Connelly but Rieger's nomenclature, see Chapter 3.[32] These values are in good agreement with the results of the DFT calculations.[32, 33] The inherently large hyperfine splittings for the ^{195}Pt nucleus compared to the ligand nuclei, (^{14}N, ^{1}H), result in a much larger observed hyperfine coupling for ^{195}Pt for similar contributions to the SOMO. Thus, although the SOMO of $[Pt(bpy)L_2]^{(n-1)+}$ is predominantly bpy bound, with small (~12 %) admixtures of Pt orbitals, their epr spectra are dominated by the metal splittings.

Combined epr-endor-theoretical studies were later carried out to map the unpaired electron density of $[Pt(bpy)Cl_2]^{1-}$.[32, 33] A second derivative of the frozen epr spectrum of $[Pt(bpy)Cl_2]^{1-}$ reveals superhyperfine coupling of the unpaired electron to two ^{14}N nuclei on the high field g_{zz} feature.[33] From the simulations of the frozen spectrum, McInnes and co-workers attributed the superhyperfine splitting to two equivalent ^{14}N nuclei of $a_{zz(N)} = 9.0 \times 10^{-4}$ cm^{-1} with nominally small values of $a_{xx(N)}$ and $a_{yy(N)}$.[33]

Endor spectra recorded at 10 K at static magnetic fields corresponding to the principal g values of $[Pt(bpy)Cl_2]^{1-}$ showed strong ^1H spectra at each of the three magnetic fields studied, each splitting occurring as a pair of lines centred on ν_H (14.092 MHz at 3500 G), separated by a_H. Weak couplings arising from the two ^{14}N nuclei of the bpy were observed at fields corresponding to g_{xx} and g_{yy}, each coupling appearing as a pair of lines separated by $2\nu_N$, (ν_N = 1.0772 MHz at 3500 G), centred on $a_N/2$.[33]

Using the equations 1.2 and 1.3, shown below to interpret the ligand superhyperfine couplings, McInnes and co-workers calculated that *ca.* 12 % of the unpaired electron density lies on each on the two bpy ^{14}N nuclei. No contribution of the ^1H nuclei to the SOMO was calculated.

$$a_{\|} = a_{iso} + 4/5\ P_p\ \alpha^2 \qquad (1.2)$$

$$a_{\perp} = a_{iso} - 2/5\ P_p\ \alpha^2 \qquad (1.3)$$

Where α^2 is the unpaired electron density in the $2p_z$ orbital of the nucleus under consideration.

P_p = electron-nuclear dipolar coupling parameter for the 2p electrons and have been reported by Morton and Preston as 138.8 and 268.5 MHz for ^{14}N and ^{13}C, respectively.[33]

a_{iso} is calculated by averaging the three anisotropic a_N splittings.

DFT (density functional theory), calculations indicate that the SOMO of $[Pt(bpy)Cl_2]^{1-}$ is dominated (> 88 %), by the b_2 antibonding LUMO of the bpy moiety, the nuclei contributing significantly to the bpy LUMO being N1, 1', C2, 2' and C5, 5'. The remainder of the SOMO is made up of small contributions from the Pt $5d_{yx}$ and $6p_z$ atomic orbitals and other ligand orbitals. The SOMO of $[Pt(bpy)Cl_2]^{1-}$ (and therefore the LUMO of the neutral form), are primarily bpy π^* based.[32, 33]

Thus the electrochemistry, UV/vis/nir, epr spectroelectrochemistry, EHMO and DFT calculations all indicate that the LUMO of $[Pt(bpy)Cl_2]$ is primarily based on the π^* antibonding orbital of the bpy moiety, with small contributions from the Pt $5d_{yz}$ and $6p_z$ orbitals. Thus the one-electron reduction product of $[Pt(bpy)Cl_2]^{1-}$ can be formulated as $[Pt(II)(bpy^{1-})Cl_2]^{1-}$.

CHAPTER 2:

Experimental Techniques

Chapter 2 Experimental Techniques

2.1 Introduction

During the course of this work a number of electrochemical and spectroelectrochemical techniques were used. This chapter aims to explain each technique and discuss their advantages and disadvantages.

2.2 Electrochemical Techniques

Electrochemical studies were carried out using a Dell GX110 PC with General Purpose Electrochemical System (GPES) version 4.8 software, connected to an autolab system containing a PGSTAT 20 potentiostat.

All electrochemical techniques employed a standard three electrode configuration. The working electrode (WE) is the electrode at which the reaction of interest is occurring. Pt and Au make good WEs as they are unreactive and stable over a wide potential range in organic media. In this work a Pt microdisc electrode of 0.5 mm diameter is used. The current is passed between the WE and a counter (CE) or auxiliary electrode. The CE has a larger surface area than the WE so that the current density is not compromised by the CE. The CE is made of a highly conducting but unreactive substance. Here a Pt rod is used.

The current in the electrochemical cell passes between the WE and the CE. However, there is an ohmic potential drop, iRs, between these two electrodes so a third electrode, the reference electrode (RE), provides a fixed potential from which the WE potential can be measured.[35] Here the RE is Ag/AgCl in a DCM (dichloromethane) solution of 0.45 M $TBABF_4$ (TBA is tetra butyl ammonium) and 0.05 M TBACl, against which the ferrocene/ferrocinium couple is measured at + 0.55 V. In order to prevent any contamination of the RE itself, or contamination of the species being studied by the RE, it is isolated from the test solution by a salt bridge.

Supporting electrolyte was added to the test solution to i) increase the conductivity of the solutions studied and ii) to eliminate migration as a mode of mass transport for the electroactive species. This allows us to consider only the diffusion controlled process. In the experiments discussed here the concentrations of electrolyte used are 0.1 M for DMF (N,N'-dimethylformamide) and MeCN (acetonitrile) and 0.3 M for DCM. Typically the supporting electrolyte used in these studies was $TBABF_4$.

The choice of solvent depends on the solubility and the stability of the compound under investigation. For a solvent to be suitable for electrochemistry it should have a compatible potential range, a high dielectric constant, an accessible temperature and a low viscosity. Ideally it should also be easy to purify. If the solvent can act as a co-ordinating ligand, this should also be taken into account.

All platinum electrodes are cleaned with concentrated nitric acid, washed with distilled water and dried before use. All solutions are purged with N_2 before use to remove dissolved oxygen and a continuous stream of N_2 is passed over the top of the solution throughout electrochemical study. Potentials are corrected to the potential for the ferrocene/ferrocinium couple, $E_{½}$ = + 0.55 V, as ferrocene is used as the internal standard. All redox potentials and peak to peak values are reported for a scan rate of 100 mV s^{-1} unless otherwise stated. The peak to peak value is given in brackets after the redox potential.

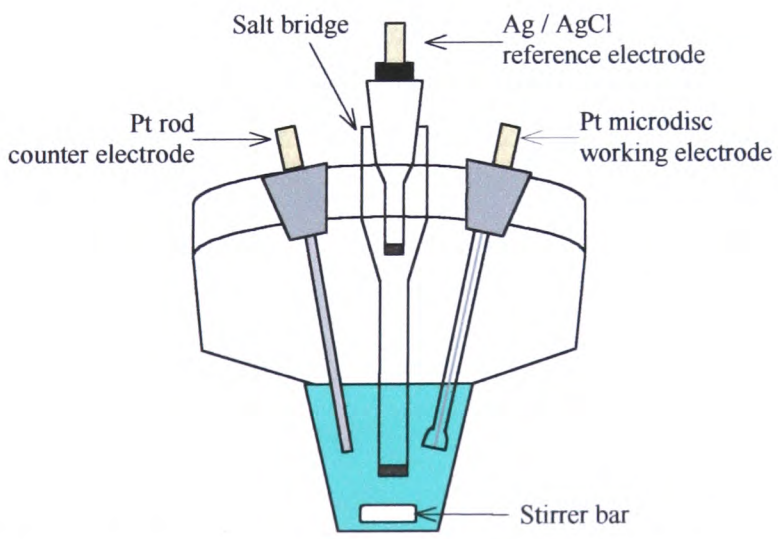

Figure 2.1 Schematic diagram of standard three electrode cell as used for cyclic voltammetry and differential pulse.

The set up of the three electrode cell is the same for cyclic voltammetry and differential pulse and is shown in Figure 2.1 above.

2.2.1 Cyclic Voltammetry

Cyclic voltammetry is a technique suited to initial electrochemical studies of new systems as it can be used to obtain information about fairly complicated electrode reactions. The technique uses stationary electrodes in a stagnant solution.

In cyclic voltammetry a three electrode set up is used, as discussed in the previous section. The potential is swept linearly between a lower limit, E_1 and an upper limit E_2, (or E_λ, the switching potential), at a rate ν. The direction of the scan is then reversed and swept back down to E_1.[35] Although it is possible to use a different scan rate on reversal, this is not usually done. By plotting potential against time we get a symmetrical triangular wave.

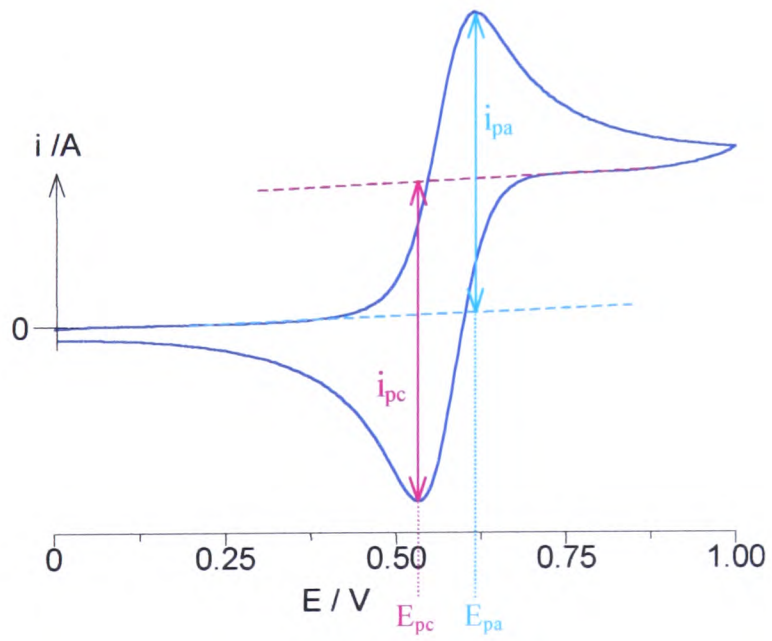

Figure 2 2 Cyclic voltammogram (of ferrocene in 0.1 M $TBABF_4$/DMF) illustrating the important parameters in the technique.

The potential sweep is followed by measuring the current passed with respect to voltage applied. This is known as a cyclic voltammogram, see Figure 2.2. The measured parameters of interest on these cyclic voltammograms are i_{pa}/i_{pc}, the ratio of peak currents, $E_{pa} - E_{pc}$, the separation of peak potentials and $(E_{pa} + E_{pc})/2$, the

half wave potential. For a fully reversible electron transfer reaction $E_{pa} - E_{pc} = 59$ mV and $i_{pa}/i_{pc} = 1.0$ at 298 K.

The shape of a reversible cyclic voltammogram, in this example an oxidation, can be explained as follows:- the potential is swept positive until it reaches a point where the electroactive species begins to be oxidised and the current increases, (by convention an oxidation has a positive current while a reduction has a negative current). As the potential increases the rate constant for the oxidation (k_{ox}) increases, but as the reaction at the WE surface proceeds, the concentration of the reduced species at the electrode surface, ($[R]_{surf}$), falls. This is known as depletion and the current is now under mass transport control. The current is now limited by the transport of the reduced species to the electrode surface from the bulk solvent and begins to fall away. Finally it reaches a constant level where R diffusing in to the surface of the electrode from the bulk solution is oxidised immediately. The potential is reversed at E_2 and the reduction of the oxidised species begins. The return peak is observed at a more negative potential than the forward peak. The shape of this return peak is governed by similar electron transfer and diffusion rate factors as discussed above for the oxidation process.

2.2.2 Stirred Voltammetry

Stirred voltammetry uses the same experimental set up as cyclic voltammetry but, as the name suggests, a stirred solution is studied. Like cyclic voltammetry the potential is stepped linearly between two potentials. The scan rate used is much slower, typically 20 mV s^{-1}. This produces a current – potential curve similar to the one shown in Figure 2.3.

Electron transfer at the working electrode is governed by conduction and diffusion. A cathodic current flow indicates a reduction while an anodic current flow indicates an oxidation. The position of the zero current also indicates whether a reduction or an oxidation is taking place.

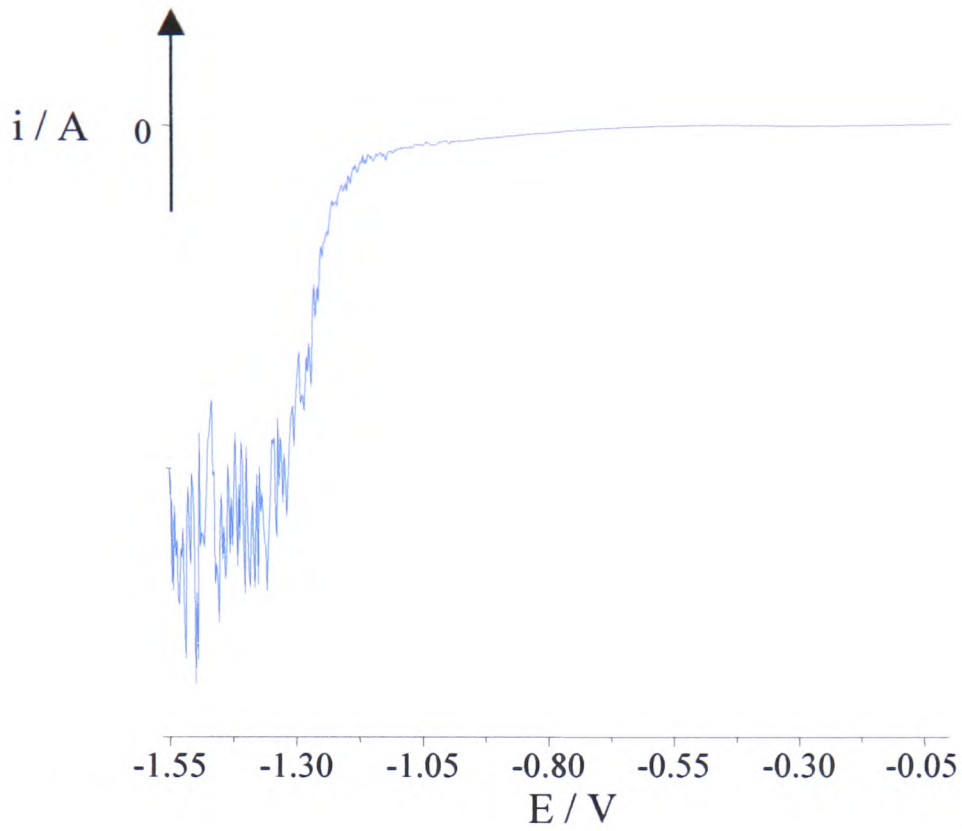

Figure 2 3 Stirred voltammogram of 5,5'-$(CO_2Et)_2$-bpy in 0.1 M $TBABF_4$/DMF.

2.2.3 Differential Pulse Voltammetry

Like cyclic voltammetry, differential pulse voltammetry employs a three electrode set up in a still solution, but unlike cyclic voltammetry the potential here is applied in a series of pulses. A potential – time plot for differential pulse voltammetry is shown in Figure 2.4.

The base potential increases between pulses although the width of the pulse remains the same. The pulse height remains constant (10 – 100 mV). The current is measured twice for each pulse sequence, once just before the pulse, τ' and again just before the end of the pulse, τ.

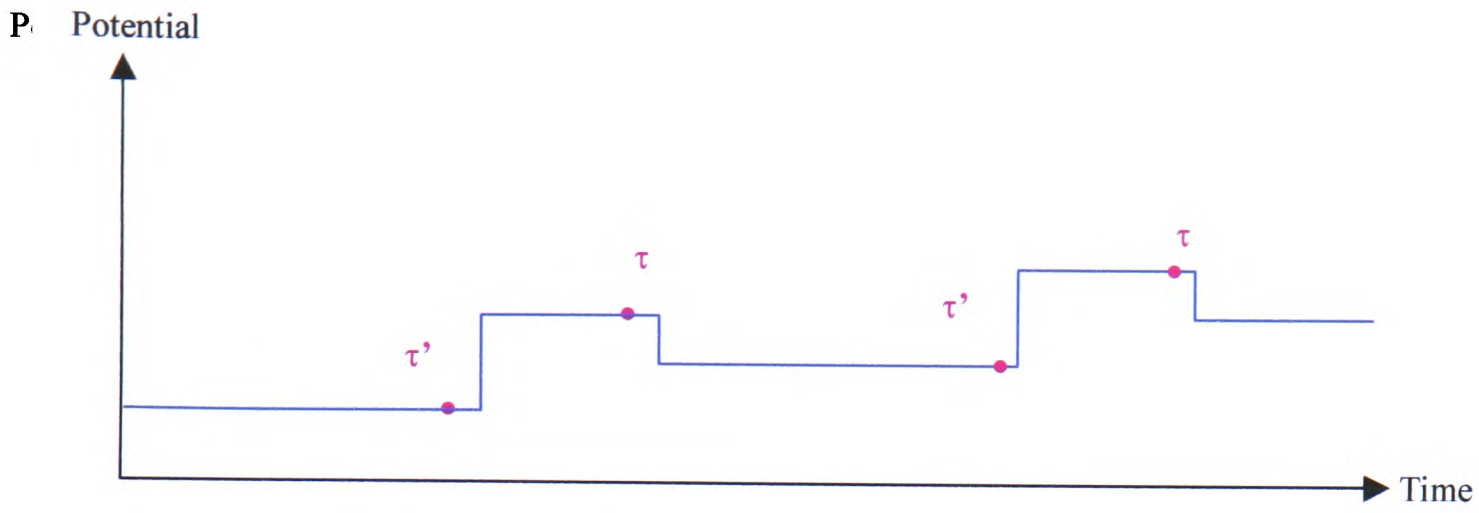

Figure 2 4 Waveform of a differential pulse voltammetry. The pink dots indicate the time at which the current is measured.

The response is presented as an average of the two currents plotted against potential, (see Figure 2.5). The peak position obtained is very similar to that obtained by cyclic voltammetry. As the data are presented as a differential this technique is very sensitive and is particularly useful for examining redox processes that occur in close proximity to each other.

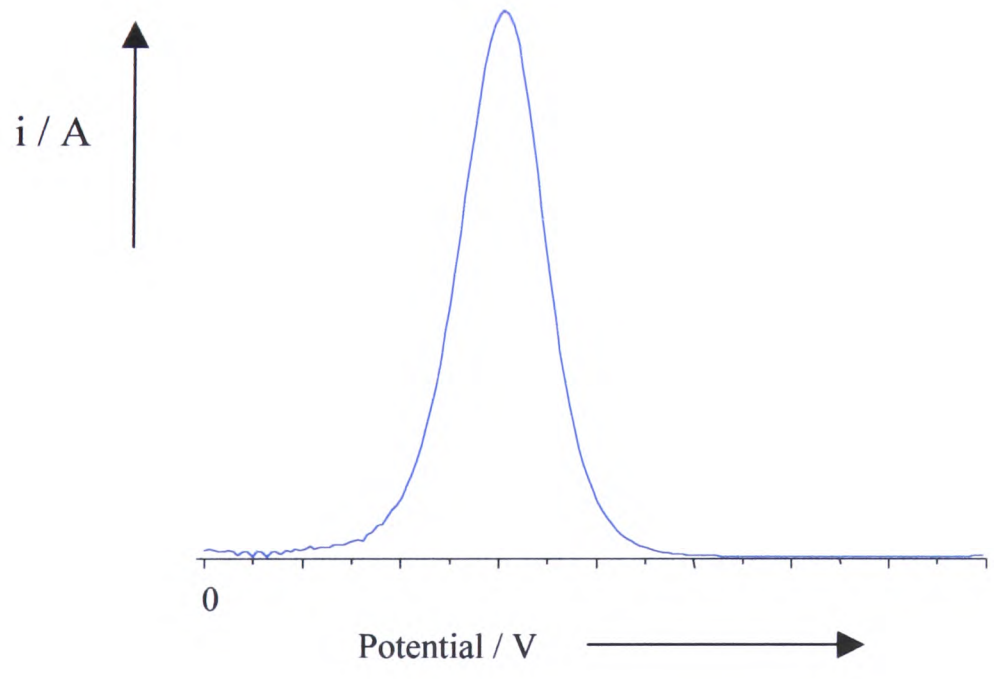

Figure 2 5 Differential pulse voltammogram of ferrocene in 0.1 M $TBABF_4$/DMF.

2.2.4 Coulometry – Bulk Electrolysis

Coulometry, or bulk electrolysis as it is also known, employs a slightly different experimental set up to the other electrochemical techniques discussed here. Although coulometry uses a basic three electrode set up, the cell used is known as an H-cell, (see Figure 2.6). As an electroactive species is being generated in bulk, it is necessary to isolate the CE to prevent any species generated there from contaminating the compound under study. In order to generate the electroactive species more efficiently a Pt gauze basket is employed as the WE.

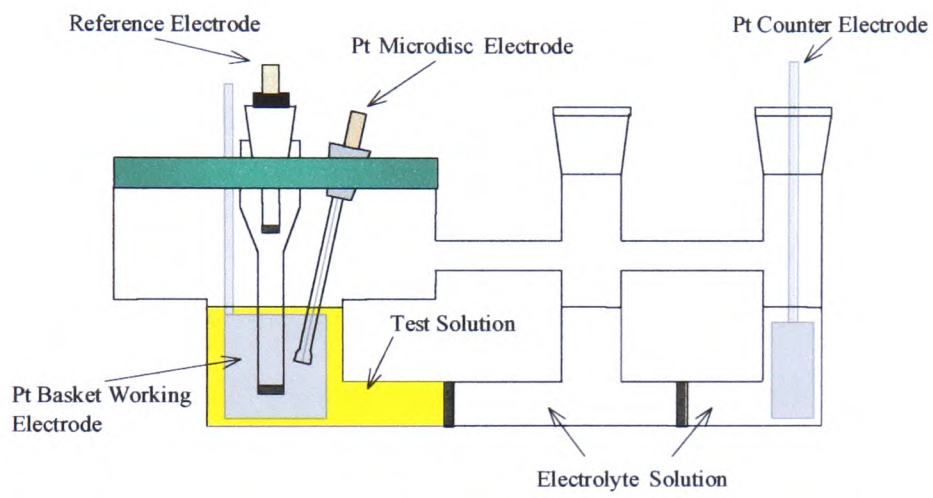

Figure 2 6 H-type cell used for bulk electrolysis.

Initial studies of the redox properties of the electroactive species are carried out using the Pt microdisc WE in a stagnant solution. When bulk electrolysis is about to begin the WE is swapped to the Pt basket and the solution is stirred rapidly to ensure good circulation of the reaction solution around the WE. If the electrogenerated species is air or temperature sensitive the technique can be carried out under N_2 at low temperature. The progress of coulometry is monitored using a plot of charge against time.

For the electron transfer to be fully achieved at the WE, the potential applied must be at least 60 mV past the $E_{1/2}$ of the reduction (or the oxidation) under study. The current flow is measured and its integral, charge Q, calculated. The complete sample of electroactive species must be reduced or oxidised.

The total charge passed and the number of moles of compound in solution can be used to calculate the number of electrons involved in a redox step using Equation 2.1 shown below.

$$Q = e\,n\,F \qquad (2.1)$$

e = no of moles of electrons
Q = charge passed / C
F = 96485 / C mol^{-1}
n = no of moles of compound

Once the desired species has been electrogenerated its electrochemistry can be studied using the Pt microdisc electrode as described in 2.2.1.

2.3 Spectroelectrochemical Techniques

There is much interest in studying electrode processes by experiments that involve more than just the usual electrochemical variables of potential, current and charge. For instance, electrochemistry can be combined with electronic spectroscopy to monitor how the formation of a reduced or oxidised species can bring about changes in the transfer of electrons between valence shell molecular orbitals. One of the main combined solution spectroelectrochemical techniques used is UV/vis detection as it has a simple experimental set up and gives a great deal of information about the system under study.

Combined electrochemistry/IR detection systems are used to a lesser extent. This is because the solvents used in electrochemistry strongly absorb the IR radiation making it difficult to monitor the IR absorption caused by the electroactive species. This problem can be overcome by the careful selection of solvent and a suitable IR handle on the electroactive species being studied. Using IR as a detection method is desirable as it should give detailed information on the structure of the redox active species and its intermediates. However, the use of IR detection has been limited in this study due to difficulties with both commercially available and home made *in situ* IR cells. The development of a new *in situ* IR cell is described later in this chapter.

One relatively under used spectroelectrochemical technique that has been utilised to great effect in this work is electron spin (or paramagnetic) resonance (epr) spectroscopy where an electroactive species containing an odd number of electrons is generated *in situ*. Epr spectroscopy is a very sensitive technique and it can produce information-rich, distinctive spectra. Additionally, *in situ* epr methods are convenient for the generation of radical ions, especially those that are not easily reduced or oxidised chemically. However, the solvent systems suited to electrochemical study are not ideal epr solvents and hence thin flat cells must be employed in epr spectroelectrochemical experiments.

2.3.1 UV/vis Spectroelectrochemical Techniques

All spectra were recorded on a Perkin-Elmer Lambda 9 spectrometer controlled by a Datalink PC running UV/winlab software.

The products of bulk electrolysis can be monitored *in situ* by UV/vis electronic absorption spectroscopy. The set up of the optically transparent thin layer electrode (OTTLE) cell, (Figure 2.7), consists of a flat quartz cell, of path length 0.05 cm, into which the Pt/Rh gauze WE fits and a quartz reservoir above the flat cell which contains the CE, a Pt wire and the RE, usually Ag/AgCl. This completes the three electrode system. The CE and RE are both separated from the electroactive solution by frits to prevent contamination of the electroactive species during bulk electrolysis.

This assembly is sealed with a lid and then placed in a PTFE block fitted with two pairs of quartz windows, inside the spectrometer. A thermocouple is fitted in the PTFE block so that the temperature can be accurately measured. The temperature is controlled by passing pre-chilled, dry N_2 between the cell and the inner pair of quartz windows. To prevent frosting of the flat cell and the windows dry, room temperature N_2 is passed between the inner and outer quartz windows of the PTFE block and the spectrometer cavity is kept under N_2.

Bulk electrolysis is performed as above and a UV/vis scan is taken every five minutes. Conversion of the electroactive species is complete when the spectrum stops changing and current flow ceases. For the redox couple to be reversible, the spectrum should revert to that of the original sample when the potential is taken back to its starting value.

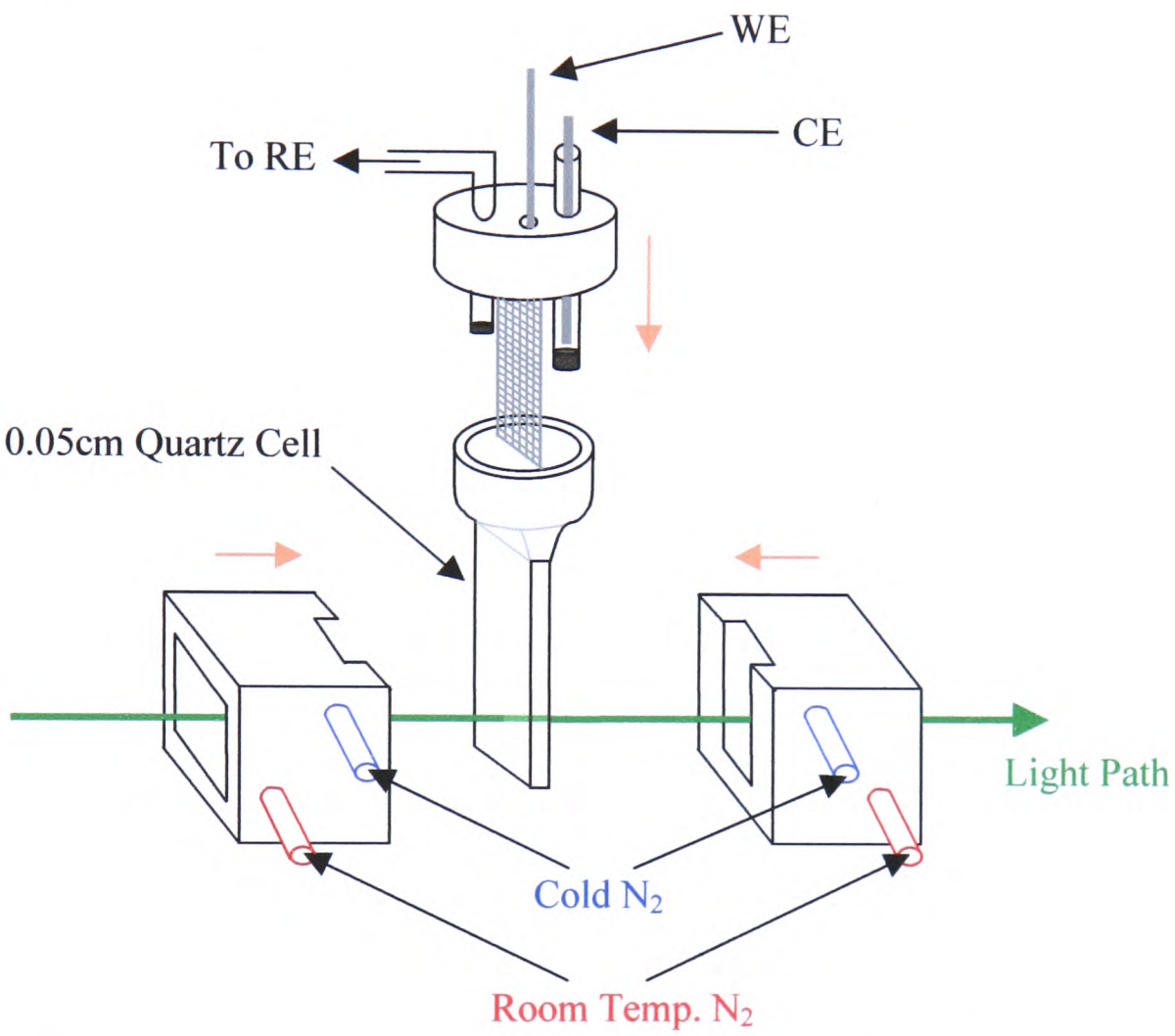

Figure 2 7 Schematic diagram of the experimental set up used for UV/vis spectroelectrochemistry.

2.3.2 Electron Paramagnetic Resonance Spectroscopy

Electron paramagnetic resonance (epr) is a powerful technique for studying complexes with unpaired electrons. It can be viewed as the electronic analogue of nuclear magnetic resonance.

All spectra were recorded on an X-band Bruker ER200D-SCR spectrometer, connected to a Datalink 486DX PC running Epr Acquisition System, version 2.42 software. *In situ* eprs were electrogenerated using a BAS CV-27 voltammograph.

Variable temperature work was carried out using a Bruker ER4111VT variable temperature unit. All epr spectra were corrected for dpph the g value of which is 2.0036 ± 0.0003. Unless stated otherwise all platinum hyperfine coupling constants have negative sign.

A typical epr spectrometer has a radiation source, usually a klystron, a sample cavity that is held between the poles of an electromagnet, a detector and a recorder system, either an X-Y plotter or a computer. The most common klystron operates in the X band region of the microwave spectrum at 9.5 GHz, but other frequencies *eg* 35 GHz, Q band, are available. The cavity size is chosen so that a standing wave is set up and the sample is then placed in the region of highest energy density. The radiation detector is a diode that converts the microwave radiation into direct current. To reduce noise and improve sensitivity the detector uses small-amplitude magnetic field modulation and is phase sensitive, resulting in the epr signal being presented as a first derivative.[36]

2.3.2.1 Theory

The basis of epr spectroscopy is the spin orientation an electron adopts along the direction defined by an applied magnetic field B.[10] The energy difference between the states $m_s = + ½$ and $m_s = - ½$ is given by Equation 2.2, below.

$$\Delta E = g\,\mu_B\,B \qquad (2.2)$$

ΔE = energy difference
g = proportionality factor
μ_B = Bohr magneton
B = applied magnetic field

μ_B is the Bohr magneton and g is a proportionality factor equal to 2.0023 for a free electron (g_e). Radical species have a g value close to 2 but for transition metal complexes the g value often lies between 1.4 and 3.0.[37]

The g value can be determined by noting the applied field needed to achieve resonant absorption for a given microwave frequency. If the complex studied is part of a single

crystal, g may be measured along different directions and used to determine the symmetry.

If a sample is exposed to electromagnetic radiation of frequency ν, a strong absorption or resonance occurs when the magnetic field satisfies the condition given in Equation 2.3.

$$h\nu = g\,\mu_B\,B \qquad (2.3)$$

h = Planck constant
ν = frequency
g = proportionality factor
μ_B = Bohr magneton
B= applied magnetic field

There are two contributions to the electronic magnetic field: the spinning of the electron on its axis, the spin magnetic moment m_s and the motion of the electron about the atomic nucleus, orbital angular momentum l. Interaction of the electron with a nucleus of $I > 0$ (I is the nuclear spin), splits the energy levels into m_I, the nuclear spin quantum number.[38] The energy level diagram, which illustrates the electronic transitions possible for a free hydrogen atom where $I = ½$ and $S = ½$ is shown below in Figure 2.8.

When the applied magnetic field B is zero, $m_s + ½$ and $m_s - ½$ levels are degenerate. However, when the sample is placed in an applied magnetic field these two energy levels diverge. The effect of the orbital angular momentum now comes into play and each of the two energy levels $m_s + ½$ and $m_s - ½$ are further split into $m_I + ½$ and $m_I - ½$ (as I for H is ½).[38] Although we now have four different energy levels between which transitions can occur, the selection rules $\Delta M_s = +1 / -1$ and $\Delta M_I = 0$, indicate that for epr spectroscopy only the two transitions shown are allowed. These two allowed transitions are shown on the epr recorder as two identical peaks, the separation between which is A_o, the energy difference between the two allowed transitions. If $I = 0$ then only one transition (between the two m_s levels) occurs and only one line, with twice the intensity of the two lines arising from the $I = ½$ case is observed.

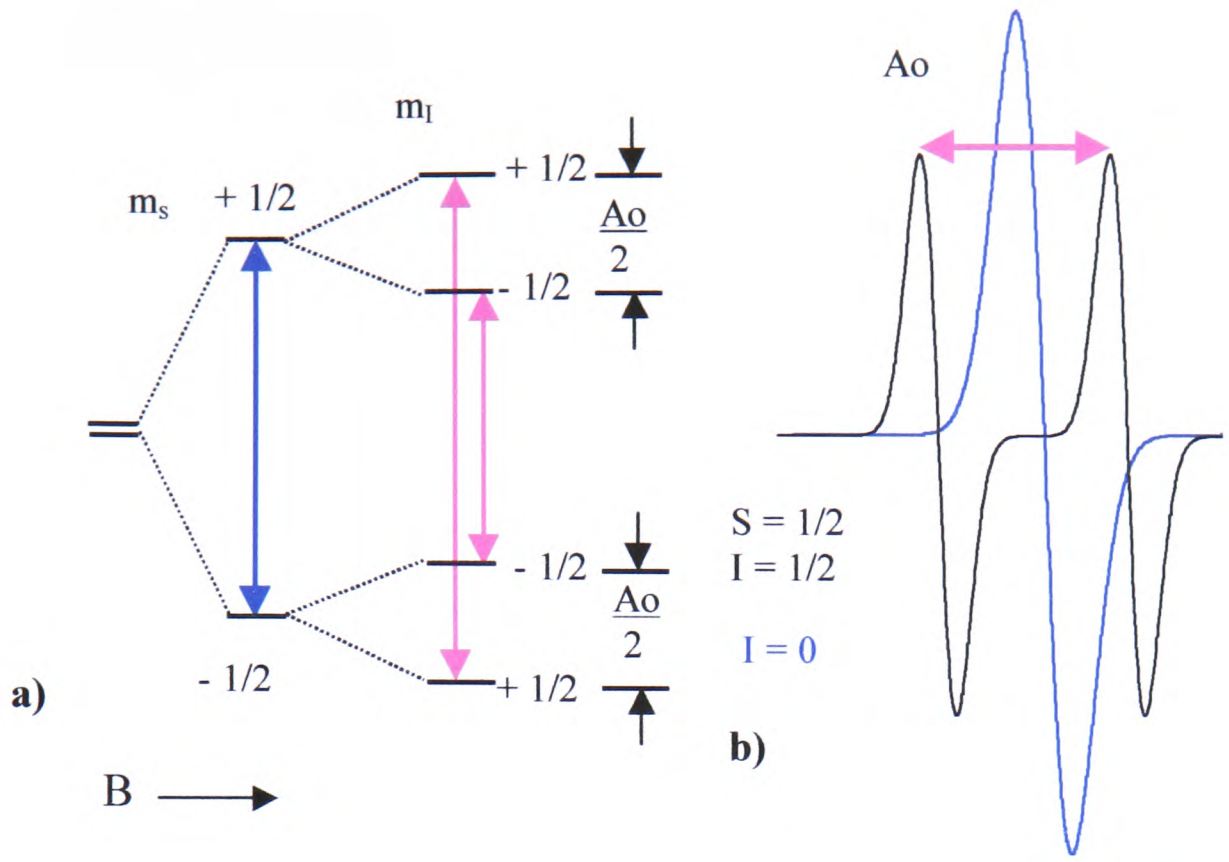

Figure 2.8 Schematic showing energy level diagrams of epr transitions for a ^{1}H nucleus when S = ½ and I = ½ with the corresponding epr signals.

If the nuclear spin of the epr active nucleus, in this case N, is 1 then the epr signal produces a different pattern, see Figure 2.9. The energy level diagram for the spin magnetic moment is the same as for hydrogen, but now m_I can be either = +1, 0, or -1. Thus each of the two original energy levels can be split into three. As the ΔM_s = +1 / -1 and $\Delta M_I = 0$ selection rules are obeyed, there are 3 allowed transitions and therefore 3 lines of equal intensity each separated by a^N.

These examples illustrate the importance of intensity in providing evidence for the location of the unpaired electron in epr spectroscopy. A three line spectrum can arise by either coupling of the unpaired electron to one N nucleus, giving three lines of equal intensity, or to two equivalent H nuclei, giving a pattern with a 1:2:1 intensity. The intensity of an epr signal is proportional to concentration and the probability of a given transition occurring. Intensity also gives information on what type of spin system is giving rise to the spectrum.

As a given magnetic nucleus of nuclear spin I can adopt 2I + 1 different orientations it can result in 2I + 1 different contributions to the local field. Consequently epr

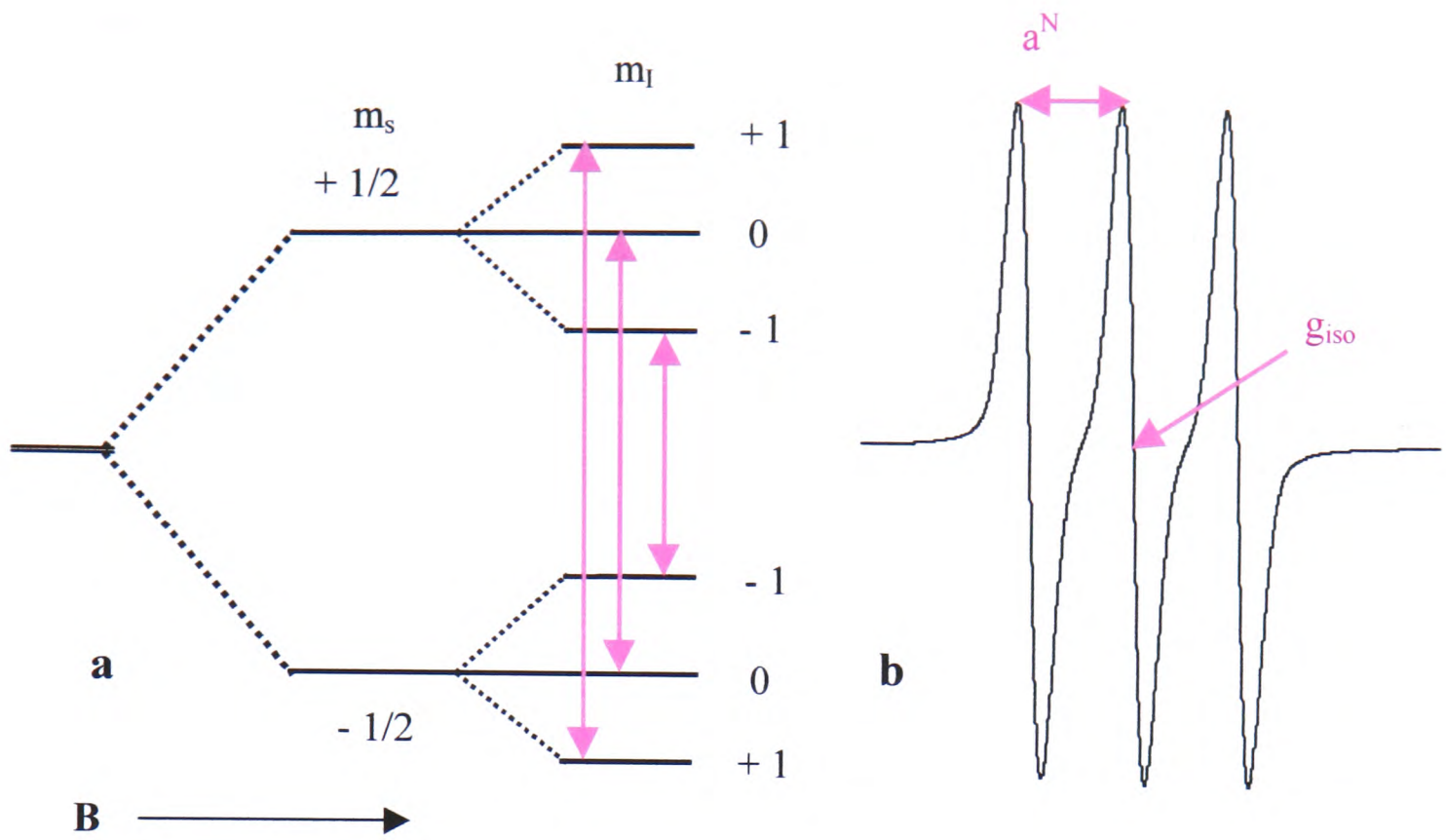

Figure 2.9 a) energy level diagram indicating allowed transitions for a ^{14}N nucleus where S = ½ and I = 1. **b)** corresponding epr signal.

spectra are often split into multiplets known as their hyperfine structure.[10] The 2I + 1 resonance conditions responsible for the hyperfine structure is written as shown in Equation 2.4.

$$h\nu = g\,\mu_B\,(B + A\,m_I) \qquad (2.4)$$

A is the hyperfine splitting constant characteristic of the nuclei itself (its magnetic moment) and the probability that an unpaired electron will be found near it.

In anisotropic systems such as frozen solutions and powders, the g factors are regarded as symmetric tensors. The tensor can be diagonalised to give three principal g factors, g_{xxx}, g_{yyy} and g_{zzz}. In a system with axial symmetry one of these terms ($g_{\|}$) is different from the other two ($g_{\perp}$) and for lower symmetries the three terms are all different.[37] This is known as a rhombic signal.

Epr spectra of transition metal complexes may be difficult to interpret but they can be used to study electron distribution. Values of $g_{\|}$ and $g_{\perp}$ can show which d orbitals are

occupied, indicating for example, the direction in which Jahn-Teller distortion has occurred. The magnitude of A, for the magnetic nuclei of the central nucleus, or of the ligands, indicates the degree to which electrons are delocalised from the central metal atom to the surrounding ligands. As the energy of the ligand orbitals approaches that of the metal, interaction between them increases. The orbital occupied by the unpaired electron becomes more ligand-like and interacts less with the metal nucleus and hence the magnitude of the metal hyperfine coupling constant will decrease.[10]

2.3.2.2 *In situ* Variable Temperature Epr

Variable temperature *in situ* epr is ideally suited to the study of unstable radicals as they are often difficult to generate chemically and can decompose if generated by bulk electrolysis at low temperature and then transferred, albeit under an inert atmosphere, into an ordinary flat cell or epr tube.

One problem with epr is that solvents absorb microwaves. To minimise this unwanted absorption, a solvent with a lower dielectric constant should be used but, this is not always practical so the pathway of the microwave through the solvent is miniinised instead.[38] Thus flat epr cells are used. However, as the working electrode is positioned in the flat cell with distant CE and RE, there are significant solution resistance effects that mean good control of the WE potential is not always possible. These effects will be discussed further in the next section.

Line broadening is another factor that must be taken into account when choosing a suitable epr solvent. In more viscous solvents the molecules tumble more slowly, leading to line broadening in the epr signal. Viscosity is affected by melting point, an important property to consider when the epr active species is generated at low temperature. For example, if an epr active compound is generated in DMF (mp = 212 K) at 233K, a temperature where the viscosity of DMF is increased, then much

of the fine structure will be lost due to line broadening. Figure 2.10 shows a range of epr spectra taken for $[Pt(4,4'\text{-}(NO_2)_2\text{-}bpyCl_2]^{2-}$ over the range 233 K – 313 K and illustrates the effect varying the temperature has on the resolution of an epr spectrum In such a case it would be better to use a less viscous solvent. DCM would be ideal as it has a significantly lower melting point and dielectric constant compared to DMF. However, solubility problems may arise in this solvent.

A standard *in situ* variable temperature epr cell is shown in Figure 2.11 and consists of a high grade quartz flat cell onto which two quartz side arms have been attached. The Pt wire WE is placed inside the cell so that it goes down into the flat part. All of the WE except that in the flat cell is covered with a teflon sleeve in order to prevent the electrolysis of the electroactive species outside the flat cell. The part of the Pt wire in the flat cell is flattened with a small amount of Pt gauze welded to it. There is a small stopper at the bottom of the flat cell for easy removal of the reaction solution. The Pt gauze CE is separated from the reaction solution by a frit. A commercially available Ag/AgCl RE is then placed in the other side arm. This cell assembly is then placed in a specially designed quartz holder in the epr cavity.

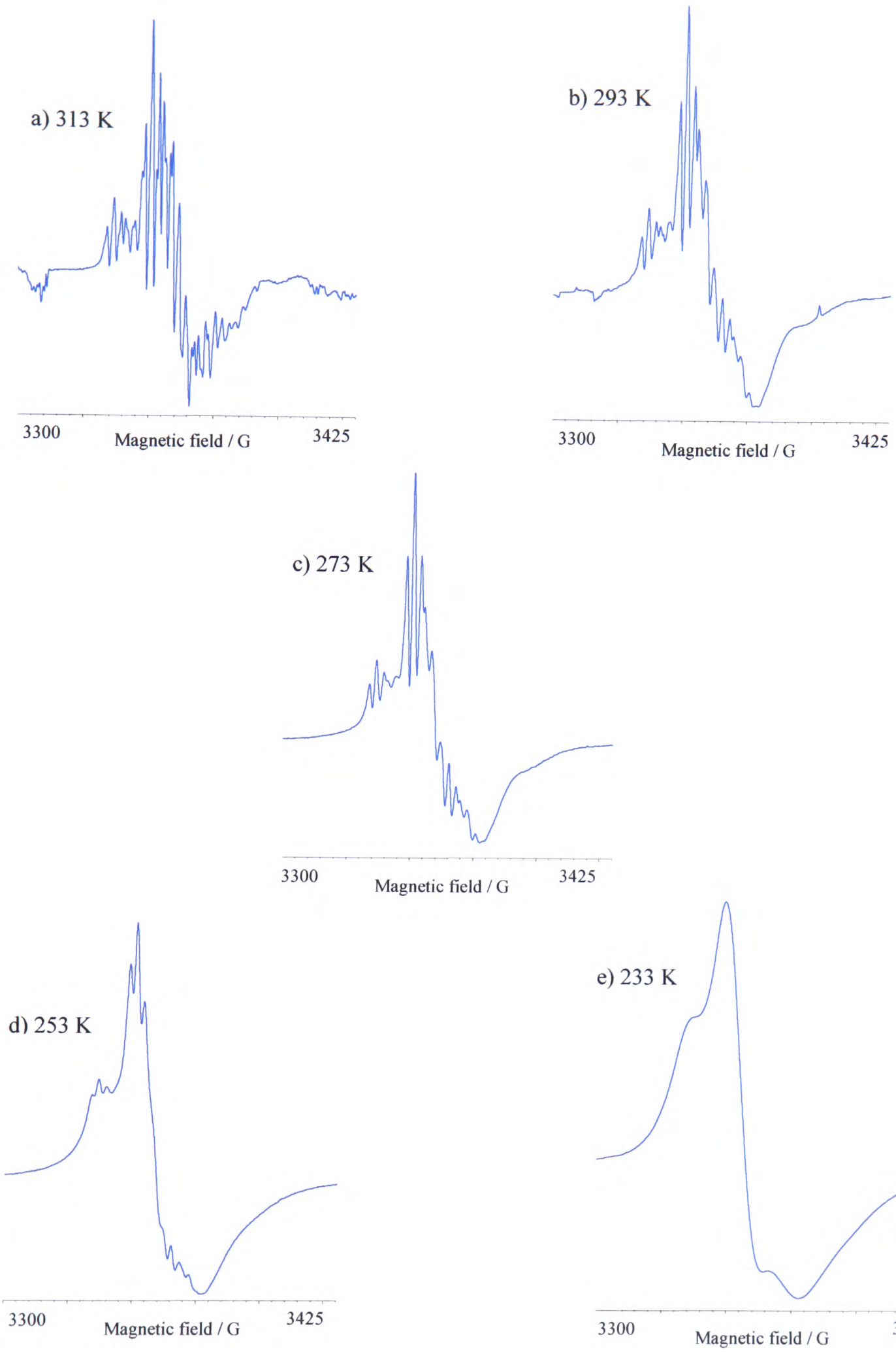

Figure 2. 10 The effect of temperature on epr signals. $[Pt(4,4'\text{-}(NO_2)_2\text{-bpy})Cl_2]^{2-}$ generated *in situ* at 273K, in 0.5 M $TBABF_4$/DMF, E_{gen} –0.75 V.

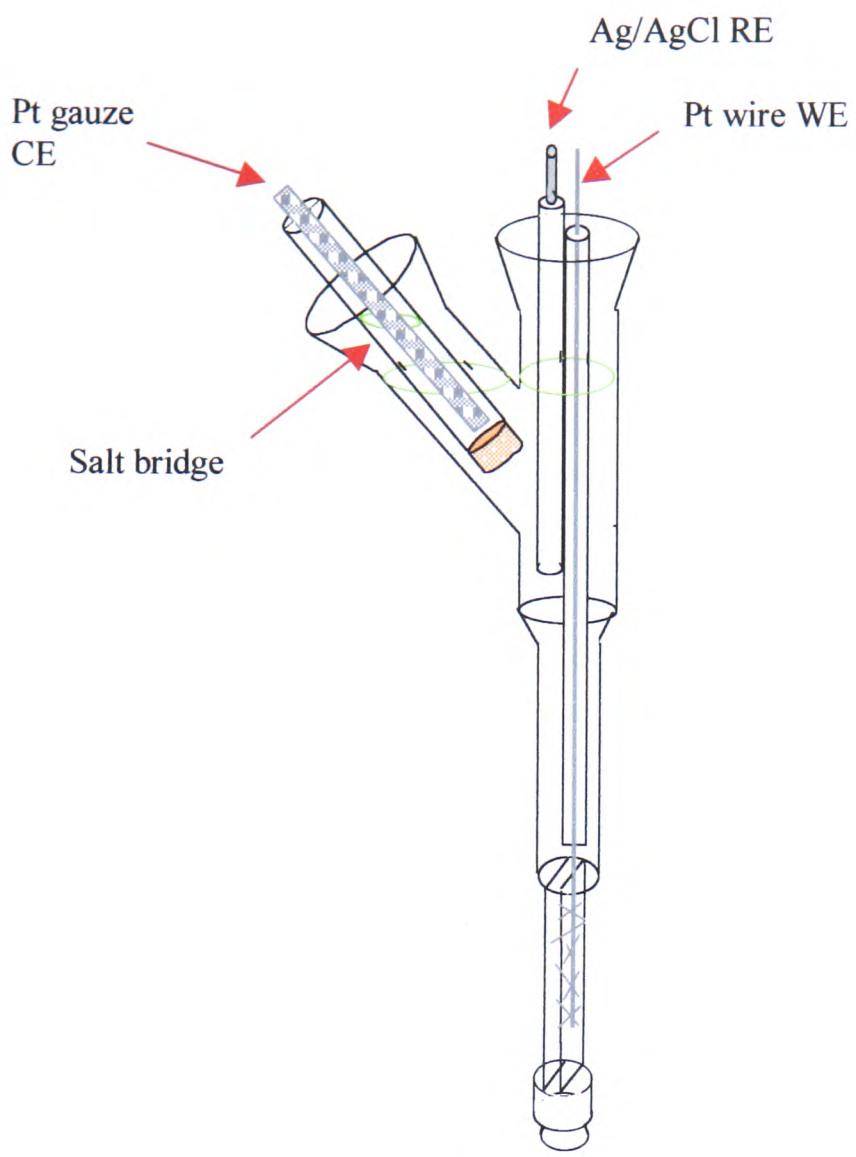

Figure 2. 11 The original set up of the *in situ*, variable temperature epr cell.

A sealed dewar containing liquid nitrogen and a heater is connected to the quartz sample holder by specially insulated tubing. Increasing the heater power causes N_2 to evaporate and move from the dewar and into the quartz holder in the epr cavity. The temperature is measured by a thermocouple that is inserted through the bottom of the quartz holder into the proximity of the flat cell. To prevent the epr cell from frosting over, room temperature N_2 is blown into the cavity and around the flat cell.

2.3.2.3 Development of a New *In situ* Epr Cell

In all of the new cell designs tested here the electroactive species used was di-2-pyridyl ketone, (dpk), dissolved in 0.1 M $TBABF_4$/DMF. The dpk solution is colourless when in its neutral form and dark blue when in the mono-reduced state.

Although the variable temperature *in situ* epr cell described in the previous section worked, alterations were made to the set up to see if the design could be improved. This section attempts to describe each change to the experimental set up and discuss its advantages and disadvantages.

Two kinds of resistive effects are observed in *in situ* epr flat cells, both brought about by the distance between the portion of the WE in the flat cell and the other two electrodes. There is an uncompensated resistance R_u, between the WE and the RE that causes the actual potential at the WE to be different from the measured potential. The other resistive effect, a non-uniform current distribution across the surface of the WE, arises due to differences in solution resistance between different points in the solution near the WE and the CE.

Altering the position of the CE. To try and minimise these effects, a number of alterations were made to the cell set up, the first being to move the positions of the electrodes in the cell.[39] The CE was moved from the side arm at the top of the cell to the bottom of the flat cell to lessen the distance between the two electrodes and induce generation of the electroactive species in the flat cell.

A small rubber bung was made to replace the glass stopper at the bottom of the cell. A small piece of Pt wire was forced through the rubber so that it protruded into the bottom of the cell. The dimensions of the variable temperature attachment meant that the Pt wire could not be connected directly to the power pack. A piece of copper wire 30 cm long was welded onto the Pt wire to overcome this problem.

With this experimental set up an epr signal was recorded almost immediately when the electrogeneration potential was applied. However, the signal always began to collapse after 30 minutes. Bubbles of gas formed in the flat part of the epr cell. This arrangement of the electrodes results in a very high current flow between the WE and the CE such that the solvent is degraded (as evidenced by gas formation). The poor electrode configuration also makes potential control of the WE difficult. This method of having the CE in the bottom of the cell was also impractical as it was difficult to fit the epr cell into the epr cavity because of the long Cu wire attached to the CE and correct positioning of the thermocouple and hence efficient temperature control proved almost impossible.

Replacing the teflon tubing. The generation of the epr active species in the original cell assembly was very slow. It was thought that the teflon tubing used to shield the WE may be blocking the top of the flat cell and preventing current flow between the electrodes. The section of WE not in the flat cell was wrapped in PTFE tape to see if this would act as a shield, while taking up less space in the cell.

However, once the current was switched on, the whole the cell, with the exception of the flat part, quickly turned dark blue. This indicated that the PTFE tape was not a successful insulator and that the epr active species was being generated preferentially in the upper part of the epr cell, this being closer to the RE and CE. For variable temperature *in situ* epr it is important that the electroactive species is generated in the flat part of the cell as this part is directly in the epr cavity and it is only in this section that the temperature can be controlled accurately.

The smallest possible diameter of teflon tubing that would fit was placed over the Pt wire WE. To allow maximum current flow between the WE in the flat part of the cell and the CE, care was taken not to block the mouth of the flat cell with the tubing.

Removing the CE from its salt bridge. In previous experiments the Pt gauze CE had always been separated from the reaction solution to prevent contamination of the

electrogenerated solution with any species generated at the CE during the course of the reaction. However, the frit will hamper the current flow in the solution and slow down the electrogeneration.

A number of test eprs were carried out with the CE placed directly into the solution. This did not affect the epr signal in any way but it did decrease the generation time of the epr active species. Thus we can conclude that if any species are electrogenerated at the CE surface, this is too distant from the flat cell to have any effect on the epr signal of the species of interest. From this point all epr experiments were carried out with the CE placed directly in the solution.

Changing the type of WE. In the original experimental set up the WE was a Pt wire flattened at one end with Pt gauze welded to it. This made cleaning of the flat cell awkward. When filled the gauze made it difficult to remove the numerous small air bubbles from the flat cell and this in turn caused background noise in the epr signal.

The original WE was replaced with a Pt wire (0.5 mm diameter). This made the removal of air bubbles from the flat cell easier. Background noise in the epr signal was significantly reduced, allowing weak signals to be observed. Thus epr could be successfully carried out on very dilute solutions. Unfortunately the generation time of the electroactive species was increased because less of the solution was in direct contact with the WE. Otherwise changing the WE to a single Pt wire is very successful.

To overcome this difficulty a narrow strip of Pt gauze (2 mm wide) was welded onto a piece of Pt wire of 0.25 mm diameter to make a WE similar to those used in the OTTLE cell. The gauze extends down inside the flat cell for its entire length. This greatly increases the contact between solution and WE and decreases the time taken for an epr signal to grow in. The higher concentration of electroactive species generated compensates for the small increase in background noise picked up in the resultant spectrum.

The variable temperature *in situ* epr set up developed and refined here, see Figure 2.12, remains unaltered from the original except for two changes. The Pt gauze CE is now placed directly into the solution under study and depending on reaction conditions such as solvent and generation temperature, either a Pt wire or gauze WE is used. These alterations decrease the solution resistance effects, minimising the potential drop between the RE and WE and maximising the current density.

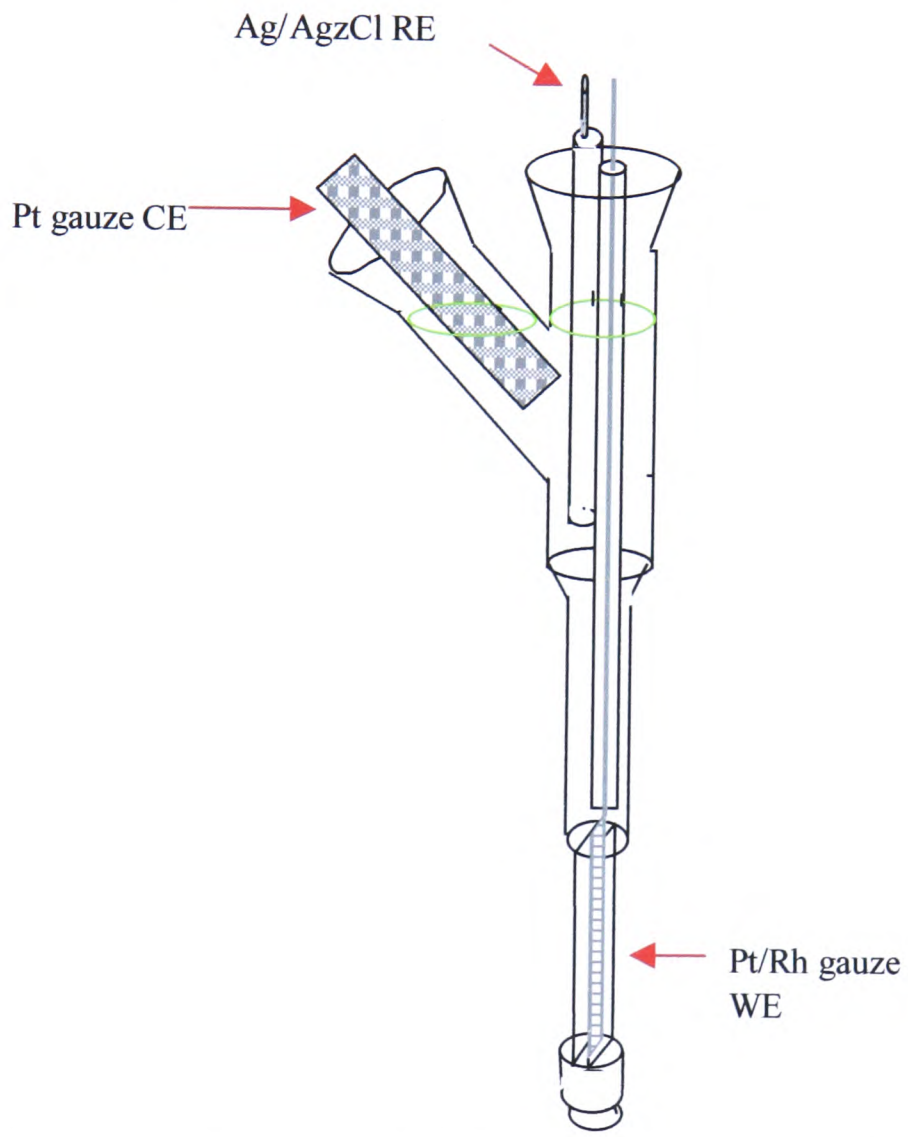

Figure 2 12 The set up of the variable temperature *in situ* epr cell, as used for the experiments detailed here. Note the WE is now a Pt gauze and the CE now sits directly in the solution.

2.3.3 IR Spectroelectrochemistry

All spectra were recorded on a Perkin Elmer Paragon 1000 FT-IR spectrometer. The electrochemistry was controlled by a Dell GX110 PC with General Purpose Electrochemical System (GPES) version 4.8 software, connected to an autolab system containing a PGSTAT 10 potentiostat.

The products of bulk electrolysis can be measured *in situ* by IR spectroscopy. Figure 2.13 shows the set up of a newly developed *in situ* IR cell. The set up consists of a solution IR cell with CsF windows with a syringe attached to each outlet. The upper syringe acts as a reservoir where the actual electrochemistry takes place. The reservoir contains an electrode configuration very similar to that used for coulometry. A Ag/AgCl RE is used, a Pt rod acts as the CE and the WE can be changed between a Pt basket for bulk electrolysis and a Pt microdisc electrode to monitor the course of the reaction. N_2 is bubbled through the solution in the reservoir to purge it of oxygen and to thoroughly mix the solution ensuring maximum conversion of the electroactive species. In this set up the counter electrode is contained within a separate compartment fitted with a conducting frit. The total cell volume is 2 ml.

The lower syringe is used to draw some of the converted species from the reservoir down into the solution IR cell so that the progress of the reaction can be monitored. Once the spectrum has been taken the solution in the cell can be easily pumped back into the reservoir and the reaction continued. There is no need to stop the electrolysis or the flow of N_2 while the IR is being run.

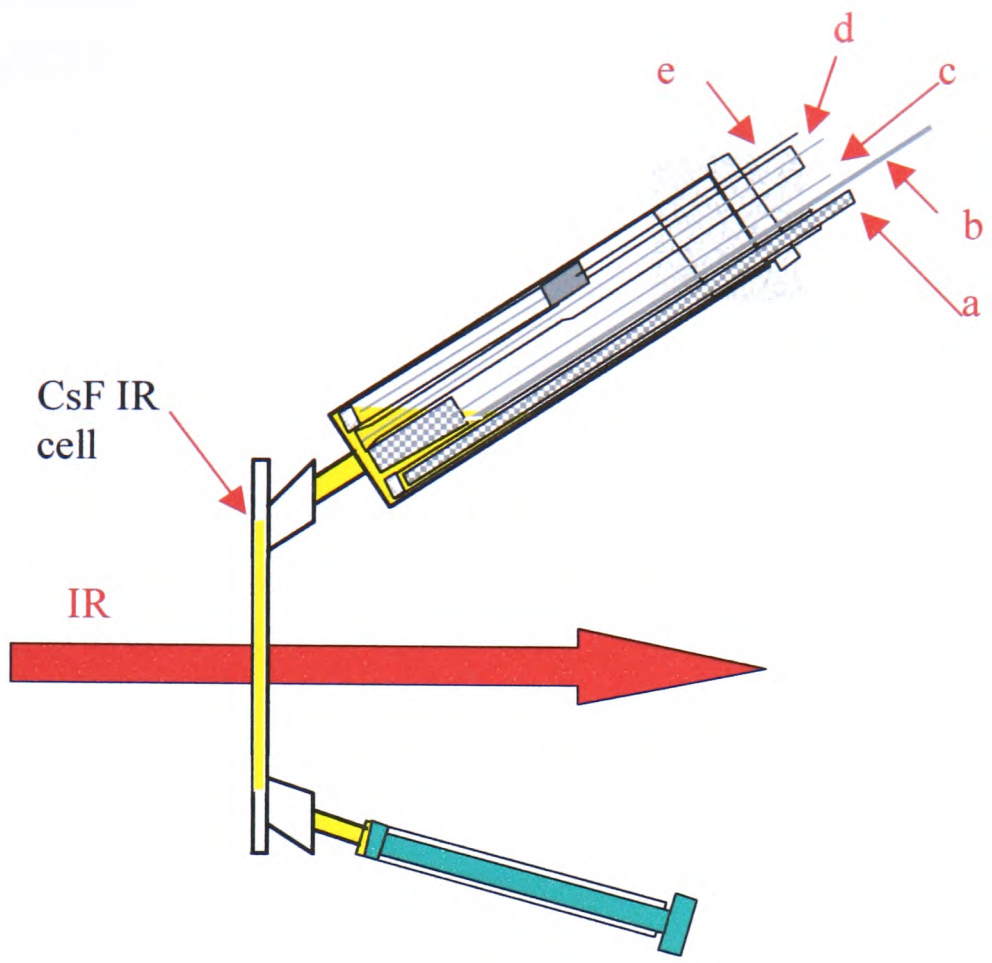

Figure 2.13 Schematic of the newly developed *in situ* IR cell: a) Pt counter electrode, b) Nitrogen outlet, c) Pt basket WE, d) Pt microdisc WE, e) Ag/AgCl RE.

This basic set up has worked well for electroactive species that are stable at room temperature. Work is in progress to develop a version that will enable *in situ* IR to be carried out at low temperature.

2.4 Emission Spectroscopy

Emission spectroscopy is a technique for studying the electronically excited states of molecules. Luminescence methods are inherently sensitive as the detection limits are one to three orders of magnitude smaller than those of absorption spectroscopy.[40] However, not all compounds exhibit emission spectra so luminescence methods are much less widely applicable than absorption methods.

All spectra were recorded on a Jobin Yvon Spex Fluoromax spectrofluorimeter, connected to a DCS Datalink PC running Instruments S.A. Datamax software. All spectra were recorded in a DMSO/EtOH solvent mix. Solution spectra were measured in disposable poly(methylmethacrylate) (PMMA) cuvettes (Fisons 4.5 ml) with a 1 cm path length. Frozen glass spectra were recorded in standard Wilmad 5 mm quartz nmr tubes contained in a liquid nitrogen filled, fused silica dewar.

The excitation source in this spectrofluorimeter is a 150 W continuous ozone-free xenon lamp, with modified Czerny-Turner spectrometers in both the emission and excitation positions. Gratings in both the excitation and emission positions allow light dispersion from 200-900 nm and the two types of experiment to be run. If the excitation wavelength is held constant and the emission spectrometer scanned, then the result is an emission spectrum. If the emission spectrometer is held at a constant wavelength and the excitation wavelength scanned, then an excitation spectrum results. Luminescence is observed at right angles to the excitation beam to minimise scattering from the solution and the cell walls.[40] Figure 2.14, shows the design of a typical spectrofluorimeter.

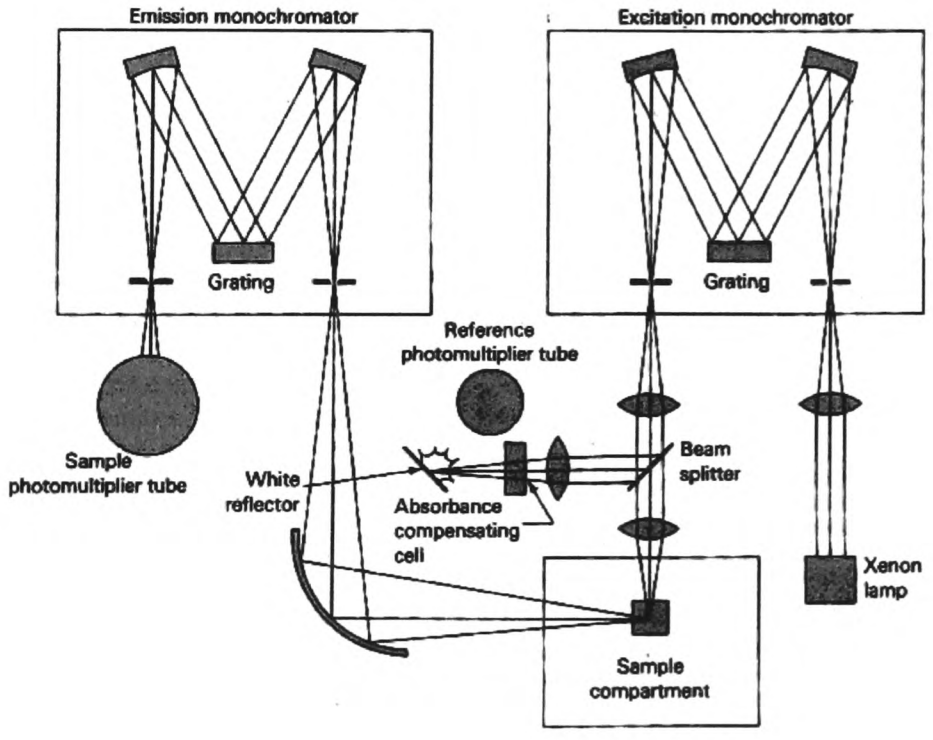

Figure 2. 14 Schematic showing the components of a spectrofluorimeter. [40]

2.4.1 Theory

A radiative decay process is one in which a molecule discards its excitation energy as a photon. Non-radiative decay is more common and occurs when the excess energy in an electronically excited state is transferred into vibration, rotation and translation of the surrounding molecules.[41] Such thermal degradation converts the excitation energy into thermal motion of the environment *ie* heat.

There are two types of radiative decay process; fluorescence and phosphorescence. They are alike in that excitation is brought about by absorption of a photon but, fluorescence differs from phosphorescence in that the electronic energy transition from the excited state back to the ground state does not involve a change in multiplicity.[40]

The sequence of steps involved in fluorescence is shown below in Figure 2.15. The initial absorption excites the molecule to an upper electronic excited state. The excited molecule is subjected to collisions with other molecules (both solvent and solute), causing it to lose energy in a process known as radiative decay until the lowest vibrational level of the excited electronic state is reached. If the surrounding molecules are unable to accept the large amount of energy needed to quench the fluorescence and return the molecule to the ground electronic state, then the molecule may undergo spontaneous emission and emit the excess energy that remains as radiation. In line with the Franck-Condon principle in which the most probable vibrational component of an electronic transition is the one involving no change in the position of the nuclei, the downward electronic transition is vertical and the fluorescence spectrum has a vibrational structure characteristic of the lower electronic state.

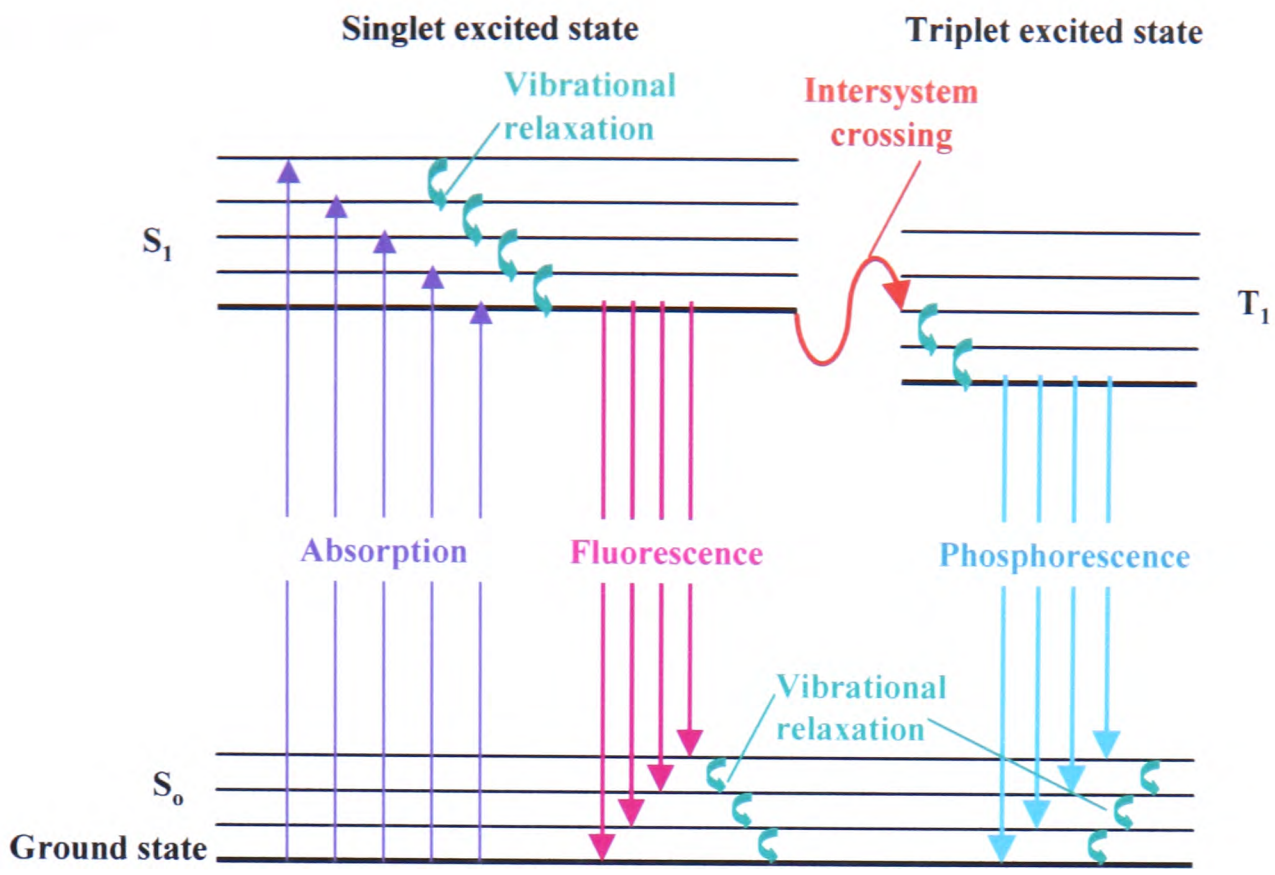

Figure 2.15 Schematic representation of energy transitions involved in a photoluminescent system.

Fluorescence occurs at lower energy than the corresponding absorption because after excitation some of the energy of the excited state molecule is transferred to the surroundings during radiationless decay of the excited states. Such a mechanism suggests that the intensity of fluorescence is dependent on the ability of the solvent molecules to accept electronic and vibrational quanta. Solvents in which the molecules have widely spaced vibrational levels can accept the large quanta of electronic energy and hence quench fluorescence.[41]

If a triplet excited state, *ie* one where the electron spins are unpaired, is present then excitation leads to phosphorescence. To achieve this the excited state must undergo intersystem crossing. The probability of this transition is greater if the vibrational levels of the two states overlap. For instance, in the singlet-triplet transition shown in Figure 2.15 the lowest singlet vibrational state overlaps one of the upper triplet vibrational levels, making the change in spin state more probable. Singlet-triplet transitions are formally spin forbidden processes, however, when a molecule contains a heavy atom such as Pt, spin-orbit coupling is large and singlet-triplet transitions

occur more readily.[41] When an excited molecule crosses into a triplet state it continues to give up energy to the surroundings and steps down the vibrational levels until it reaches the lowest energy vibrational level of the excited triplet state. The excited molecule is trapped here because, in line with Hund's rule, the triplet is always lower in energy than the corresponding singlet. The molecule is able to emit weakly to the ground state as the large spin orbit coupling responsible for the intersystem crossing also allows the radiative transition between the triplet excited state and the singlet ground state.

Phosphorescence spectra appear at much lower energy than the corresponding excitation and fluorescence spectra due to the energy difference between the singlet and triplet excited states.[40] This shift to lower energy compared to the excitation spectra is often used to distinguish between fluorescence and phosphorescence.

CHAPTER 3:

5,5'-Disubstituted Bipyridines and Their Complexes With Platinum(II).

Chapter 3 5,5'-Disubstituted Bipyridines and Their Complexes With Platinum(II).

Reported in this chapter are the synthesis, redox chemistry and spectroelectrochemistry (UV/vis/nir, epr) of a series of complexes of the general formula [Pt(5,5'-$(X)_2$-bpy)Cl_2] where X is Me, CO_2Et, CO_2Me, and NH_2. In this chapter evidence is presented that the electronic character of the redox orbital is similar in each case, *ie* it is the lowest unoccupied π^* orbital of the $(X)_2$-bpy ligand. Comparison with [Pt(4,4'-$(X)_2$-bpy)Cl_2] complexes indicates that the 5,5'- position is electronically the more important site of substitution on the bipyridine ligand.

3.1 Introduction

There has been considerable interest in synthesising derivatives of the 2,2'-bipyrine (bpy) ligand.[42-46] By altering the positions of the substituents or the substituents themselves it is possible to tune the photophysical and electrochemical properties of the ligand itself and any complexes derived from it. Investigations have centred on di-substituted *tris*-bpy complexes of Ru(II) because such complexes have uses in display devices,[47] as water-oxidation catalysts[1] and as luminescent sensors for organic molecules,[3] metal cations[48] and lanthanides.[4]

Ruthenium bpy complexes have several interesting chemical and spectral properties. They have strong visible absorptions arising from their characteristic MLCT transitions which produce long lived excited triplet states. These excited states have redox chemistry which differ from that of the ground state.[49, 50] In addition, Ru(II) in an octahedral ligand field is inert to ligand substitution, which allows the ground state redox chemistry to be studied without complications from ligand exchange reactions.[51]

Elliott and Hershenhart carried out extensive electrochemical and spectral investigations on a variety of bpy ligands and their *tris* complexes with Ru.[51] The

position and type of substitution was varied systematically. They found the presence of certain electron withdrawing substituents on the bpy ring has a stabilising effect on the low formal oxidation states in these ruthenium complexes, thus allowing several additional reductions to be observed, compared to unsubstituted $[Ru(bpy)_3]^{2+}$. Such a substituent is also expected to red-shift absorption MLCT maxima and related emission spectra. Spectral studies indicate that reduction electrons are almost totally localised on a single bpy ligand, forming a chelated bpy $^{1-}$ radical anion rather than delocalised over the whole complex as was previously thought.[51, 52]

To date most work on di-substituted 2,2'-bipyridines has been carried out on the 4,4' position. This may be due to the difficulty in synthesising the ligands substituted in the 5 and 5' positions as these positions on 2,2'-bpy are unreactive to electrophilic attack and nitration at these sites has been reported as unsuccessful.[44, 53] Originally it was believed that 4,4' positions on di-substituted bpy were electronically the most important sites of substitution but, in their study of bipyridinecarbonitrile complexes of Mo and W, Baxter and co-workers concluded that the nitrile substituents in the 5,5'-dicarbonitrile-2,2'-bpy complex exert a greater electron-withdrawing effect upon the metal than in the isomeric 4,4'-dicarbonitrile-2,2'-bpy complex.[54] Furthermore, DFT (density functional theory) calculations carried out on 2,2'-bipyridine show that the electron density at the 5,5' position is significantly greater that at the 4,4' position. Hence we would expect substitution at the 5,5' position to have a greater effect on the electronic character of the species than substitution at the 4,4' position.[33]

A number of authors have attempted to correlate the physical properties of disubstituted bipyridines with σ, the Hammett parameter of the substituent X. σ can be viewed as the measure of the electron withdrawing (positive σ values) or donating (negative σ values) power of X.[55] Connor *et al.* report a linear correlation of σ_p with the absorption and emission maxima of $[Mo(4,4'\text{-}(X)_2\text{-bpy})(CO)_4]$, (X is Cl, CO_2Me, NMe_2, OMe, Me and CMe_3).[56] Pichot *et al.* note a rough linear correlation between the reduction potentials of the free ligands and σ_p of the electron withdrawing groups for $[Ru(5,5'\text{-}(X)_2\text{-bpy})_3]^{2+}$ [47]. A much better linear correlation between the first

reduction potential of the free ligand and the first ligand-based reduction of the corresponding ruthenium *tris* complexes was found.[51]

The electrochemical properties of 5,5'-disubstituted bpy have been exploited in the development of a water-oxidation catalyst.[1] Controlled-potential electrolysis of *cis*-Ru(II)$L_2(OH_2)_2^{2+}$, (where L_2 is 5,5'-$(COOH)_2$-bpy), in 0.5 M H_2SO_4 solution leads to the formation of a relatively durable and active molecular water-oxidation catalyst. The actual active catalyst is an oxobridged dimer, $[L_2(H_2O)Ru\text{-}O\text{-}Ru(OH_2)L_2]^{4+}$ which is highly effective in mediating the thermal and visible light induced generation of oxygen from water. Rotzinger and co-workers attributed the greatly enhanced catalytic activity and durability of the dimeric complex to the introduction of the carboxylic acid substituents in the 5,5' position of the bpy in place of the 4,4' positions that had previously been used.[1]

A few platinum complexes of derivatised bpys have been reported. Yoo *et al.* reported on the synthesis of [Pt(3,3'-$(X)_2$-bpy)Cl_2] where X is COOH or CH_2OH.[57] X-ray structures indicate that the two pyridine rings of the bpy ligand in both compounds cannot attain the coplanar state owing to the steric bulkiness of the substituents at the 3,3' positions. The solvolysis of [Pt(3,3'-$(COOH)_2$-bpy)Cl_2] in DMF leads to the formation of *cis*-[Pt$(Me_2SO)_2Cl_2$], the first example of both amine donors in a Pt amine complex having been displaced by solvent DMSO molecules without invoking the dissociation of the co-ordinated chloride atoms. The driving force for the dissociation of bpy from the complex is attributed to the steric interaction between the carboxylic acid groups in the 3,3' position.[57] Other reports have noted the UV/vis absorption spectra of [Pt(4,4'-$(X)_2$-bpy)$(CN)_2$], (where X = H, Me, COOH, ^{t}Bu) and [Pt(4,4'-$(X)_2$-bpy)Cl_2], (X = Me, Ph).[31, 58]

In his thesis McInnes describes the synthesis, redox chemistry and spectroelectrochemistry of a series of complexes of the type [Pt(4,4'-$(X)_2$-bpy)Cl_2] where X = NH_2, OEt, Me, H, Ph, Cl, CO_2Me and NO_2. He concluded that the presence of electron withdrawing substituents causes both the free and bound ligand

to reduce at more positive potentials, while electron donating substituents have the opposite effect.[25]

A literature search gave only one example of a platinum complex derivatised at the 5 and 5' positions. Che *et al.* report on the photophysics and photochemistry of $[Pt(5,5'\text{-}(Me)_2\text{-}bpy)(CN)_2]$.[59] The UV/vis spectrum shows an intense $\pi \rightarrow \pi^*$ transition at 320 nm as well as intense photoluminescence (emission maximum, 502 nm) in fluid solution at room temperature. Cyclic voltammetry at room temperature in DMF shows the complex undergoes two ligand-centred reductions, (at –1.59 V and –2.23 V *vs* $Ag/AgNO_3$ (0.1 M)). An irreversible oxidation of the Pt(II) complex occurs at ~1.1 V. The excited $\pi \rightarrow \pi^*$ triplet of $[Pt(5,5'\text{-}(Me)_2\text{-}bpy)(CN)_2]$ is a powerful one electron oxidant and reductant which undergoes oxidative and reductive quenching with inorganic and organic substrates.[59]

It is the complexes of general formula $[Pt(5,5'\text{-}(X)_2\text{-}bpy)Cl_2]$ where X is changed from an electron-donor ($X= NH_2$) to an electron acceptor ($X= CO_2Et$) that will be discussed in this chapter. The comparison of $E_{1/2}$ values for $[Pt(5,5'\text{-}(X)_2\text{-}bpy)Cl_2]$ and the Hammett parameter σ_m with the corresponding values for the 4,4' analogue indicate that the 5,5' position on the bpy ligand is electronically the more important site of substitution. Work reported here suggests the reduction electron of the mono-reduced species enters an orbital that is primarily ligand based.

3.2 Results and Discussion

3.2.1 5,5'-$(X)_2$-bpy

3.2.1.1 Redox Chemistry of 5,5'-$(X)_2$-bpy

Cyclic voltammetric studies of the ligands, 5,5'-$(Me)_2$-bpy, 5,5'-$(CO_2Me)_2$-bpy and 5,5'-$(CO_2Et)_2$-bpy in 0.1 M $TBABF_4$/DMF at 293 K reveal a fully reversible one electron reduction process at potentials from –1.23 V to –2.21 V, see Table 3.1. The cyclic voltammogram of 5,5'-$(CO_2Et)_2$-bpy is shown in Figure 3.1. Coulometric studies at 233 K confirm a one electron reduction process in each case.

Table 3.1 Redox potentials of the ligands 5,5'-$(X)_2$-bpy.

Ligands	$E_{1/2}$ / V	$E_{1/2}$ / V
bpy	-2.05 (0.100) [a]	
5,5'-$(Me)_2$-bpy	-2.21 (0.006) [b]	
5,5'-$(CO_2Me)_2$-bpy	-1.25 (0.115)	-1.64 (0.115)
5,5'-$(CO_2Et)_2$-bpy	-1.23 (0.061)	-1.61 (0.152)

(a) PhD thesis of E.J.L. McInnes, University of Edinburgh, 1995.[25] (b) from differential pulse. The separation between peak potentials $E_{pa} - E_{pc}$ (/V) are given in parentheses.

No reduction processes are observed for 5,5'-$(NH_2)_2$-bpy, this was attributed to the redox processes occurring at potentials more negative than the solvent breakdown (*ca.* –2.3 V), see later in this section. This observation is in agreement with previous studies on 4,4'-disubstituted bpy ligands. McInnes reported that electron donating substituents at the 4,4' positions facilitate reduction of the ligand at more negative potentials.[25] Electron withdrawing substituents have the opposite effect. The ligand 5,5'-$(NH_2)_2$-bpy was not studied further.

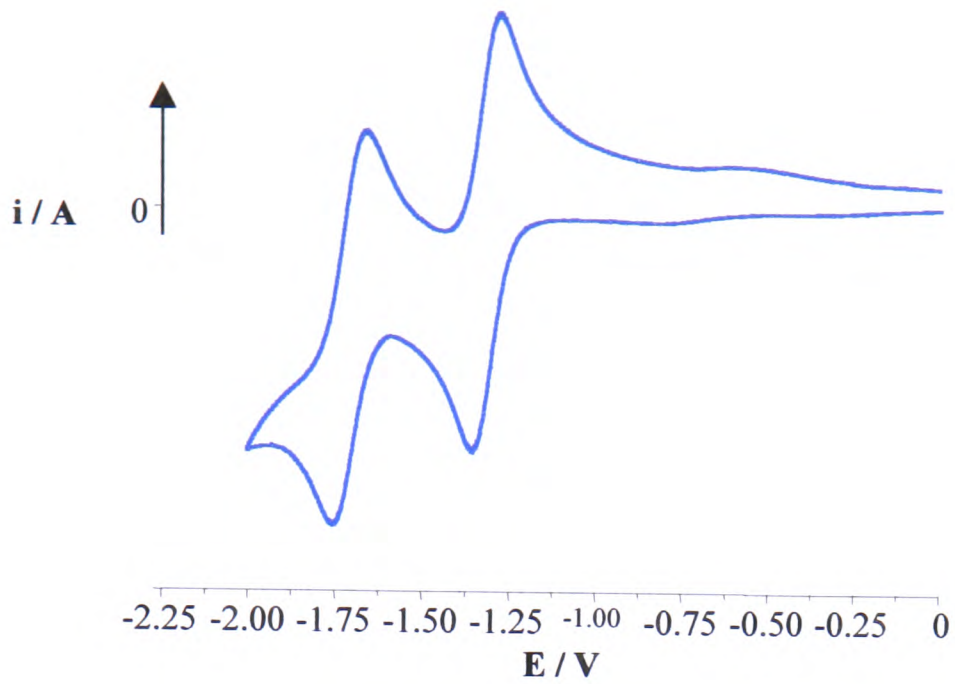

Figure 3. 1 Cyclic voltammogram of 5,5'-$(CO_2Et)_2$-bpy, scan rate 0.1 V/s, in 0.1 M $TBABF_4$/DMF at 293 K.

The second reduction of 5,5'-$(Me)_2$-bpy could not be observed, again because the reduction process occurs at potentials more negative than the solvent breakdown.

For the ligands 5,5'-$(CO_2Me)_2$-bpy and 5,5'-$(CO_2Et)_2$-bpy a second reduction process is observed at potentials 380-390 mV more negative than the first. In his work on the 4,4'-disubstituted bpys, McInnes notes a separation of 490 mV between the first and second reduction potentials of 4,4'-$(CO_2Me)_2$-bpy and assigns this potential separation as corresponding to the spin pairing of the second reduction electron with the first.[25] In line with this assignment, the potential separation shown for the 5,5' analogues was also attributed to the second reduction electron entering the same π^* orbital as the first reduction electron. This assignment is supported by epr studies, see section 3.2.1.3, where the mono-reduced species is paramagnetic but the di-reduced species is diamagnetic leading to collapse of the epr signal.

There is a linear correlation plot between the Hammett parameter σ_m and the $E_{1/2}$ of the first reduction potential of the ligand, see Figure 3.2. Such a correlation is indicative of a similar reaction mechanism in each case, *viz* reduction of the bpy ligand. Thus electron donating substituents destabilise the LUMO and electron withdrawing substituents stabilise the LUMO of 5,5'-$(X)_2$-bpy compared to bpy. By

extrapolating the line of the Hammett plot the $E_{1/2}$ value for the first reduction of 5,5'-$(NH_2)_2$-bpy can be estimated. Such an extrapolation gives an estimated $E_{1/2}$ = -2.4 V, see green data point on Figure 3.2. Thus the reduction of 5,5'-$(NH_2)_2$-bpy does indeed lie out with the solvent window, in line with earlier work.[25]

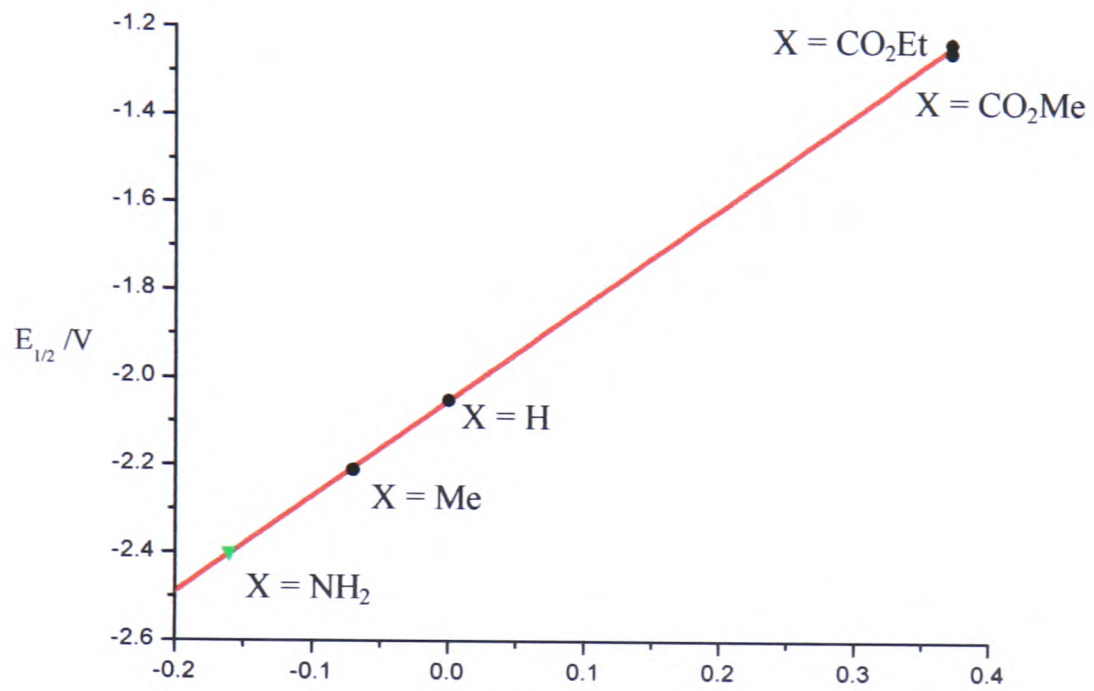

Figure 3. 2 Plot of $E_{1/2}$ of first reduction of 5,5'-$(X)_2$-bpy *vs* Hammett parameter σ_m of the substituent X.

3.2.1.2 UV/vis/nir Spectroelectrochemistry

In the UV/vis/nir spectra of both 5,5'-$(CO_2Me)_2$-bpy and 5,5'-$(CO_2Et)_2$-bpy the high energy band at 33,100 cm^{-1} (ε = 16,500 M^{-1} cm^{-1}) and 32,900 cm^{-1} (ε = 26,600 M^{-1} cm^{-1}) respectively, were assigned as internal bpy $\pi \rightarrow \pi^*$ transitions, see Figures 3.3 – 3.6 and Table 3.3. These peaks are at lower energy than the corresponding $\pi \rightarrow \pi^*$ transition for unsubstituted bpy (35,300 cm^{-1}, ε = 12,900 M^{-1} cm^{-1}) as electron withdrawing groups on the 5,5' positions have the effect of stabilising the LUMO with respect to bpy. A similar correlation is observed in the reduction potentials of the

free ligands where the first reductions of both 5,5'-$(CO_2Me)_2$-bpy and 5,5'-$(CO_2Et)_2$-bpy are at less negative potentials than the first reduction of bpy.

When the UV/vis spectra of the ligands are run in methanol rather than DMF a second peak, attributed to the $\pi \rightarrow \pi^*$ transitions of the HOMO-LUMO-1 is recorded. The difference in peak position of the two peaks gives the energy difference between the LUMO and LUMO-1 levels of the ligand, see Table 3.2.

From Table 3.2 it can be observed that the peak positions for the $\pi \rightarrow \pi^*$ HOMO-LUMO transitions occur at lower energy for the ligands where X is an electron withdrawing group (X = CO_2Et and CO_2Me). This effect arises because electron withdrawing groups on the 5,5' positions of bpy stabilise the LUMO with respect to unsubstituted bpy. Conversely, where X is an electron donating group, *ie* 5,5'-$(Me)_2$-bpy, the LUMO is destabilised with respect to bpy and an increase in the energy of the $\pi \rightarrow \pi^*$ peak positions compared to bpy is expected. However, although this is not observed for the UV/vis spectra, the results of the electrochemistry, see Table 3.1, indicate that the LUMO of 5,5'-$(Me)_2$-bpy does indeed lie at higher energy than that of the unsubstituted bpy. This seemingly anomalous result can be explained by taking into account the effect the electron donating Me group has on the HOMO of 5,5'-$(Me)_2$-bpy. The HOMO of 5,5'-$(Me)_2$-bpy must also be destabilised compared to bpy. Furthermore the destabilisation of the HOMO must be greater than for the LUMO to account for the observed $\pi \rightarrow \pi^*$ energy.

The spectrum of bpy^{1-} has three sets of absorption bands that are diagnostic for the presence of co-ordinated bpy^{1-}: i) a nir band at *ca.* 10 kcm^{-1} comprising of three peaks (or shoulders), ii) a doublet visible band at *ca.* 20 kcm^{-1} and iii) an intense near UV band at *ca.* 25 kcm^{-1}.[29]

Table 3 2 Energy differences between LUMO and LUMO-1 levels of the 5,5'-$(X)_2$-bpy in MeOH.

Ligand	$\pi \rightarrow \pi^*$ HOMO-LUMO / cm^{-1}	$\pi \rightarrow \pi^*$ HOMO-LUMO-1 / cm^{-1}	ΔE / cm^{-1}
bpy	35,600	42,600	7,000
5,5'-$(Me)_2$-bpy	34,800	41,200	6,400
5,5'-$(CO_2Me)_2$-bpy	33,700	39,200	5,500
5,5'-$(CO_2Et)_2$-bpy	33,600	39,200	5,600

The mono and di-reduced species of 5,5'-$(CO_2Me)_2$-bpy and 5,5'-$(CO_2Et)_2$-bpy were studied by OTTLE techniques at 233 K, see below. The spectra of 5,5'-$(CO_2Me)_2$-bpy^{1-} and 5,5'-$(CO_2Et)_2$-bpy^{1-} were shown to contain peaks at similar positions to bpy^{1-}, see Figures 3.3 – 3.5. Therefore it can be inferred that the electronic character of the frontier orbitals of bpy and the 5,5'-$(CO_2Me)_2$-bpy and 5,5'-$(CO_2Et)_2$-bpy derivatives are similar *ie* that the MO on the ligands are primarily based on the bpy part of the molecule. The nir band at 10-15 kcm^{-1} comprising of several peaks is clearly visible in the spectra of both mono-reduced ligands and can be assigned as SOMO to LUMO-1 transitions.[28] The doublet in the visible region at ~ 20 kcm^{-1} and the intense near UV band at ~ 25 kcm^{-1} are less easily distinguished. Both ligands have a series of peaks in the region 20- 25 kcm^{-1} that can be tentatively assigned as intra ligand transitions of bpy^{1-}. Any additional bands must be due to electronic transitions to orbitals that have significant contributions from the CO_2R groups. Absorption bands involve transitions to/from the semi-occupied MO

(SOMO). The electron withdrawing nature of the CO_2R substituents in the 5,5' positions make the peak positions move to slightly lower energy compared to unsubstituted bpy^{1-}. This energy shift arises because the electron withdrawing substituents stabilise the LUMO thereby increasing the energy between the LUMO π^* and other, higher energy π^* anti-bonding orbitals. The isosbestic point on the UV/vis/nir spectra should be noted; at 30,600 cm^{-1} for 5,5'-$(CO_2Et)_2$-$bpy^{0/1-}$, indicating the clean conversion between the neutral and mono-reduced species. On reduction, the peak corresponding to the $\pi \rightarrow \pi^*$ intra ligand transitions of neutral bpy at 34,000 cm^{-1} collapses.

On reduction to the di-reduced species the spectra of both ligands under go a similar change, see Figure 3.6 and Table 3.3, with the triplet at 10 –15 kcm^{-1} collapsing and an intense doublet at 19-21 kcm^{-1} growing in. For the 5,5'-$(CO_2Et)_2$-$bpy^{1-/2-}$ couple the peaks at 24,000 cm^{-1} (ε = 4,900 M^{-1} cm^{-1}), 22,900 cm^{-1} (ε = 6,100 M^{-1} cm^{-1}) and 22,200 cm^{-1} (ε = 9,900 M^{-1} cm^{-1}) collapse while peaks at 20,600 cm^{-1} (ε = 6,600 M^{-1} cm^{-1}) and 19,000 cm^{-1} (ε = 5,800 M^{-1} cm^{-1}) grow in accordingly.

In their study on the electronic spectra of bpy^{1-} and bpy^{2-} König and Kremer assigned the spectrum of bpy^{2-} as consisting of two bands; one at *ca.* 16.4 kcm^{-1} and a second very intense band at *ca.* 26.8 kcm^{-1}. A diffuse structure at shorter wavelength was also observed.[29] The spectra of 5,5'-$(CO_2Me)_2$-bpy^{2-} and 5,5'-$(CO_2Et)_2$-bpy^{2-} show intense doublets in the region 19-21 kcm^{-1} which may mask the less intense band that appears at 16.4 kcm^{-1} in the UV/vis of bpy^{2-}, see Figure 3.6 and Table 3.3. As for the mono-anionic species, the electron withdrawing nature of the CO_2R substituents move the peak positions to lower energy compared to unsubstituted bpy^{2-}. These intense transitions are from the LUMO (now doubly occupied) to higher energy unoccupied π^* anti-bonding orbitals.

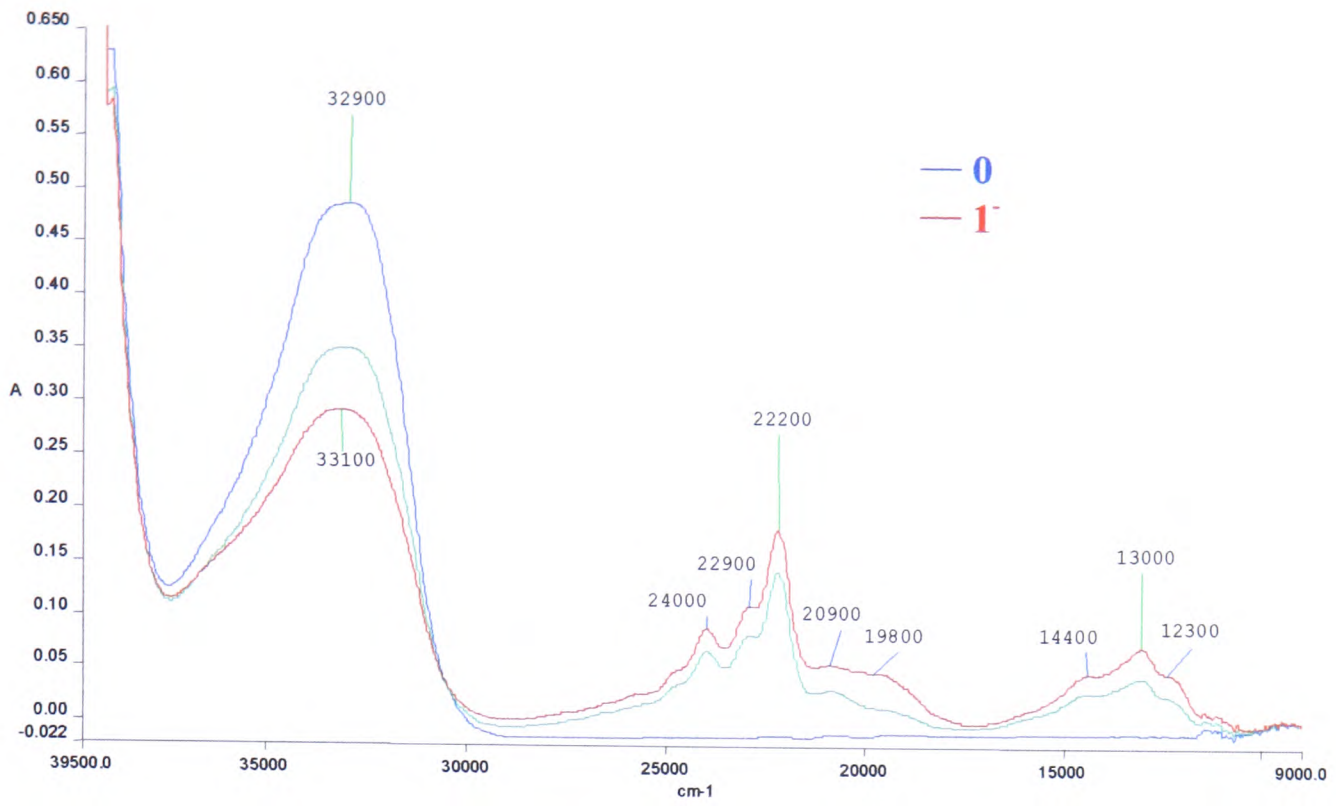

Figure 3. 3 UV/vis of 5,5'-$(CO_2Et)_2$-$bpy^{0/1-}$ at 233 K in 0.1 M $TBABF_4$/DMF. E_{gen} = -1.56 V.

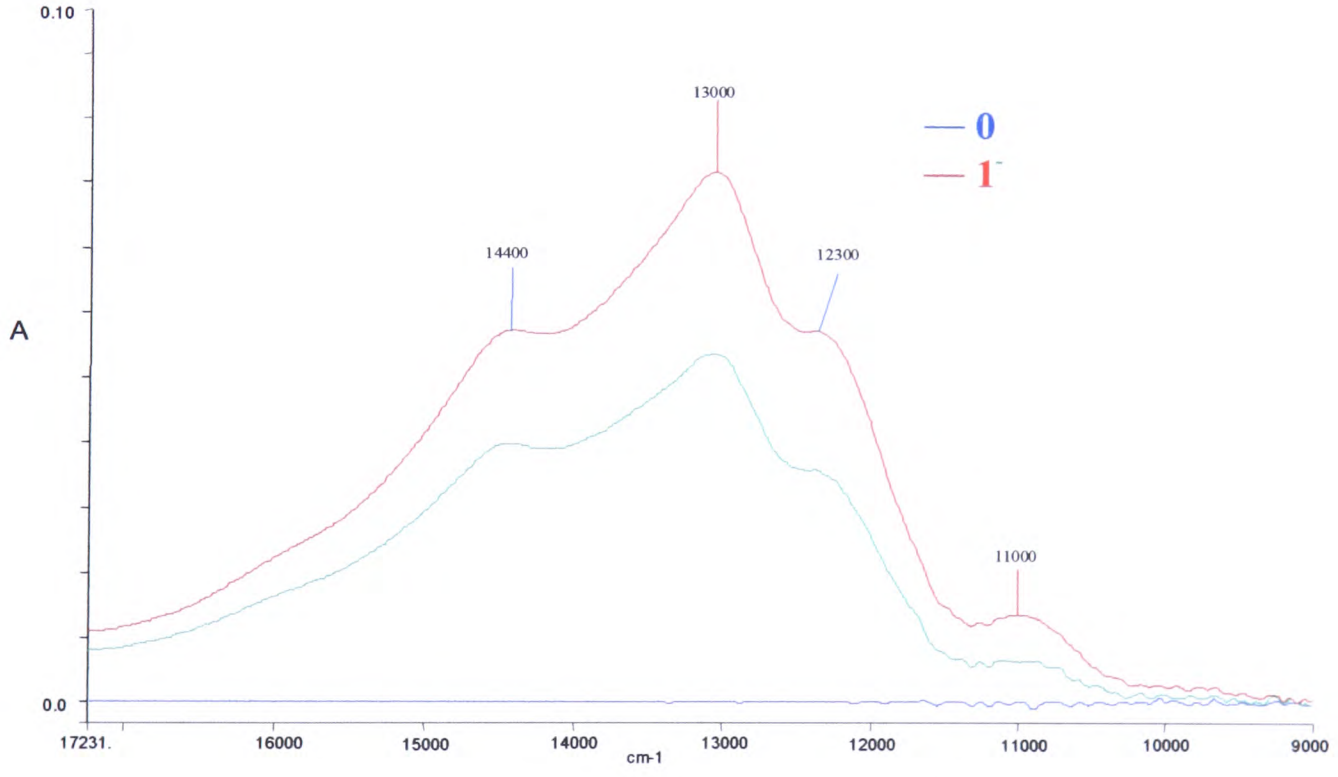

Figure 3. 4 Peaks in nir band of 5,5'-$(CO_2Et)_2$-$bpy^{0/1-}$ in 0.1 M $TBABF_4$/DMF at 233 K. E_{gen} = -1.56 V.

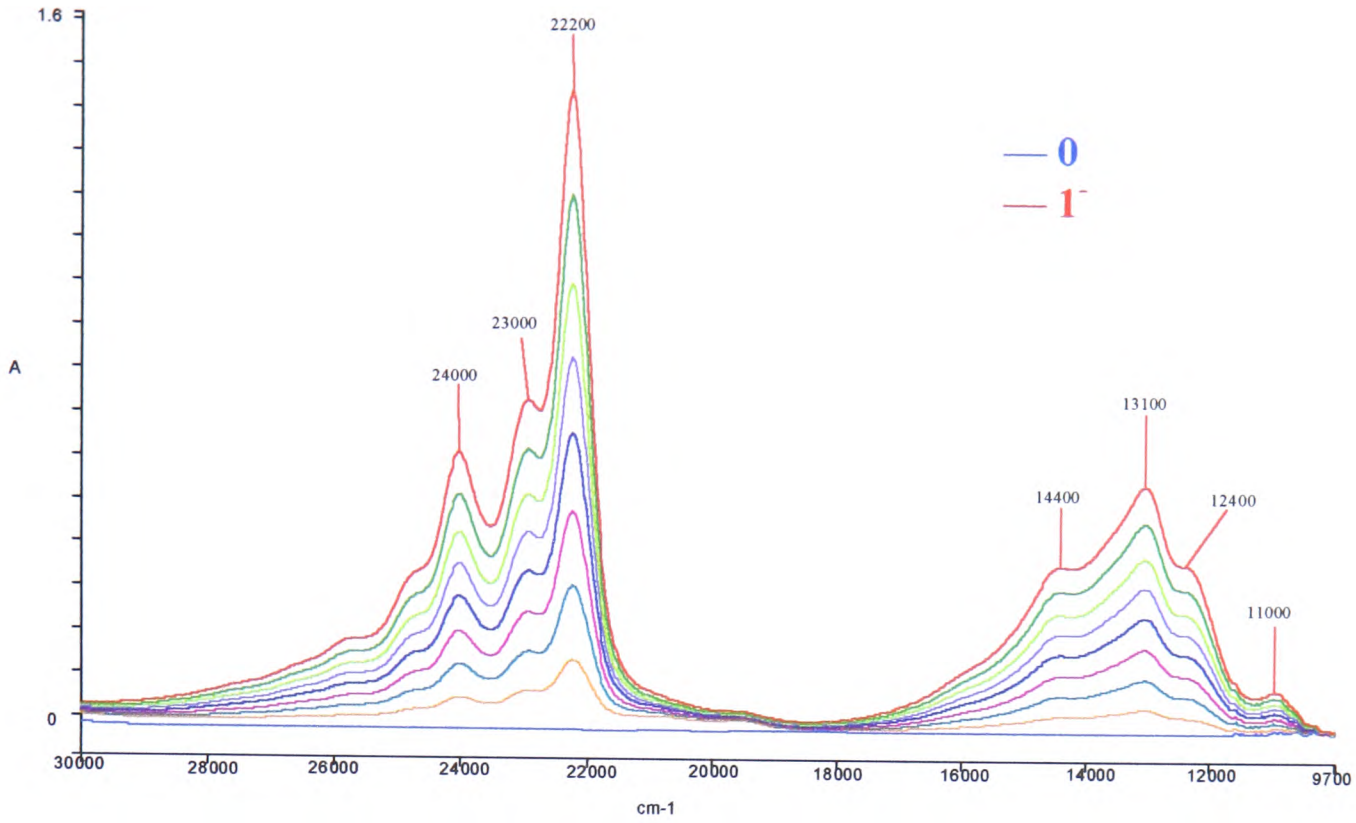

Figure 3.5 UV/vis spectrum of 5,5'-$(CO_2Me)_2$-$bpy^{0/1-}$ at 233 K in 0.1 M $TBABF_4$/DMF. E_{gen} = -1.55 V.

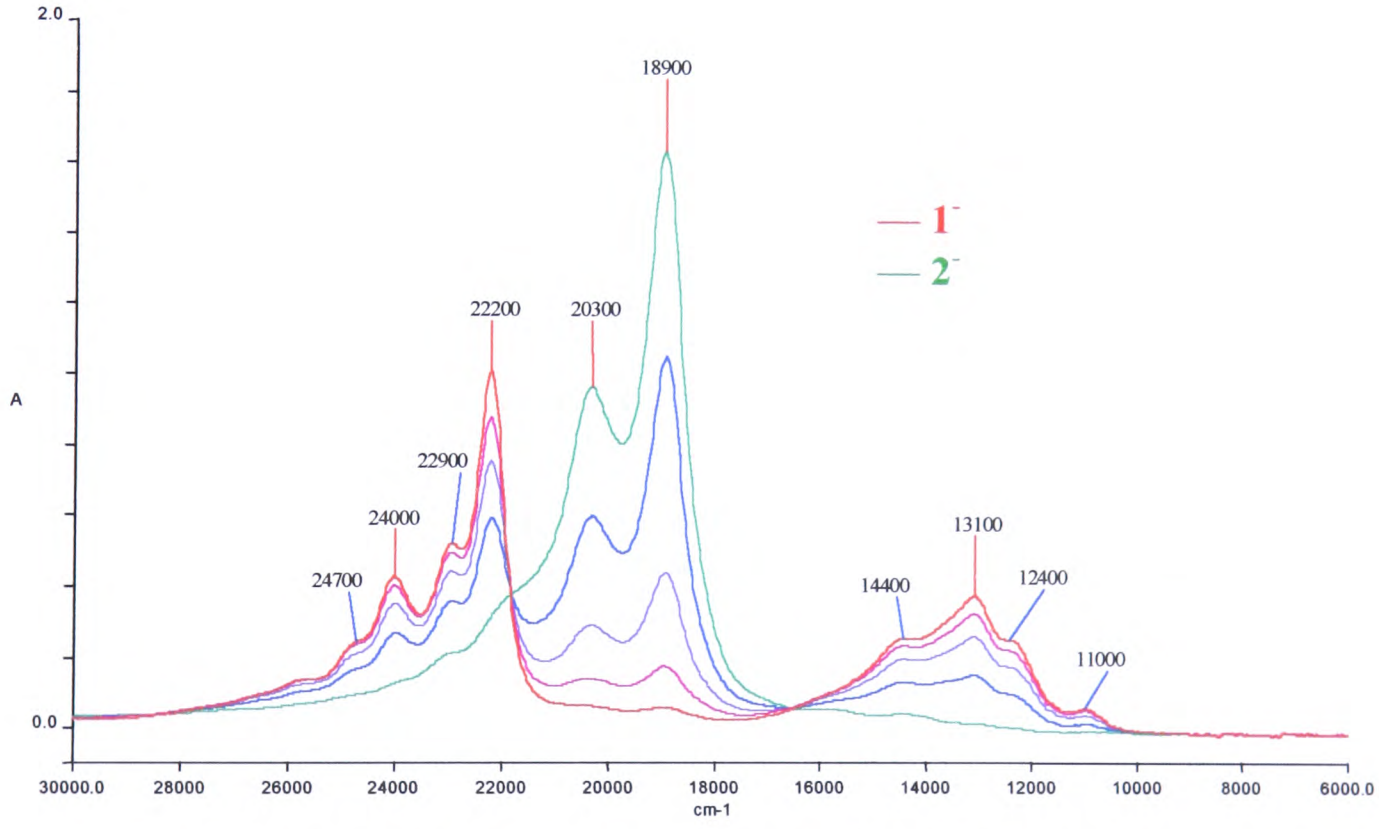

Figure 3.6 UV/vis of 5,5'-$(CO_2Me)_2$-$bpy^{1-/2-}$ in 0.1 M $TBABF_4$/DMF at 233 K. E_{gen} = -1.90 V.

The effect is more dramatic for 5,5'-$(CO_2Me)_2$-$bpy^{1-/2-}$ with the peaks at 24,000 cm^{-1} (ε = 17,700 M^{-1} cm^{-1}), 22,900 cm^{-1} (ε = 21,800 M^{-1} cm^{-1}) and 22,200 cm^{-1} (ε = 42,200 M^{-1} cm^{-1}) collapsing and very intense peaks at 20,300 cm^{-1} (ε = 40,300 M^{-1} cm^{-1}) and 18,900 cm^{-1} (ε = 68,100 M^{-1} cm^{-1}) growing in their place. Again these transitions are from the LUMO (now doubly occupied) to higher energy unoccupied π^* anti-bonding orbitals. Such changes in peak positions in the visible region lead to pronounced colour changes. 5,5'-$(CO_2Me)_2$-bpy^{1-} is bright green while 5,5'-$(CO_2Me)_2$-bpy^{2-} is bright orange. Isosbestic points at 21,800 cm^{-1} and 16,500 cm^{-1} for 5,5'-$(CO_2Me)_2$-$bpy^{1-/2-}$ indicate the clean conversion between the mono and di-reduced species. The electrochemistry of the ligands indicates that spin pairing of the reduction electron occurs for the reasons given in section 3.2.1.1. The UV/vis/nir spectral changes are fully reversible on setting the electrode potential back to 0 V, *ie* the electron transfer processes are fully chemically reversible.

The UV/vis spectroelectrochemistry of the ligands 5,5'-$(Me)_2$-bpy and 5,5'-$(NH_2)_2$-bpy could not be studied as the reduction processes occur at more negative potentials than the solvent breakdown.

Table 3 3 Peak positions and molar extinction coefficients, ε, of 5,5'-$(CO_2Me)_2$-$bpy^{0/1-/2-}$ and 5,5'-$(CO_2Et)_2$-$bpy^{0/1-/2-}$ in 0.1 M $TBABF_4$/DMF at 233 K.

Oxidation state	5,5,'-$(CO_2Me)_2$-bpy	5,5'-$(CO_2Et)_2$-bpy
	Peak position / cm^{-1} (ε / M^{-1} cm^{-1})	Peak position /cm^{-1} (ε / M^{-1} cm^{-1})
0	33,100 (16,500)	32,900 (26,600)
1^-	33,500 (3,300) 25,600 (5,700) 24,700 (10,100) 24,000 (17,700) 22,900 (21,800) 22,200 (42,200) 14,400 (10,700) 13,100 (15,600) 12,400 (10,600) 11,000 (2,300)	33,100 (16,000) 24,700 (2,700) 24,000 (4,900) 22,900 (6,100) 22,200 (9,900) 21,000 (3,000) 19,800 (2,700) 14,400 (2,600) 13,000 (4,000) 12,300 (2,600) 11,000 (800)
2^-	23,900 (5,400) 23,000 (8,700) 21,900 (15,500) 20,300 (40,300) 18,900 (68,100)	33,500 (10,400) 23,100 (4,300) 22,800 (5,800) 22,200 (7,800) 20,600 (6,600) 19,000 (5,800)

3.2.1.3 Epr spectroelectrochemistry

In situ electrochemical reduction of 5,5'-$(CO_2Me)_2$-bpy and 5,5'-$(CO_2Et)_2$-bpy in 0.1 M $TBABF_4$/DMF solution at 273 K yields the epr active mono-reduced species. Molecular Orbital calculations using CaChe software, (using PM3 calculation with a PM3 wavefunction) carried out on 5,5,'-$(CO_2Me)_2$-bpy indicate the LUMO lies on the

bpy ligand, mainly on the carbon nuclei at the 2,2' and 5,5' positions and on the two nitrogen nuclei. In addition, the carbon nuclei at the 3,3', 4,4' and 6,6' positions make equally small contributions to the LUMO. The epr spectrum of 5,5'-$(CO_2Me)_2$-bpy^{1-} can be simulated with coupling to the two equivalent ^{14}N nuclei on the bpy (1.05 G), and two lots of six equivalent ^{1}H nuclei (0.42 G and 1.3 G), see Figure 3.7. As the two halves of the epr spectrum are equivalent, for clarity only the low field half of the spectrum is shown in Figure 3.7. While this differs from the results obtained from the CaChe calculations, the simulation compares favourably with the experimental spectrum. The six ^{1}H nuclei with a coupling of 0.42 G were assigned as the hydrogens of the two equivalent methyl groups. Although the six ^{1}H nuclei on the bpy were simulated as being equivalent, the CaChe calculations indicate that the carbon atoms on the bpy ring give different, but similar contributions to the LUMO, see Table 3.4. However, the spectrum could not be successfully simulated when the hydrogen nuclei were split into three separate equivalent pairs. PM3 molecular mechanics method is a fairly low level calculation. To calculate the nucleic contributions to the LUMO more accurately would require higher level calculations, *ie* density functional theory (DFT) calculations. Despite this, PM3 calculations are very useful as a guide to the contributions each nucleus makes to the LUMO.

Table 3 4 Table of MO coefficients^2 obtained for PM3 calculation on 5,5'-$(CO_2Me)_2$-bpy and the theoretical A^H values obtained from the McConnell equation.

Atom number	MO coefficient^2	A^H / G
C 3	0.045945	1.03
C 4	0.043287	0.97
C 5	0.135086	3.04
C 6	0.039770	0.89

If these numbers for the MO coefficients^2 are put into the McConnell equation, see Equation 3.1, the theoretical values for the hyperfine splittings can be obtained, see Table 3.4. The values for C_3, C_4 and C_6 are all similar and the differences between them are close to the simulation linewidth, see Figure 3.7. Thus the epr spectrum of

5,5'-$(CO_2Me)_2$-bpy^{1-} can be simulated showing coupling to six equivalent ^1H nuclei bound to the bpy as the linewidth is insufficient to differentiate between the ^1H coupling values.

$$A^H = Q\,\rho \quad (3.1)$$

A^H = hyperfine splitting for H.

Q = 22.5 G

ρ = spin density of the unpaired electron.

By simulating the epr signal as discussed above, the epr spectral results for 5,5'-$(CO_2Me)_2$-bpy^{1-} are in agreement with the UV/vis/nir results; namely that the reduction electron resides in a molecular orbital primarily located on the bpy ligand with a minor contribution from the substituent. Despite this small contribution to the LUMO the substituent remains electronically important.

The epr spectrum of 5,5'-$(CO_2Et)_2$-bpy^{1-} can be simulated using the same basic pattern as the CO_2Me analogue, with coupling of the reduction electron as shown in Figure 3.8. The larger set of six ^1H couplings is assigned to the bpy ring hydrogens, the smaller to the two equivalent methyl groups. In addition, the set of four ^1H nuclei with a coupling of 0.135 G are attributed to the two CH_2 groups on the CO_2Et substituents. The spectrum of 5,5'-$(CO_2Et)_2$-bpy^{1-} is not as well resolved as its methyl analogue. The overall width of the epr signals is approximately the same in both cases (*ca.* 18 G). The lower resolution must therefore arise from the overlapping proton signals from the six CH_3 and four CH_2 protons of the ethyl groups. Once again the molecular orbital occupied by the reduction electron in 5,5'-$(CO_2Et)_2$-bpy^{1-} is primarily based on the bpy part of the molecule.

The epr active species 5,5'-$(Me)_2$-bpy^{1-} could not be generated *in situ* or by bulk electrochemical reduction as the first reduction potential lies at more negative values than the solvent breakdown.

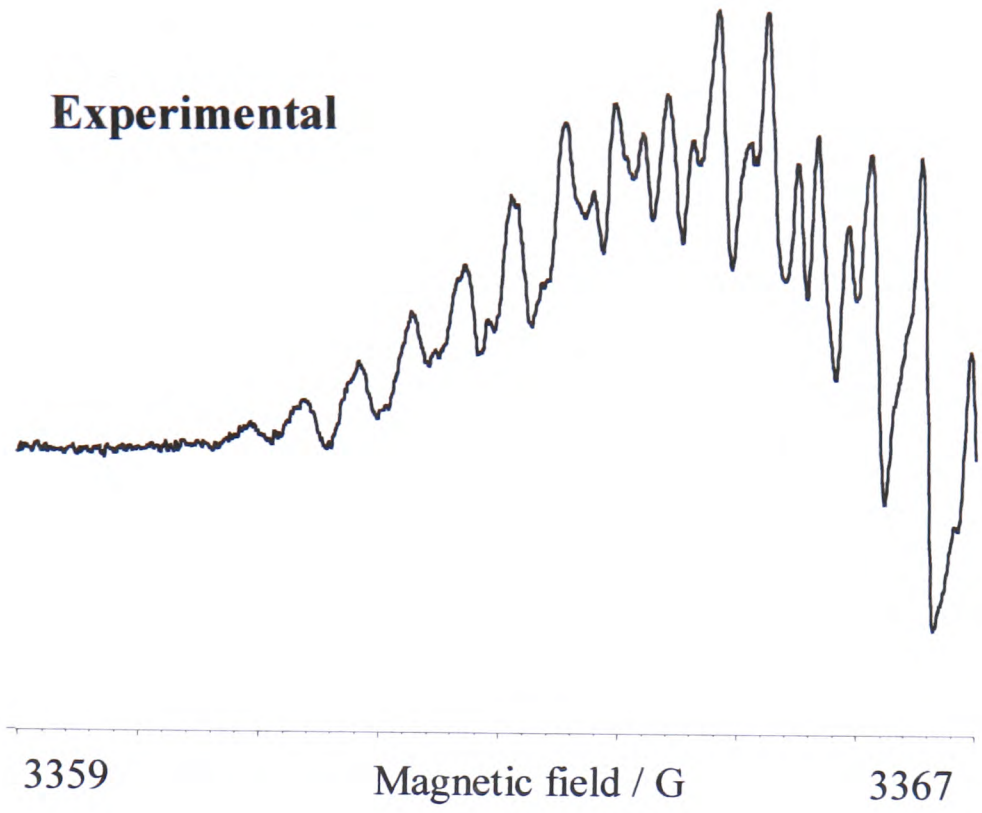

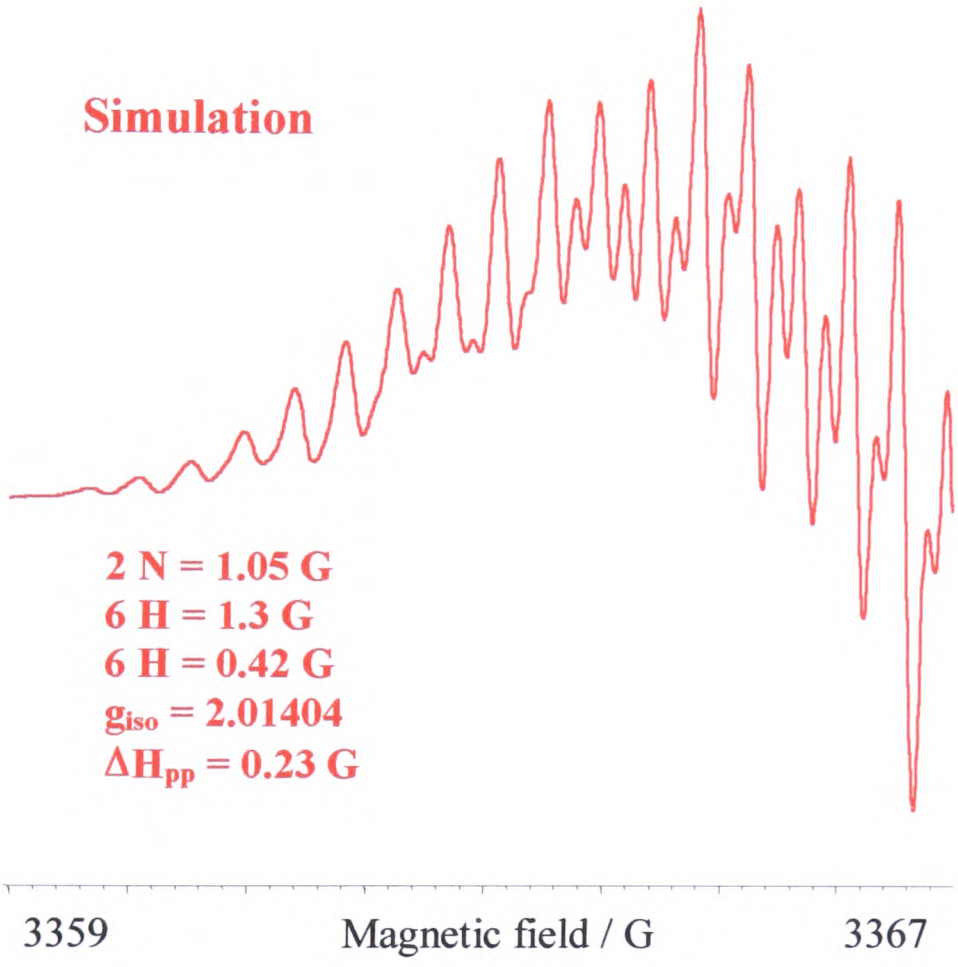

Figure 3.7 Epr of 5,5'-$(CO_2Me)_2$-bpy)$^{1-}$ generated *in situ* in 0.1 M $TBABF_4$/DMF at 273 K and E_{gen} – 1.55 V. The black spectrum is the signal obtained experimentally, the red spectrum is the simulation.

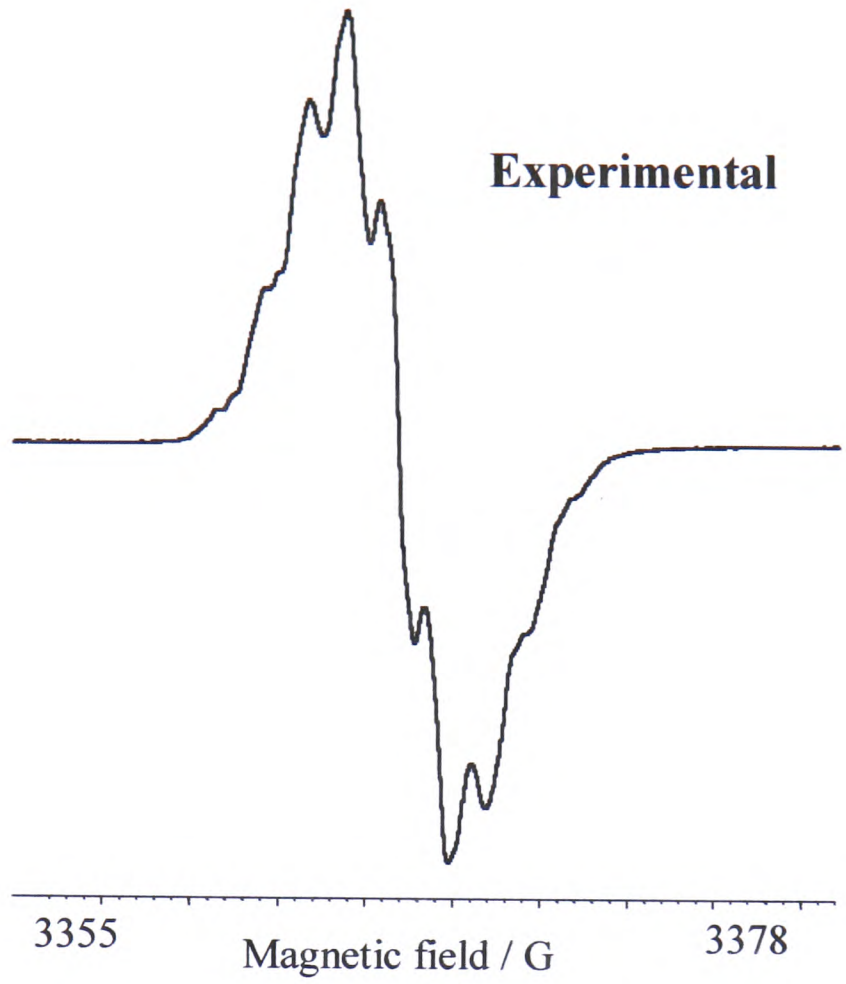

Figure 3. 8 Epr of 5,5'-$(CO_2Et)_2$-bpy^{1-} generated *in situ* in 0.1 M $TBABF_4$/DMF at 273 K and E_{gen} – 1.5 V. The black spectrum is the signal obtained experimentally, the red spectrum is the simulation.

3.2.2 [Pt(5,5'-$(X)_2$-bpy)Cl_2]

3.2.2.1 Redox Chemistry of [Pt(5,5'-$(X)_2$-bpy)Cl_2]

Cyclic voltammetric studies of the complexes [Pt(5,5'-$(X)_2$-bpy)Cl_2] where X = Me, CO_2Me and CO_2Et were carried out at 293 K in 0.1 M $TBABF_4$/DMF and all revealed a fully reversible, one electron reduction in the range –1.17 V to –0.52 V, see Table 3.5, below. A second reduction process is observed at potentials 490 – 650 mV more negative than the first. As with the ligands, the potential separation between the reduction processes for the corresponding complexes is associated with the spin pairing energy of the two added electrons in the redox-active orbital. The second reduction is fully reversible for [Pt(5,5'-$(CO_2Me)_2$-bpy)Cl_2] and [Pt(5,5'-$(CO_2Et)_2$-bpy)Cl_2], (see Figure 3.9) and quasi-reversible for [Pt(5,5'-$(Me)_2$-bpy)Cl_2].

The reduction of [Pt(5,5'-$(NH_2)_2$-bpy)Cl_2] is irreversible even at 223 K and no anodic peak is observed. The three irreversible reductions are observed at –1.22 V, –1.66 V and –1.92 V with an associated daughter product at –0.12 V, see Figure 3.10. The first reduction at –1.22 V is due to reduction of the 5,5'-$(NH_2)_2$-bpy ligand, the subsequent reduction peaks at –1.66 V and –1.92 V are probably due to redox chemistry of the daughter product. Thus the electron transfer is followed by a rapid chemical reaction. The nature of the daughter product was not investigated further.

Table 3. 5 Redox potentials of [Pt(5,5'-$(X)_2$-bpy)Cl_2] in 0.1 M $TBABF_4$/DMF.

Complex	E_1 / V	E_2 / V	$E_1 - E_2$ / V
[Pt(bpy)Cl_2]	-1.06 (0.070)[a]	-1.79 (0.110)[a]	0.73
[Pt(5,5'-$(Me)_2$-bpy)Cl_2]	-1.17 (0.081)	-1.82 (0.156)	0.65
[Pt(5,5'-$(CO_2Me)_2$-bpy)Cl_2]	-0.52 (0.070)	-1.01 (0.083)	0.49
[Pt(5,5'-$(CO_2Et)_2$-bpy)Cl_2]	-0.53 (0.074)	-1.03 (0.071)	0.50
[Pt(5,5'-$(NH_2)_2$-bpy)Cl_2][b]	-1.22[c]	-1.66[c]	-

The values in parentheses are $E_{pa} - E_{pc}$. (a) PhD thesis of E. J. L. McInnes, University of Edinburgh, 1995.[25] (b) 223 K, (c) no anodic peak was observed, cathodic peak quoted at 223K.

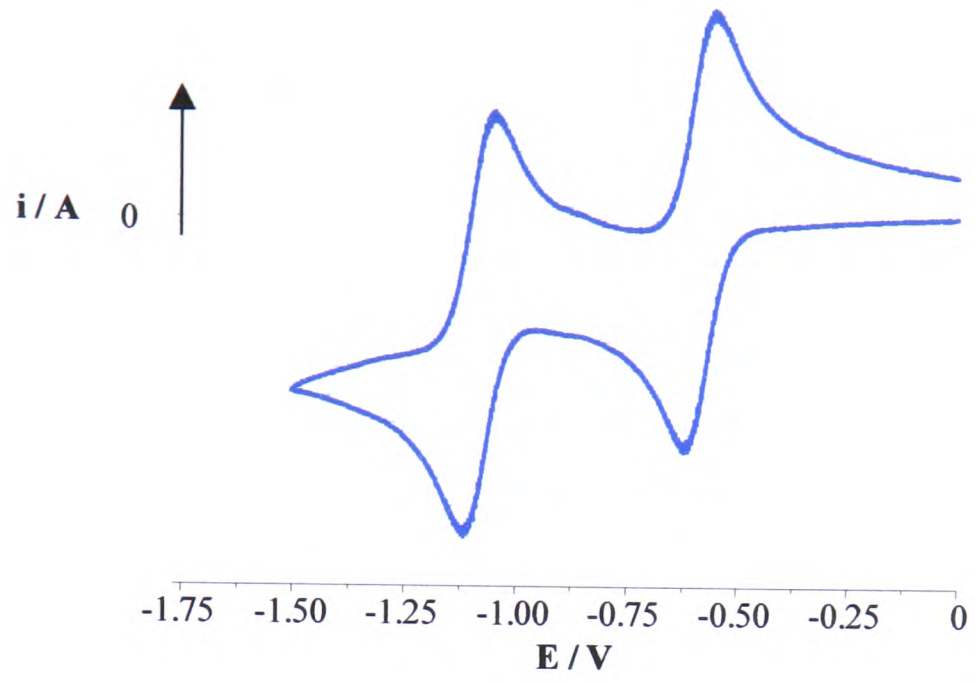

Figure 3. 9 Cyclic voltammogram of [Pt(5,5'-$(CO_2Et)_2$-bpy)Cl_2], scan rate 0.1 V/s, at 293 K in 0.1 M $TBABF_4$/DMF.

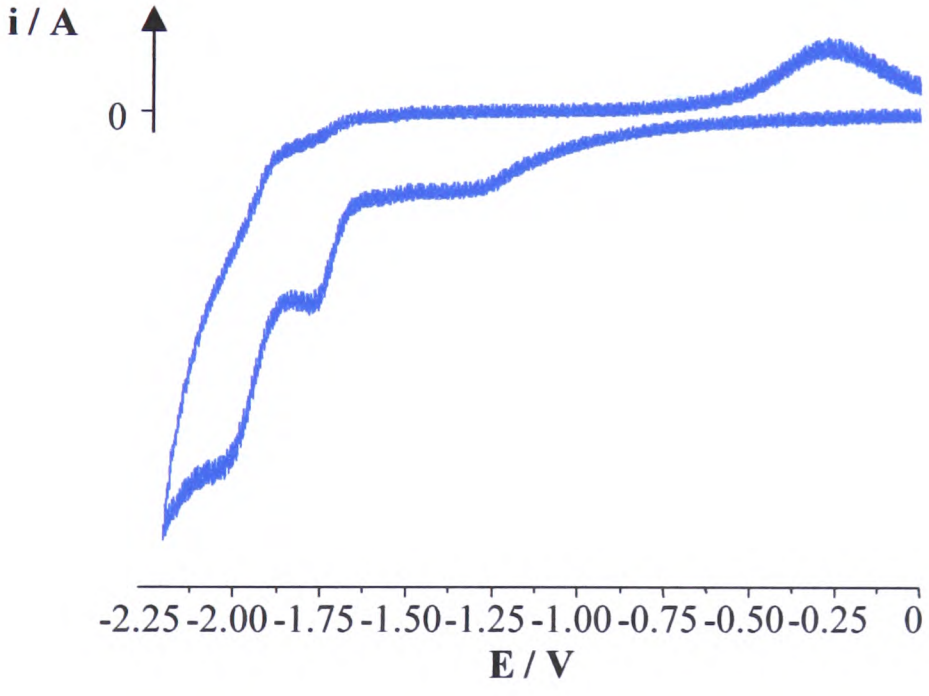

Figure 3. 10 Cyclic voltammogram of [Pt(5,5'-$(NH_2)_2$-bpy)Cl_2], scan rate 0.1 V/s, at 223 K in 0.1 M $TBABF_4$/DMF

The redox results of [Pt(5,5'-$(X)_2$-bpy)Cl_2] were compared with those for the 4,4' analogue previously obtained by McInnes[25] in order to ascertain whether the 4,4' or 5,5' positions are electronically the most important sites of substitution. Previous studies found that the $E_{1/2}$ of the first reduction process of [Pt(4,4'-$(X)_2$-bpy)Cl_2] complexes varies linearly with Hammett parameter σ_p of the substituent X.[25] Such a correlation implies that a similar reaction is taking place in each case, *ie* the reduction of the bipyridyl moiety. The same rationale can be applied to [Pt(5,5'-$(X)_2$-bpy)Cl_2] complexes as plotting the $E_{1/2}$ of the first reduction process against σ_m for the substituent X gives a straight line, see Figure 3.11. Plotting the $E_{1/2}$ values and Hammett parameters σ_m and σ_p for both [Pt(5,5'-$(X)_2$-bpy)Cl_2] and the 4,4' analogue on the same graph allows direct comparison of how the substituent position on the bpy ligand effects the electrochemistry of the complex, see Figure 3.11 and Table 3.6.

From Figure 3.11 it is clear that the line for [Pt(5,5'-$(X)_2$-bpy)Cl_2] complexes has a steeper gradient than the 4,4' substituted bpys. This implies that changing the substituent at the 5,5' position has a greater effect on the electrochemistry of the complex than changing the substituents at the 4,4' position. Hence we conclude that the 5,5' position on the bipyridyl ligand is electronically the more important site of substitution.

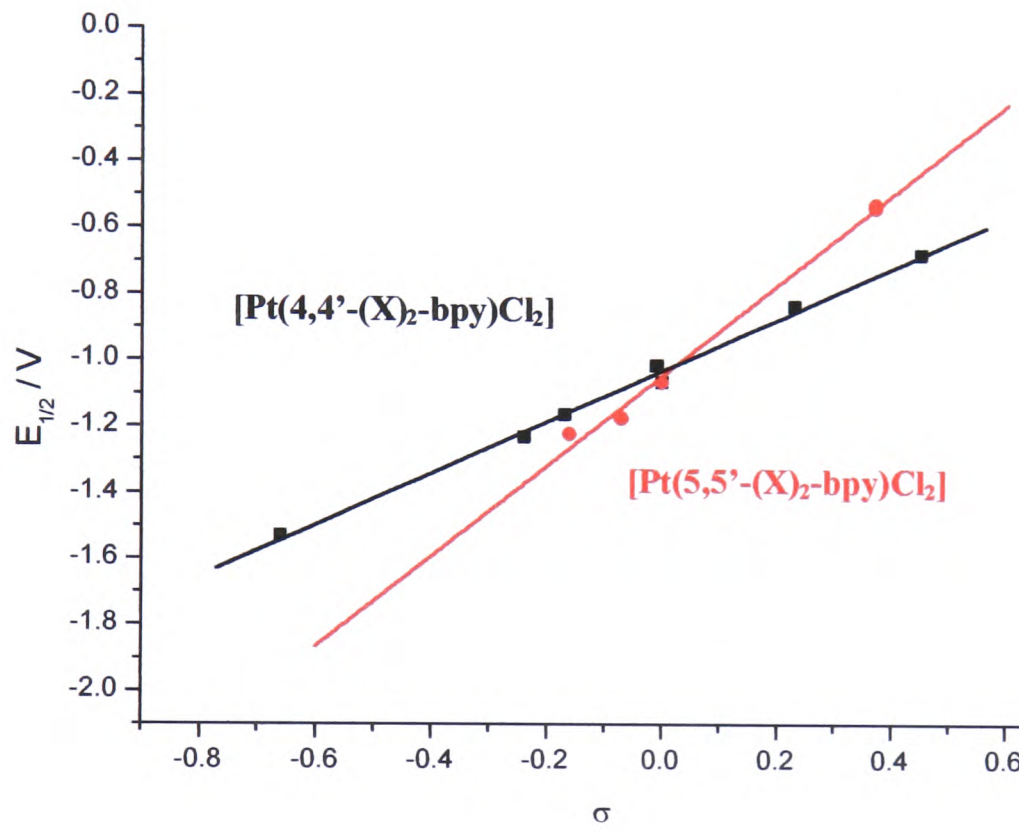

Figure 3. 11 $E_{1/2}$ of [Pt(4,4'-$(X)_2$-bpy)Cl_2] *vs* Hammett parameter σ_p overlaid with the $E_{1/2}$ of [Pt(5,5'-$(X)_2$-bpy)Cl_2] *vs* Hammett parameter σ_m.

Table 3 6 Hammett parameters, σ_p and σ_m, and the $E_{1/2}$ values of the first reduction processes for [Pt(4,4'-$(X)_2$-bpy)Cl_2] and [Pt(5,5'-$(X)_2$-bpy)Cl_2] as plotted in Figure 3.11

Substituent X	**[Pt(4,4'-$(X)_2$-bpy)Cl_2]**		**[Pt(5,5'-$(X)_2$-bpy)Cl_2]**	
	σ_p[a]	$E_{1/2}$ / V[b]	σ_m[a]	$E_{1/2}$ / V
NH_2	-0.66	-1.53[c]	-0.16	-1.22[d]
OEt	-0.24	-1.23		
Me	-0.17	-1.16	-0.07	-1.17
Ph	-0.01	-1.01		
H	0.00	-1.06	0.00	-1.06
Cl	0.23	-0.83		
CO_2Me	0.45	-0.67	0.37	-0.52
CO_2Et	0.45		0.37	-0.53

(a) Hammett parameter for substituent X, Hansch *et al.*.[60] (b) $E_{½}$ values for [Pt(4,4'-$(X)_2$-bpy)Cl_2] from PhD thesis of E. J. L. McInnes, University of Edinburgh, 1995.[25] (c) anodic peak not observed, cathodic peak quoted. (d) anodic peak not observed, cathodic peak at 223 K quoted.

3.2.2.2 UV/vis/nir Spectroelectrochemistry

The UV/vis/nir spectroelectrochemistry of [Pt(5,5'-$(Me)_2$-bpy)Cl_2], [Pt(5,5'-$(CO_2Me)_2$-bpy)Cl_2] and [Pt(5,5'-$(CO_2Et)_2$-bpy)Cl_2] was carried out at approximately 233 K in 0.1 M $TBABF_4$/DMF. The spectra of all three neutral species are similar, with a high energy band at 33-36 kcm^{-1}, an intense doublet at 29 – 31 kcm^{-1} and a band in the region 24 – 27 kcm^{-1}, see Figures 3.12 – 3.15 and Tables 3.7 and 3.8. The lowest energy band was assigned as a MLCT (d - π^*) while the higher energy bands were assigned as bpy $\pi \rightarrow \pi^*$ internal transitions.

As previously discussed in section 3.2.1.2, the UV/vis/nir spectrum of Na^+ (bpy^{1-}) has three characteristic features that are diagnostic for the presence of co-ordinated bpy^{1-}. These are a nir band at *ca.* 10 kcm^{-1} comprising of three peaks (or shoulders), a doublet in the visible region at *ca.* 20 kcm^{-1} and an intense band in the near UV at *ca.* 25 kcm^{-1}. On reduction of [Pt(5,5'-$(Me)_2$-bpy)Cl_2], see Figure 3.12 and Table 3.7, to its mono-reduced anion, the spectra obtained is similar to that obtained for Na^+ (bpy^{1-}), with a broad band at 10 – 15 kcm^{-1} and several peaks in the region 20 –25 kcm^{-1}. The band growth is characteristic of this type of species with the bpy^{1-} transitions increasing while the corresponding bpy $\pi \rightarrow \pi^*$ internal transitions at 29,900 cm^{-1} (ε = 15,800 M^{-1} cm^{-1}) and 31,200 cm^{-1} (ε = 19,300 M^{-1} cm^{-1}) are collapsing. Note the isosbestic points at 35,100 cm^{-1}, 31,700 cm^{-1} and 29,400 cm^{-1}, indicating a clean conversion from the neutral complex to the mono-reduced anion. On resetting the electrode potential to 0 V the UV/vis/nir changes are completely reversible, *ie* the electron transfer is fully chemically reversible. The similarity of the UV/vis/nir spectral results for the reduction of [Pt(5,5'-$(Me)_2$-bpy)Cl_2]^0 to [Pt(5,5'-$(Me)_2$-bpy)Cl_2]$^{1-}$ to the spectrum of Na^+ (bpy^{1-}) indicates the additional electron enters an orbital which is primarily based on the $(Me)_2$-bpy ligand and more precisely is based on the bpy part of the ligand. Thus the one electron reduction product can be formulated as [Pt(II)(5,5'-$(Me)_2$-$bpy)^{1-}Cl_2$]$^{1-}$. The di-reduced species

could not be studied as the second reduction of $[Pt(5,5'\text{-}(Me)_2\text{-}bpy)Cl_2]$ lies outwith the solvent window.

Table 3 7 Peaks positions and molar extinction coefficients,ε, for $[Pt(5,5'\text{-}(Me)_2\text{-}bpy)Cl_2]^{0/1-}$ at 233 K in 0.1 M $TBABF_4$/DMF.

Oxidation state	Peak position / cm^{-1}, (ε / M^{-1} cm^{-1}).
0	35,800 (21,800) 32,200 (sh) (6,700) 31,200 (10,700) 29,900 (15,800) 28,000 (sh) (2,900) 26,500 (3,400)
1^-	35,200 (19,300) 32,700 (sh) (11,300) 27,600 (11,700) 24,200 (6,200) 23,000 (6,500) 21,400 (6,000) 20,100 (sh) (6,200) 19,800 (6,300) 10,100 (2,200)

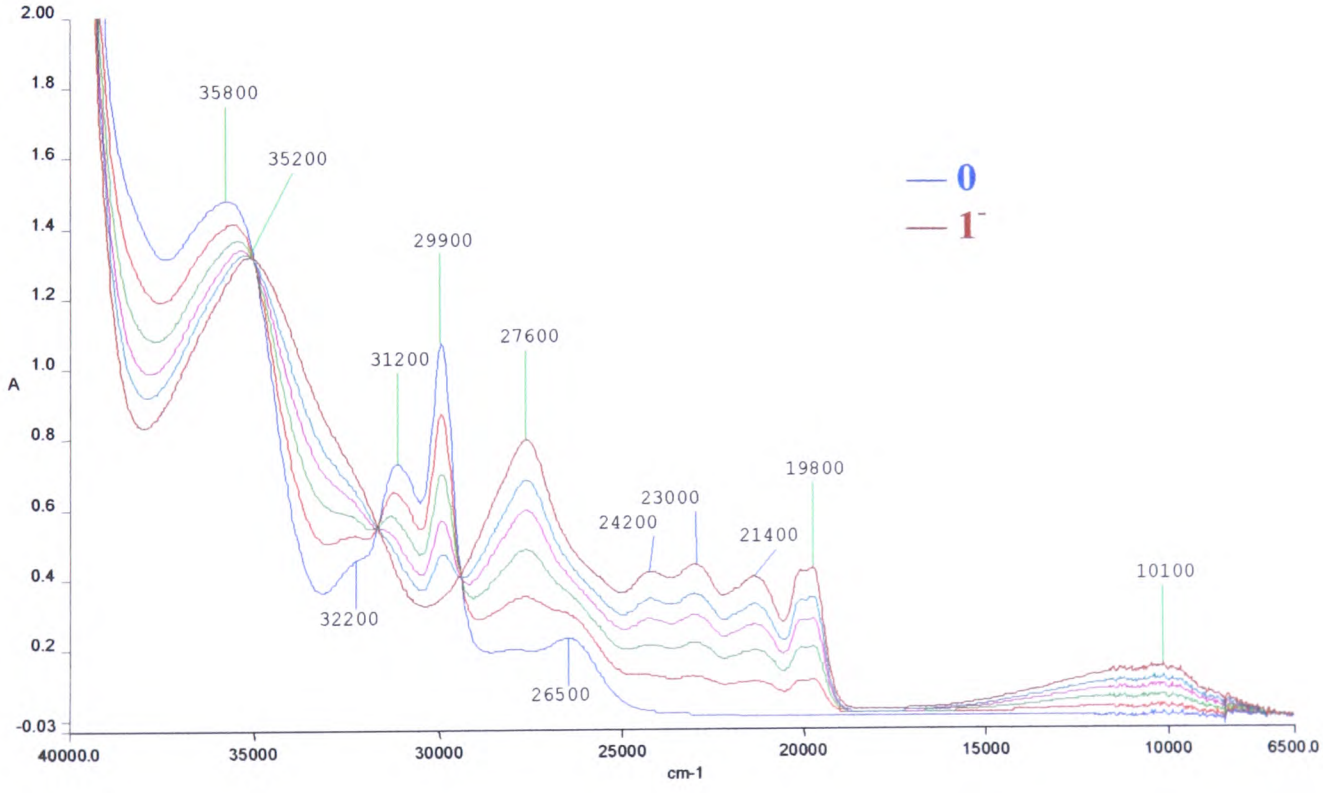

Figure 3. 12 UV/vis/nir spectra of $[Pt(5,5'\text{-}(Me)_2\text{-}bpy)Cl_2]^{0/1-}$, E_{gen} = -1.52 V, at 233 K in 0.1 M $TBABF_4$/DMF.

The UV/vis/nir spectra of the one electron reduction products of [Pt(5,5'-$(CO_2Me)_2$-bpy)Cl_2] and [Pt(5,5'-$(CO_2Et)_2$-bpy)Cl_2] are similar but differ from the spectra obtained for [Pt(5,5'-$(Me)_2$-bpy)Cl_2], see Figures 3.13 – 3.15 and Table 3.8. The broad nir band observed at 10-15 kcm^{-1} for 5,5'-$(CO_2Me)_2$-bpy^{1-} and the ethyl analogue, see Figures 3.3 – 3.5, shifts to higher energy compared to the free ligand and now appears at 15,900 cm^{-1} (ε = 3,400 M^{-1} cm^{-1}) in [Pt(5,5'-$(CO_2Me)_2$-bpy)Cl_2]$^{1-}$ and 16,200 cm^{-1} (ε = 6,900 M^{-1} cm^{-1}) in [Pt(5,5'-$(CO_2Et)_2$-bpy)Cl_2]$^{1-}$. This blue shift arises because on complexation, the LUMO of the compound is stabilised with respect to the free ligand. Thus the energy gap between the LUMO and LUMO-1 increases causing all the associated transitions from the SOMO of co-ordinated bpy^{1-} to also increase in energy. Consequently, for [Pt(5,5'-$(CO_2Me)_2$-bpy)Cl_2]$^{1-}$ the bands at 15,900 cm^{-1} (ε = 3,400 M^{-1} cm^{-1}), 18,800 cm^{-1} (ε = 1,900 M^{-1} cm^{-1}), 20,500 cm^{-1} (ε = 2,400 M^{-1} cm^{-1}), 21,900 cm^{-1} (ε = 2,000 M^{-1} cm^{-1}) and 24,900 cm^{-1} (ε = 7,300 M^{-1} cm^{-1}) were all assigned as co-ordinated bpy^{1-} transitions. The same assignment was made for the bands at 16,200 cm^{-1} (ε = 6,900 M^{-1} cm^{-1}), 18,800 cm^{-1} (ε = 4,200 M^{-1} cm^{-1}), 20,500 cm^{-1} (ε = 5,000 M^{-1} cm^{-1}), 22,000cm^{-1} (ε = 4,200 M^{-1} cm^{-1}) and 24,900 cm^{-1} (ε = 11,900 M^{-1} cm^{-1}) for [Pt(5,5'-$(CO_2Et)_2$-bpy)Cl_2]$^{1-}$. From the similarity between the UV/vis/nir spectral results of the free ligands 5,5'-$(CO_2Me)_2$-bpy^{1-} and 5,5'-$(CO_2Et)_2$-bpy^{1-} and their corresponding mono-anionic Pt complexes it can be inferred that the electronic character of the frontier orbitals is similar in all four case *ie* that the MO on [Pt(5,5'-$(X)_2$-bpy)Cl_2]$^{1-}$ where (X = CO_2Me or CO_2Et) is based primarily on the bpy part of the molecule just as it is in the free ligand.

During the conversion between [Pt(5,5'-$(X)_2$-bpy)Cl_2]$^{0/1-}$ (where X = CO_2Me or CO_2Et), isosbestic points are visible for both complexes, indicating complete conversion between the two redox species with no decomposition. For [Pt(5,5'-$(CO_2Me)_2$-bpy)Cl_2]$^{0/1-}$ the isosbestic point is at 28,600cm^{-1}, see Figure 3.13. For [Pt(5,5'-$(CO_2Et)_2$-bpy)Cl_2]$^{0/1-}$ the isosbestic points are at 32,400 cm^{-1} and 30,900 cm^{-1}, see Figure 3.14.

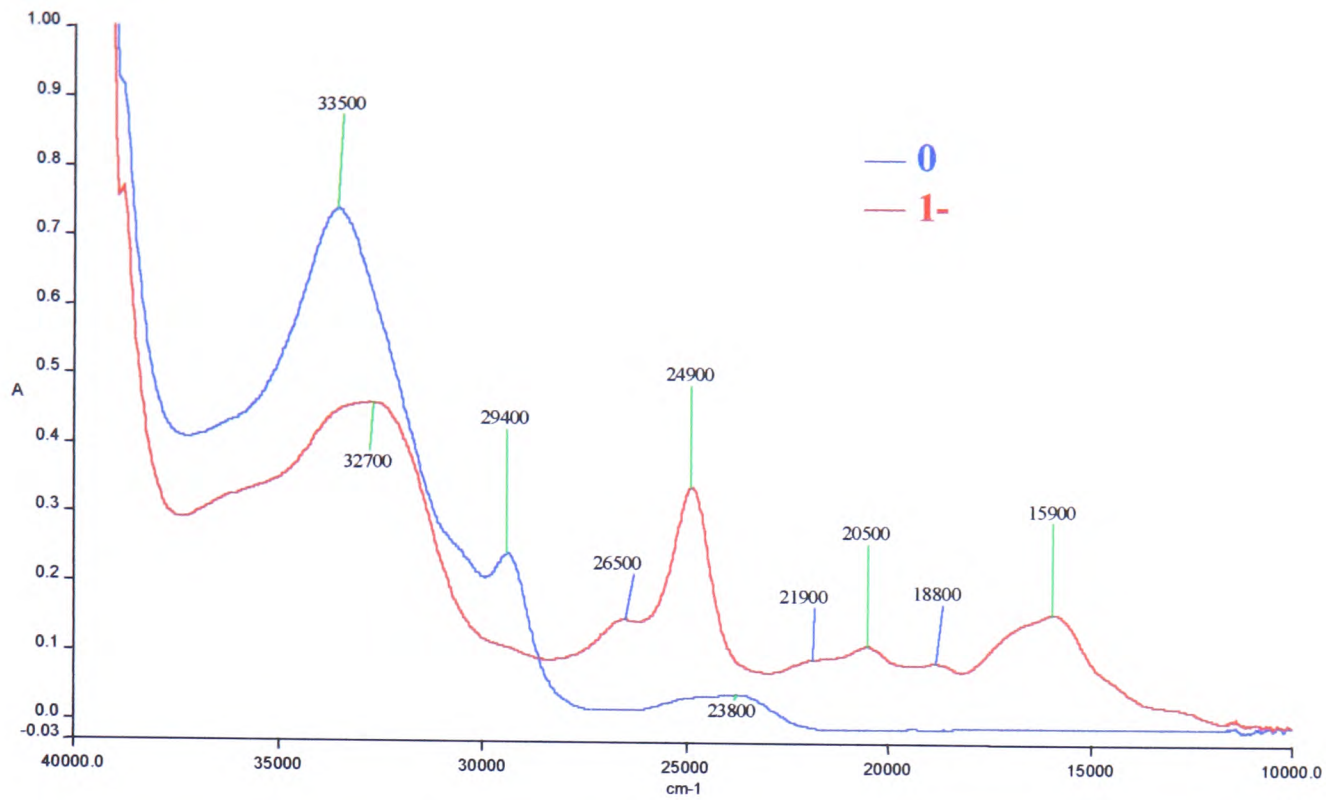

Figure 3. 13 UV/vis/nir spectra of $[Pt(5,5'\text{-}(CO_2Me)_2\text{-}bpy)Cl_2]^{0/1-}$, E_{gen} = -0.86 V, at 233 K in 0.1 M $TBABF_4$/DMF.

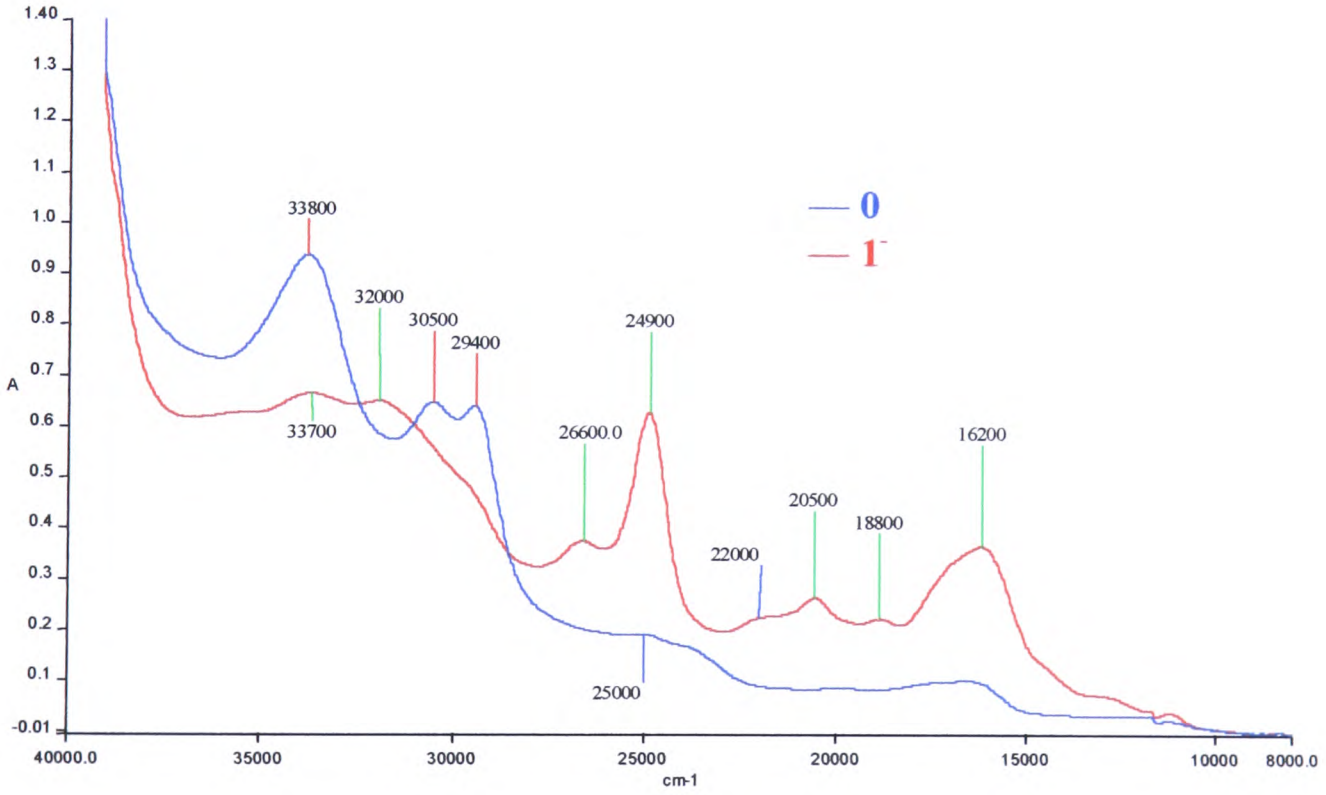

Figure 3. 14 UV/vis/nir spectra of $[Pt(5,5'\text{-}(CO_2Et)_2\text{-}bpy)Cl_2]^{0/1-}$, E_{gen} = -0.86 V at 233 K in 0.1 M $TBABF_4$/DMF.

On reduction to the di-reduced species both complexes again undergo a similar change, see Figure 3.15 and Table 3.8, with an intense doublet growing in at 20 – 23 kcm^{-1}. For the UV/vis spectrum of 5,5'-$(X)_2$-bpy^{2-} (where X = CO_2Me, CO_2Et), this doublet grows in at 19 – 21 kcm^{-1}, see Figure 3.6 and is diagnostic of co-ordinated bpy^{2-} [29]. As with the mono-anionic complexes, this shift to higher energy is brought about by complexation. The strong resemblance between the UV/vis/nir spectra for 5,5'-$(CO_2Me)_2$-$bpy^{1-/2-}$ and $[Pt(5,5'-(CO_2Me)_2-bpy)Cl_2]^{1-/2-}$ again justifies the assignment of the MO of the complex as being based mainly on the bpy moiety, with little contribution from the Pt MOs.

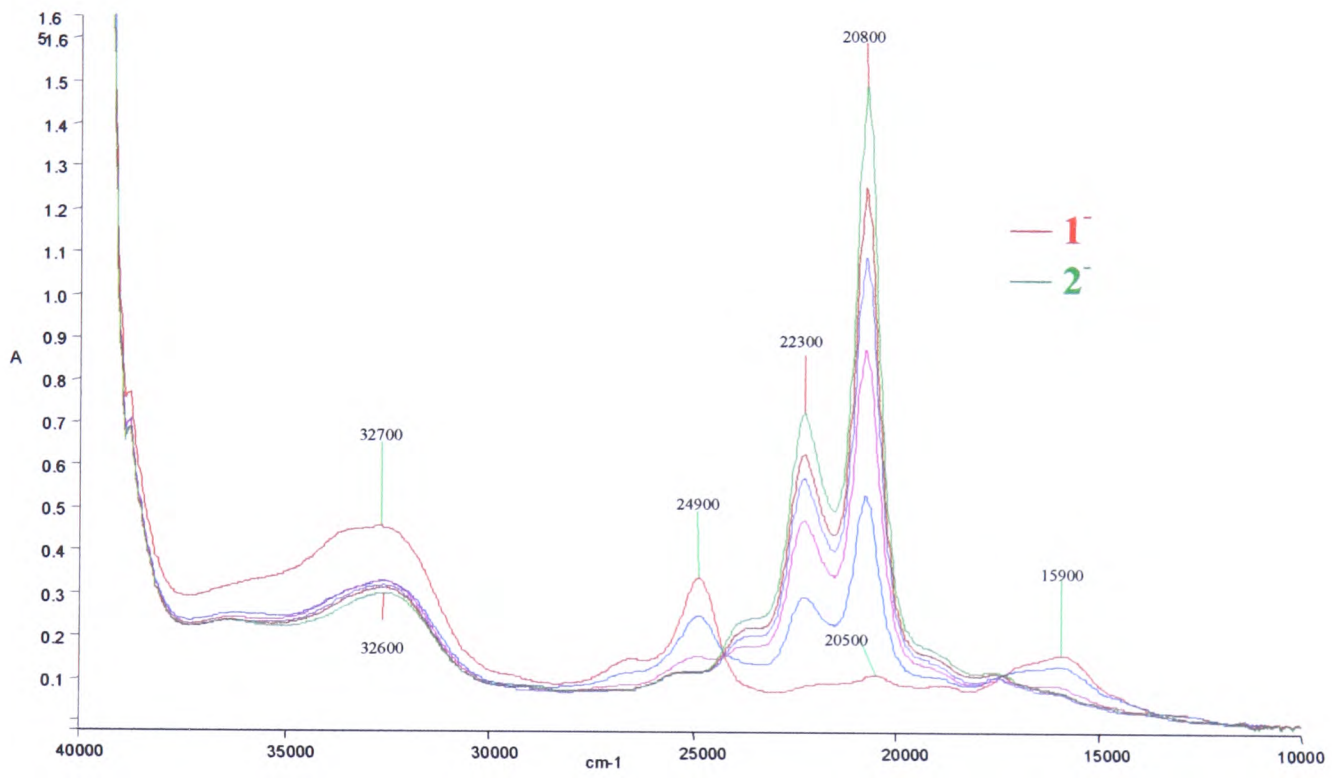

Figure 3. 15 UV/vis/nir spectra of $[Pt(5,5'-(CO_2Me)_2-bpy)Cl_2]^{1-/2-}$, E_{gen} = -1.25 V, at 233 K in 0.1 M $TBABF_4$/DMF.

During the conversion of $[Pt(5,5'-(CO_2Me)_2-bpy)Cl_2]^{1-}$ to $[Pt(5,5'-(CO_2Me)_2-bpy)Cl_2]^{2-}$ the peaks at 15,900 cm^{-1}, 24,900 cm^{-1}, 26,300 cm^{-1} and 32,700 cm^{-1} (ε = 9,900 M^{-1} cm^{-1}) collapse while the peaks at 20,800 cm^{-1} (ε = 32,400 M^{-1} cm^{-1}) and 22,500 cm^{-1} (ε = 15,700 M^{-1} cm^{-1}) grow in accordingly. The isosbestic points at 24,300 cm^{-1} and 17,300 cm^{-1} are clearly visible.

For the $[Pt(5,5'\text{-}(CO_2Et)_2\text{-}bpy)Cl_2]^{1-/2-}$ couple the peaks at 16,200 cm^{-1}, 18,800 cm^{-1}, 20,500 cm^{-1}, 22,000 cm^{-1}, 24,900 cm^{-1} and 26,600 cm^{-1} all collapse and the doublet grows in at 20,800 cm^{-1} (ε = 49,300 M^{-1} cm^{-1}) and 22,200 cm^{-1} (ε = 29,000 M^{-1} cm^{-1}). Three isosbestic points arise at 32,500 cm^{-1}, 31,100 cm^{-1} and 28,500 cm^{-1}. Electrochemical data, along with the results from epr, see section 3.2.2.3, suggests that spin pairing of the two reduction electrons occurs as it does with the free ligands. Thus these intense peaks are assigned as intraligand transitions from the now doubly occupied LUMO to higher energy, empty π^* anti-bonding orbitals. The intense peaks in $5,5'\text{-}(CO_2Me)_2\text{-}bpy^{2-}$ and $5,5'\text{-}(CO_2Et)_2\text{-}bpy^{2-}$ were assigned in the same way.

For both $[Pt(5,5'\text{-}(CO_2Me)_2\text{-}bpy)Cl_2]^{0/1-/2-}$ and $[Pt(5,5'\text{-}(CO_2Et)_2\text{-}bpy)Cl_2]^{0/1-/2-}$ all spectral changes are reversible . On switching the electrode potential back to 0 V complete regeneration of the starting spectrum is achieved.

As discussed earlier, the complexes of $[Pt(5,5'\text{-}(X)_2\text{-}bpy)Cl_2]$ all give rise to yellow solutions with UV/vis spectra similar to that of $[Pt(bpy)Cl_2]$. The lowest energy feature in each case is the metal-to-ligand ($Pt^{II} \rightarrow X_2\text{-}bpy\ \pi^*$) charge transfer (MLCT) transition. In agreement with this assignment there is a linear correlation between the first reduction potential E_1 and the MLCT absorption maximum, ν_{max}, see Figure 3.16.

Table 3 8 Peak positions and molar extinction coefficients, ε, for $[Pt(5,5'\text{-}(CO_2Me)_2\text{-}bpy)Cl_2]^{0/1-/2-}$ and $[Pt(5,5'\text{-}(CO_2Et)_2\text{-}bpy)Cl_2]^{0/1-/2-}$ in 0.1 M $TBABF_4$/DMF at 233 K.

Oxidation state	**$[Pt(5,5'\text{-}(CO_2Me)_2\text{-}bpy)Cl_2]$**	**$[Pt(5,5'\text{-}(CO_2Et)_2\text{-}bpy)Cl_2]$**
	Peak position / cm^{-1} ( ) ε /M^{-1} cm^{-1}	Peak position / cm^{-1} ( ) ε /M^{-1} cm^{-1}
0	33,500 (15,900), 29,400 (5,200), 23,800 (856)	37,600 (18,900), 33,800 (24,000), 30,500 (12,300), 29,400 (14,200), 24,800 (2,800), 23,800 (3,200)
1^-	32,700 (9,900), 26,500 (3,200), 24,900 (7,300), 21,900 (2,000), 20,500 (2,400), 18, 800 (1,900), 15,900 (3,400)	33,700 (12,600), 31,900 (12,200), 29,700 (9,300), 26,600 (7,100), 24,900 (11,900), 22,000 (4,200), 20,500 (5,000), 18,800 (4,200), 16,200 (6,900)
2^-	36,400 (5,100), 32,700 (6,500), 23, 600 (5,300), 22,300 (15,700), 20,800 (32,400), 19,000 (3,700), 17,600 (2,600)	32600 (11,500), 25,100 (6,300), 23,600 (11,400), 22,200 (29,000), 20,800 (49,300), 19,200 (8,600), 17,500 (6,500)

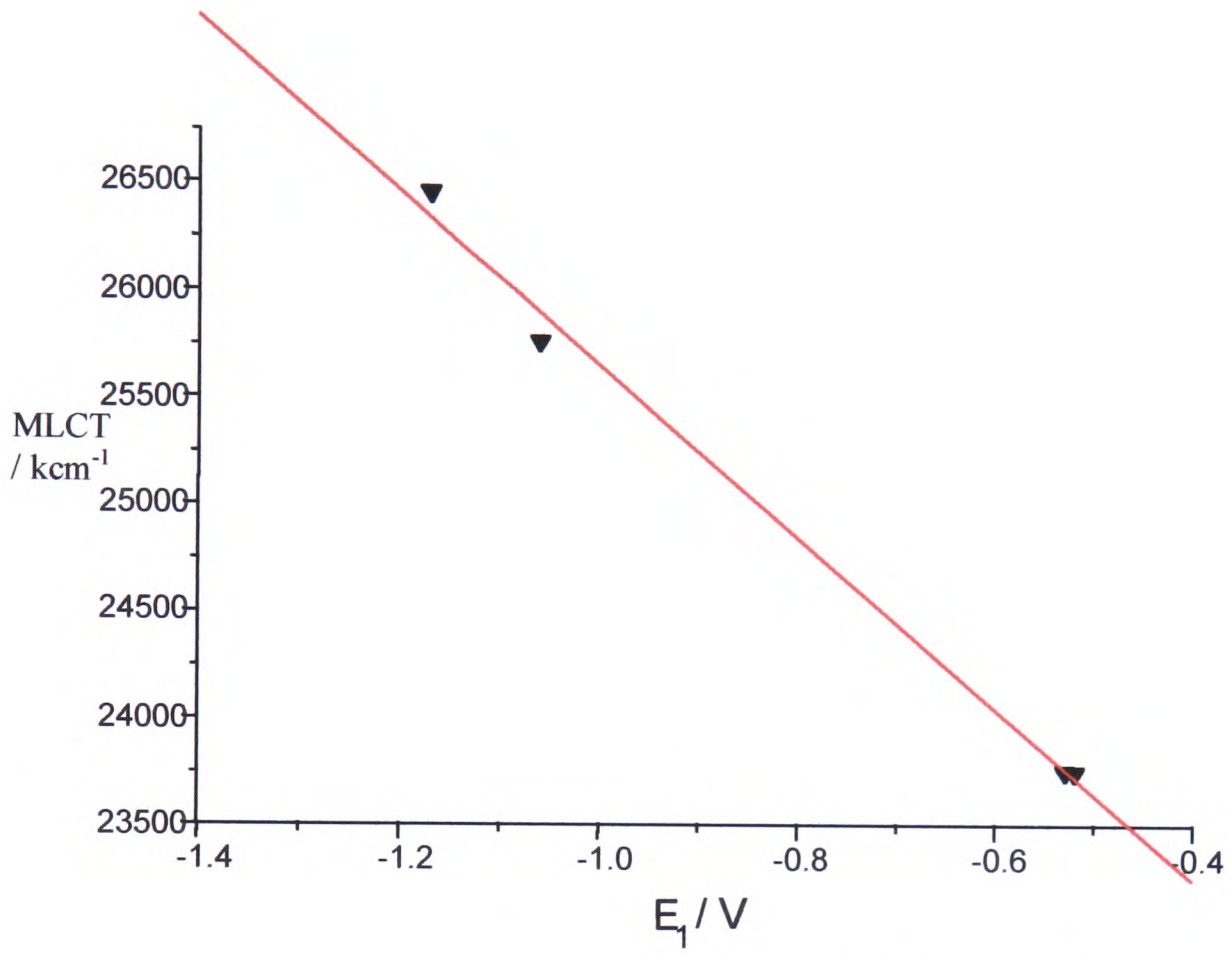

Figure 3.16 Plot of E_1 *vs* MLCT ν_{max} for [Pt(5,5'-$(X)_2$-bpy)Cl_2].

3.2.2.3 Epr Spectroelectrochemistry

Reduction of the $[Pt(5,5'\text{-}(X)_2\text{-}bpy)Cl_2]$ complexes to their mono-reduced state gives epr active solutions. However, if the complex is then converted to its di-reduced form it becomes diamagnetic and the epr signal collapses. This is in agreement with the redox chemistry of the complexes where the potential separation between the two reduction processes indicates that spin pairing occurs between the first and second reduction electrons that is, that both reduction electrons are in the same orbital. The solution epr spectra of $[Pt(5,5'\text{-}(Me)_2\text{-}bpy)Cl_2]^{1-}$, $[Pt(5,5'\text{-}(CO_2Me)_2\text{-}bpy)Cl_2]^{1-}$ and $[Pt(5,5'\text{-}(CO_2Et)_2\text{-}bpy)Cl_2]^{1-}$ are all similar, showing coupling of the reduction electron to the ^{195}Pt nucleus, (natural abundance 34 %, I = ½), see Table 3.9. The epr signal is a broad central line with ^{195}Pt satellites. Any superhyperfine coupling of the reduction electron to ligand nuclei is unresolved, see Figure 3.17. All spectra were generated *in situ* in 0.1 M $TBABF_4$/DMF.

Table 3 9 Solution epr parameters for $[Pt(5,5'\text{-}(X)_2\text{-}bpy)Cl_2]^{1-}$ in 0.1 M $TBABF_4$/DMF.

$[Pt(5,5'\text{-}(X)_2\text{-}bpy)Cl_2]^{1-}$ X =	E_{gen} / V	^{195}Pt coupling / G	g_{iso}	ΔH_{pp} / G
H [a, b]	-1.50	-54	1.998	-
Me [c]	-1.60	-60	1.998	19
CO_2Me [c]	-0.80	-38	1.996	12.5
CO_2Et [c]	-0.80	-39	1.994	9.8

(a) PhD thesis of E. J. L. McInnes, University of Edinburgh, 1995.[25] (b) generated at room temperature. (c) generated at 273 K.

On cooling to 173 K rhombic X-band epr spectra are obtained for $[Pt(5,5'\text{-}(CO_2Me)_2\text{-}bpy)Cl_2]^{1-}$, see Figure 3.19, $[Pt(5,5'\text{-}(CO_2Et)_2\text{-}bpy)Cl_2]^{1-}$ and $[Pt(5,5'\text{-}(Me)_2\text{-}bpy)Cl_2]^{1-}$, see Table 3.10. They are similar to the frozen glass

spectrum obtained for $[Pt(bpy)Cl_2]^{1-}$, see Table 3.10 and may be treated similarly. ^{195}Pt hyperfine coupling to g_1 and g_2 is observed. However, the high field g_3 ^{195}Pt coupling is not resolved in any of the spectra. A_3 can be estimated from the magnitudes of A_{iso}, A_1 and A_2 (equation 3.2).

$$A_3 = 3A_{iso} - (A_1 + A_2) \quad (3.2)$$

The second derivative spectra of $[Pt(5,5'\text{-}(Me)_2\text{-}bpy)Cl_2]$ and $[Pt(5,5'\text{-}(CO_2Et)_2\text{-}bpy)Cl_2]$ were simulated to improve the resolution on the g_3 features of the frozen spectra, see Table 3.10. The g values and Pt A_1, A_2 and A_3 values obtained are in good agreement with the g_{iso} and Pt hyperfine coupling constants obtained for the first derivative spectra. A_3 values for ^{14}N could also be obtained and were best simulated assuming coupling to two equivalent nitrogens, see Table 3.10.

Table 3 10 Epr parameters of $[Pt(5,5'\text{-}(X)_2\text{-}bpy)Cl_2]^{1-}$ in 0.1 M $TBABF_4$/DMF at 173 K. Values in blue are simulation parameters obtained for the 2nd derivative spectra.

$[Pt(5,5'\text{-}(X)_2\text{-}bpy)Cl_2]^{1-}$	g_{iso}	g_1	g_2	g_3	A_{iso} / G	A_1 / G	A_2 / G	A_3 / G	$A_3(2N)$ / G
Me	1.998	2.041	2.011	1.938	-60	-60	-91	-29	
					(56)	(57)	(85)	(26)	
		2.041	2.012	1.939		-64	-92	-25	12
H [a]	1.998	2.038	2.009	1.935	-58	-60	-86	-23	
					(54)	(56)	(81)	(21)	
CO_2Me	1.996	2.024	2.002	1.946	-38	-41	-61	-12	
					(36)	(39)	(57)	(11)	
CO_2Et	1.994	2.027	2.004	1.947	-39	-40	-60	-17	
					(37)	(38)	(56)	(16)	
		2.037	2.013	1.958		-38	-52	-20	6.5

(a) 77 K in 0.1 M $TBABF_4$/DMF, PhD thesis of E. J. L. McInnes, University of Edinburgh, 1995.[25] (Values in parentheses are A / 10^{-4} cm^{-1}).

The Gaussian linewidths for $[Pt(5,5'\text{-}(CO_2Et)_2\text{-}bpy)Cl_2]^{1-}$ and $[Pt(5,5'\text{-}(Me)_2\text{-}bpy)Cl_2]^{1-}$ are $W_1 = 10$ G, $W_2 = 8$ G and $W_3 = 9$ G and $W_1 = 16$ G, $W_2 = 12$ G and $W_3 = 14$ G respectively. The structure on g_3 is far more sensitive to the magnitude of the N superhyperfine coupling than to the Pt hyperfine coupling.

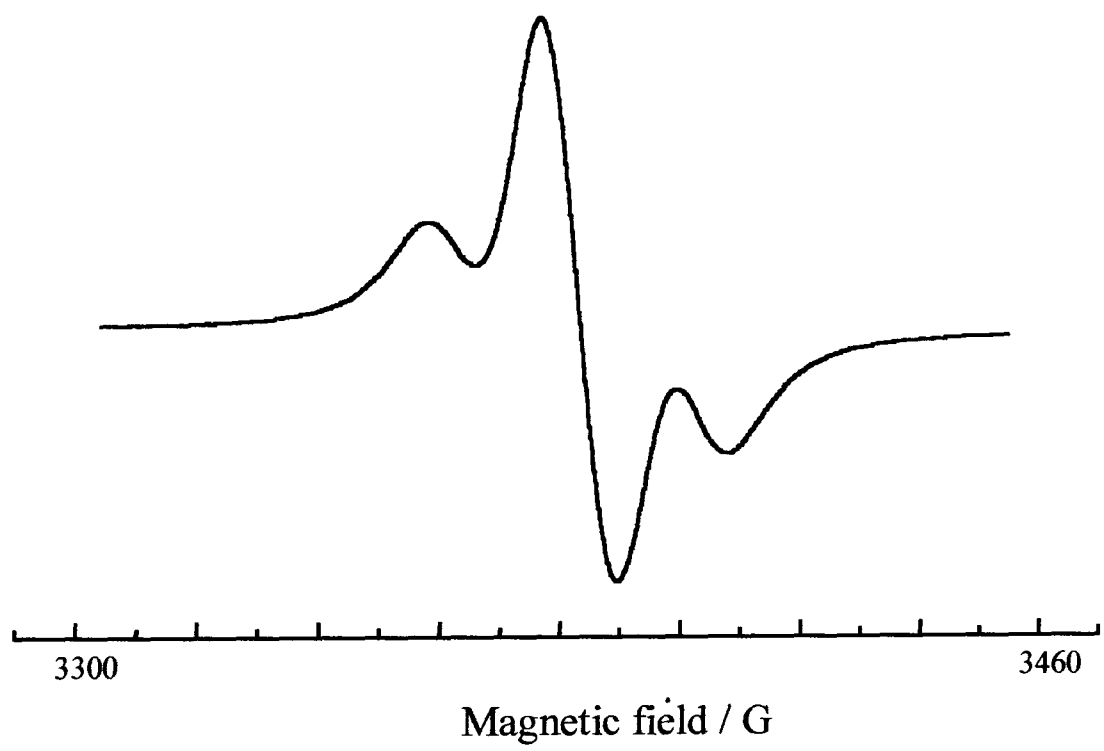

Figure 3. 17 Solution epr of $[Pt(5,5'\text{-}(CO_2Me)_2\text{-}bpy)Cl_2]^{1-}$ generated *in situ* at 273 K in 0.1 M $TBABF_4$/DMF, $E_{gen} = -0.80$ V.

The average of $g_1 + g_2 + g_3$ is in good agreement with g_{iso}. The similarity of the epr signals of the complexes of $[Pt(5,5'\text{-}(X)_2\text{-}bpy)Cl_2]$, where X = H, Me, CO_2Me and CO_2Et) indicates a common ground state in each case. The small shift in g_{iso} from the free electron value, g_e of 2.0023 suggests that there is only a small admixture of metal orbitals in the SOMO and that the reduction electron is therefore based mainly on the bpy ligand. McInnes *et al.* have previously made quantitative estimates of the Pt 5d and 6p orbital admixture to the SOMO of $[Pt(bpy)L_2]^{1-}$ [33] and $[Pt(4,4'\text{-}(X)_2\text{-}bpy)Cl_2]^{1-}$.[32] As the electrochemical and spectroscopic properties of $[Pt(5,5'\text{-}(X)_2\text{-}bpy)Cl_2]$ are very similar to the 4,4' analogue, the Pt 5d and 6p contributions to the SOMO can be calculated in the same way, using the equations given by Connelly and co-workers,[61] but Rieger's nomenclature.[62]

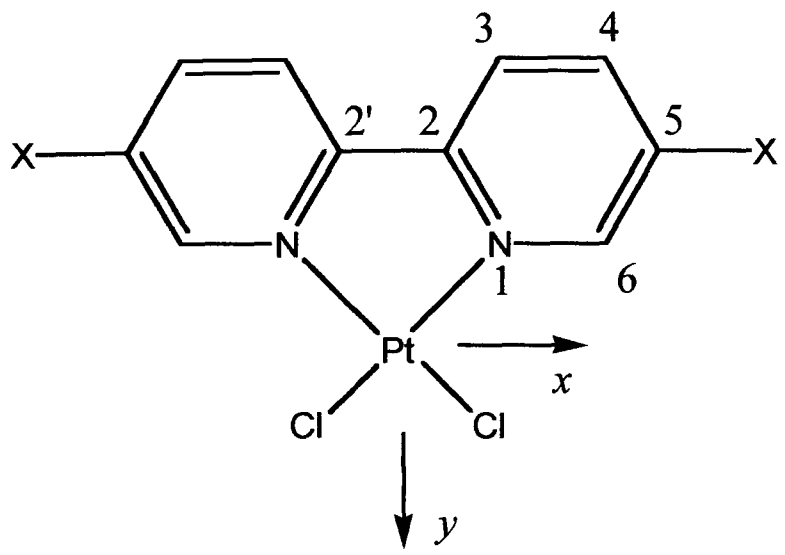

Figure 3.18 Structure, principal axis system and numbering scheme of $[Pt(5,5'\text{-}(X)_2\text{-bpy})Cl_2]$. The *z* axis is perpendicular to the plane of the molecule.

If we assume the SOMO of $[Pt(5,5'\text{-}(X)_2\text{-bpy})Cl_2]^{1-}$ is of b_2 symmetry (in C_{2v} point symmetry), with the axes as defined by Figure 3.18, then the metal contribution to the SOMO can be calculated by equations 3.3 – 3.5.[32] These equations make the assumption that spin orbit coupling can be ignored.

$$A_{xx} = A_s - (4/7)\, P_d\, a^2 - (2/5)\, P_p\, b^2 \qquad (3.3)$$

$$A_{yy} = A_s + (2/7)\, P_d\, a^2 - (2/5)\, P_p\, b^2 \qquad (3.4)$$

$$A_{zz} = A_s + (2/7)\, P_d\, a^2 + (4/5)\, P_p\, b^2 \qquad (3.5)$$

Where a^2 and b^2 = the unpaired electron spin density in the $5d_{yz}$ and $6p_z$ orbitals respectively, *ie* a^2 is the metal $5d_{yz}$ admixture to the SOMO.

P_d and P_p = electron-nuclear dipolar coupling parameters with $P_d = 549 \times 10^{-4}$ cm^{-1} and $P_p = 402 \times 10^{-4}$ cm^{-1} [32].

A_s = the isotropic Fermi contact term.

A values were converted from G to cm^{-1} using the equation:

$a\ (cm^{-1}) = (A_1 \times g_1) / 2.142 \times 10^4$

In keeping with the previous studies on $[Pt(4,4'\text{-}(X)_2\text{-bpy})Cl_2]$[32] and $[Pt(bpy)L_2]$,[33] A_{xx} was assigned as the largest hyperfine term (A_2) and A_{zz} was assigned as the

smallest hyperfine term, A_3. In C_{2v} symmetry the g and metal hyperfine axes must be coincident and we therefore assign g_2 to g_{xx}. The values of a^2 and b^2 obtained are given in Table 3.11.

Table 3 11 Platinum $5d_{yz}$ and $6p_z$ admixtures to the SOMO of $[Pt(5,5'\text{-}(X)_2\text{-bpy})Cl_2]^{1-}$ and $[Pt(4,4'\text{-}(X)_2\text{-bpy})Cl_2]^{1-}$.

X	$[Pt(5,5'\text{-}(X)_2\text{-bpy})Cl_2]^{1-}$			$[Pt(4,4'\text{-}(X)_2\text{-bpy})Cl_2]^{1-}$ [a]		
	a^2	b^2	Total Pt	a^2	b^2	Total Pt
Me	0.060	0.064	0.12	0.033	0.075	0.11
H[a]	0.051[a]	0.075[a]	0.13	0.051	0.075	0.13
CO_2Me	0.038	0.058	0.10	0.055	0.067	0.12
CO_2Et	0.038	0.046	0.08	-	-	-

(a) values from McInnes *et al.*. [32]

For each complex the contributions from the metal orbitals to the SOMO consist of almost equally small amounts of $5d_{yz}$ and $6p_z$ although the latter is always slightly larger. The total Pt contributions to the SOMO are in the range 8 – 13 % and confirm that the reduction electron enters a predominantly ligand based orbital in each case. The contribution of the Pt-based orbitals to the SOMO of the 5,5'-$(X)_2$-bpy derivatives is approximately the same as for the 4,4'-derivatives and it would be unwise to deliberate extensively on the small differences. However, it would appear that the electron donating Me group results in an increased Pt contribution to the SOMO when in the 5,5' position rather than the 4,4' one and electron withdrawing CO_2Me groups result in a smaller Pt contribution when substituted in the 5,5' position. This observation is in agreement with the Hammett plots and confirms that the 5,5' positions on the 2,2'-bipyridine are electronically more important than the 4,4' positions. Ideally, more 5,5' substituted bpys should be investigated, however such species will be difficult to synthesise.

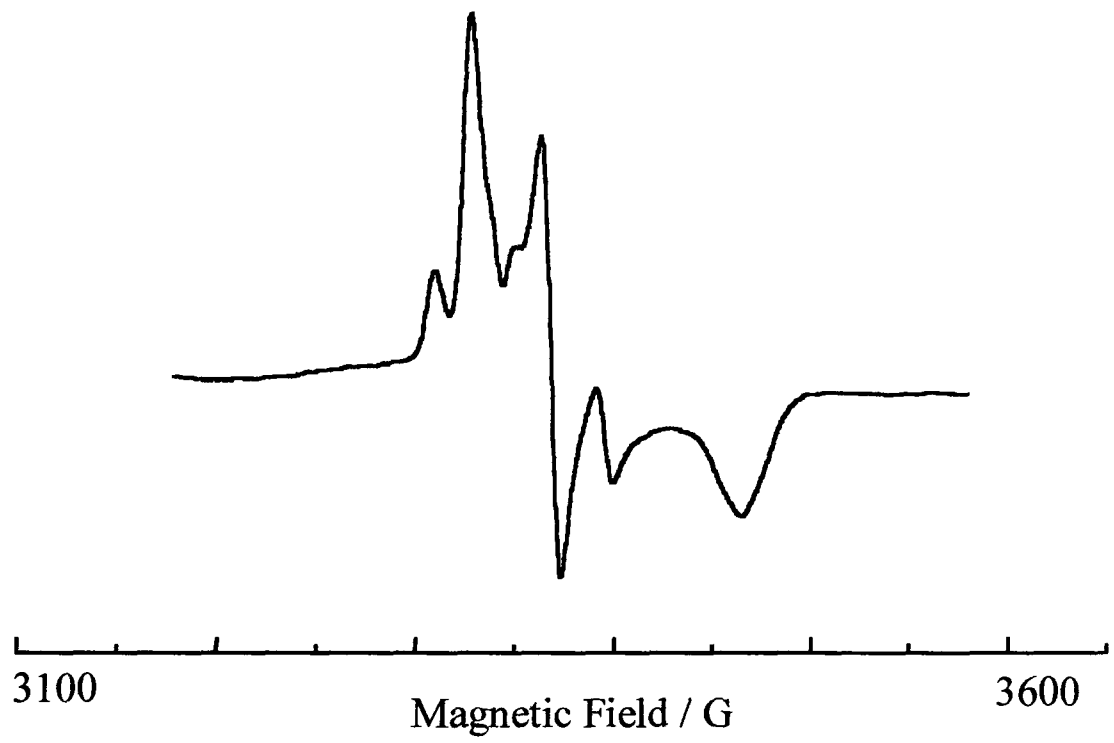

Figure 3.19 173 K X-band epr spectrum of $[Pt(5,5'\text{-}(CO_2Me)_2\text{-}bpy)Cl_2]^{1-}$ in 0.1 M $TBABF_4$/DMF.

3.3 Conclusions

The redox chemistry of 5,5'-$(X)_2$-bpy and [Pt(5,5'-$(X)_2$-bpy)Cl_2], where X = Me, CO_2Me, CO_2Et, can be explained in terms of the two reduction electrons entering the same orbital, in this case the lowest unoccupied π^* orbital of the $(X)_2$-bpy ligand. The one exception occurs where X = NH_2, as in this case the first reduction is followed by a rapid chemical reaction. Systematic variation of X allows us to control the energy of the π^* LUMO. Electron withdrawing substituents stabilise the LUMO, while electron donating substituents have the opposite effect.

Comparison of the gradients on a plot of the Hammett parameters σ_m and σ_p against the first reduction potentials of [Pt(5,5'-$(X)_2$-bpy)Cl_2] and [Pt(4,4'-$(X)_2$-bpy)Cl_2] indicates that the 5,5' position is electronically the more important site of substitution. Analysis of the epr spectra of the mono-reduced complexes indicates that the reduction electron enters an orbital primarily based on the bpy ligand and this conclusion is in agreement with the UV/vis spectra of the reduced species.

3.4 Experimental

All reagents were commercially available and used as supplied, with the exception of the ligands whose preparation is detailed here. Elemental analysis was conducted by the microanalytical services of Edinburgh University.

3.4.1 Synthesis of 5,5'-$(X)_2$-bpy

3.4.1.1 Synthesis of 5,5'-$(Me)_2$-bpy

The method followed was as reported by Sasse and Whittle[43], Badger and Sasse[63] and Whittle[44] although some alteration was made to the procedure, with 3-picoline being used in place of pyridine.

Raney-nickel slurry (125 g) was placed in a three-necked, round bottom flask fitted with a condenser, a pressure equalised dropping funnel and an interchangeable tap between the pump and the nitrogen outlet. The flask was placed in a water bath at 90°C, the top of the condenser stoppered and the water removed from the Raney-nickel slurry under vacuum. When the Raney-nickel was dry the apparatus was back filled with nitrogen. Degassed 3-picoline was cautiously added to the flask via the dropping funnel. The mixture was kept under nitrogen and refluxed at 125 °C for 50 hours.

The Raney-nickel was quickly filtered off and washed with a little hot 3-picoline. The orange filtrate was vacuum distilled to remove any unreacted 3-picoline. The crude 5,5'-$(Me)_2$-bpy was extracted with boiling light petroleum (bp 60-80 °C) and purified by chromatography using alumina as the stationary phase and light petroleum (bp 60-80 °C) as the eluent and recrystallised from light petroleum (bp 60-80 °C). 5,5'-$(Me)_2$-bpy was obtained as white needle-like crystals. CHN analysis of $C_{12}H_{12}N_2$: calculated 78.23 % C, 6.56 % H, 15.21 % N; found 78.25 % C, 6.51 % H, 15.13 % N.

3.4.1.2 Synthesis of 5,5'-$(CO_2Et)_2$-bpy

5,5'-$(Me)_2$-bpy (1.030 g, 5.59×10^{-3} moles) was added to an aqueous solution of potassium permanganate (5.665 g) and heated until decolourisation of the permanganate.[44, 64] The precipitated manganese dioxide was removed by filtration and the filtrate extracted with diethyl ether to remove any unreacted 5,5'-$(Me)_2$-bpy. The crude acid was precipitated from the filtrate by addition of concentrated hydrochloric acid. (Percentage yield 97.7 %). CHN analysis for $C_{12}H_8N_2O_4$: calculated 59.02 % C, 3.30 % H, 11.47 % N; found 58.81 % C, 3.09 % H, 12.89 % N.

5,5'-$(COOH)_2$-bpy (1.333 g, 5.46×10^{-3} moles), ethanol (20 ml) and concentrated sulphuric acid (5 g, ~ 2.6 ml) were heated under reflux at 125 °C for 18 hours.[44] The reaction mixture was poured into water and the crude 5,5'-$(CO_2Et)_2$-bpy obtained as precipitate. The product was recrystallised from ethanol as fine, white, needle like crystals, (Percentage yield 90.3 %). CHN analysis for $C_{16}H_{16}N_2O_4$: calculated 63.99 % C, 5.37 % H, 9.33 % N; found 63.65 % C, 5.18 % H, 9.34 % N.

3.4.1.3 Synthesis of 5,5'-$(CO_2Me)_2$-bpy

5,5'-$(CO_2Me)_2$-bpy was synthesised by the same method as 5,5'-$(CO_2Et)_2$-bpy, with methanol used in place of ethanol.[44] (Percentage yield 69.5 %). CHN analysis for $C_{14}H_{12}N_2O_4$: calculated 61.74 % C, 4.44 % H, 10.29 % N; found 61.26 % C, 4.33 % H, 10.15 % N.

3.4.1.4 Synthesis of 5,5'-$(NH_2)_2$-bpy

This ligand was synthesised in a four step reaction as described by Whittle.[44] Synthesis of 5,5'-$(CONHNH_2)_2$-bpy. A mixture of 5,5'-$(CO_2Et)_2$-bpy (0.601 g, 2×10^{-3} moles), ethanol (3 ml) and hydrazine hydrate (3 ml) was heated under reflux at 115 °C for 3 hours. The creamy insoluble product was removed by filtration, washed with boiling ethanol and dried to give 5,5'-$(CONHNH_2)_2$-bpy (Percentage yield 88.5 %).

CHN analysis for $C_{12}H_{12}N_6O_2$: calculated 52.93 % C, 4.44 % H, 30.87 % N; found 51.61 % C, 4.64 % H, 29.39 % N.

Finely powdered 5,5'-$(CONHNH_2)_2$-bpy (0.468 g, 1.7×10^{-3} moles) was suspended in concentrated hydrochloric acid (9.5 ml) and the mixture cooled to 0 °C. A cold solution of sodium nitrite in water (2 ml) was added dropwise with stirring, keeping the temperature below 10 °C. The mixture was left to react overnight, below 10 °C. Water was then added to the reaction to precipitate the white 5,5'-$(CON_3)_2$-bpy. The precipitate was collected, washed with water and hot ethanol and dried to give 5,5'-$(CON_3)_2$-bpy (Percentage yield 90.2 %). CHN analysis for $C_{12}H_6N_8O_2$: calculated 48.99 % C, 2.06 % H, 38.08 % N; found 49.71 % C, 3.20 % H, 26.53 % N.

The diazide (0.455 g, 1.5×10^{-3} moles) was suspended in a mixture of ethanol (13.5 ml) and o-xylene (13.5 ml) and refluxed for 9 hours. The resulting precipitate was recrystallised from ethanol to give 5,5'-$(NHCO_2CH_2CH_3)_2$-bpy (Percentage yield 58.2 %). CHN analysis for $C_{16}H_{18}N_4O_4$: calculated 58.17 % C, 5.49 % H, 16.96 % N; found 58.09 % C, 5.43 % H, 16.72 % N.

A mixture of 5,5'-$(NHCO_2CH_2CH_3)_2$-bpy (0.250 g, 7.57×10^{-3} moles), ethanol (4 ml) and 2.5 N NaOH solution (4 ml) was stirred at 70 –80 °C for 24 hours. The mixture was cooled and the product collected and recrystallised from water containing a few drops of ammonia. 5,5'-$(NH_2)_2$-bpy was obtained as pale yellow crystals. CHN analysis for $C_{10}H_{10}N_4$: calculated 64.49 %C, 5.41 % H, 30.09 % N; found 62.40 % C, 5.26 % H, 28.58 % N.

3.4.2 Synthesis of Pt (II) Complexes of 5,5'-$(X)_2$-bpy

All complexes were prepared by the following general procedure. A suspension of appropriate ligand (1.2 equivalents) was heated under reflux, with stirring, in an aqueous solution of $K_2[PtCl_4]$ (1 equivalent). The resultant precipitate was collected by filtration, washed with water and dried under vacuum. All compounds were

recrystallised from a hot, saturated solution of N,N'-dimethylformamide. Reflux times, percentage yields and analyses are given in Table 3.12 below.

Table 3 12 Syntheses and analyses of the complexes [Pt(5,5'-$(X)_2$-bpy)Cl_2].

Complex	Reflux time / hours	Colour	Yield / %	C / %	H / %	N / %
[Pt(5,5'-$(Me)_2$-bpy)Cl_2]	15	green / yellow	60.9	32.01[a]	2.69	6.22
				31.81[b]	2.66	6.12
[Pt(5,5'-$(CO_2Et)_2$-bpy)Cl_2]	15	dark red	62.5	33.93	2.85	4.95
				34.05	2.82	4.88
[Pt(5,5'-$(CO_2Me)_2$-bpy)Cl_2]	15	yellow	69.5	31.24	2.25	5.20
				33.56	2.36	5.62
[Pt(5,5'-$(NH_2)_2$-bpy)Cl_2] [c]	1.5	orange / brown	99.4	26.56	2.23	12.39
				28.95	2.79	13.24

[a] calculated, [b] found, [c] not recrystallised

CHAPTER 4:

A Comparison of the Ligands 4,4'-$(NO_2)_2$-bpy, 4-NO_2-bpy and 4-NO_2-py and Their Complexes With Pt (II) and Pd (II).

Chapter 4 A Comparison of the Ligands 4,4'-$(NO_2)_2$-bpy, 4-NO_2-bpy and 4-NO_2-py and Their Complexes With Pt (II) and Pd (II)

Reported in this chapter is the synthesis, redox chemistry and spectroelectrochemistry (UV/vis/nir, epr) of the ligands 4,4'-$(NO_2)_2$-bpy and 4-NO_2-bpy and their corresponding complexes [Pt(4,4'-$(NO_2)_2$-bpy)Cl_2], [Pd(4,4'-$(NO_2)_2$-bpy)Cl_2], [Pt(4-NO_2-bpy)Cl_2], and [Pd(4-NO_2-bpy)Cl_2]. Good evidence is presented that in each case the redox orbital is the lowest unoccupied π^* orbital based primarily on the 4-NO_2-py portion of the bipyridine ligand. Electro and spectroelectrochemical studies on the ligand 4-NO_2-pyridine (py) and [Pt(4-NO_2-py)$_2Cl_2$] confirm this assignment of the redox orbital. In the case of [Pd(4-NO_2-py)$_2Cl_2$], the lowest energy unoccupied orbital is based on the Pd metal centre.

4.1 Introduction

A number of papers give details of how to synthesise 4,4'-$(NO_2)_2$-bpy and its mono-functionalised analogue 4-NO_2-bpy.[42, 65, 66] However, there are very few published papers on the behaviour of these ligands or on their complexes with transition metals.[67, 68]

4-NO_2-bpy has been reported to undergo two consecutive irreversible reductions at –1.55 V and –2.38 V.[67] However, the electrochemistry of 4-NO_2-bpy reported here indicates that 4-NO_2-bpy undergoes a fully reversible one electron reduction at –0.72 V and a second quasi-reversible reduction at a potential 900 mV more negative, see Section 4.2.1.1. In contrast, 4,4'-$(NO_2)_2$-bpy underwent two consecutive one electron, reversible reductions at –0.80 V and –0.91 V.[67] These waves were attributed to the reduction of the bpy π system. Weiner *et al.* noted that the electron withdrawing nitro substituents lowered the potential necessary for the reduction of the π system relative to the unsubstituted bpy.

X-ray crystallography of 4,4'-$(NO_2)_2$-bpy indicates that the molecule sits on a centre of symmetry and is almost planar.[68] The nitro group is slightly displaced from the best plane through the atoms of the pyridine ring and the two pyridine rings are slightly offset. Pilkington and co-workers explained the small angle C2-N1-C6 of 117.8 (1)° by the fact that the lone pair at the N atom needs more space than an N-C bonding pair. The C2-C2' distance is *ca.* 0.1 Å longer than the C-C bonds in the ring and has strong single bond character. Analysis of the crystal packing of 4,4'-$(NO_2)_2$-bpy revealed molecular tapes formed by C-H···O hydrogen bonds.[68]

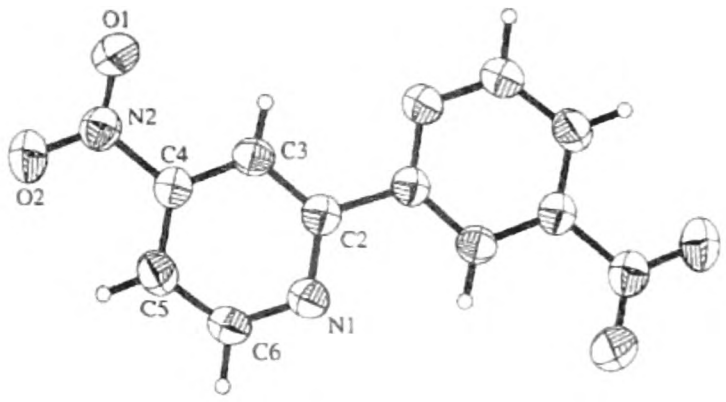

Figure 4. 1 Molecular structure of 4,4'-$(NO_2)_2$-bpy showing the atomic numbering and the 50 % probability displacement ellipsoids.[68]

A literature search revealed only one reference for the synthesis, properties and complexation of 4-NO_2-py.[67] In their studies on the iron(II), cobalt(II) and ruthenium(II) complexes of pyridines and bipyridines substituted either with $(Et)_3P$ groups or nitro groups Weiner *et al.* noted that the complex $Et_4N^+[Co(4\text{-}NO_2\text{-}py)Br_3]$ showed a metal → pyridine charge transfer transition at 26,300 cm^{-1}. However, this transition was missing in studies of the $(Et)_3P$-substituted pyridine complex of Co(II). This led Weiner and co-workers to the conclusion that in this pyridyl ring system the nitro group was more effective in lowering the metal-ligand charge transfer (MLCT) energy than the $(Et)_3P$ group.[67]

From resonance Raman vibrational spectra Basu and co-workers concluded that a considerable portion of the charge transferred in the MLCT excited state for

$[Ru(4\text{-}NO_2\text{-}bpy)_3]^{2+}$ resides on the nitro substituent, *ie* that the ligand π^* orbital is localised mainly on the nitro group.[69, 70] Basu *et al.* explained the lack of luminescence for 4-NO_2-bpy and the corresponding Ru(II) complex as being due to the rapid vibrational depopulation of the excited state *via* coupling of the nitro group to the solvent, eg *via* hydrogen bonding. However, emission spectra for $[Ru(4,4'\text{-}(NO_2)_2\text{-}bpy)_3]^{2+}$ centred at 700 nm in an EtOH/H_2O 4:1 v/v solution at 293 K was reported by Cook *et al.*.[71, 72] This emission is red shifted compared to the emission for $[Ru(bpy)_3]^{2+}$ which occurs at 630 nm under the same conditions.[71]

Studies on the series of complexes $[(4,4'\text{-}(X)_2\text{-}bpy)Ru(CO)_2Cl_2]$ indicated that electron donor substituents shifted the absorption maximum of the MLCT transition to lower wavelength while electron withdrawing substituents such as NO_2 had the opposite effect. Density functional theory (DFT) calculations on this series of complexes indicated that the electronic effect of the substituent altered the HOMO-LUMO energies and that $[(4,4'\text{-}(NO_2)_2\text{-}bpy)Ru(CO)_2Cl_2]$ has the lowest HOMO-LUMO energy difference and hence the MLCT transition at longest wavelength.[73]

Only one paper detailing the electrochemistry of a 4-nitro-substituted bpy Pt complex could be found in the literature. McInnes and co-workers noted that the complex $[Pt(4,4'\text{-}(NO_2)_2\text{-}bpy)Cl_2]$ undergoes four consecutive one electron reductions with a very small potential separation of 180 mV between E_1 and E_2.[74] Both the mono and di-reduced complexes can be electrogenerated, giving epr active solutions. Thus $[Pt(4,4'\text{-}(NO_2)_2\text{-}bpy)Cl_2]$ has a nearly degenerate pair of predominantly ligand based π^* orbitals.

It is the ligands 4,4'-$(NO_2)_2$-bpy and 4-NO_2-bpy and their corresponding complexes with Pt(II) and Pd(II) that will be discussed in this chapter. With the exception of the Pt(II) and Pd(II) complexes of 4,4'-$(NO_2)_2$-bpy, the results of the electrochemistry and spectroelectrochemistry indicate that the redox orbital is localised on the NO_2-py moiety of the bpy ligand. In the case of $[M(4,4'\text{-}(NO_2)_2\text{-}bpy)Cl_2]$, M = Pt(II) or Pd(II), the results of the electrochemistry and the spectroelectrochemistry indicate

that the LUMO-LUMO-1 energy gap is smaller than the spin pairing energy and the redox orbitals (LUMO and LUMO-1) are delocalised over the whole ligand. This is further confirmed by comparison with the electrochemical and epr results obtained for the study of 4-NO_2-py and [Pt(4-NO_2-py)$_2$$Cl_2$]. The redox chemistry of [Pt(4,4'-(NO_2)$_2$-bpy)Cl_2] is reinvestigated.

4.2 Results and Discussion

4.2.1 The Ligands: 4,4'-$(NO_2)_2$-bpy, 4-NO_2-bpy and 4-NO_2-py

4.2.1.1 Redox Chemistry of the Ligands

Cyclic voltammetric studies of 4-NO_2-bpy and 4-NO_2-py at 293 K in 0.1 M $TBABF_4$/DMF solution reveals similar electrochemical behaviour in each case. For 4-NO_2-bpy a fully reversible one electron reduction at –0.72 V (0.098) is observed, along with a second, poorly defined, quasi-reversible reduction at –1.63 V (0.210), see Figure 4.2. Cyclic voltammetry of 4-NO_2-py reveals a fully reversible one electron reduction at –0.74 V (0.110) and a second irreversible reduction at –1.92 V, see Figure 4.3. The first reduction of both ligands is electrochemically reversible, as indicated by the linear response to a plot of i_p *vs* $\nu^{1/2}$. The very similar half wave potentials of 4-NO_2-py and 4-NO_2-bpy suggest that the redox orbital is located on the 4-NO_2-py part of the ligand and that the py substituent at the 2 position on the 4-NO_2-bpy is slightly electron withdrawing compared to H.

The redox chemistry of 4,4'-$(NO_2)_2$-bpy is more complex. Cyclic voltammetric studies on 4,4'-$(NO_2)_2$-bpy in 0.1 M $TBABF_4$/DMF at 293 K show that the ligand undergoes two reversible one electron reductions at –0.64 V (0.081) and –0.79 V (0.085), see Figure 4.4, and a third poorly defined irreversible process at –1.87 V. This is in good agreement with previous electrochemical studies on the ligand.[25] The two reversible reductions are electrochemically reversible as indicated by their linear i_p *vs* $\nu^{1/2}$ response. The small separation potential between E_1 and E_2 of 150 mV is inconsistent with the spin pairing energy of the two reduction electrons in the same π^* orbital.

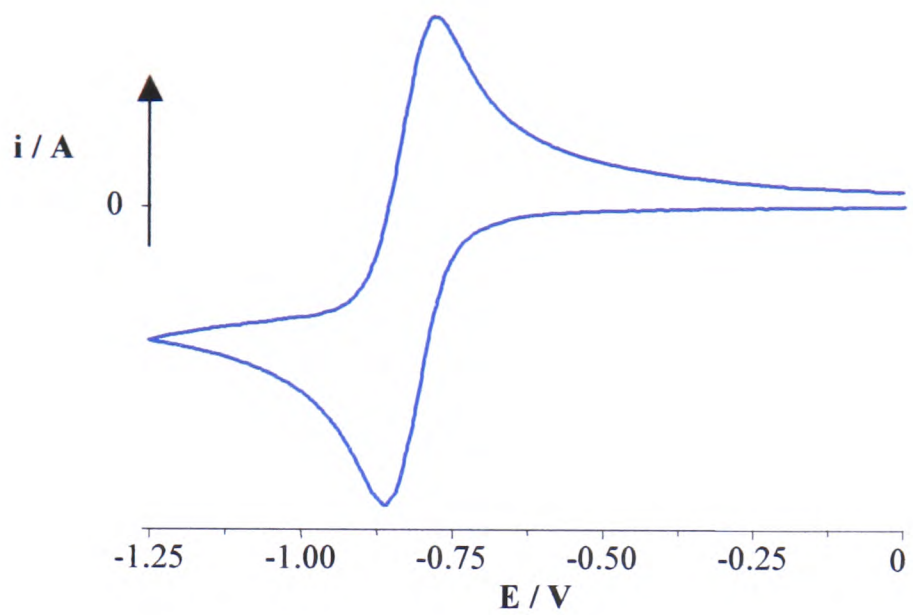

Figure 4. 2 Cyclic voltammogram of 4-NO_2-bpy in 0.1 M $TBABF_4$/DMF at 298 K, scan rate 0.1 V/s.

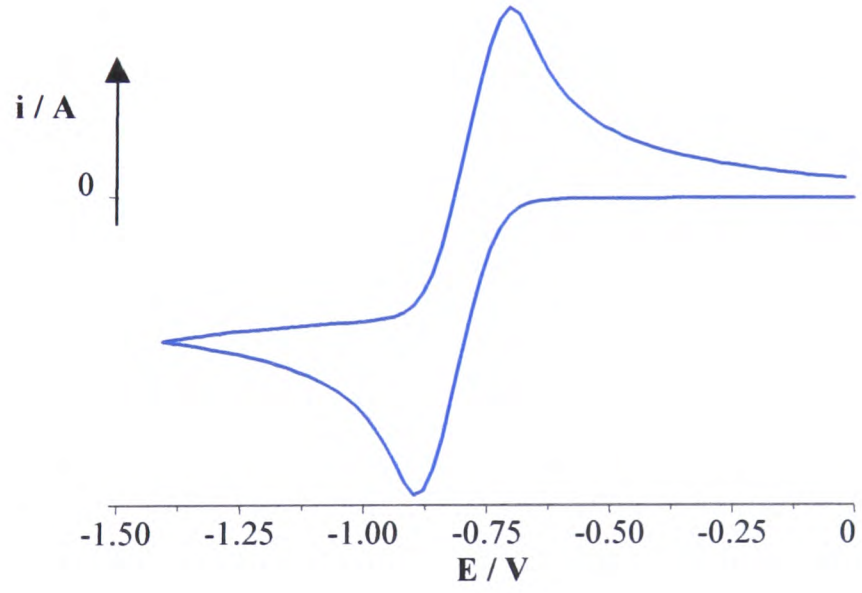

Figure 4. 3 Cyclic voltammogram of 4-NO_2-py in 0.1 M $TBABF_4$/DMF at 298 K, scan rate 0.1 V/s.

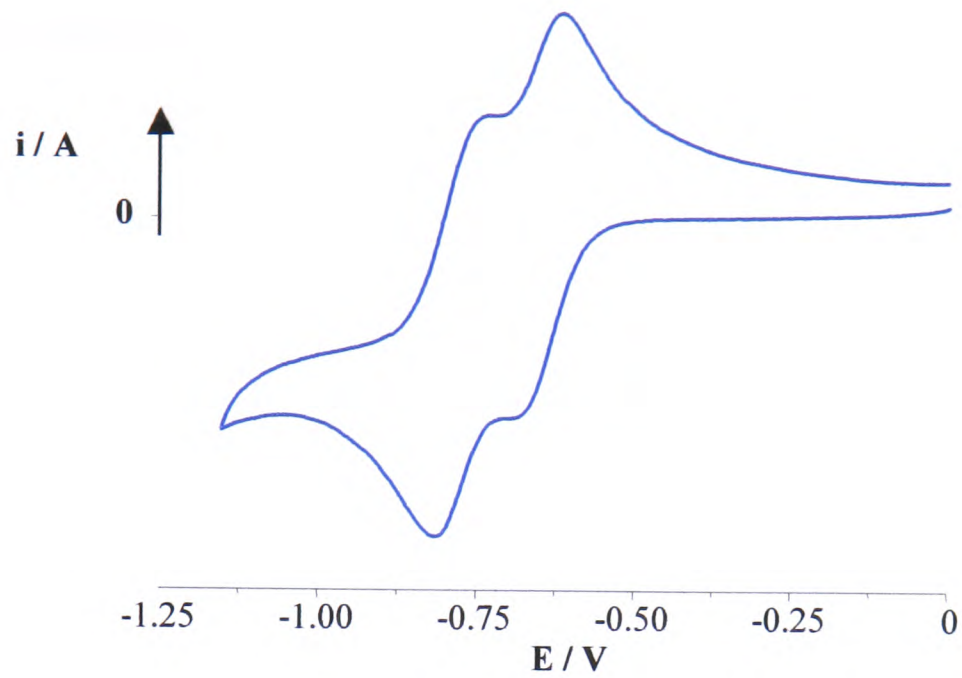

Figure 4. 4 Cyclic voltammogram of 4,4'-$(NO_2)_2$-bpy in 0.1 M $TBABF_4$/DMF at 298 K, scan rate 0.1 V/s.

Table 4. 1 Redox potentials of 4-NO_2-py, 4-NO_2-bpy and 4,4'-$(NO_2)_2$-bpy in 0.1 M $TBABF_4$/DMF at 298 K.

Ligand	E_1 / V	E_2 / V	E_3 / V
4-NO_2-py	-0.74 (0.110)	-1.92[a]	-
4-NO_2-bpy	-0.72 (0.098)	-1.63 (0.210)	-
4,4'-$(NO_2)_2$-bpy	-0.64 (0.130)	-0.79 (0.130)	-1.87[a]

The values in parentheses are $E_{pa} - E_{pc}$. (a) no anodic peak was observed, cathodic peak quoted.

4.2.1.2 UV/vis/nir Spectroelectrochemistry

The UV/vis/nir spectra of 4,4'-$(NO_2)_2$-bpy and 4-NO_2-py are similar, see Figures 4.7, 4.5 and Table 4.2. A high energy band is observed at 35,100 cm^{-1} (ε = 6,600 M^{-1} cm^{-1}) and 32,100 cm^{-1} (ε = 7,100 M^{-1} cm^{-1}) for 4-NO_2-py and 4,4'-$(NO_2)_2$-bpy respectively. In both cases this band was assigned as a $\pi \rightarrow \pi^*$ transition of the ligand. More specifically they can be assigned to a $\pi \rightarrow \pi^*$ transition located on the 4-NO_2-py part of the ligand. The UV/vis spectrum of 4-NO_2-bpy is slightly different, having two peaks at 35,700 cm^{-1} (ε = 11,100 M^{-1} cm^{-1}) and 31,600 cm^{-1} (ε = 3,500 M^{-1} cm^{-1}). Again these peaks were assigned as being $\pi \rightarrow \pi^*$ transitions. In the 4-NO_2-bpy there are two ring systems, arising from the 4-NO_2-py and py moieties. Both will exhibit $\pi \rightarrow \pi^*$ transitions almost independent of each other since in solution it is envisaged that the two rings will be oriented at 90° to each other. The $\pi \rightarrow \pi^*$ transition of py occurs at 40,000 cm^{-1}.[75] Hence the 35,700 cm^{-1} band is assigned to a $\pi \rightarrow \pi^*$ transition on py and the 31,600 cm^{-1} band to a $\pi \rightarrow \pi^*$ transition on 4-NO_2-py.

Upon reduction of 4-NO_2-py to its mono-reduced species, two new peaks grow in at 31,500 cm^{-1} (ε = 6,600 M^{-1} cm^{-1}) and 21,800 cm^{-1} (ε = 2,400 M^{-1} cm^{-1}). These bands were assigned as intraligand transitions involving the partially filled lower energy π^* orbital of 4-NO_2-py^{1-}, see Figure 4.5.

The UV/vis/nir spectrum of 4-NO_2-bpy^{1-} shows similarities to the spectrum of 4-NO_2-py^{1-}. On reduction of 4-NO_2-bpy to 4-NO_2-bpy^{1-} intense bands at 35,000 cm^{-1} (ε = 17,200 M^{-1} cm^{-1}), with a broad shoulder at lower energy, see Table 4.2 and 20,600 cm^{-1} (ε = 4,800 M^{-1} cm^{-1}) grow in. A broad band in the nir region at 13-18 kcm^{-1} (ε = 900 M^{-1} cm^{-1}) is also observed. The *in situ* spectra obtained for the 4,4'-$(NO_2)_2$-$bpy^{0/2-}$ conversion is very similar to that obtained for 4-NO_2-bpy^{1-}, see Figures 4.6 and 4.7. Again an intense, high energy band, this time at 32,400 cm^{-1} (ε = 15,800 M^{-1} cm^{-1}) grows in along with a peak at 20,700 cm^{-1} (ε = 8,000 M^{-1} cm^{-1})

and a broad band at 13-18 kcm^{-1} (ε = 1,600 M^{-1} cm^{-1}). During the reduction of 4,4'-$(NO_2)_2$-bpy the spectrum simply grew in as shown in Figure 4.7 with no obvious differences in band envelopes during the two electron reduction. Thus the spectrum of [4,4'-$(NO_2)_2$-bpy]$^{1-}$ must be very similar to that of [4,4'-$(NO_2)_2$-bpy]$^{2-}$.

As previously discussed in Section 3.2.1.2 the absorption spectrum of bpy^{1-} has three sets of absorption bands that are diagnostic for the presence of co-ordinated bpy^{1-}; i) an ir band at *ca.* 10 kcm^{-1} comprising of three peaks or shoulders, ii) a doublet visible band at *ca.* 20 kcm^{-1} and iii) an intense near UV band at *ca.* 25 kcm^{-1}.[29] The spectra of nitro substituted bpys shows none of the bands characteristic of bpy^{1-} and therefore it can be argued that the reduction electron enters a molecular orbital with substantial amounts of NO_2 character. This is due to the strong electron withdrawing character of the NO_2 substituent.

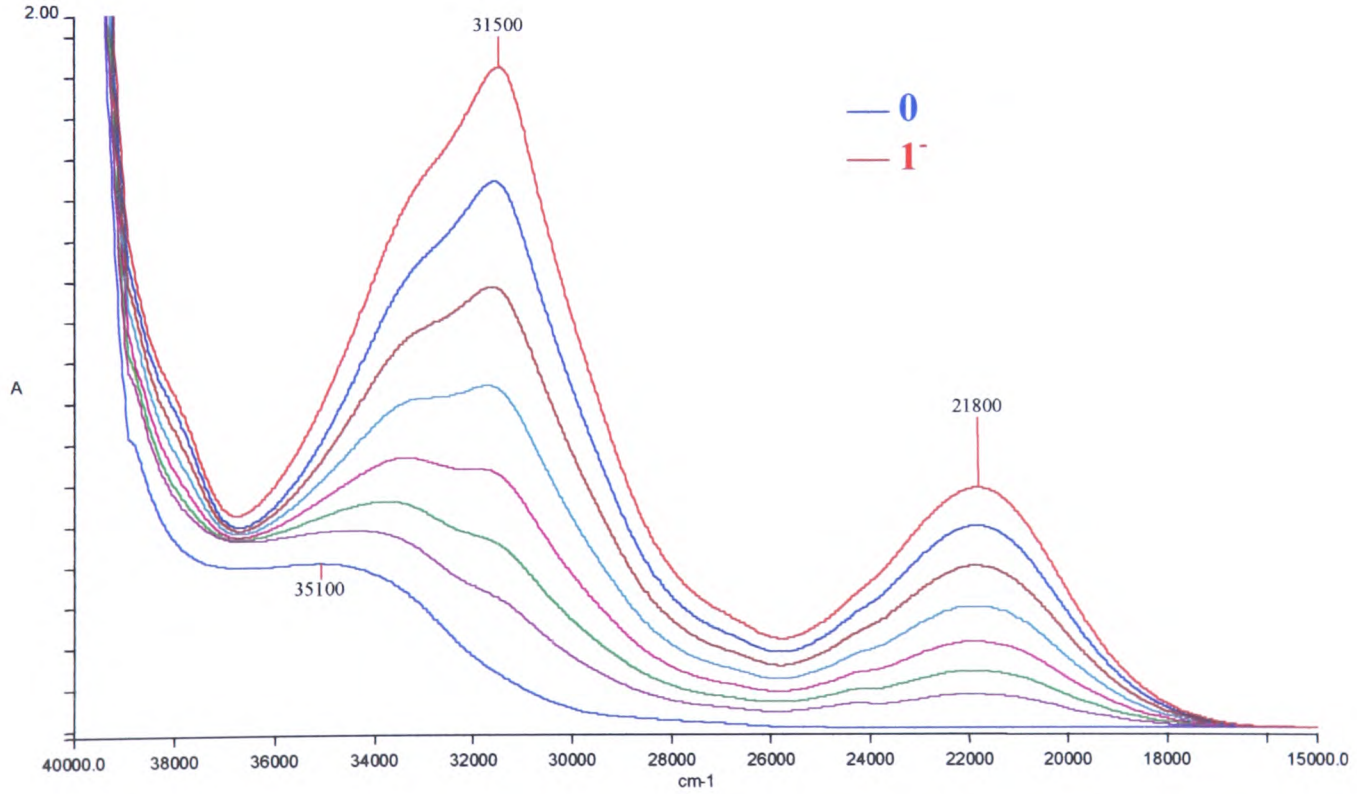

Figure 4. 5 UV/vis of 4-NO_2-$py^{0/1-}$ at 233 K in 0.1 M $TBABF_4$/DMF, E_{gen} = -1.3 V.

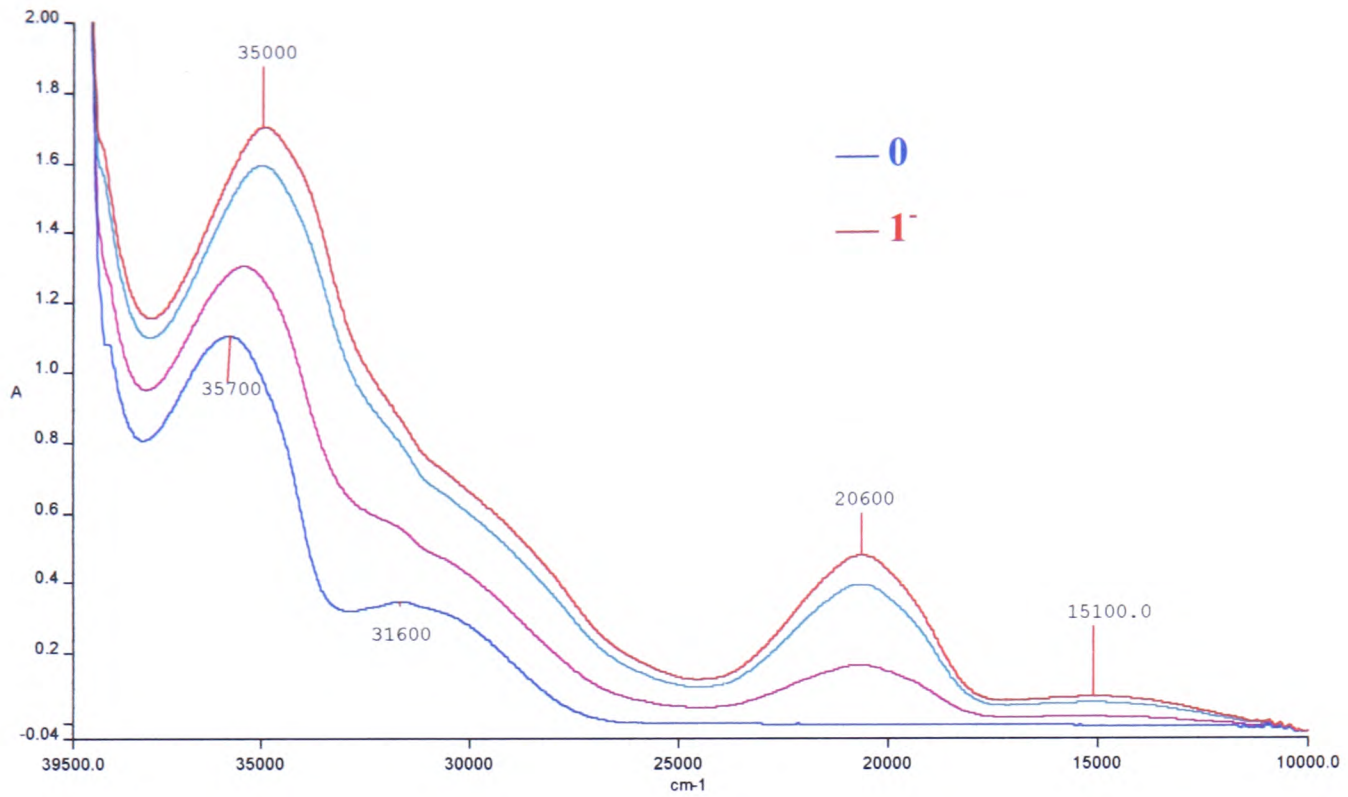

Figure 4. 6 UV/vis of 4-NO_2-bpy$^{0/1-}$ at 233 K in 0.1 M $TBABF_4$/DMF, E_{gen} = -1.3 V.

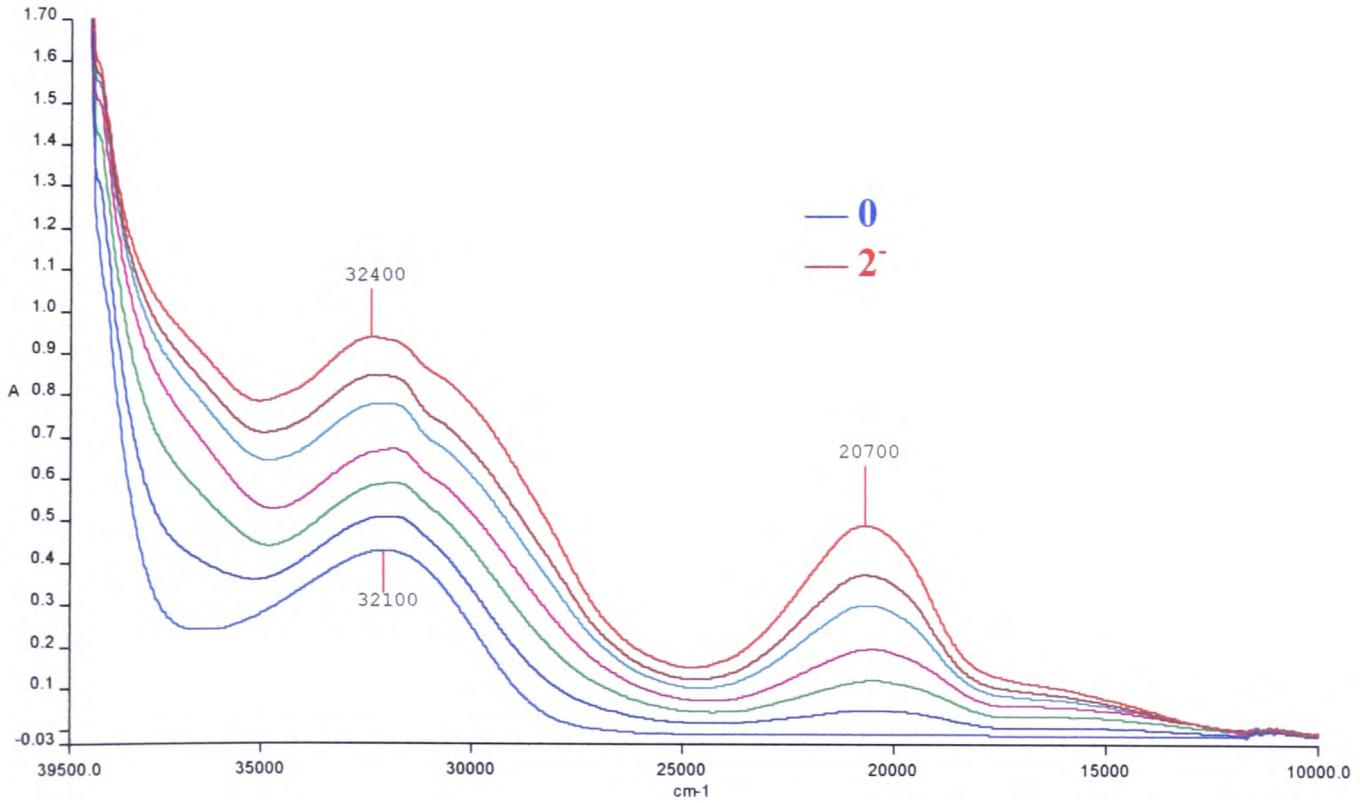

Figure 4. 7 UV/vis of 4,4'-$(NO_2)_2$-bpy)$Cl_2^{0/2-}$ at 233 K in 0.1 M $TBABF_4$/DMF, E_{gen} = -1.2 V.

In their study on the electronic absorption spectra of $bpy^{0/1-/2-}$, König and Kremer assigned the spectrum of bpy^{2-} as consisting of two bands, one at *ca.* 16.4 kcm^{-1} and a second very intense band at *ca.* 26.8 kcm^{-1}.[29] The spectrum of 4,4'-$(NO_2)_2$-bpy^{2-} does not resemble this spectrum. Given the small potential separation of 150 mV between E_1 and E_2 of 4,4'-$(NO_2)_2$-bpy, see Section 4.2.1.1 and the striking similarity between the spectra of 4-NO_2-bpy^{1-} and 4,4'-$(NO_2)_2$-bpy^{2-}, see Figures 4.6 and 4.7, it would appear that the second reduction electron of 4,4'-$(NO_2)_2$-bpy^{2-} enters an empty orbital close in energy to the LUMO which also has strong 4-NO_2-py character, *ie.* the first reduction electron enters the LUMO and this electron is localised on the 4-NO_2-py part of the ligand. The second reduction electron then enters the LUMO-1, (which is close in energy to the LUMO) and it too is confined to a 4-NO_2-py moiety rather than being delocalised over the whole ligand. Mono and di-reduced [Pt(4,4'-$(NO_2)_2$-bpy)Cl_2] both give epr active solutions. McInnes *et al.* attributed this as being due to the LUMO-LUMO-1 energy gap being less than the spin pairing energy for the two reduction electrons and that the complex must possess an almost degenerate pair of low lying empty orbitals.[74] 4,4'-$(NO_2)_2$-bpy^{2-} is also epr active, see Section 4.2.1.3.

On comparing the three spectra of 4-NO_2-py^{1-}, 4-NO_2-bpy^{1-} and 4,4'-$(NO_2)_2$-bpy^{2-} a trend is visible. All three spectra show an intense, high energy band in the range 31.5-35 kcm^{-1} and a second band at 20.6-21.8 kcm^{-1}. For the spectrum of 4-NO_2-py^{1-} the reduction electron can only be localised on the 4-NO_2-py. The similarity between the three spectra provides further weight to the assignment of the spectra of 4-NO_2-bpy^{1-} and 4,4'-$(NO_2)_2$-bpy^{2-} as being due to the transitions between π-symmetry orbitals based on the 4-NO_2-py moiety with little delocalisation of the reduction electron over the extended ring system. In solution the planes of the two 4-NO_2-py rings of 4,4'-$(NO_2)_2$-bpy may be orthogonal to one another and hence the unpaired electrons may well be isolated on the individual ring systems rather than delocalised over the whole ligand.

On converting 4-NO_2-bpy^{1-} to 4-NO_2-bpy^{2-} the peak at 35,000 cm^{-1} remains very much unchanged, although it shifts slightly to 34,800 cm^{-1} (ε = 17,300 M^{-1} cm^{-1}), see

Figure 4.8. The broad shoulder at 28.9-32 kcm^{-1} collapses to reveal a peak at 30,500 cm^{-1} (ε = 6,100 M^{-1} cm^{-1}). The band at 20.6 kcm^{-1} also collapses. As for 4,4'-$(NO_2)_2$-bpy^{2-} this spectrum bears little resemblance to that of bpy^{2-}, see above. Isosbestic points are visible at 23.6 kcm^{-1} and 29.2 kcm^{-1} indicating clean conversion between the reduced species. However, it must be noted that this second reduction is irreversible as there is no change in the spectrum on switching the generation potential back to 0 V.

The *in situ* spectra showing the conversion of 4,4'-$(NO_2)_2$-bpy^{2-} to 4,4'-$(NO_2)_2$-bpy^{3-} the peak at 32,400 cm^{-1} is shifted to lower energy at 29,900 cm^{-1} (ε = 15,800 M^{-1} cm^{-1}) and the band at 20,700 cm^{-1} collapses to be replaced by a broad band at 20-25 kcm^{-1} (ε = 2,900 M^{-1} cm^{-1}), see Figure 4.9. This spectrum bears no resemblance to the spectra characteristic of bpy^{1-} or bpy^{2-} and the band at 20,700 cm^{-1}, which is characteristic of the reduction electron being localised on the 4-NO_2-py part of the ligand collapses. The isosbestic points at 23,800 cm^{-1}, 31,200 cm^{-1} and 35,700 cm^{-1} indicate the clean conversion of 4,4'-$(NO_2)_2$-bpy^{2-} to 4,4'-$(NO_2)_2$-bpy^{3-}.

The reductions 4-NO_2-$py^{0/1-}$, 4-NO_2-$bpy^{0/1-}$ and 4,4'-$(NO_2)_2$-$bpy^{0/2-}$ are all fully reversible because on resetting the generation potential back to 0 V the original spectra are regenerated. However, by the same method, the third reduction of 4,4'-$(NO_2)_2$-bpy is irreversible, as is the second reduction of 4-NO_2-bpy.

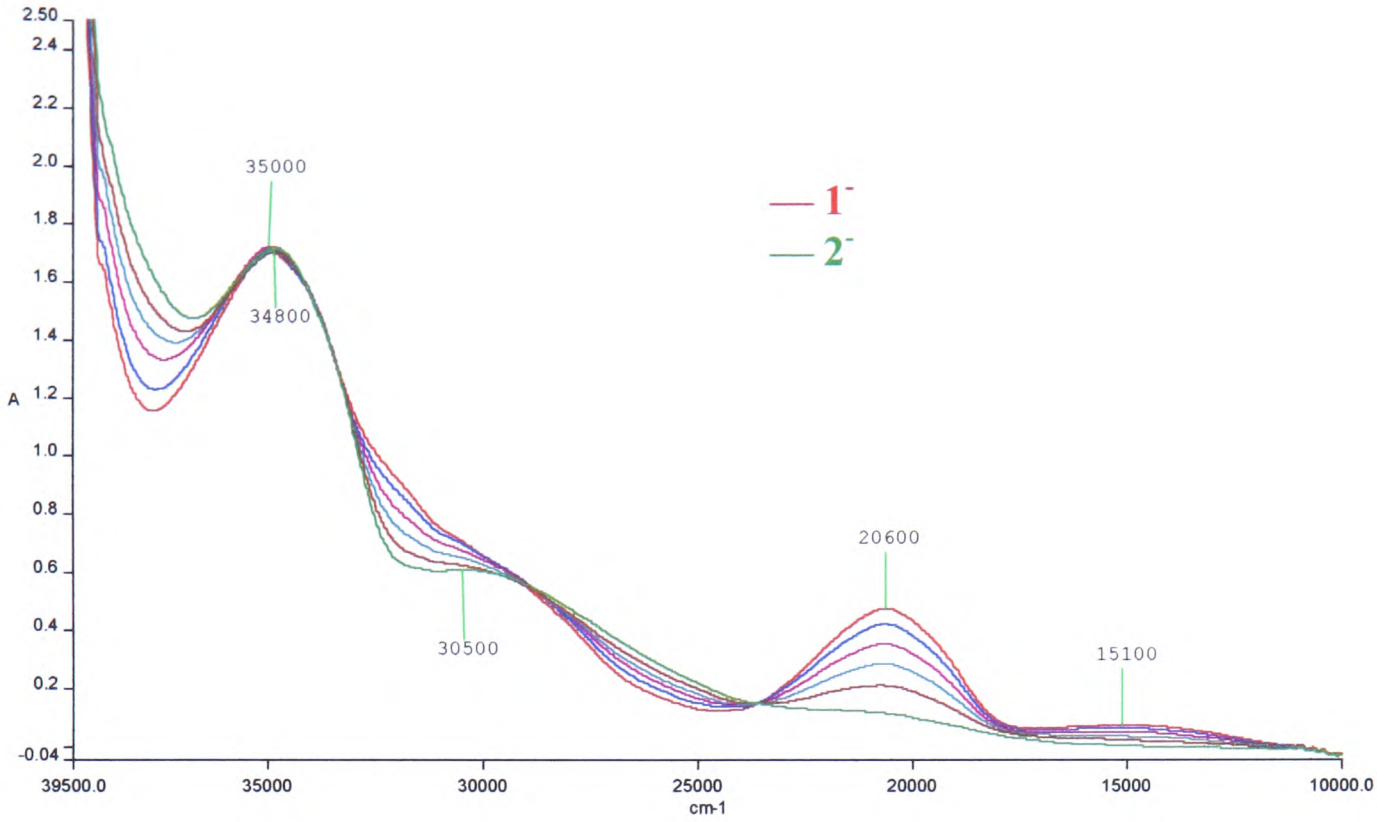

Figure 4. 8 UV/vis spectra of 4-NO_2-$bpy^{1-/2-}$ at 233 K in 0.1 M TBABF4/DMF, E_{gen} = -2.0V.

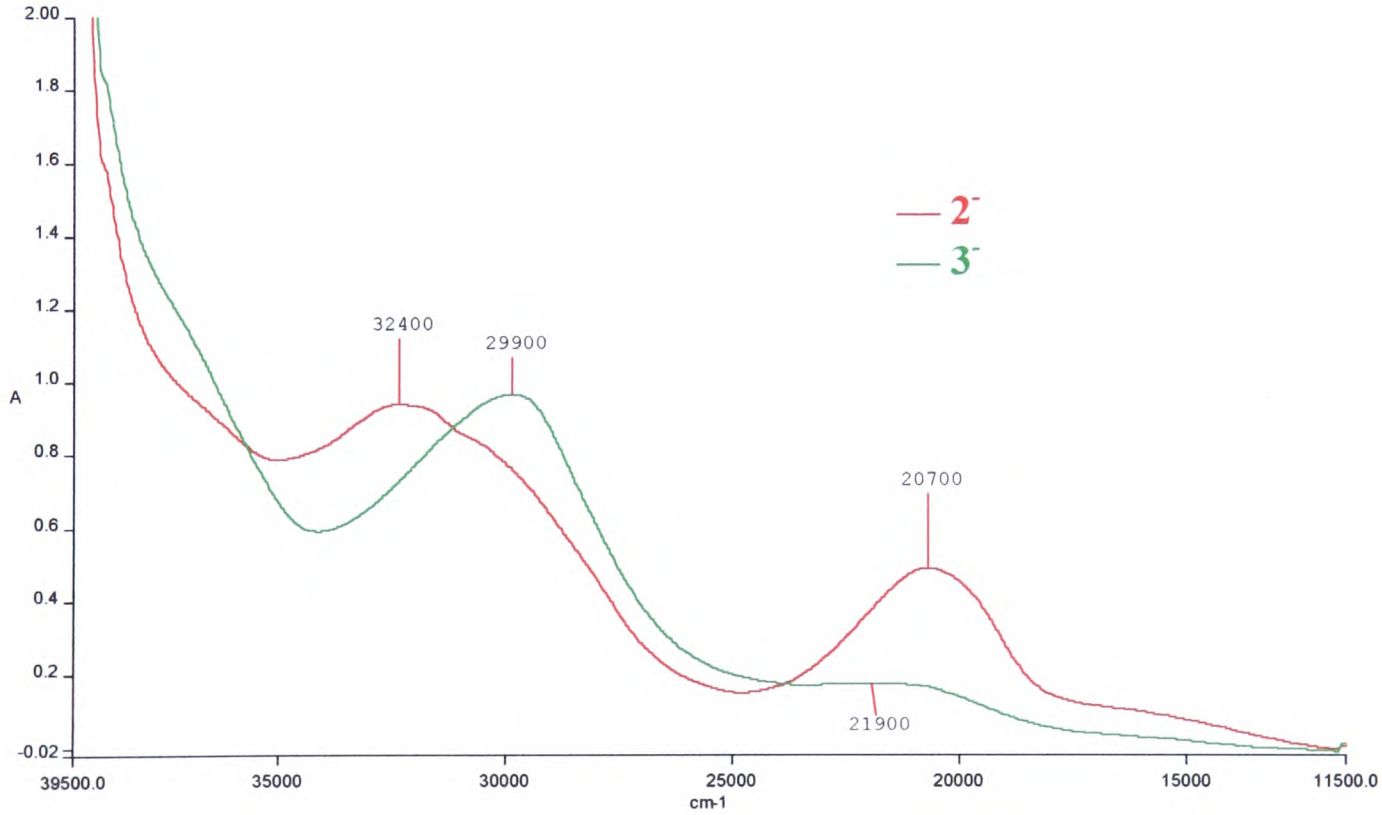

Figure 4. 9 UV/vis spectra of 4,4'-$(NO_2)_2$-$bpy^{2-/3-}$ at 233 K in 0.1 M $TBABF_4$/DMF, E_{gen} = -2.2 V.

Table 4. 2 Peak positions and molar extinction coefficients, ε, for 4-NO_2-$py^{0/1-}$, 4-NO_2-$bpy^{0/1-/2-}$ and 4,4'-$(NO_2)_2$-$bpy^{0/2-/3-}$ in 0.1 M $TBABF_4$/DMF at 233 K.

Oxidation state	4-NO_2-py	4-NO_2-bpy	4,4'-$(NO_2)_2$-bpy
	Peak position / cm^{-1} (ε / M^{-1} cm^{-1})	Peak position / cm^{-1} (ε / M^{-1} cm^{-1})	Peak position / cm^{-1} (ε / M^{-1} cm^{-1})
0	35,100 (1,700)	35,700 (11,100) 31,600 (3,500)	32,100 (7,100)
1^-	sh 33,000 (5,500) 31,500 (6,600) 21,800 (2,400)	35,000 (17,200) sh 32,000 (9,400) 28,900 (5,500) 20,600 (4,800) 13-18 (900)	-
2^-	-	34,800 (17,300), 30,500(6,100), 20-24 (1300)	32,400 (15,400) 20,700 (8,000)
3^-	-	-	29,900 (15,800) 20-25 (2,900)

4.2.1.3 Epr Spectroelectrochemistry

In situ electrochemical reduction of 4-NO_2-py in 0.3 M $TBABF_4$/DCM at 233 K yields the epr active mono-reduced species, the basic structure of which has 11 lines, see Figure 4.11. The mono-reduced solution is orange in colour. Using CaChe software, performing a PM3 calculation with a PM3 wavefunction, molecular orbital calculations indicated that the LUMO was delocalised over the whole 4-NO_2-py ligand. The four carbon nuclei contribute to the LUMO as two inequivalent pairs. The ring nitrogen also contributes to the LUMO, see Figure 4.10.

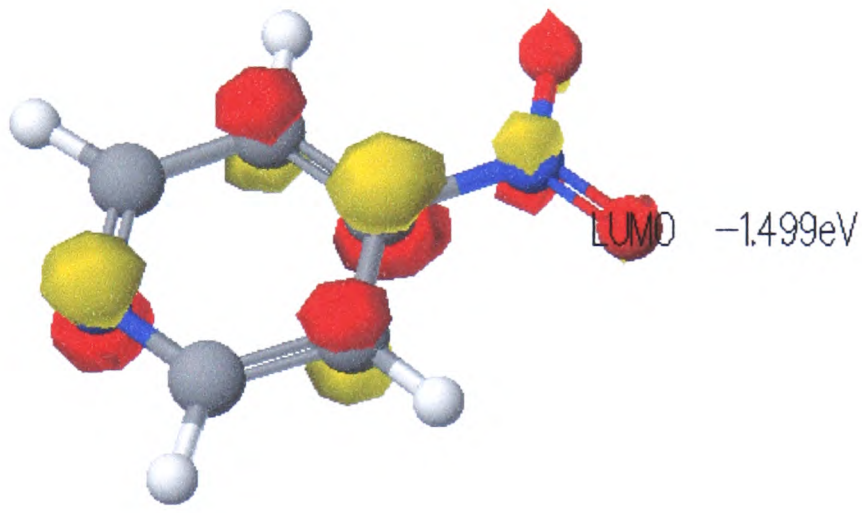

Figure 4. 10 LUMO of 4-NO_2-py using Molecular Orbital calculations, PM3 calculations with a PM3 Wavefunction.

The experimental epr spectrum of 4-NO_2-py^{1-} can be simulated with coupling to two ^{14}N nuclei (8.43 G and 2.43 G) and to two pairs of ^{1}H nuclei (3.04 G and 0.45 G), see Figure 4.11. From the results of the CaChe calculations it was not possible to assign the ^{14}N couplings to either the nitro group nitrogen or py ring nitrogen. However, the CaChe calculations did allow the assignment of the ^{1}H couplings. The ^{1}H pair with the largest coupling was assigned as the meta hydrogens on the py ring. The hydrogen pair with the smaller coupling was attributed to the hydrogens in the ortho positions of the py ring as shown in Figure 4.10.

Using the McConnell Equation, see Equation 3.1, the relationship between the spin density ρ, obtained from the CaChe calculations and the A^H, the hyperfine splitting obtained from the simulation, can be tested. If the McConnell equation holds, Q should lie between 20 and 30 G.

$$Q = 0.45 / 0.0366 \qquad Q = 3.04 / 0.1678$$
$$= 12.30 \text{ G} \qquad = 18.12 \text{ G}$$

Both calculated values of Q are lower than predicted. However, this discrepancy can be explained as the McConnell equation applies to aromatic systems such as benzene. 4-NO_2-py differs from benzene as the ring heteroatom and the NO_2 substituent effect the π system. Despite this, the calculated Q values are the correct order of magnitude and the qualitative description of the LUMO obtained from the CaChe calculations is compatible with the simulation.

When generated *in situ* at 273 K in 0.1 M $TBABF_4$/DMF, 4-NO_2-bpy^{1-} is also epr active. Figure 4.12 shows the spectrum obtained at 313 K, with a modulation amplitude of 4 G. As for 4-NO_2-py^{1-} an 11 line spectrum was visible. The best simulation was achieved by assuming the reduction electron was localised on the 4-NO_2-py part of the ligand, as indicated by CaChe calculations carried out on the ligand. The simulation was best achieved using coupling to two ^{14}N nuclei (8.25 G and 2.44 G) and a pair of ^1H nuclei (2.98 G). On decreasing the modulation to 0.4 G a more resolved spectrum was observed, see Figure 4.13. This spectrum was simulated making only small changes to the values used in the less resolved spectrum, but with coupling to an extra ^1H nucleus. This spectrum was simulated with coupling to two ^{14}N nuclei (8.20 G and 2.55 G), a pair of ^1H nuclei (2.96 G) and a lone ^1H nucleus (0.4 G). The similar coupling constant values of the unpaired electron to the ligand nuclei for 4-NO_2-py^{1-} and 4-NO_2-bpy^{1-} provide strong evidence for similar assignment of the nuclei. Thus the pair of equivalent protons are assigned as the 3 and 5 position protons on either side of the nitro group and the smallest coupled proton to the 6 position on the 4-NO_2-py part of the ligand. As for 4-NO_2-py the N couplings could not be assigned to a particular nitrogen nucleus.

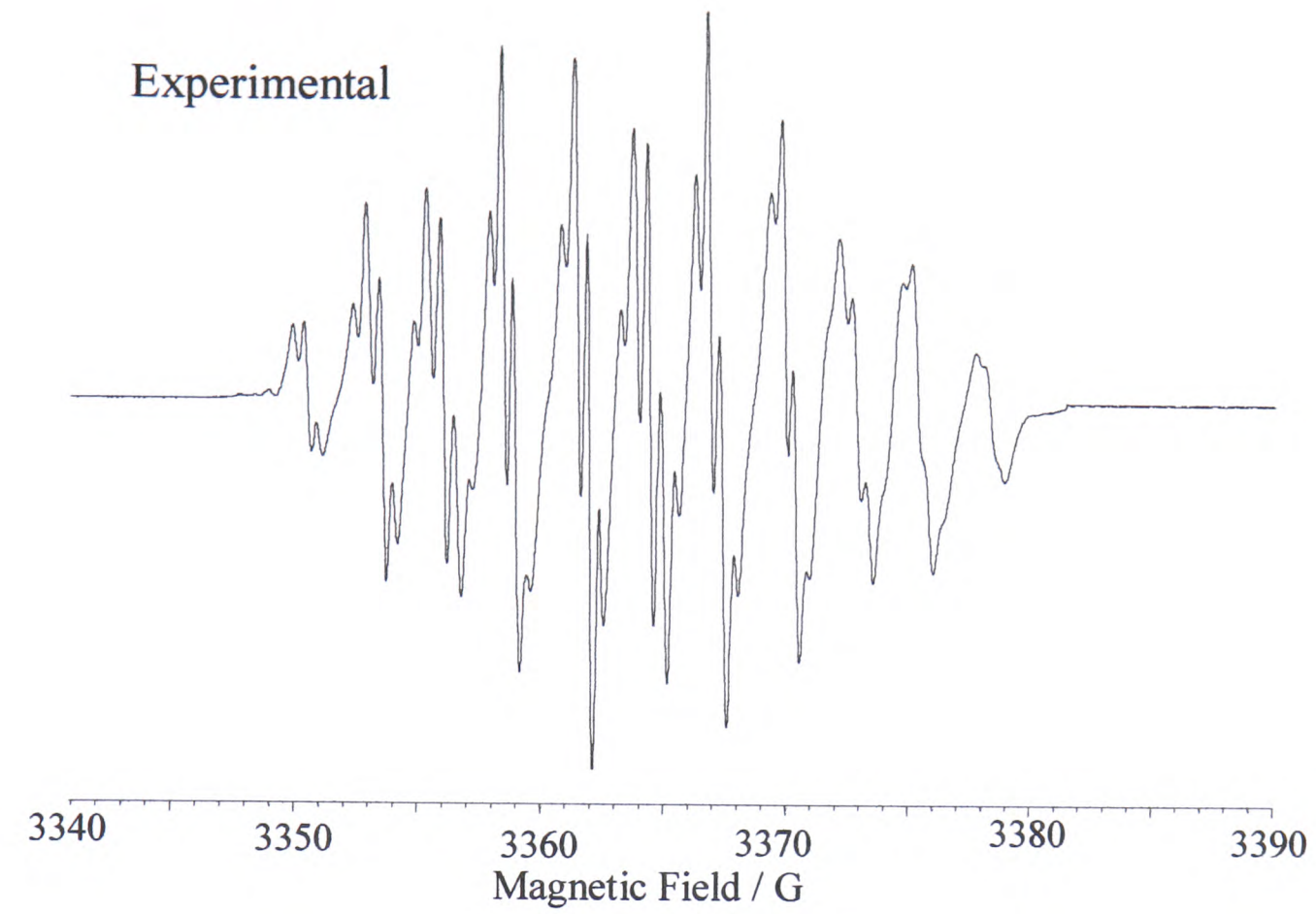

Figure 4.11 Epr of 4-NO_2-py^{1-} generated *in situ* in 0.3 M $TBABF_4$/DCM and E_{gen} = -1.15 V. The black spectrum is the signal obtained experimentally, the red spectrum is simulation.

On generating 4,4'-$(NO_2)_2$-bpy^{2-} *in situ* at 253 K in 0.3 M $TBABF_4$/DCM an 11 line spectrum similar to those observed for 4-NO_2-py^{1-} and 4-NO_2-bpy^{1-} was obtained, see Figure 4.14. However, unlike the ligands studied previously, the spectrum of 4,4'-$(NO_2)_2$-bpy^{2-} did not show any greater resolution on changing the temperature or decreasing the modulation. CaChe calculations carried out on the ligand show that the LUMO is based on one 4-NO_2-py moiety and the LUMO-1 is based on the other 4-NO_2-py moiety. The energy gap between the LUMO and LUMO-1 is very small. As for 4-NO_2-bpy^{1-}, the spectrum was simulated with the LUMO based on the 4-NO_2-py moiety, with coupling to two ^{14}N nuclei (7.95 G and 2.65 G) and to an equivalent pair of ^{1}H nuclei (2.4 G).

Table 4. 3 Values used in the epr simulations of 4-NO_2-py^{1-}, 4-NO_2-bpy^{1-} and 4,4'-$(NO_2)_2$-bpy^{2-}.

	4-NO_2-py^{1-}	4-NO_2-bpy^{1-}	4,4'-$(NO_2)_2$-bpy^{2-}
^{14}N / G	8.43	8.2	7.95
^{14}N / G	2.43	2.55	2.65
2 × ^{1}H / G	3.04	2.96	2.4
^{1}H / G	0.45 (× 2)	0.4	-
g_{iso}	2.0055	2.0056	2.0077
ΔH_{pp} / G	0.3	0.31	0.8

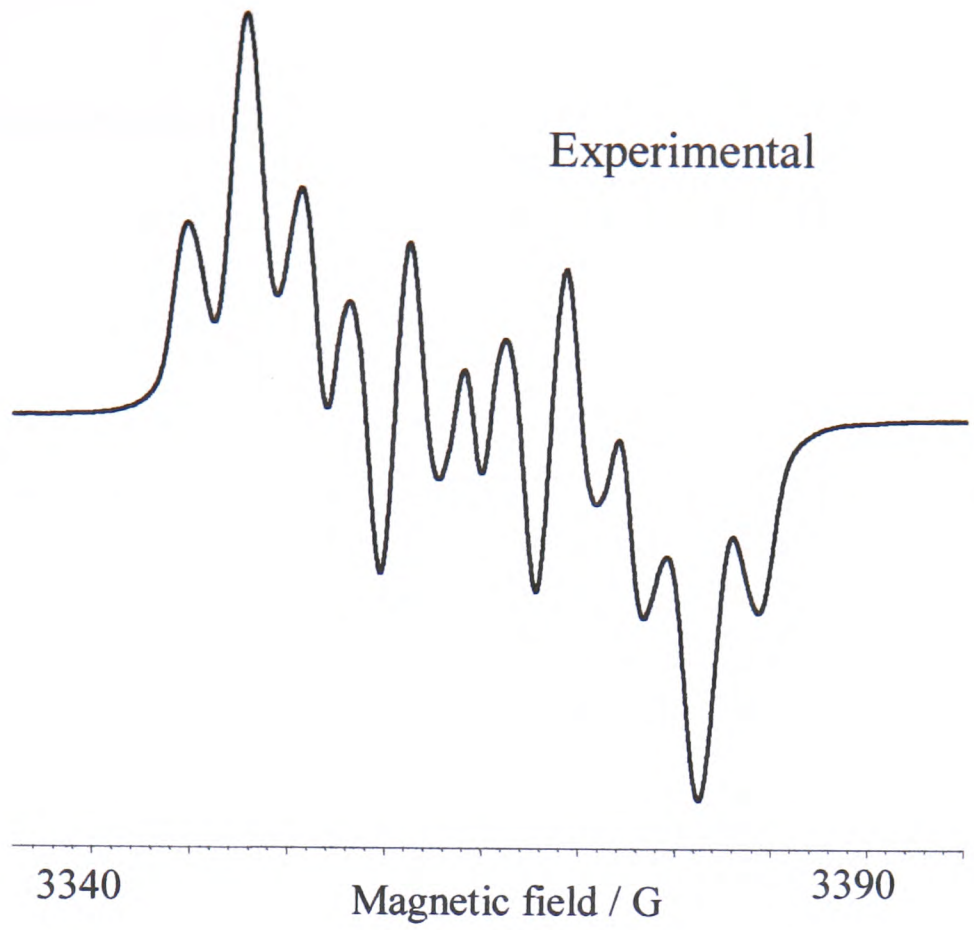

Figure 4. 12 Epr of 4-NO_2-bpy^{1-} generated *in situ* at 273 K in 0.1 M TBABF_4/DMF, spectrum taken at 313 K, E_{gen} = -1.15 V. Modulation 4 G.

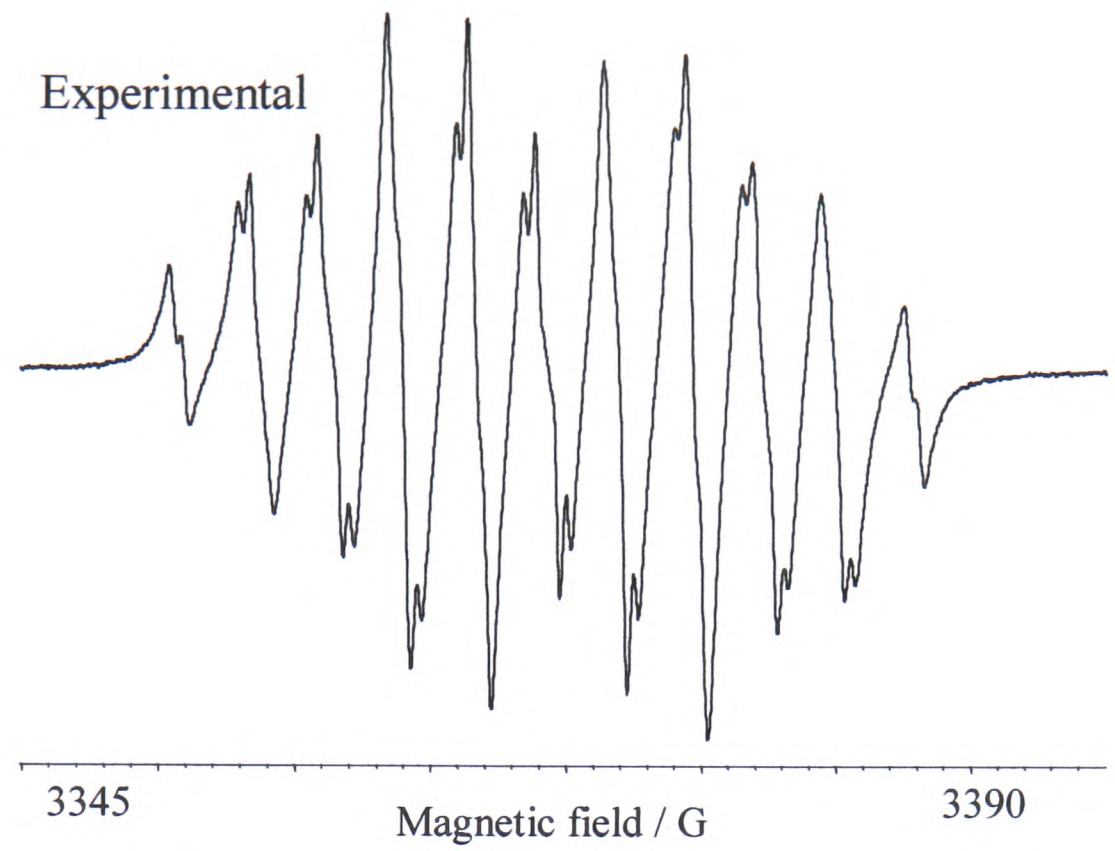

Figure 4. 13 Epr of 4-NO_2-bpy^{1-} generated *in situ* at 273 K, spectrum taken at 313 K in 0.1 M $TBABF_4$/DMF, E_{gen} = -1.15 V. Modulation amplitude 0.4 G.

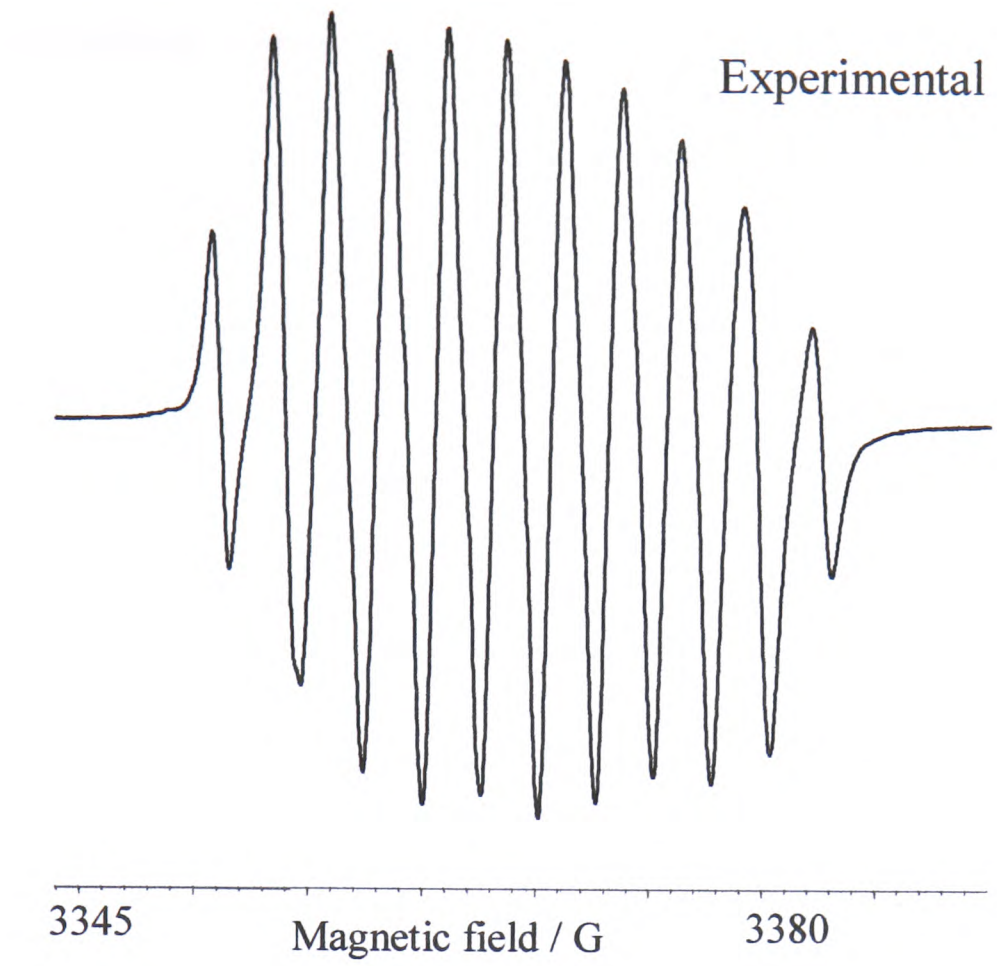

Figure 4.14 Epr of 4,4'-$(NO_2)_2$-bpy^{2-} generated *in situ* at 253 K in 0.3 M $TBABF_4$/DCM, E_{gen} = -1.1 V. The black spectrum is the experimental signal, the red spectrum is the simulation.

This puzzling lack of resolution for the spectrum of 4,4'-$(NO_2)_2$-bpy^{2-} can be explained on making a closer examination of the values used in the simulation, see Table 4.3. Firstly, 7.95 G, the value used for the largest ^{14}N coupling, is a multiple of the smaller ^{14}N coupling (2.65 G). Secondly, for 4,4'-$(NO_2)_2$-bpy^{2-} the difference between the smallest ^{14}N coupling (2.65 G) and the largest ^{1}H coupling (2.4 G) is only 0.25 G, a significantly smaller value than for the other two ligands. For the simulations of 4-NO_2-py^{1-} and 4-NO_2-bpy^{1-} this difference is greater than the line width, which is *ca.* 0.3 G in each case, so the difference between the coupling will be observed. For 4,4'-$(NO_2)_2$-bpy^{2-} the difference between the smaller N and the H pair (0.25 G) will not be observed as the line width is 0.8 G. However, on taking the line width of this simulation down to 0.4 G no more resolution is observed. Thus, there must be an additional factor causing this lack of resolution. McInnes attributed the difference in line width for [Pt(4,4'-$(NO_2)_2$-bpy)Cl_2]$^{1-}$ and [Pt(4,4'-$(NO_2)_2$-bpy)Cl_2]$^{2-}$ to an "electron hopping" mechanism on the mono-reduced complex.[25] In the mono-anion the reduction electron can be thermally excited to the low lying excited state (the LUMO-1 of the neutral molecule). This hopping causes line broadening in the observed epr signal. The lack of resolution in the spectrum for 4,4'-$(NO_2)_2$-bpy^{2-} can also be attributed to odd electron hopping because although the solution is mainly in the di-reduced form, (the di-anion does not exhibit electron hopping as both low lying MOs are occupied), the solution may not be fully reduced and will contain a some of the mono-anion. The electron hopping on this residual 4,4'-$(NO_2)_2$-bpy^{1-} will broaden the signal sufficiently to prevent greater resolution of the 4,4'-$(NO_2)_2$-bpy^{2-} spectrum.

From the epr studies of the ligands 4-NO_2-bpy and 4,4'-$(NO_2)_2$-bpy it would appear that the reduction electron enters an orbital that is based on the 4-NO_2-py moiety rather than being delocalised over the whole of the bpy ligand. The simulations compare well with that of 4-NO_2-py^{1-}. During UV/vis/nir studies on 4-NO_2-$py^{0/1-}$, 4-NO_2-$bpy^{0/1-}$ and 4,4'-$(NO_2)_2$$bpy^{0/1-/2-}$ the reduction electron was assigned as entering a MO that was not localised on the bpy part of the ligand. The fact that 4,4'-$(NO_2)_2$-bpy^{2-} is epr active means that the LUMO-LUMO-1 energy gap of

4,4'-$(NO_2)_2$-bpy is less than the spin pairing energy of the two added electrons, consistent with the small potential separation of 150 mV between E_1 and E_2.

4.2.2 Complexes with Pt(II) and Pd(II)

4.2.2.1 Redox Chemistry

Cyclic voltammetric studies of [Pt(4,4'-$(NO_2)_2$-bpy)Cl_2] in 0.1 M $TBABF_4$/DMF at 293 K revealed four consecutive one electron reductions in the range 0 to -2 V, see Figure 4.15. The first two reduction processes at –0.26 V (0.066) and –0.45 V (0.084) are fully reversible while the third reduction at –1.06 V (0.116) is quasi-reversible and the fourth at –1.73 V is irreversible. It is easier to reduce the complexed ligand than the free ligand and hence complexation must stabilise the LUMO based on the 4,4'-$(NO_2)_2$-bpy. The first two reductions are electrochemically reversible as indicated by the linear response to a plot of i_p *vs* $\nu^{1/2}$. As for the free ligand the potential separation between E_1 and E_2 of 190 mV is too small to be considered a spin pairing process *ie* the second reduction electron enters a different orbital from the first.[25] Thus the redox chemistry suggests that the spin pairing energy is greater than the LUMO – LUMO-1 gap. The $E_1 - E_3$ and $E_2 - E_4$ separations of 800 mV and 1280 mV could be consistent with spin pairing processes. The electrochemistry is in good agreement with previous studies on [Pt(4,4'-$(NO_2)_2$-bpy)Cl_2].[25]

The redox chemistry of [Pd(4,4'-$(NO_2)_2$-bpy)Cl_2] is very similar to that of the Pt analogue with cyclic voltammetry in 0.1 M $TBABF_4$/DMF at 293 K showing two reversible reductions at –0.26 V (0.068) and –0.43 V (0.091) and a third irreversible reduction at –1.08 V, see Figure 4.16, which shows only the redox response of the first two processes. The similarity of the first two reduction potentials of [Pd(4,4'-$(NO_2)_2$-bpy)Cl_2] and [Pt(4,4'-$(NO_2)_2$-bpy)Cl_2] indicates that changing the metal centre has very little effect on the electrochemistry and therefore the first two

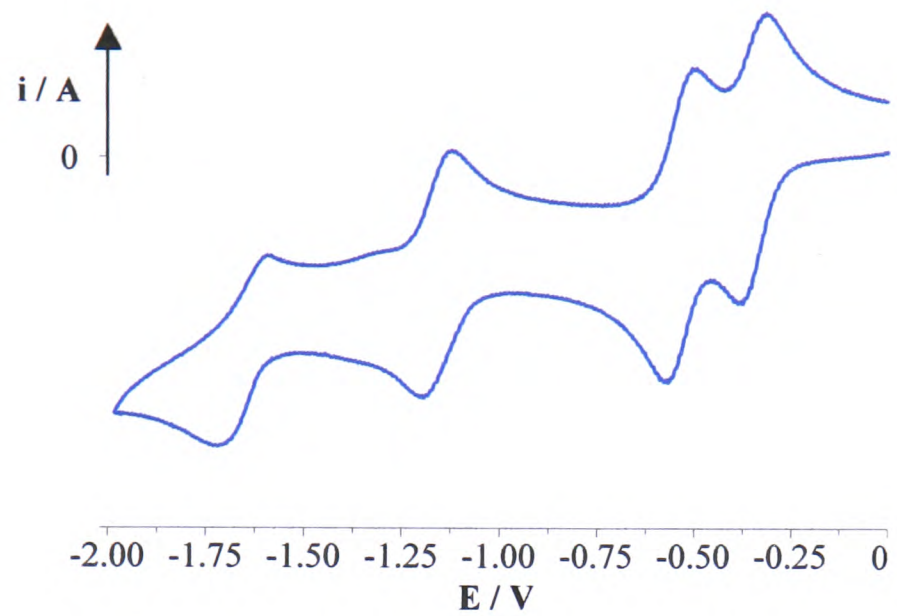

Figure 4. 15 Cyclic voltammogram of [Pt(4,4'-$(NO_2)_2$-bpy)Cl_2], scan rate 0.1 V/s, at 293 K in 0.1 M $TBABF_4$/DMF.

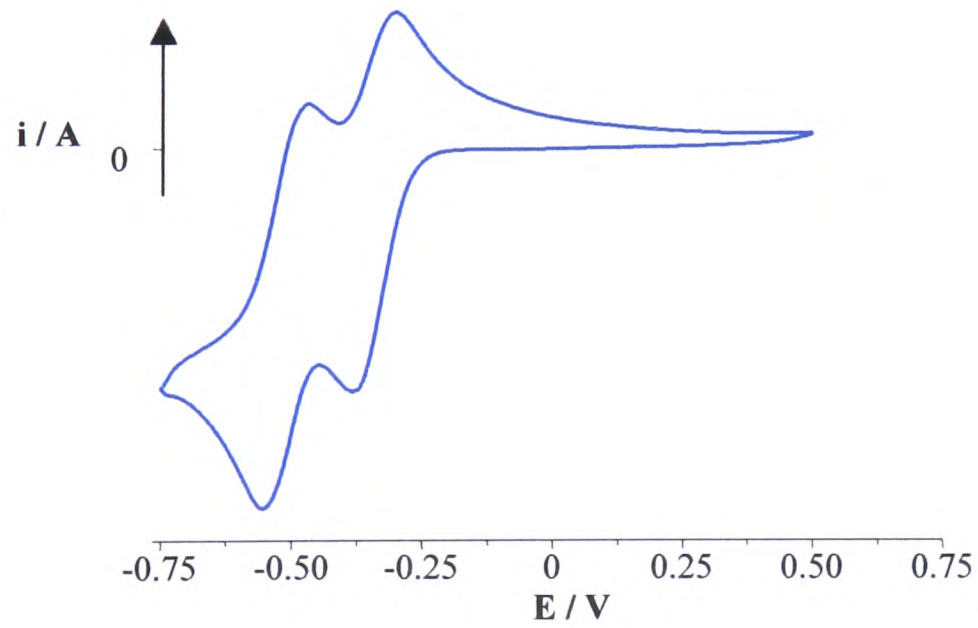

Figure 4. 16 Cyclic voltammogram of [Pd(4,4'-$(NO_2)_2$-bpy)Cl_2], scan rate 0.1 V/s, at 293 K in 0.1 M $TBABF_4$/DMF.

reductions must be ligand based. The third reduction of [Pd(4,4'-$(NO_2)_2$-bpy)Cl_2] may be based on the Pd rather than being the third ligand based reduction. The irreversibility of this process and the absence of a fourth reduction in the cyclic voltammogram supports this hypothesis.

The cyclic voltammetric study of [Pt(4-NO_2-bpy)Cl_2] in 0.1 M $TBABF_4$/DMF at 293 K is shown in Figure 4.17. Several consecutive one electron reductions are revealed in the range 0 to –2 V. Only the first two reductions at –0.34 V (0.057) and –0.93 V (0.071) are fully reversible, with the first reduction also being electrochemically reversible as indicated by a linear response to a plot of i_p *vs* $\nu^{1/2}$. As for 4,4'-$(NO_2)_2$-bpy complexation of the ligand stabilises the LUMO resulting in a shift to positive potential of 380 mV for the first reduction compared to the free ligand, see Section 4.2.1.1.

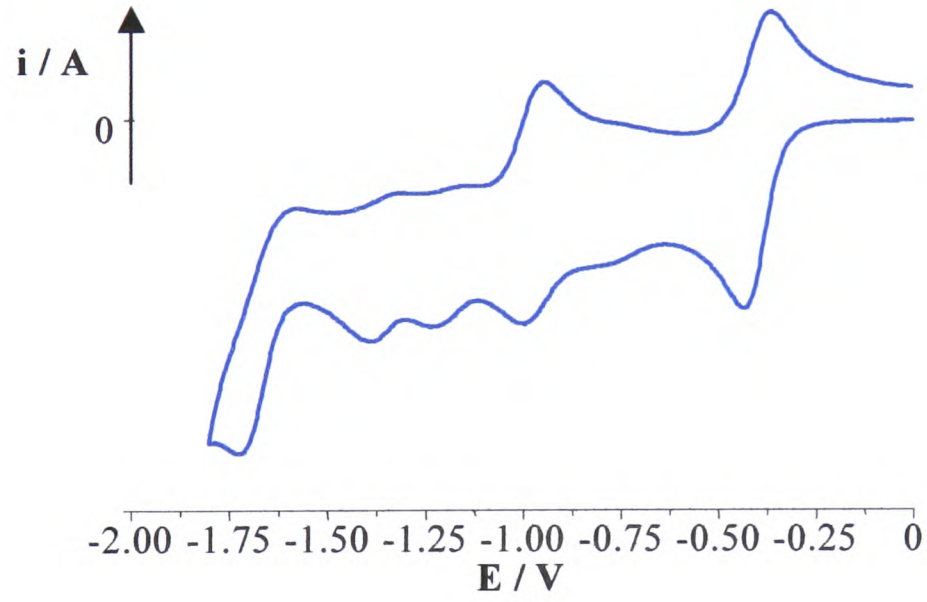

Figure 4. 17 Cyclic voltammogram of [Pt(4-NO_2-bpy)Cl_2], scan rate 0.1 V/s, at 293 K in 0.1 M $TBABF_4$/DMF.

Cyclic voltammetric studies of [Pd(4-NO_2-bpy)Cl_2] in 0.1 M $TBABF_4$/DMF at 293 K show a reversible one electron reduction at –0.34 V (0.072) and a second quasi reversible reduction at –0.82 V (0.233), see Figure 4.18. Note that if the cyclic voltammetric potential is reversed after the first reduction but before the second

reduction, then the height of the return wave is equal to the height of the forward wave. For [Pd(4-NO_2-bpy)Cl_2] and the Pt analogue the first reduction is at –0.34 V for both complexes, indicating that changing the metal centre has no effect on the first reduction potential. Hence, the first reduction on both complexes is based on the 4-NO_2-bpy ligand.

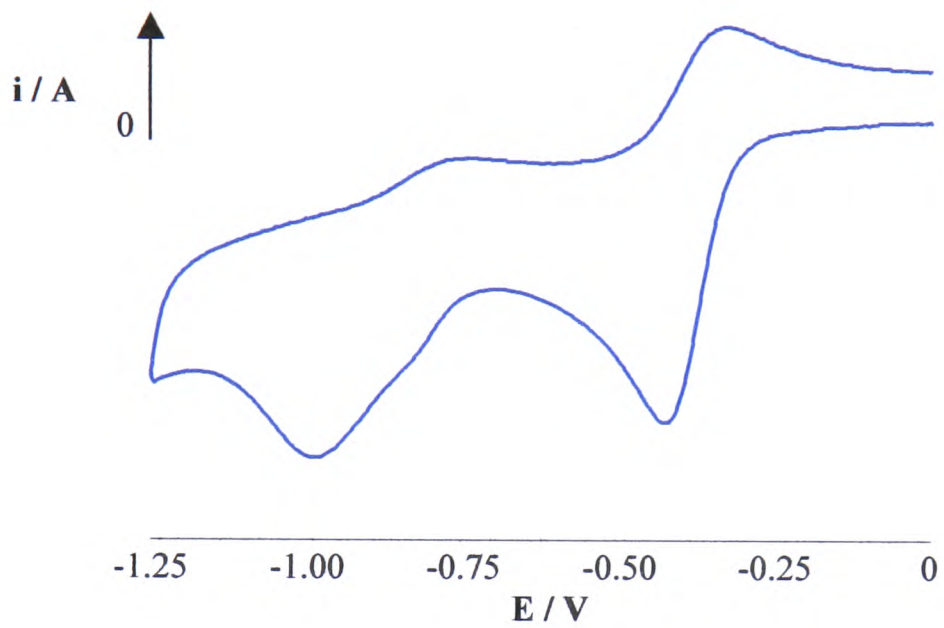

Figure 4. 18 Cyclic voltammogram of [Pd(4-NO_2-bpy)Cl_2], scan rate 0.1 V/s, at 293 K, in 0.1 M $TBABF_4$/DMF.

The redox chemistry of the Pt and Pd complexes of 4-NO_2-py differs from that of [Pt(4-NO_2-bpy)Cl_2], [Pt(4,4'-$(NO_2)_2$-bpy)Cl_2] and the Pd analogues. The cyclic voltammetric studies of [Pt(4-NO_2-py)$_2Cl_2$] in 0.1 M $TBABF_4$/DMF at 293 K reveal one fully reversible reduction at –0.47 V (0.110) followed by a quasi-reversible reduction at –1.30 V (0.197) and an irreversible reduction at –1.58 V, see Figures 4.19-20. Although the linear response to a plot of i_p *vs* $\nu^{1/2}$ indicated that the first reduction was electrochemically reversible, the value for $E_{pa} - E_{pc}$ for the reduction, at 0.110 V, was larger than the 59 mV expected for a fully reversible electron transfer reaction. In addition, differential pulse studies of the reduction showed possible splitting of the differential pulse peak, indicating that more than one electron was involved in the process.

These anomalous results were attributed to the two 4-NO_2-py ligands on $[Pt(4\text{-}NO_2\text{-}py)_2Cl_2]$ behaving independently of one another and undergoing reduction at very similar potentials. Coulometric studies at 293 K in 0.1 M $TBABF_4$/DMF confirmed that the first reduction at –0.47 V was in fact a two electron process. In solution the neutral complex is yellow, becoming bright pink on reduction to $[Pt(4\text{-}NO_2\text{-}py)_2Cl_2]^{2-}$. The di-reduced solution is stable at room temperature under N_2, but decomposes rapidly on coming into contact with air. As it was not known whether the complex was formed as its *cis* or *trans* isomer crystals were grown for X-ray crystallography. X-ray crystallography indicated that $[Pt(4\text{-}NO_2\text{-}py)_2Cl_2]$ was synthesised in its *trans* form, see Figure 4.21. Relevant bond lengths and angles are shown in Table 4.4.

The structure shows that the Pt centre is only very slightly distorted from regular square planar geometry, with the angles at Pt almost equal to the ideal 90° and 180°. The planes of the two pyridine rings are tilted out of the PtN_2Cl_2 plane by approximately 45° in opposite directions to one another in order to alleviate interaction of ring protons with the chloride ligands. The NO_2 group is in the plane of the py ring. All bond lengths are comparable with related structures.

Table 4. 4 Selected bond lengths (Å) and angles (°) for *trans*-[Pt(4-NO_2-py)$_2Cl_2$].

Bond lengths / Å		**Bond angles / °**	
Pt(1) – N(1A)	2.006(5)	N(1B) – Pt(1) – N(1A)	179.17(17)
Pt(1) – Cl(2)	2.3019(16)	N(1B) – Pt(1) – Cl(2)	90.54(14)
O(1A) – N(2A)	1.215(7)	Cl(2) – Pt(1) – Cl(1)	178.95(5)
N(1A) – C(2A)	1.331(7)	C(2A) – N(1A) – C(6A)	119.1(5)
C(2A)- C(3A)	1.372(8)	N(1A) – C(2A) – C(3A)	123.3(6)
N(2A) – C(4A)	1.467(8)	C(5A) – C(4A) – N(2A)	119.7(6)
		O(1A) – N(2A) – C(4A)	118.0(5)
		O(1A) – N(2A) – O(2A)	124.7(6)
		4-NO_2-ring A –PtN_2Cl_2 plane	53.3
		4-NO_2-ring B –PtN_2Cl_2 plane	51.4

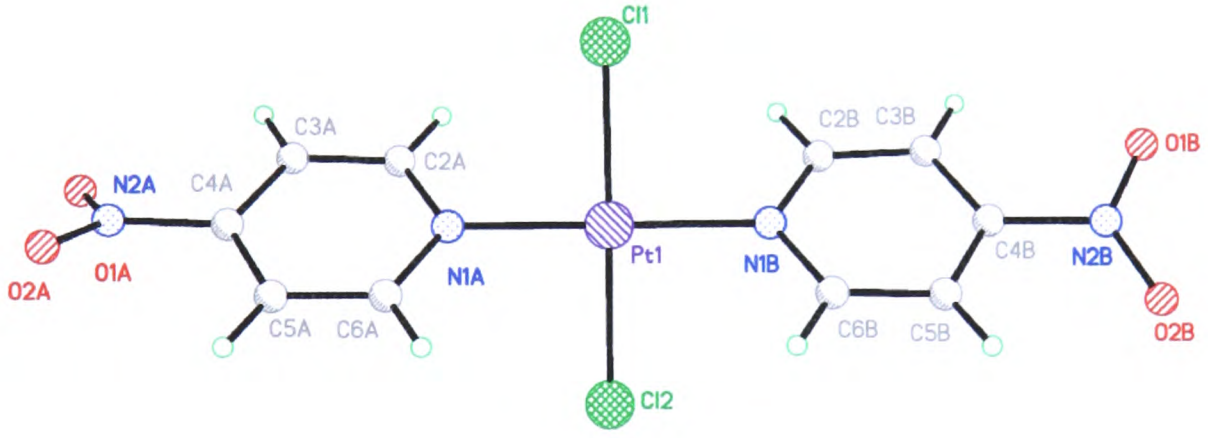

Figure 4. 21 Crystal structure of *trans*-[Pt(4-NO_2-py)$_2Cl_2$].

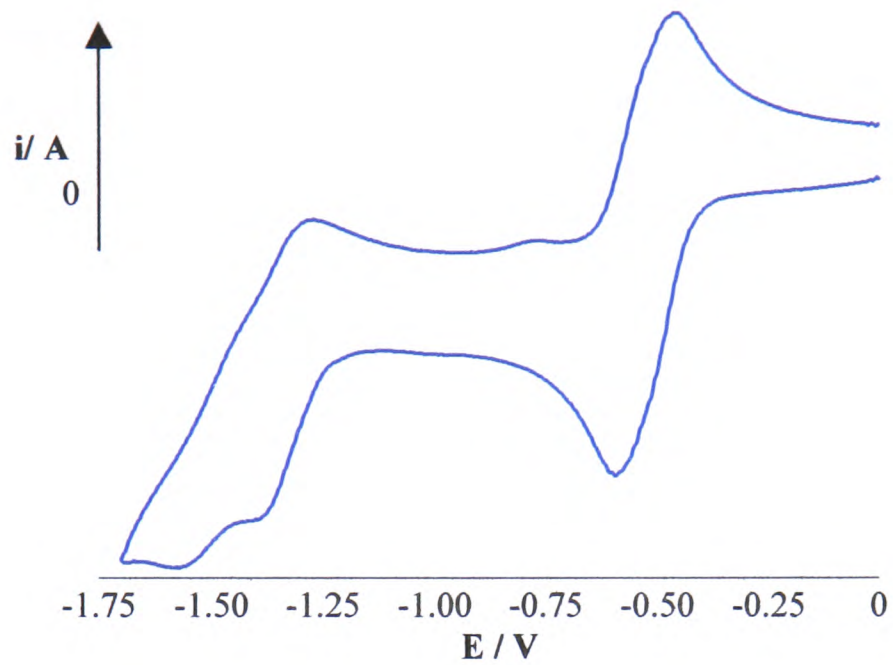

Figure 4. 19 Cyclic voltammogram of $[Pt(4\text{-}NO_2\text{-}py)_2Cl_2]$, scan rate 0.1 V/s, at 293 K in 0.1 M $TBABF_4$/DMF.

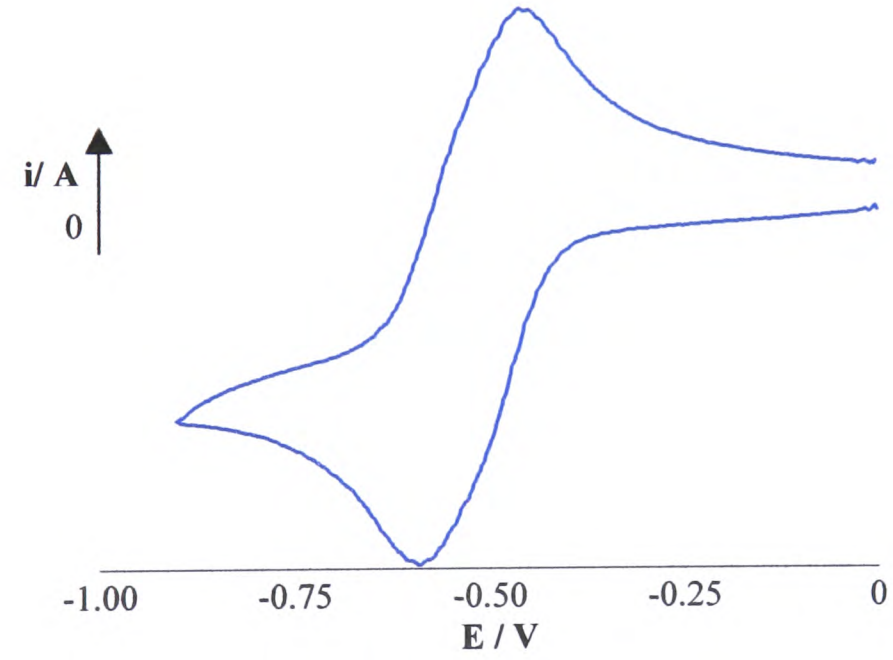

Figure 4. 20 Cyclic voltammogram of $[Pt(4\text{-}NO_2\text{-}py)_2Cl_2]$, scan rate 0.1 V/s, at 293 K in 0.1 M $TBABF_4$/DMF.

Repeating the electrochemical studies on the crystals of *trans*-[Pt(4-NO_2-py)$_2$$Cl_2$] under the same experimental conditions as before gave the first reduction at –0.47 V (0.132). Differential pulse studies on the same solution shows that the first reduction is split into two peaks at -0.45 V and –0.52 V, see Figure 4.22. Thus in [Pt(4-NO_2-py)$_2$$Cl_2$] there is little communication between the two 4-NO_2-py ligands and they are reduced independently of one another, but at very similar potentials.

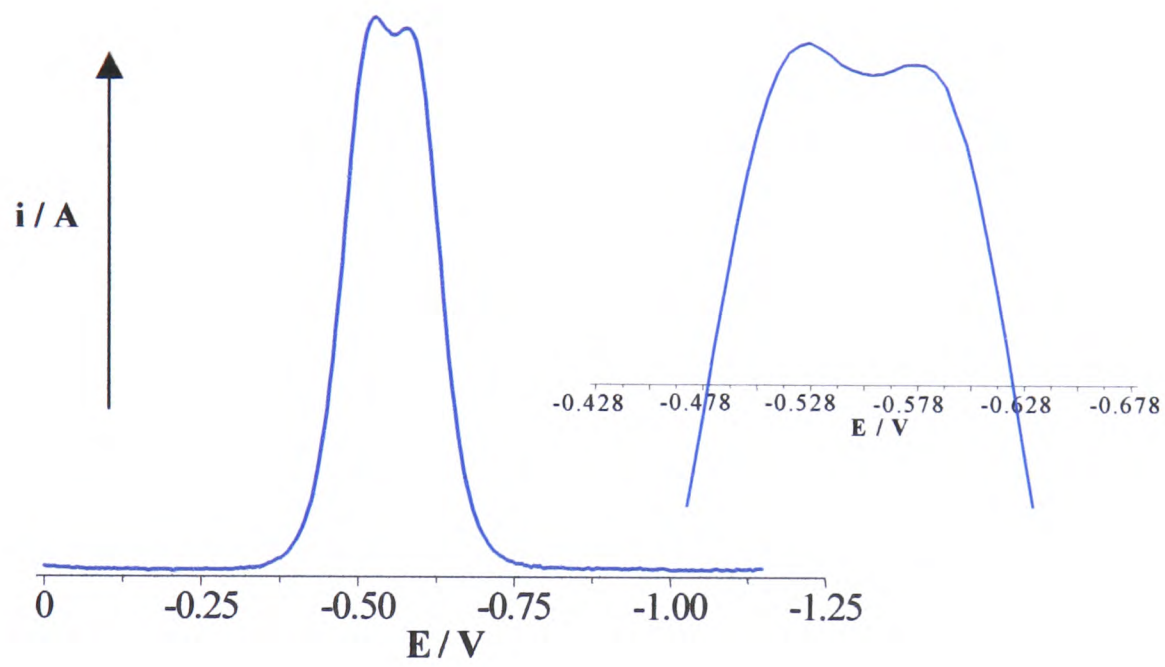

Figure 4. 22 Differential pulse voltammogram of *trans*-[Pt(4-NO_2-py)$_2$$Cl_2$] at 293 K in 0.1 M $TBABF_4$/DMF. Insert shows the splitting of the peak caused by the reduction of the two 4-NO_2-py ligands in greater detail.

In order to produce a *cis* 4-NO_2-py Pt complex to mimic the behaviour of [Pt(4,4'-(NO_2)$_2$-bpy)Cl_2], [Pt(4-NO_2-py)$_2$(ox)] was synthesised. Electrochemical studies on [Pt(4-NO_2-py)$_2$(ox)] in 0.1 M $TBABF_4$/DMF at 293 K reveal a two electron, fully reversible reduction at –0.48 V(0.118) followed by a second quasi-reversible reduction at –1.36 V (0.340), see Figure 4.23. Thus the electrochemistry is unaffected by substituting the bidentate oxalate for the chloride ligands, indicating that the first reduction at –0.48 V shows the two 4-NO_2-py ligands being reduced independently but at very similar potentials just as they are in [Pt(4-NO_2-py)$_2$$Cl_2$].

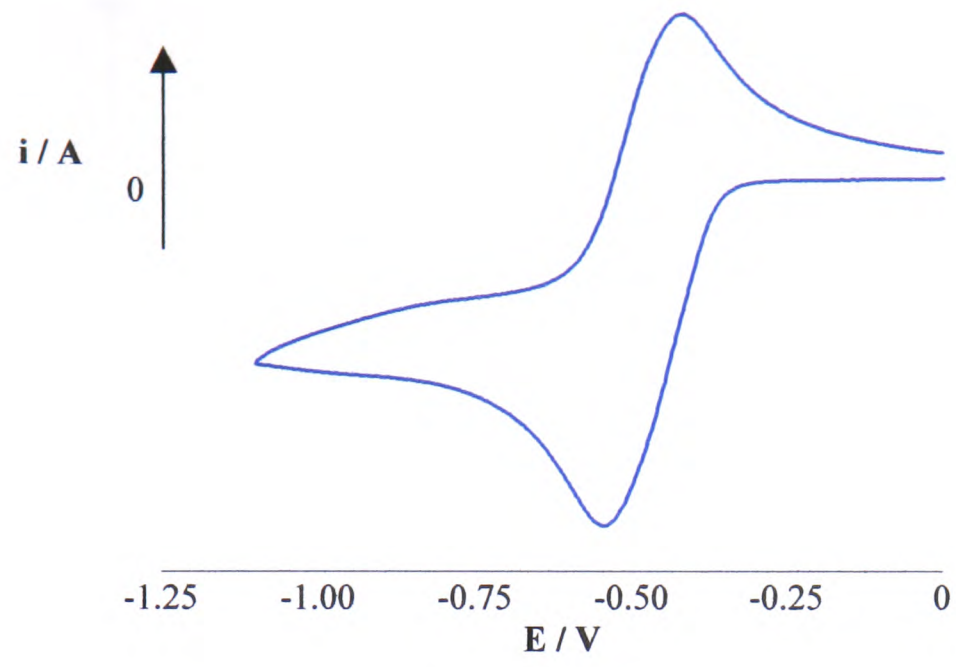

Figure 4. 23 Cyclic voltammogram of [Pt(4-NO_2-py)$_2$(ox)], scan rate 0.1 V/s, at 293 K, in 0.1 M $TBABF_4$/DMF.

Cyclic voltammetric studies on [Pd(4-NO_2-py)$_2$$Cl_2$] in 0.1 M $TBABF_4$/DMF at 293 K show two irreversible reductions at –0.39 V and –0.52 V, followed by a much larger fully reversible reduction at –0.75 V (0.108) and an irreversible reduction at –1.98 V. The first three redox processes are shown in Figure 4.24. Coulometric studies reveal that on holding the potential at -0.68 V the two irreversible reductions at –0.39 V and –0.52 V disappear, leaving only the reversible reduction at –0.75 V. This is the same potential at which free 4-NO_2-py is reduced, see Section 4.2.1.1. Thus the first two reductions are Pd based as indicated by their irreversibility and the reductions at –0.75 V and –1.98 V are the reductions of the free 4-NO_2-py that is liberated on decomposition of [Pd(4-NO_2-py)$_2$$Cl_2$]. Hence, the LUMO of Pd must be lower in energy that that of 4-NO_2-py. However, at 233 K [Pd(4-NO_2-py)$_2$$Cl_2$] no longer decomposes on reduction and the two irreversible reductions at -0.39 V and -0.52 V are replaced by a reversible two electron reduction at –0.46 V (0.076), see Figure 4.24. The linear response to the plot of i_p *vs* $\nu^{1/2}$ indicates that the reduction is electrochemically reversible. As the reduction potential is very close to that of the Pt analogue, ($E_{1/2}$ = -0.47 V), this reduction was attributed to the reduction of the two bound 4-NO_2-py ligands.

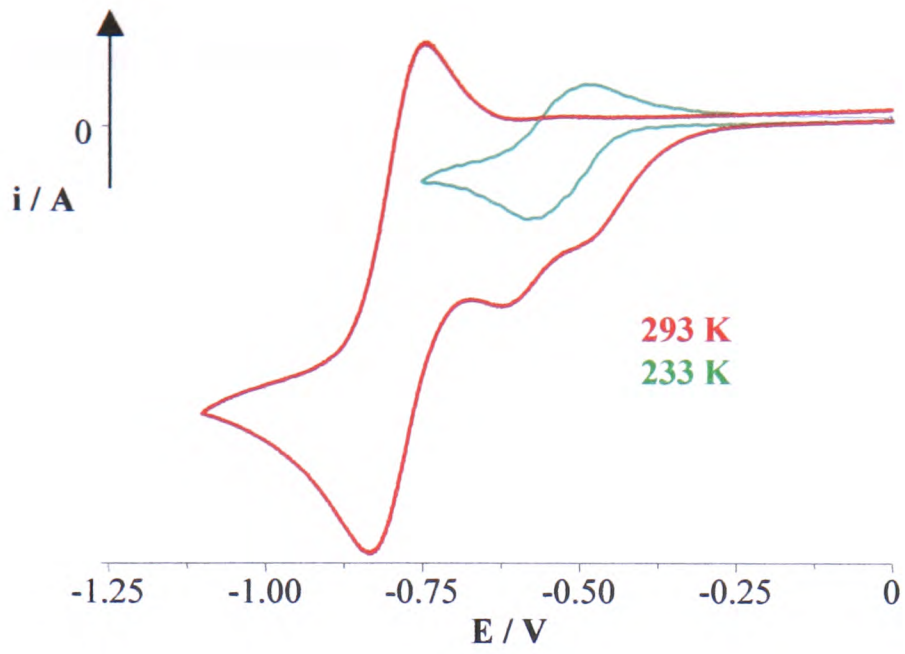

Figure 4. 24 Cyclic voltammograms of [Pd(4-NO_2-py)$_2Cl_2$], showing the effect of temperature on reversibility. Scan rate 0.1 V/s, in 0.1 M $TBABF_4$/DMF. Red at 293 K, green at 233 K.

4.2.2.2 UV/vis/nir Spectroelectrochemistry

In situ UV/vis/nir spectra were recorded for the reductions of $[Pt(4\text{-}NO_2\text{-}py)_2Cl_2]$ and $[Pt(4\text{-}NO_2\text{-}py)_2(ox)]$ in 0.1 M $TBABF_4$/DMF at 233K. The spectra of the neutral species are very similar with $[Pt(4\text{-}NO_2\text{-}py)_2Cl_2]$ having a broad band with three shoulders at 33,800 cm^{-1} (ε = 9,700 M^{-1} cm^{-1}), 30,900 cm^{-1} (ε = 8,200 M^{-1} cm^{-1}) and 27,900 cm^{-1} (ε = 5,600 M^{-1} cm^{-1}), see Figure 4.25. $[Pt(4\text{-}NO_2\text{-}py)_2(ox)]$ has a similar broad band with shoulders at 31,500 cm^{-1} (ε = 7,300 M^{-1} cm^{-1}) and 28,300cm^{-1} (ε = 4,100 M^{-1} cm^{-1}), see Figure 4.26. For each case the lowest energy shoulders were attributed to MLCT transitions and all other peaks were assigned as $\pi \rightarrow \pi^*$ intraligand transitions. Upon reduction to the di-anionic species both complexes show the same spectral changes, with an intense triplet growing in at very similar wavenumber. For $[Pt(4\text{-}NO_2\text{-}py)_2Cl_2]^{2-}$ the peaks are at 30,300 cm^{-1} (ε = 15,100 M^{-1} cm^{-1}), 25,800 cm^{-1} (ε = 17,800 M^{-1} cm^{-1}) and 19,200 cm^{-1} (ε = 11,100 M^{-1} cm^{-1}). In the case of $[Pt(4\text{-}NO_2\text{-}py)_2(ox)]^{2-}$ the peaks are observed at 30,700 cm^{-1} (ε = 8,000 M^{-1} cm^{-1}), 26,000 cm^{-1} (ε = 9,000 M^{-1} cm^{-1}) and 19,200 cm^{-1} (ε = 4,700 M^{-1} cm^{-1}), with an additional shoulder at 37,200 cm^{-1} (ε = 9,100 M^{-1} cm^{-1}), see Figure 4.26. $[Pt(4\text{-}NO_2\text{-}py)_2Cl_2]^{0/2-}$ shows isosbestic points at 33.9 kcm^{-1} and 36.5 kcm^{-1} indicating a clean conversion between the neutral and di-reduced species. Given the striking similarity between the two spectra the reduction electrons must be localised on the 4-NO_2-py ligands. This is in good agreement with the electrochemical and epr studies on the complexes, see Sections 4.2.2.1 and 4.2.2.3. For both $[Pt(4\text{-}NO_2\text{-}py)_2Cl_2]^{0/2-}$ and $[Pt(4\text{-}NO_2\text{-}py)_2(ox)]^{0/2-}$ the reductions are reversible as the original spectra are regenerated when the E_{gen} is switched back to 0 V. The spectrum of 4-NO_2-py^{1-}, see Figure 4.5, consists of two intense absorptions at 21,800 cm^{-1} and 31,500 cm^{-1} which have been assigned to the transitions of the additional electron in the π^* LUMO to higher energy π^* antibonding orbitals of the 4-NO_2-py ligand. In reduced $[Pt(4\text{-}NO_2\text{-}py)_2L]$, L = Cl_2 or ox, similar transitions might be expected and are therefore assigned to the bands at approximately 19,200 cm^{-1} and

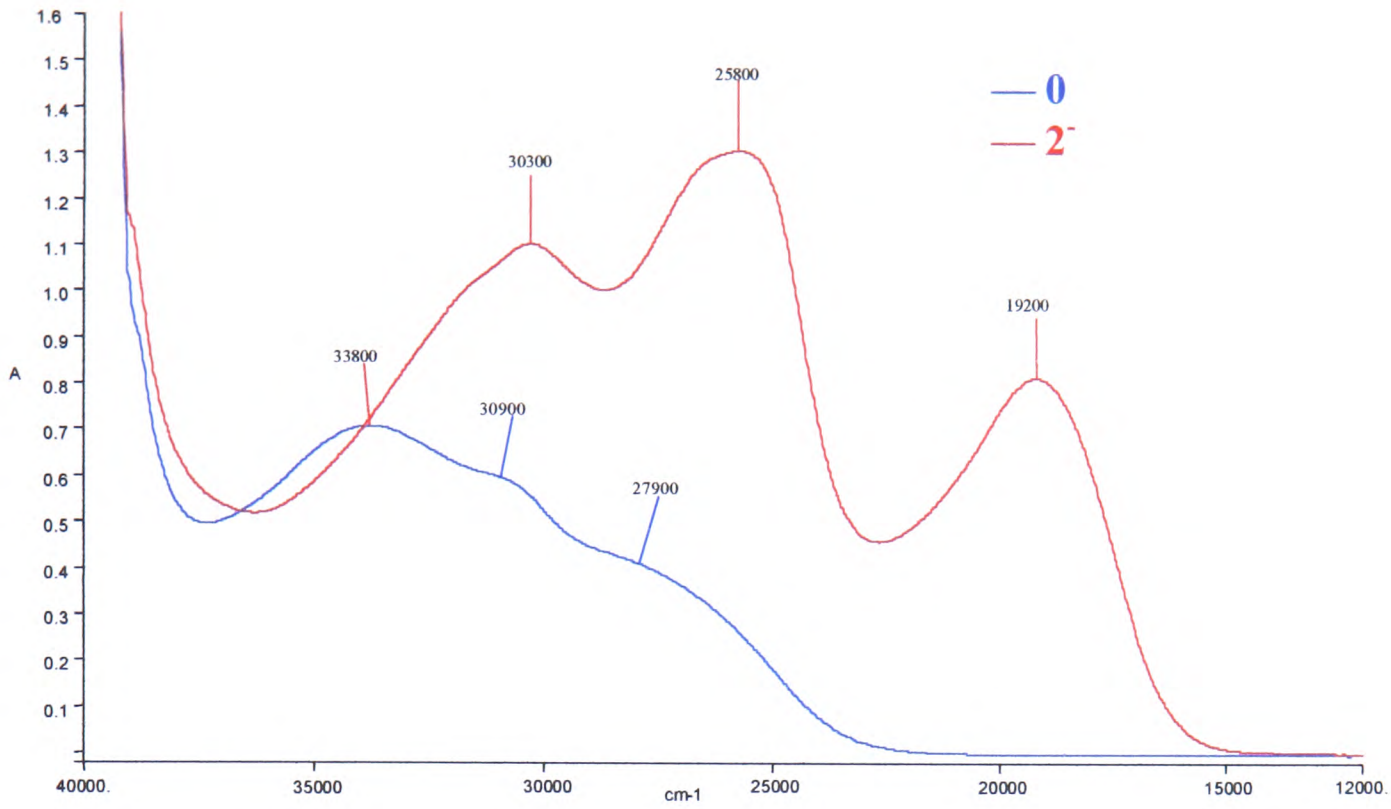

Figure 4. 25 UV/vis spectra of $[Pt(4\text{-}NO_2\text{-}py)_2Cl_2]^{0/2-}$, E_{gen} = -0.96 V, at 233 K in 0.1 M $TBABF_4$/DMF.

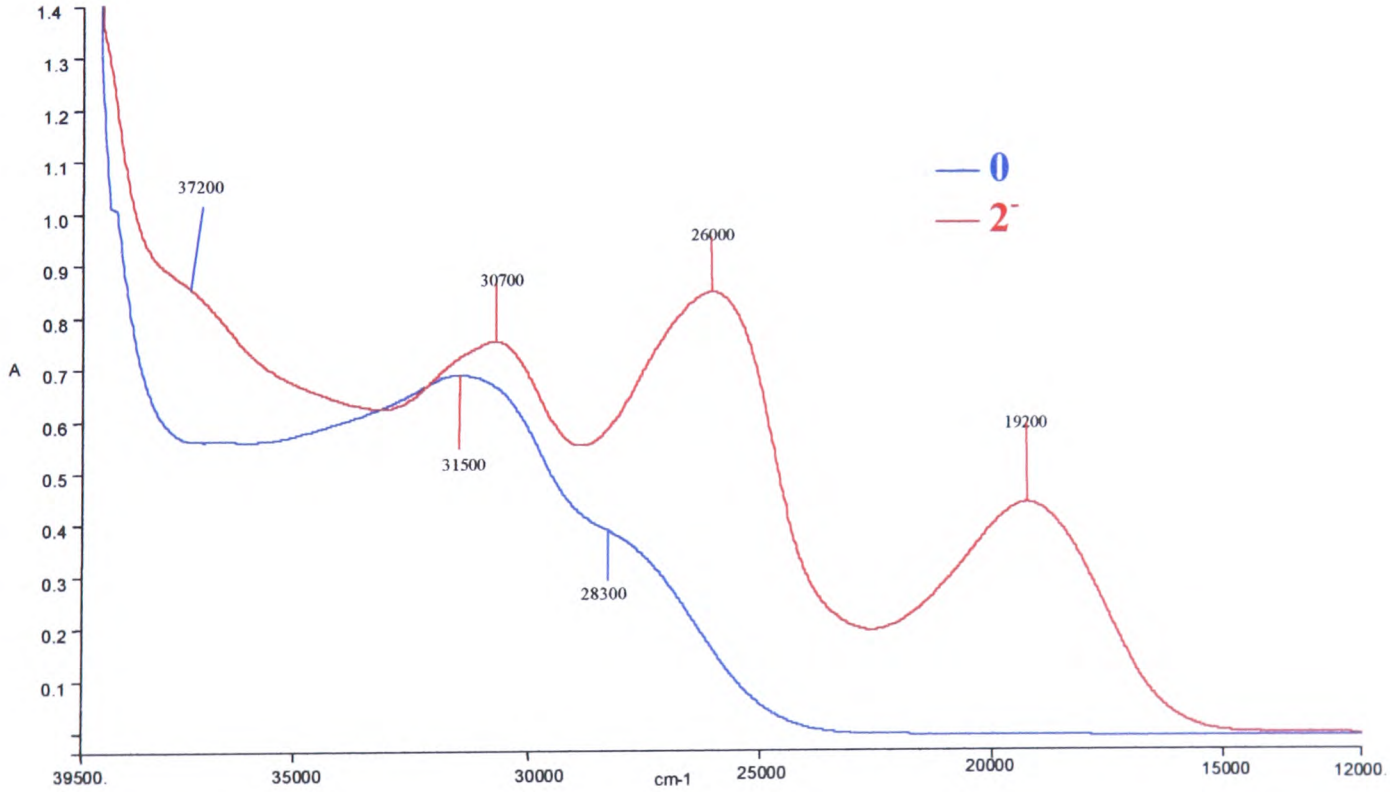

Figure 4. 26 UV/vis spectra of $[Pt(4\text{-}NO_2\text{-}py)_2(ox)]^{0/2-}$, E_{gen} = -0.91 V at 233 K in 0.1 M $TBABF_4$/DMF.

30,500 cm^{-1}. Note that the extinction coefficients are larger in the complex than in the free ligand. This is expected as every mole of the complex contains two moles of ligand. The additional band at 25,800 cm^{-1} in $[Pt(4\text{-}NO_2\text{-}py)_2Cl_2]^{2-}$ and 26,000 cm^{-1} in $[Pt(4\text{-}NO_2\text{-}py)_2(ox)]^{2-}$ must therefore be assigned to a metal-to-ligand-charge transfer from Pt(II) to the reduced 4-NO_2-py ligand. The reduction processes can therefore be assigned as follows:

$$[Pt(II)(4\text{-}NO_2\text{-}py^0)_2Cl_2] \xrightarrow{+e^-} [Pt(II)(4\text{-}NO_2\text{-}py^{1-})(4\text{-}NO_2\text{-}py^0)Cl_2]^{1-}$$

$$\xrightarrow{+e^-} [Pt(II)(4\text{-}NO_2\text{-}py^{1-})_2Cl_2]^{2-}$$

The UV/vis spectra of $[Pt(4,4'\text{-}(NO_2)_2\text{-}bpy)Cl_2]$ and $[Pd(4,4'\text{-}(NO_2)_2\text{-}bpy)Cl_2]$ in 0.1 M $TBABF_4$/DMF at 233 K show very similar spectra except for the presence of a MLCT band at 23,000 cm^{-1} (ε = 4,800 M^{-1} cm^{-1}) for $[Pt(4,4'\text{-}(NO_2)_2\text{-}bpy)Cl_2]$. In line with studies by McInnes the MLCT band was assigned as a Pt 5d - π^* transition.[25] The analogous Pd 4d - π^* MLCT would be expected to appear at much higher energy and hence is absent from the visible region of the spectrum. Higher energy bands are observed at 29,900 cm^{-1} (ε = 12,200 M^{-1} cm^{-1}) and 32,400 cm^{-1} (ε = 13,300 M^{-1} cm^{-1}) for $[Pt(4,4'\text{-}(NO_2)_2\text{-}bpy)Cl_2]$ and at 29,600 cm^{-1} (ε = 8,800 M^{-1} cm^{-1}), 33,300 cm^{-1} (ε = 9,100 M^{-1} cm^{-1}) and 36,800 cm^{-1} (ε = 11,000 M^{-1} cm^{-1}) for the Pd analogue, see Figures 4.27 and 4.28. These were assigned as a mixture of intraligand $\pi \rightarrow \pi^*$ and higher energy MLCT transitions. This is in good agreement with previous UV/vis/nir studies on these complexes.[25]

On reduction to $[Pd(4,4'\text{-}(NO_2)_2\text{-}bpy)Cl_2]^{1-}$ a broad band grows in the nir region at 7,100 cm^{-1} (ε = 1,300 M^{-1} cm^{-1}), as well as two bands at 18,100 cm^{-1} (ε = 2,500 M^{-1} cm^{-1}) and 19,500 cm^{-1} (ε = 3,200 M^{-1} cm^{-1}), see Figure 4.27. Two of the higher energy bands at 29,900 cm^{-1} (ε = 9,400 M^{-1} cm^{-1}) and 36,800 cm^{-1} (ε = 14,100 M^{-1} cm^{-1}) have also continued to grow. The spectrum of $[Pt(4,4'\text{-}(NO_2)_2\text{-}bpy)Cl_2]^{1-}$ is even more complicated but shows growth of a broad band at 6,800 cm^{-1} (ε = 2,100 M^{-1} cm^{-1}) and two bands at 17,600 cm^{-1} (ε = 3,000 M^{-1} cm^{-1}) and

19,300 cm^{-1} (ε = 3,700 M^{-1} cm^{-1}), similar to those observed for the mono-reduced Pd analogue. Additional bands at 21,300 cm^{-1} (ε = 5,300 M^{-1} cm^{-1}), 28,300 cm^{-1} (ε = 9,700 M^{-1} cm^{-1}) and 31,700 cm^{-1} (ε = 11,300 M^{-1} cm^{-1}) also grow in, see Figure 4.28 and Table 4.5. The spectra of $[Pt(4,4'\text{-}(NO_2)_2\text{-bpy})Cl_2]^{0/1-}$, in Figure 4.28, shows isosbestic points at 28.3 kcm^{-1} and 34.3 kcm^{-1} indicating clean conversion between the neutral and mono-reduced species.

The UV/vis/nir spectra of reduced 4,4'-$(NO_2)_2$-bpy and $[Pd(4,4'\text{-}(NO_2)_2\text{-bpy})Cl_2]^{1-}$ show bands around 20,000 cm^{-1}. The band at 29,600 cm^{-1} in the Pd complex increases in intensity as the ligand is reduced as in Figure 4.27. The two most obvious differences between the spectra of the reduced free ligand (Figure 4.7) and the reduced $[Pd(4,4'\text{-}(NO_2)_2\text{-bpy})Cl_2]^{1-}$ are the structures of the band at 19,500 cm^{-1} and the broad band at 7,100 cm^{-1} in the reduced complex. The band in the spectrum of $[Pd(4,4'\text{-}(NO_2)_2\text{-bpy})Cl_2]^{1-}$ at 7,100 cm^{-1} is probably related to the broad, low energy band in the near IR region of the spectrum of the reduced ligand. Although the spectra of 4,4'-$(NO_2)_2$-bpy^{1-} and $[Pd(4,4'\text{-}(NO_2)_2\text{-bpy}]^{1-}$ show the same basic trend they differ in the details of the spectra. This can probably be accounted for in the different orientation of the 4-NO_2-py rings with respect to one another in the free and bound states. As argued previously the free ligand has non-interacting (and presumably orthogonal) 4-NO_2-py rings. Such an orientation is not possible when the ligand is bound to a metal centre. The spectrum of $[Pd(4,4'\text{-}(NO_2)_2\text{-bpy})Cl_2]^{1-}$ with bands at 7.1 kcm^{-1}, a doublet at *ca.* 19 kcm^{-1} and an intense band in the UV region at *ca.* 30 kcm^{-1} has similar features to that of co-ordinated bpy^{1-}, which shows a band at *ca.* 10 kcm^{-1}, a doublet at *ca.* 20 kcm^{-1} and an intense band at *ca.* 25 kcm^{-1}. Therefore the bands in the spectrum of mono-reduced $[Pd(4,4'\text{-}(NO_2)_2\text{-bpy})Cl_2]$ are assigned as transitions to/from the singly occupied π^* orbital on the bidentate ligand. Thus the reduction electron must be delocalised over the both ring systems rather than confined to a 4-NO_2-py moiety as it is in the free ligand. The shifts in band position between the two spectra must be due to the electronic effects of the nitro groups. The spectrum of $[Pt(4,4'\text{-}(NO_2)_2\text{-bpy})Cl_2]^{1-}$ contains the same features as its Pd analogue and these bands are assigned to similar electronic transitions. Additional features in

the spectrum of the reduced Pt complex must be due to the electronic transitions involving the Pt(II) metal centre. Once again the site of the reduction is based on the ligand bound to a Pt(II) metal centre.

On di-reduction the broad nir bands blue shift to 10,200 cm^{-1} (ε = 2,600 M^{-1} cm^{-1}) for $[Pd(4,4'\text{-}(NO_2)_2\text{-bpy})Cl_2]^{2-}$ and 9,200 cm^{-1} (ε = 3,500 M^{-1} cm^{-1}) for the Pt analogue. In both complexes the bands at *ca.* 19 kcm^{-1} intensify and blue shift, see Figures 4.29 – 4.31. The major difference between the spectra of $[Pd(4,4'\text{-}(NO_2)_2\text{-bpy})Cl_2]^{2-}$ and $[Pt(4,4'\text{-}(NO_2)_2\text{-bpy})Cl_2]^{2-}$ is the presence of an intense peak at 23,000 cm^{-1} (ε = 14,900 M^{-1} cm^{-1}) for $[Pt(4,4'\text{-}(NO_2)_2\text{-bpy})Cl_2]^{2-}$, which in line with previous work by McInnes was assigned as a MLCT transition, see Figure 4.28.[25] All other bands were assigned as intraligand electronic transitions from and to the partially occupied LUMO and LUMO-1 orbitals of the parent complex. $[Pd(4,4'\text{-}(NO_2)_2\text{-bpy})Cl_2]^{1-/2-}$ shows a clean isosbestic point at 8.0 kcm^{-1}, while $[Pt(4,4'\text{-}(NO_2)_2\text{-bpy})Cl_2]^{1-/2-}$ shows isosbestic points at 7.8 kcm^{-1}, 25.4 kcm^{-1} and 32.7 kcm^{-1} indicating a clean conversion between redox states for both complexes. In DMF solution $[Pt(4,4'\text{-}(NO_2)_2\text{-bpy})Cl_2]^{2-}$ is claret coloured.

Unlike the Pd analogue, $[Pt(4,4'\text{-}(NO_2)_2\text{-bpy})Cl_2]$ undergoes a third reduction, the most notable features of which are the collapse and blue shift of the broad nir band to 11,400 cm^{-1} (ε = 1,600 M^{-1} cm^{-1}), the collapse of the band at *ca.* 19 kcm^{-1} to be replaced by a band at 18,400 cm^{-1} (ε = 3,500 M^{-1} cm^{-1}) and the blue shift of the MLCT band to 23,900 cm^{-1} (ε = 14,000 M^{-1} cm^{-1}), see Figure 4.28 and Table 4.5. The third reduction electron is anticipated to spin pair with the electron in the LUMO leaving one unpaired electron (and a hole) in the LUMO-1 orbital. Thus the UV/vis/nir spectrum of $[Pt(4,4'\text{-}(NO_2)_2\text{-bpyCl}_2]^{3-}$ should resemble that of the mono- and di-reduced analogues with bands slightly shifted due to the differing electronic populations. Band assignments are as before, namely all are intraligand charge transfers apart from the MLCT band at 23,900 cm^{-1}. The band at *ca.* 5,000 cm^{-1} can be assigned to the electronic transition from the LUMO to LUMO-1, see Figures 4.32

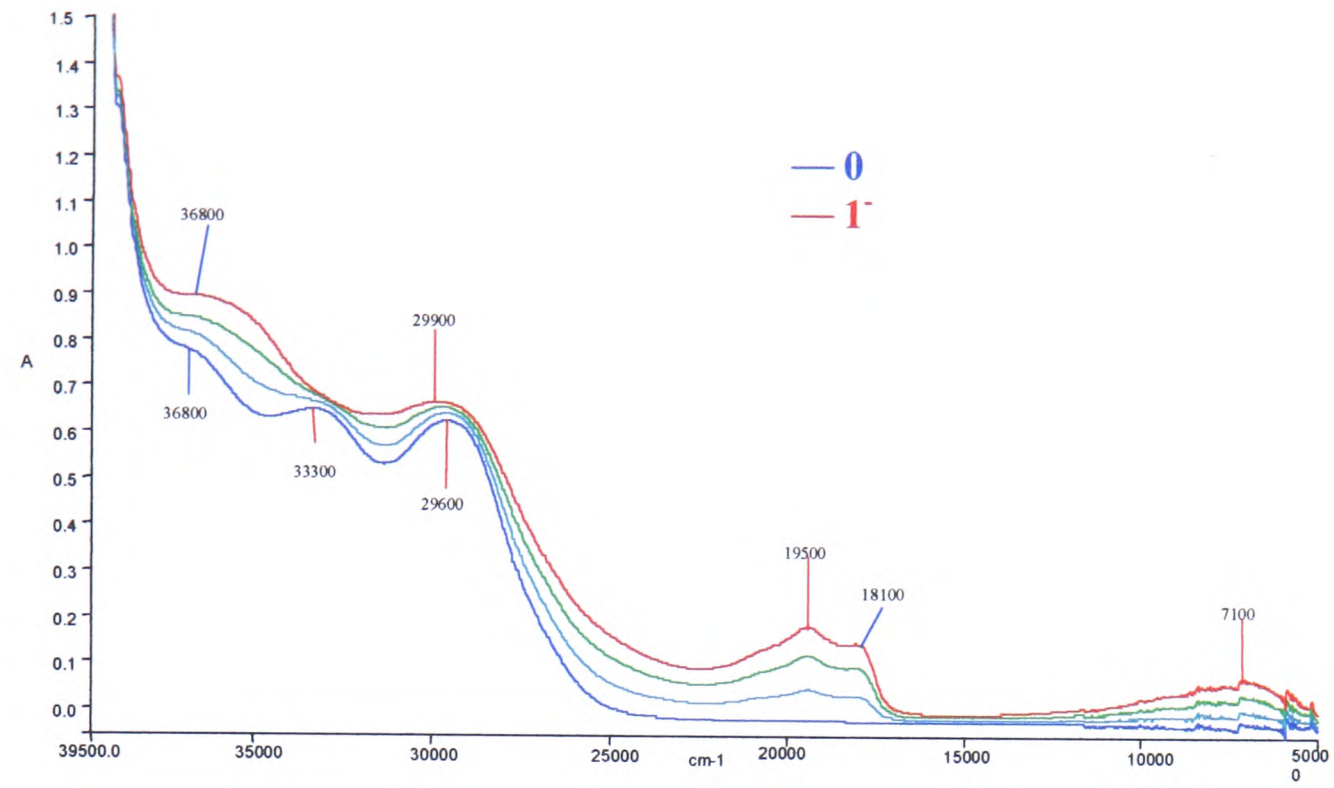

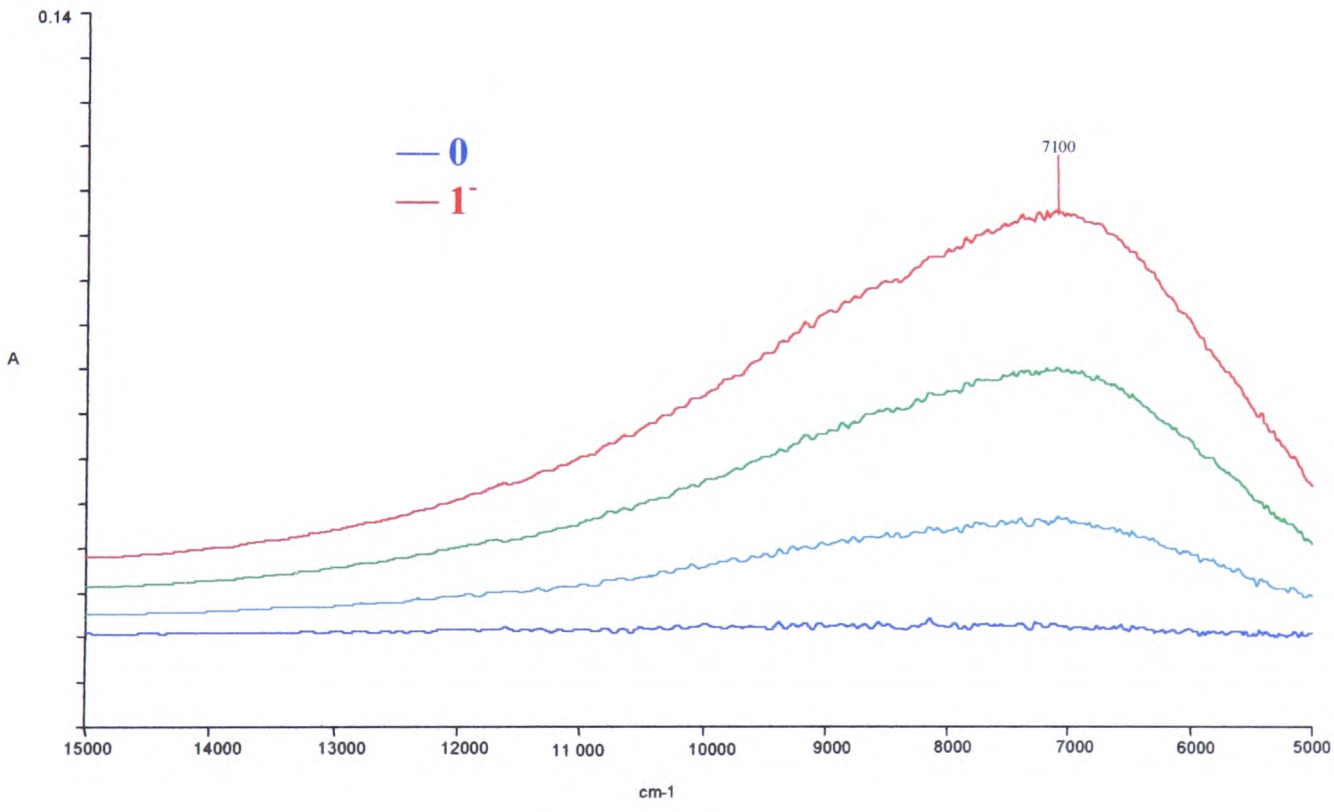

Figure 4. 27 UV/vis/nir spectra of $[Pd(4,4'\text{-}(NO_2)_2\text{-}bpy)Cl_2]^{0/1-}$, E_{gen} –0.44 V, at 233 K in 0.1 M $TBABF_4$/DMF. The insert shows the nir band in greater detail.

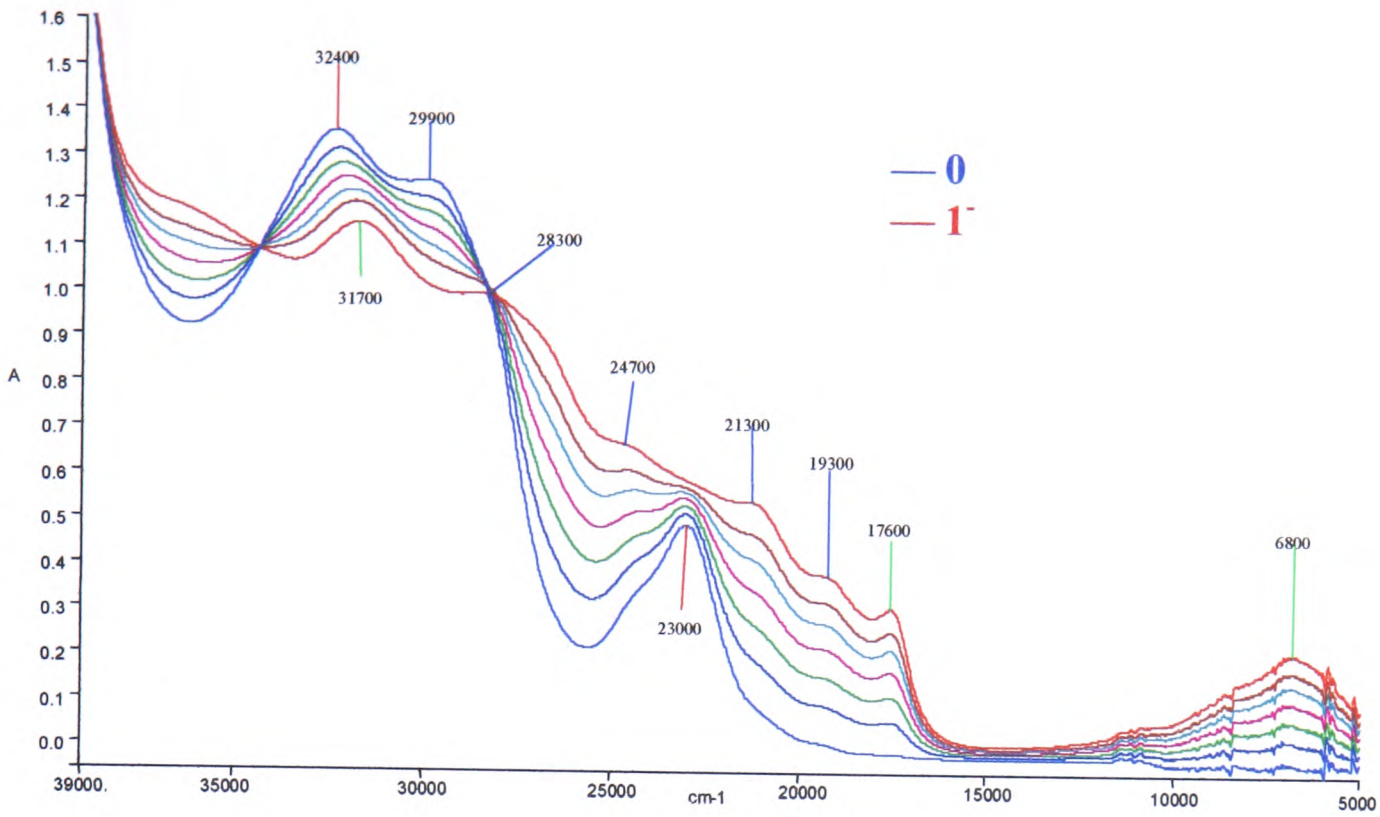

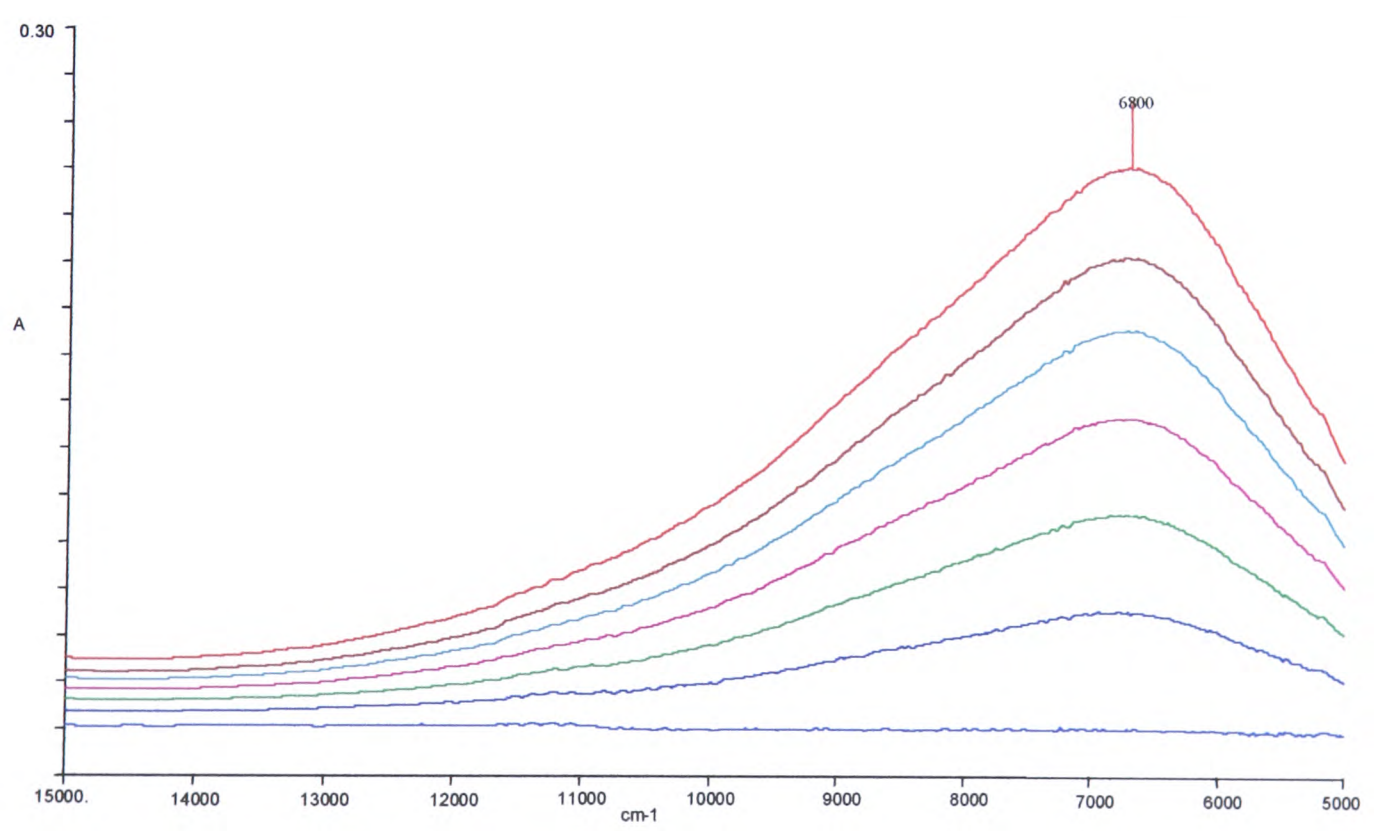

Figure 4. 28 UV/vis/nir of $[Pt(4,4'\text{-}(NO_2)_2\text{-}bpy)Cl_2]^{0/1-}$, E_{gen} = -0.43 V, 233 K in 0.1 M $TBABF_4$/DMF. The insert shows the nir band in greater detail.

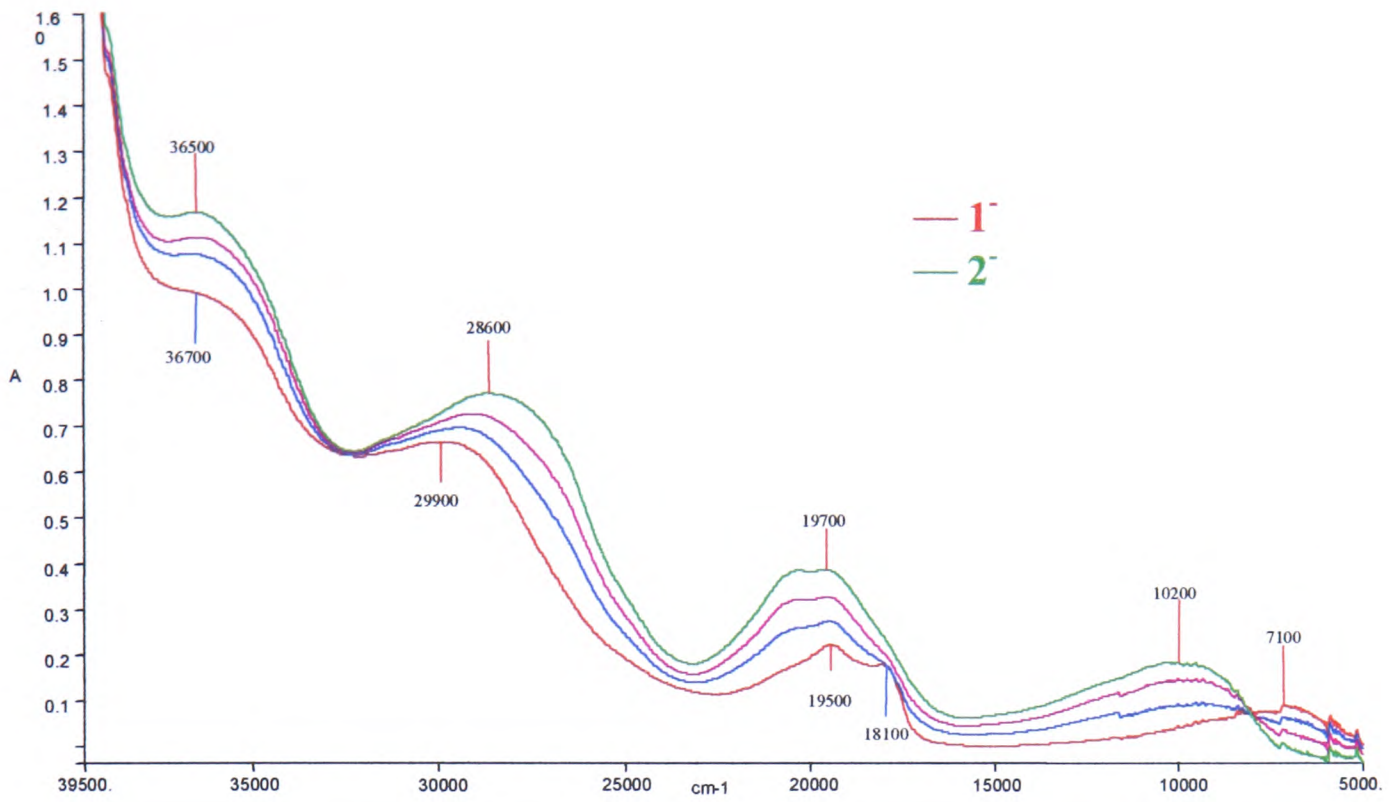

Figure 4. 29 UV/vis/nir spectra of $[Pd(4,4'\text{-}(NO_2)_2\text{-}bpy)Cl_2]^{1-/2-}$, E_{gen} = -0.76 V, at 233 K in 0.1 M $TBABF_4$/DMF.

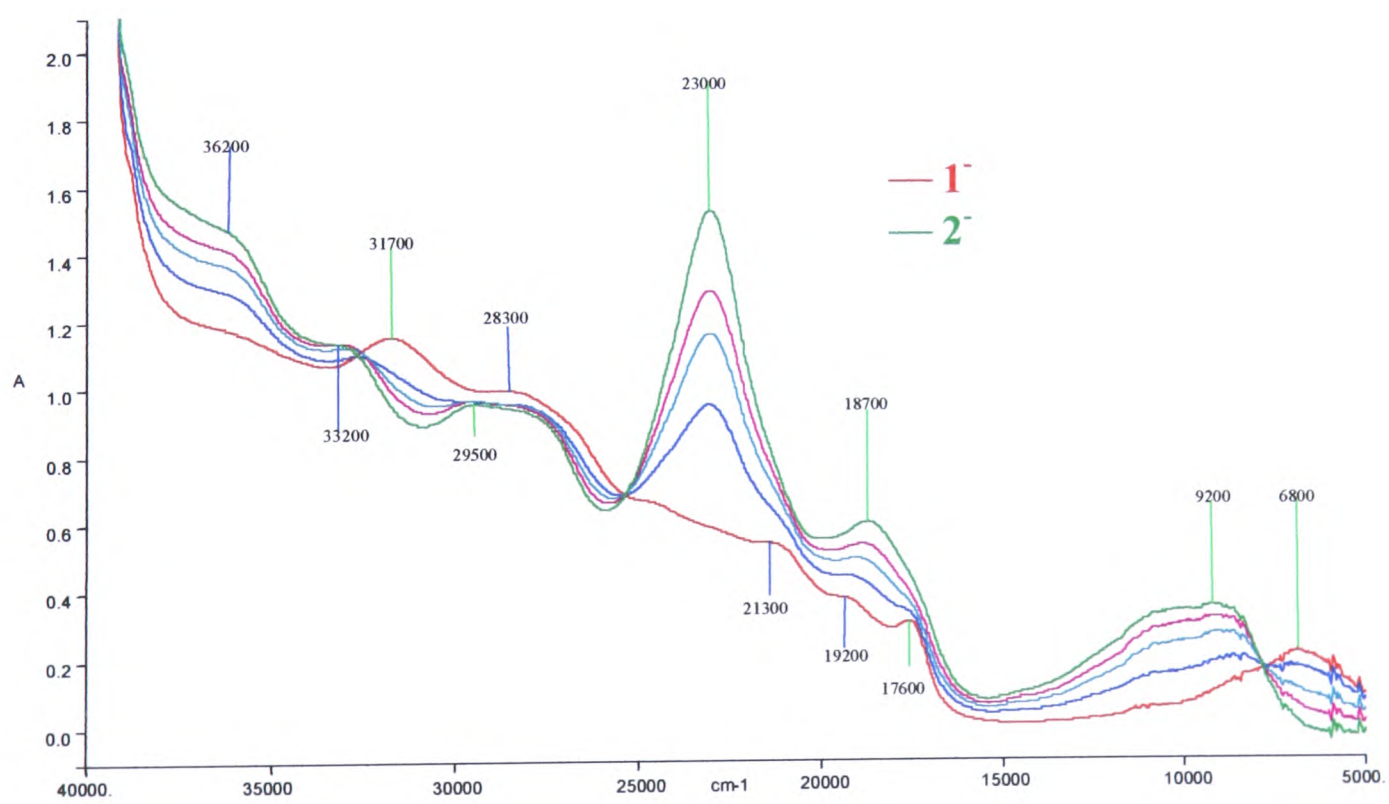

Figure 4. 30 UV/vis/nir of $[Pt(4,4'\text{-}(NO_2)_2\text{-}bpy)Cl_2]^{1-/2-}$, E_{gen} = -0.91 V, at 233 K in 0.1 M $TBABF_4$/DMF.

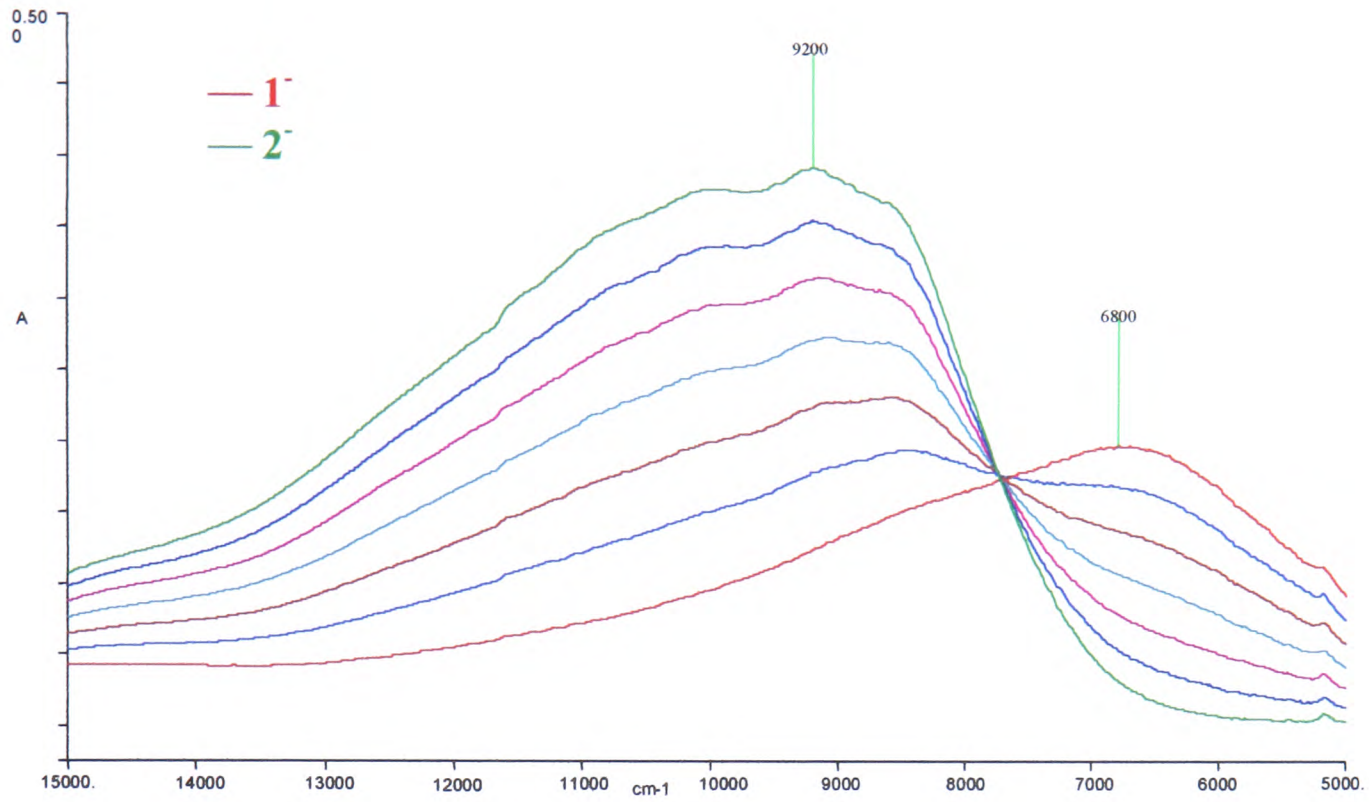

Figure 4.31 nir band of $[Pt(4,4'\text{-}(NO_2)_2\text{-}bpy)Cl_2]^{1-/2-}$, E_{gen} = -0.91 V, at 233 K in 0.1 M $TBABF_4$/DMF.

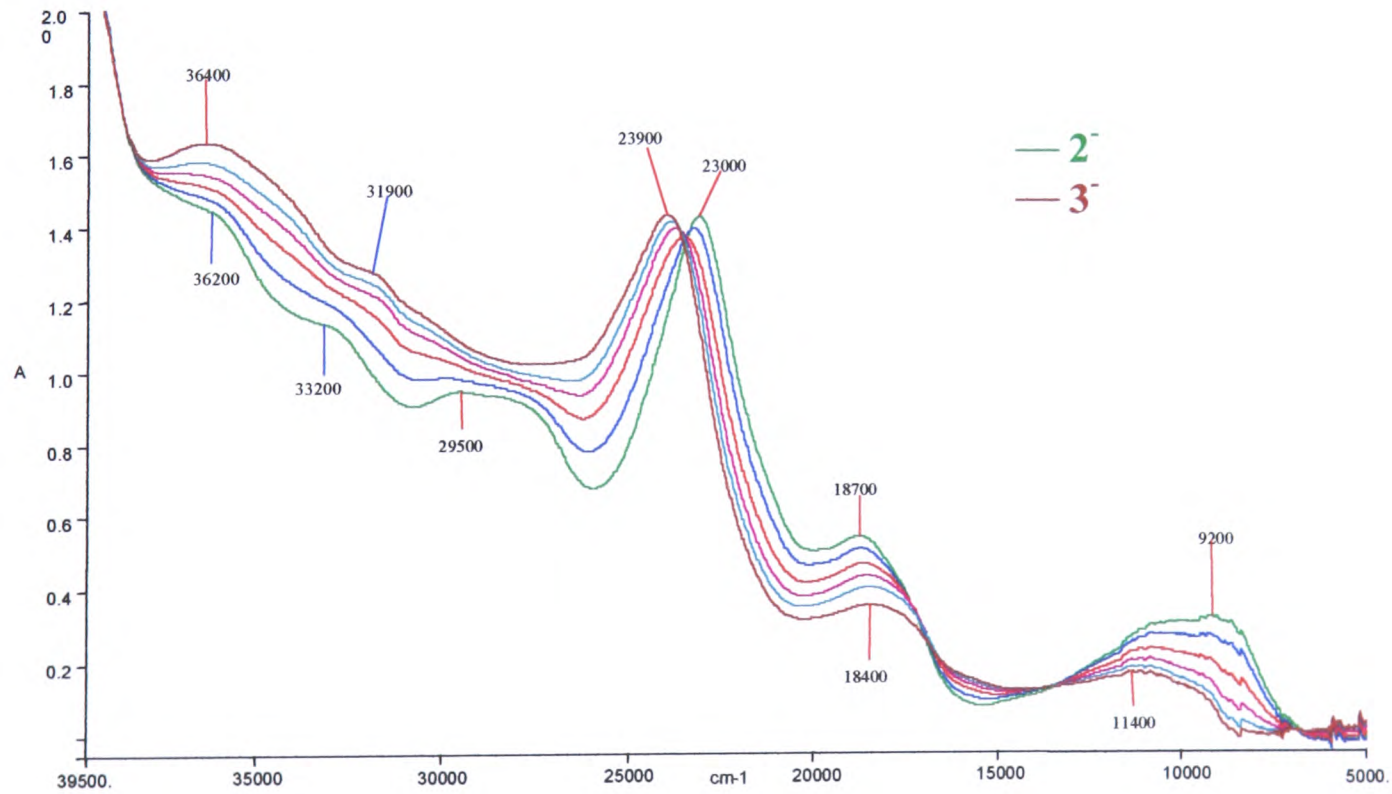

Figure 4. 32 Uv/vis/nir spectra of $[Pt(4,4'\text{-}(NO_2)_2\text{-}bpy)Cl_2]^{2-/3-}$, E_{gen} = -1.44 V, at 233 K in 0.1 M $TBABF_4$/DMF.

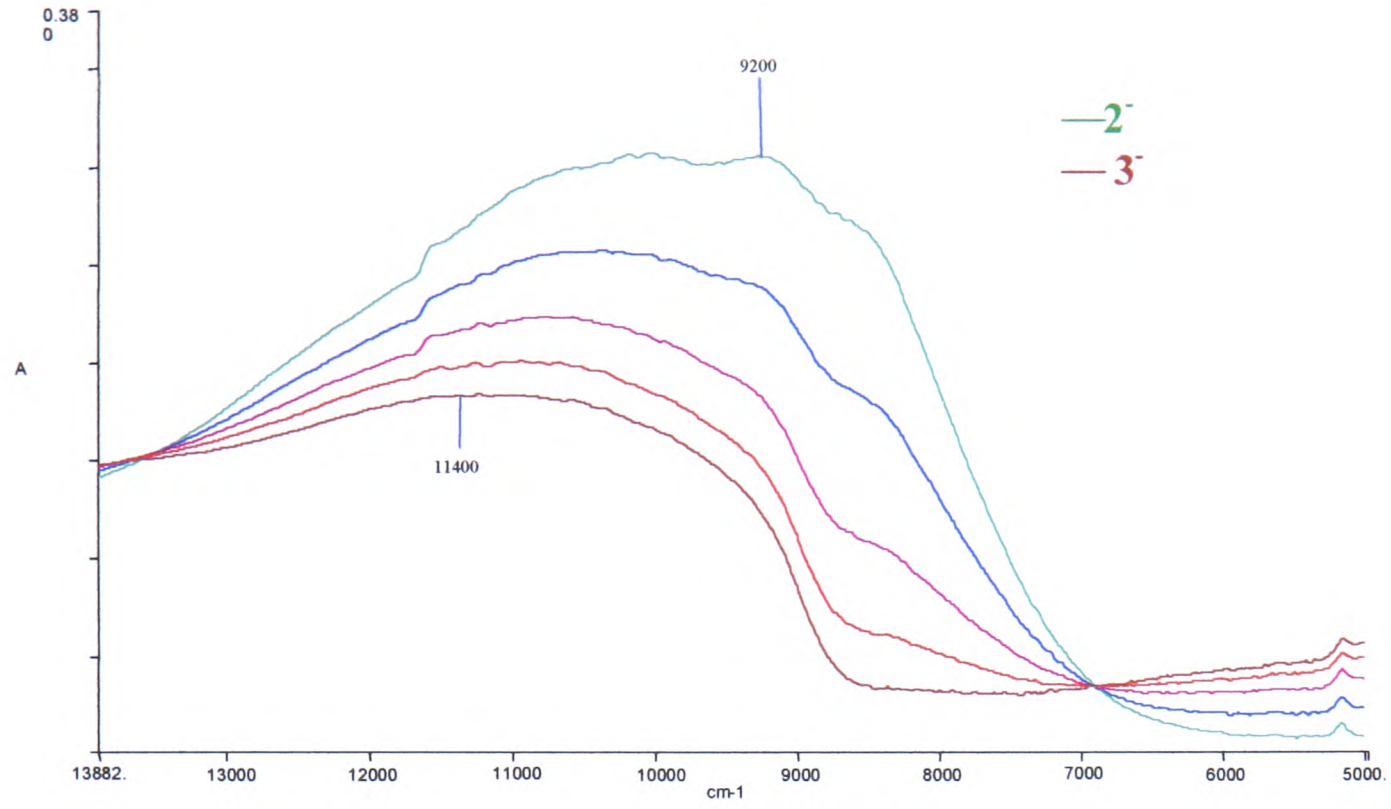

Figure 4. 33 nir band of $[Pt(4,4'\text{-}(NO_2)_2\text{-}bpy)Cl_2]^{2-/3-}$, E_{gen} = -1.44 V, at 233 K In 0.1 M $TBABF_4$/DMF. Band at *ca.* 5,000 cm^{-1} is electronic transition from LUMO to LUMO-1.

and 4.33. This electronic transition is expected in $[Pt(4,4'\text{-}(NO_2)_2\text{-}bpy)Cl_2]^{1-}$, but is obscured by the nir band at 6,800 cm^{-1}, see Figure 4.28. The energy gap between the two levels is known to be very small.[74] However, the band position gives a larger LUMO LUMO-1 energy gap than expected as it includes the spin pairing energy of the two electrons in the LUMO-1 level. The progression in band energies with one-electron reductions indicates a commonality of reduction sites. Epr studies of $4,4'\text{-}(NO_2)_2\text{-}bpy^{2-}$ suggests that the two unpaired electrons are each localised on one $4\text{-}NO_2$-py ring and that the two rings are probably orthogonal to one another .Such a geometric option is not available on ligation. The UV/vis/nir spectral results are in agreement with the LUMO and LUMO-1 orbitals on $[Pt(4,4'\text{-}(NO_2)_2\text{-}bpy)Cl_2]$ and the Pd analogue being delocalised over both ring systems. Isosbestic points at 6.7 kcm^{-1}, 13.4 kcm^{-1}, 17.0 kcm^{-1} and 23.5 kcm^{-1} indicate a clean conversion between the di- and tri-reduced forms of $[Pt(4,4'\text{-}(NO_2)_2\text{-}bpy)Cl_2]$, with no decomposition. All reduction steps for $[Pd(4,4'\text{-}(NO_2)_2\text{-}bpy)Cl_2]^{0/1-/2-}$ and $[Pt(4,4'\text{-}(NO_2)_2\text{-}bpy)Cl_2]^{0/1-/2-/3-}$ are fully reversible. $[Pd(4,4'\text{-}(NO_2)_2\text{-}bpy)Cl_2]^{1-}$ is pink and the di-anionic species is a

darker red. In contrast, the mono and di-anionic species of [Pt(4,4'-$(NO_2)_2$-bpy)Cl_2] are deepening shades of red and the tri-anionic species is brown.

The UV/vis/nir spectrum of [Pt(4-NO_2-bpy)Cl_2] in 0.1 M $TBABF_4$/DMF shows a MLCT band at 24,000 cm^{-1} (ε = 6,000 M^{-1} cm^{-1}) (5d - π^*) and two intense higher energy bands at 32,000 cm^{-1} (ε = 14,200 M^{-1} cm^{-1}) and 37,200 cm^{-1} (ε = 20,300 M^{-1} cm^{-1}) which were assigned as being due to intraligand $\pi \rightarrow \pi^*$ and higher energy MLCT transitions, see Figure 4.34. The ν_{max} of the MLCT band for this complex is observed at higher energy than for the di-nitro substituted complex (23,000 cm^{-1}) This is due to there being only one nitro group on the bpy ligand as electron withdrawing nitro groups stabilise the ligand LUMO thereby decreasing the energy of any MLCT transitions. For unsubstituted [Pt(bpy)Cl_2] in DMF the MLCT transition is observed at 25,700 cm^{-1}.[27] As expected the UV/vis/nir spectrum for [Pd(4-NO_2-bpy)Cl_2] shows no MLCT peak as the 4d - π^* transition is expected to take place at a much higher energy than the Pt 5d - π^* MLCT. The spectrum for [Pd(4-NO_2-bpy)Cl_2] shows peaks at 31,400 cm^{-1} (ε = 17,600 M^{-1} cm^{-1}) and 32,600 cm^{-1} (ε = 16,900 M^{-1} cm^{-1}), see Figure 4.35. Both peaks were assigned as $\pi \rightarrow \pi^*$ intraligand transitions.

On generating [Pt(4-NO_2-bpy)Cl_2]$^{1-}$ at 227 K in 0.1 M $TBABF_4$/DMF a broad band grows in the nir region at 10,500 cm^{-1} (ε = 3,000 M^{-1} cm^{-1}), see Figure 4.34. A similar nir band is observed in the reduced species of [Pt(4,4'-$(NO_2)_2$-bpy)Cl_2] and [Pd(4,4'-$(NO_2)_2$-bpy)Cl_2]. Additional bands also grow in at 16,700 cm^{-1} (ε = 4,200 M^{-1} cm^{-1}), 17,700 cm^{-1} (ε = 4,500 M^{-1} cm^{-1}), 20,600 cm^{-1} (ε = 5,400 M^{-1} cm^{-1}), 22,800 cm^{-1} (ε = 11,900 M^{-1} cm^{-1}) and 36,600 cm^{-1} (29,800 M^{-1} cm^{-1}). The peak at 32,100 cm^{-1}, previously assigned as a $\pi \rightarrow \pi^*$ intraligand transition, does not collapse on reduction as expected. From previous work on free 4-NO_2-bpy it is known that the reduction electron is localised on the 4-NO_2-py moiety rather than being delocalised over the whole of the ligand. Thus the peak at 32,100 cm^{-1} may be due to $\pi \rightarrow \pi^*$ intraligand transitions on the unsubstituted

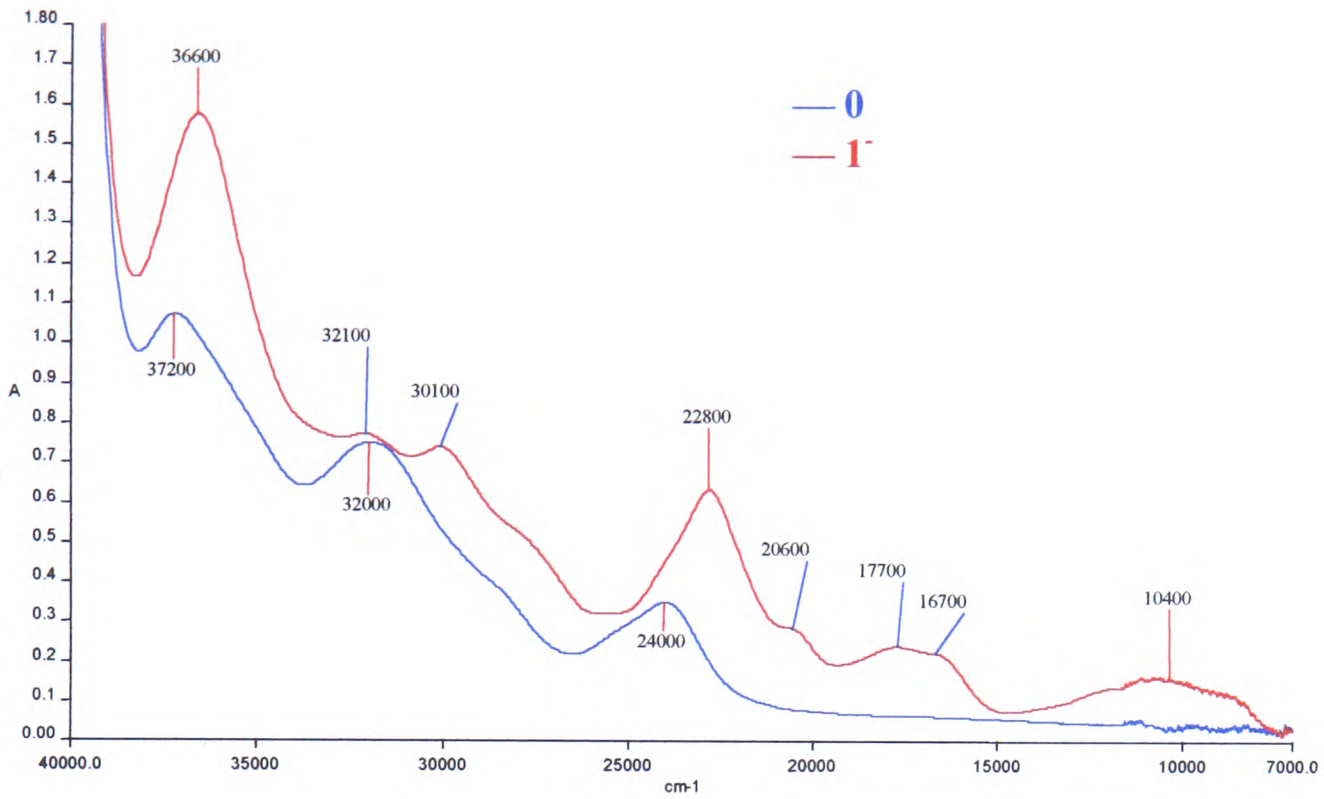

Figure 4. 34 Uv/vis/nir spectra of $[Pt(4\text{-}NO_2\text{-}bpy)Cl_2]^{0/1-}$, E_{gen} = -0.69 V, at 227 K in 0.1 M $TBABF_4$/DMF.

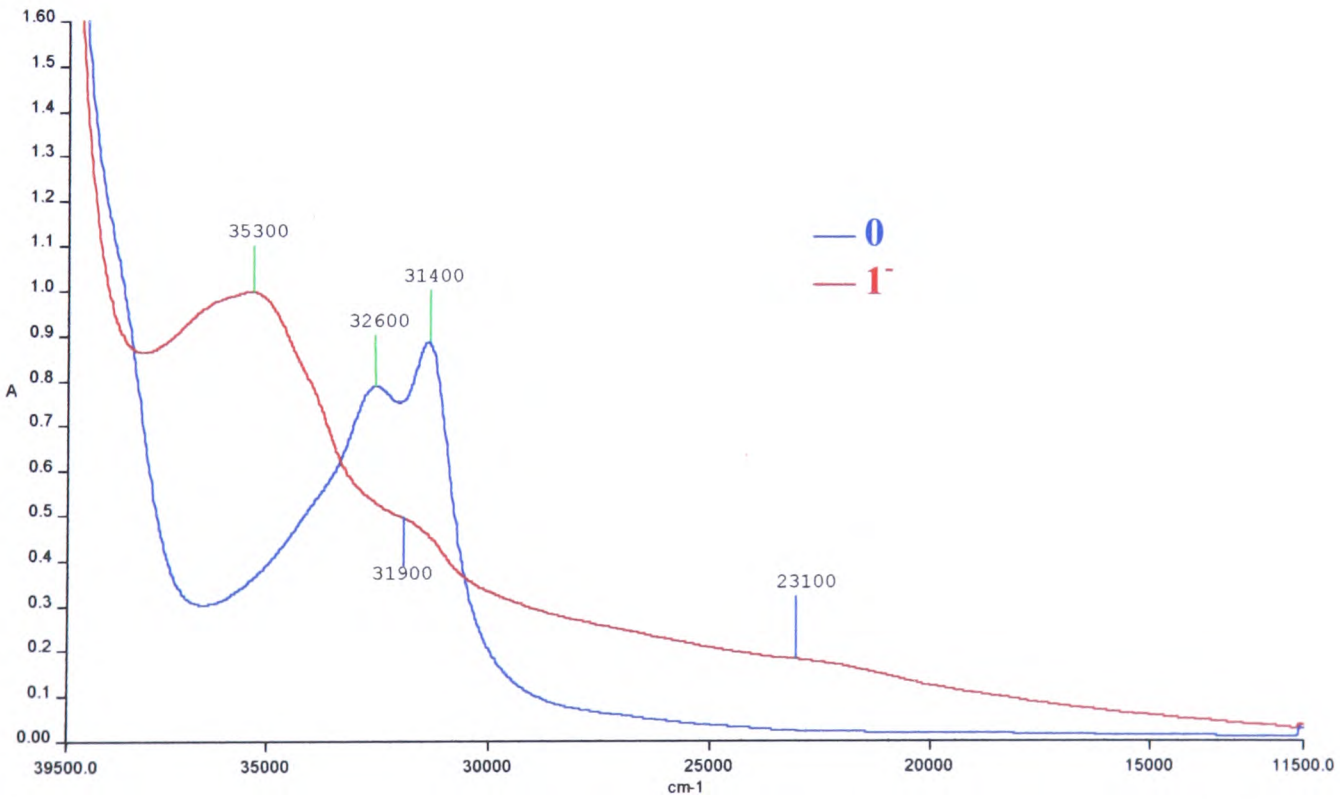

Figure 4. 35 UV/vis/nir spectra of $[Pd(4\text{-}NO_2\text{-}bpy)Cl_2]^{0/1-}$, E_{gen} = -0.59 V, at 228 K in 0.1 M $TBABF_4$/DMF.

py ring of the bpy ligand. On reduction of $[Pd(4\text{-}NO_2\text{-}bpy)Cl_2]^0$ to $[Pd(4\text{-}NO_2\text{-}bpy)Cl_2]^{1-}$ the bands at 31,500 cm^{-1} and 32,600 cm^{-1} collapse, to be replaced by a broad shoulder in the range 15 – 30 kcm^{-1} (ε = 3,700 M^{-1} cm^{-1}) and an intense high energy band at 35,300 cm^{-1} (ε = 20,600 M^{-1} cm^{-1}) with a lower energy shoulder at 31,900 cm^{-1} (ε = 10,200 M^{-1} cm^{-1}). These peaks were assigned as intraligand transitions of the reduced 4-NO_2-bpy ligand, as the spectrum of 4-NO_2-bpy^{1-} shows a similar intense peak and lower energy shoulder in the UV region, see Figure 4.35. Isosbestic points are observed at 30.6 kcm^{-1}, 33.4 kcm^{-1} and 38.0 kcm^{-1} in the spectra showing the reduction of $[Pd(4\text{-}NO_2\text{-}bpy)Cl_2]^{0/1-}$, indicating the mono-anionic species is generated without decomposition.

On undergoing a second reduction to give $[Pt(4\text{-}NO_2\text{-}bpy)Cl_2]^{2-}$, the broad nir band blue shifts and increases in intensity giving a band at 11,900 cm^{-1} (ε = 4,400 M^{-1} cm^{-1}), see Figure 4.36. All bands in the region 15 – 23 kcm^{-1} collapse while an intense high energy band at 32,700 cm^{-1} (ε = 25,100 M^{-1} cm^{-1}) grows in. This band has three shoulders at lower energy; 23,700 cm^{-1} (ε = 7,100 M^{-1} cm^{-1}), 25,300 cm^{-1} (ε = 9,500 M^{-1} cm^{-1}) and 27,100 cm^{-1} (ε = 11,400 M^{-1} cm^{-1}). The highest energy UV band is slightly red shifted at 36,400 cm^{-1} (ε = 32,600 M^{-1} cm^{-1}). All of these bands were assigned as combinations of $\pi \rightarrow \pi^*$ intraligand and MLCT transitions.

In $[Pt(4\text{-}NO_2\text{-}bpy)Cl_2]^{2-}$ the second reduction electron enters the same orbital (LUMO) as the first reduction electron. Therefore, transitions from the filled redox active orbital, the LUMO in the parent complex, will be present although shifted in energy from equivalent transitions in $[Pt(4\text{-}NO_2\text{-}bpy)Cl_2]^{1-}$. These transitions will be more intense as the orbital is now doubly occupied and therefore the probability of the transition occurring will be increased. Conversely, transitions from π orbitals into the LUMO will now be forbidden since the LUMO is fully occupied in the di-reduced species. Thus the band at 11.9 kcm^{-1} in $[Pt(4\text{-}NO_2\text{-}bpy)Cl_2]^{2-}$ and 10.5 kcm^{-1} in $[Pt(4\text{-}NO_2\text{-}bpy)Cl_2]^{1-}$ is assigned to an intraligand charge transfer band from the doubly and singly occupied redox orbital to a higher level antibonding π^*. On double

occupancy the band shifts to higher energy since the population of any orbital results in a decrease in the absolute energy of that particular orbital and hence the energy difference to other anti-bonding orbitals will be increased. The bands at 16.7 kcm^{-1}, 17.7 kcm^{-1}, 20.6 kcm^{-1} and 22.8 kcm^{-1} in $[Pt(4\text{-}NO_2\text{-}bpy)Cl_2]^{1-}$ all collapse on di-reduction and are therefore assigned to electronic transitions from the filled ligand based π or metal based orbitals into the singly occupied LUMO. The difficulty in making definite assignments to absorption bands is well known, but the task is made easier if there are several related compounds whose spectra can be compared as is the case here.

König and Kremer assigned the UV/vis spectrum of bpy^{2-} has having a band at *ca.* 16.4 kcm^{-1} and a second very intense peak at *ca.* 26.8 kcm^{-1}.[29] As the UV/vis/nir spectrum of $[Pt(4\text{-}NO_2\text{-}bpy)Cl_2]^{2-}$ shows no such peaks the two reduction electrons cannot be localised on the bpy part of the ligand. Thus they must either be localised on the NO_2 groups or on the 4-NO_2-py parts of the ligand as indicated by earlier epr studies on 4-NO_2-bpy^{1-}, see Section 4.2.1.3. The reductions $[Pd(4\text{-}NO_2\text{-}bpy)Cl_2]^{0/1-}$ and $[Pt(4\text{-}NO_2\text{-}bpy)Cl_2]^{0/1-/2-}$ are fully reversible because on switching the generation potential back to 0 V the original spectrum is regenerated.

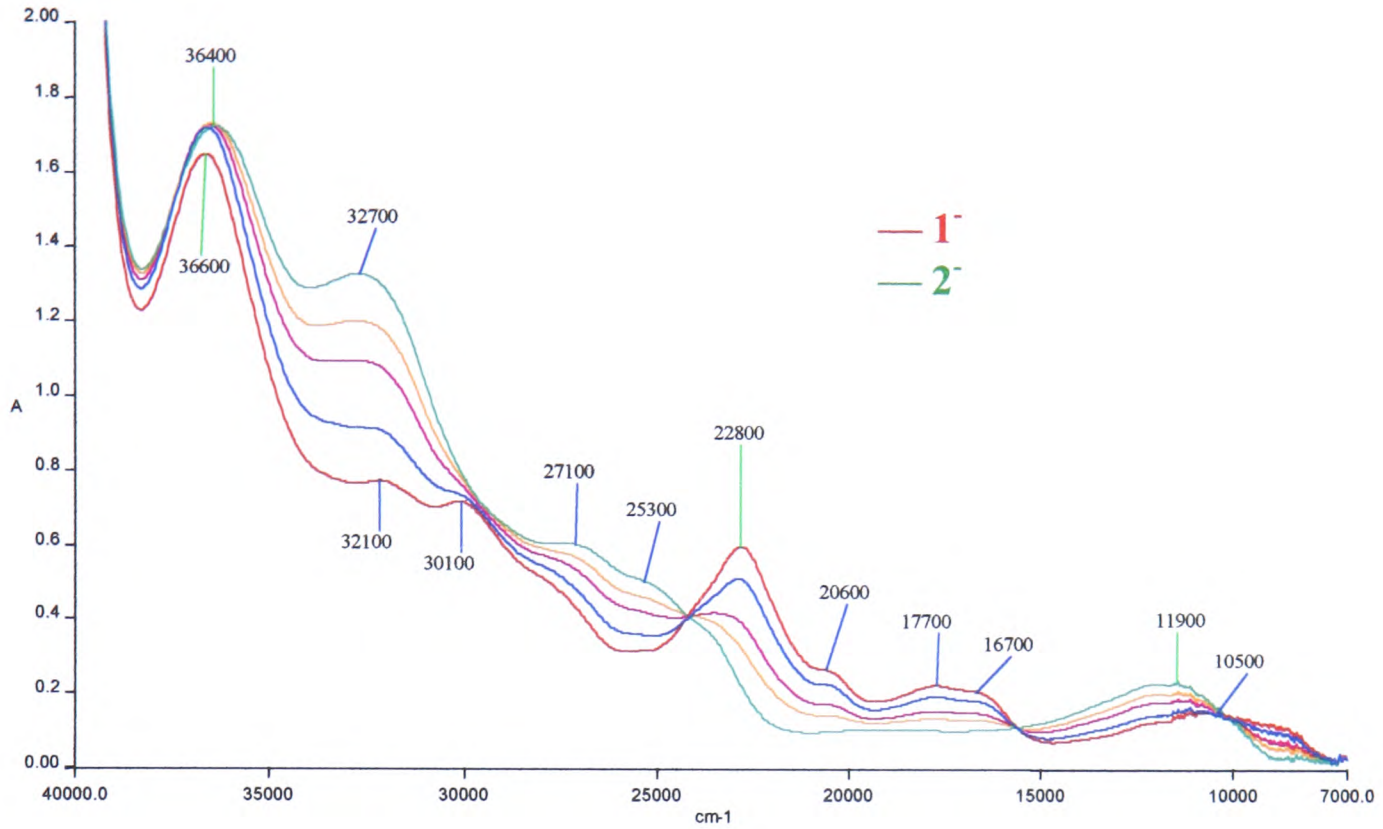

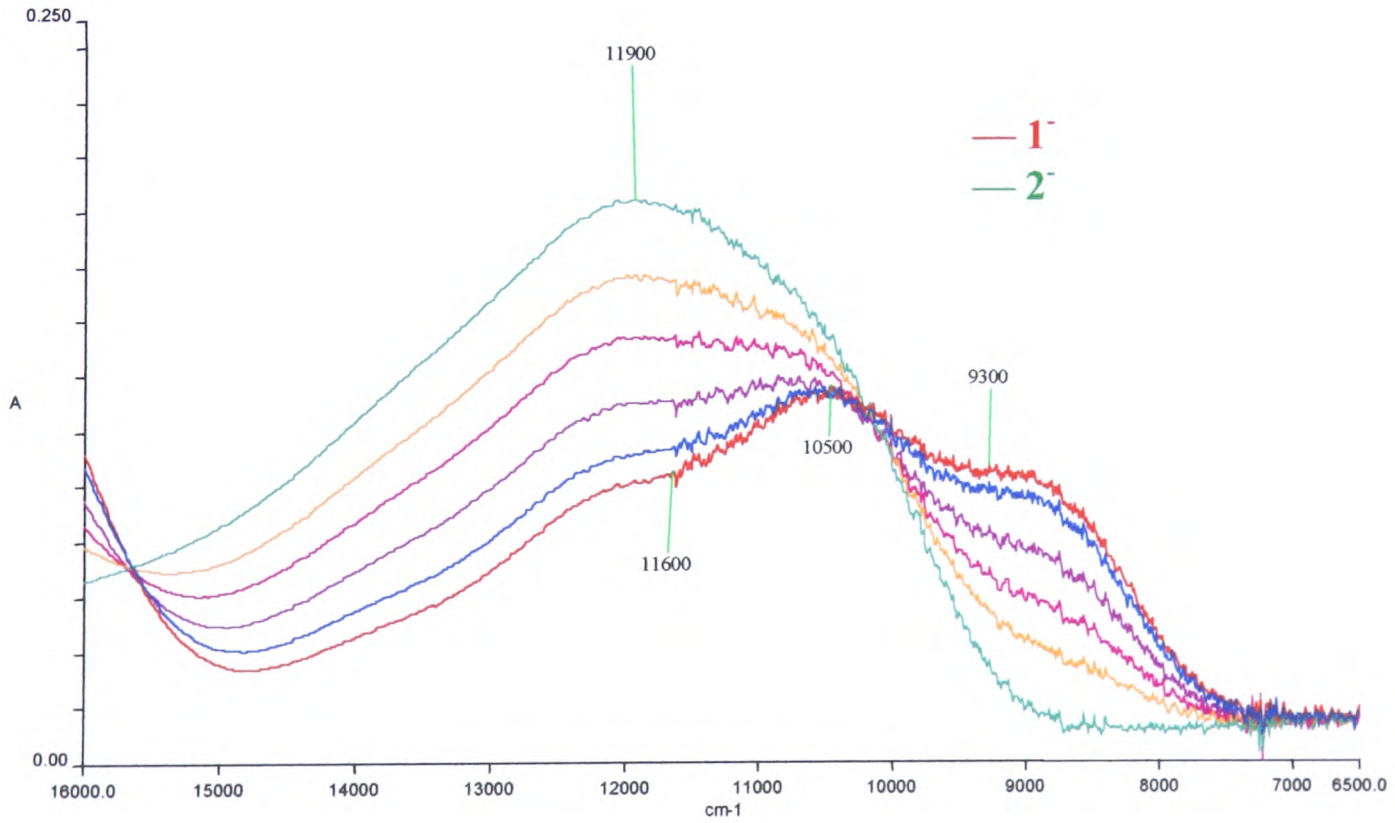

Figure 4. 36 UV/vis/nir of $[Pt(4\text{-}NO_2\text{-}bpy)Cl_2]^{1-/2}$, E_{gen} = -1.12 V, at 227 K in 0.1 M $TBABF_4$/DMF. The insert shows the nir band in greater detail.

Table 4. 5 Peak positions and molar extinction coefficients, ε, of $[Pt(4,4'\text{-}(NO_2)_2\text{-}bpy)Cl_2]^{0/1-/2-/3-}$ and $[Pd(4,4'\text{-}(NO_2)_2\text{-}bpy)Cl_2]^{0/1-/2-}$ in 0.1 M $TBABF_4$/DMF at 233K.

Oxidation state	$[Pt(4,4'\text{-}(NO_2)_2\text{-}bpy)Cl_2]$	$[Pd(4,4'\text{-}(NO_2)_2\text{-}bpy)Cl_2]$
	Peak position / cm^{-1} ($\varepsilon = M^{-1} cm^{-1}$)	**Peak position / cm^{-1} ($\varepsilon = M^{-1} cm^{-1}$)**
0	32,400 (13,300), 29,900 (12,200), 24,200 (sh) (3,500), 23,000 (4,800)	36,800 (11,000), 33,300 (9,100), 29,600 (8,800)
1^-	36,500 (sh) (11,600), 31,700 (11,300), 28,300 (9,700), 24,700 (6,500), 21,300 (5,300), 19,300 (3,700), 17,600 (3,0000, 6,800 (2,100)	36,800 (14,100), 29,900 (9,400), 19,500 (3,200), 18,100 (2,500), 7,100 (1,300)
2^-	36,200 (14,400), 33,200 (11,100), 29,500 (9,300), 23,000 (14,900), 18,700 (5,900), 9,200 (3,500)	36,500 (16,900), 28,600 (11,200), 20,300 (5,700), 19,700 (5,700), 10,200 (2,600)
3^-	36,400 (16,000), 31,900 (sh) (12,500), 23,900 (14,000), 18,400 (3,500), 11,400 (1,600)	

Table 4. 6 Peak positions and molar extinction coefficients, ε, of $[Pt(4\text{-}NO_2\text{-}bpy)Cl_2]^{0/1-/2-}$ and $[Pd(4\text{-}NO_2\text{-}bpy)Cl_2]^{0/1-}$ in 0.1 M $TBABF_4$/DMF at 227 K and 228 K respectively.

Oxidation state	$[Pt(4\text{-}NO_2\text{-}bpy)Cl_2]$	$[Pd(4\text{-}NO_2\text{-}bpy)Cl_2]$
	Peak position / cm^{-1} (ε / M^{-1} cm^{-1})	**Peak position / cm^{-1} (ε / M^{-1} cm^{-1})**
0	37,200 (20,300), 32,000 (14,200), 28,900 (sh) (7,900), 24,000 (6,600)	32,600 (16,900), 31,400 (17,600)
1^-	36,600 (29,800), 32,100 (14,600), 30,100 (13,900), 27,900 (sh) (9,800), 22,800 (11,900), 20,600 (5,400), 17,700 (4,500), 16,700 (4,200), 10,500 (3,000)	35,300 (20,600), 31,900 (sh) (10,200), 15 - 30 (3,700)
2^-	36,400 (32,600), 32,700 (25,100), 27,100 (11,400), 25,300 (9,500), 23,700 (7,100), 11, 900 (4,400)	-

Table 4. 7 Peak positions and molar extinction coefficients, ε,of $[Pt(4\text{-}NO_2\text{-}py)_2Cl_2]^{0/2-}$ and $[Pt(4\text{-}NO_2\text{-}py)_2(ox)]^{0/2-}$ in 0.1 M $TBABF_4$/DMF at 233 K.

Oxidation state	$[Pt(4\text{-}NO_2\text{-}py)_2Cl_2]$	$[Pt(4\text{-}NO_2\text{-}py)_2(ox)]$
	Peak position / cm^{-1} (ε / M^{-1} cm^{-1})	Peak position / cm^{-1} (ε / M^{-1} cm^{-1})
0	33,800 (9,700), 30,900 (8,200), 27,900 (5,600)	31,500 (7,300), 28,300 (sh) (4,100)
2^-	30,300 (15,100), 25,800 (17,800), 19,200 (11,100)	37,200 (sh) (9,100), 30,700 (8,000), 26, 000 (9,000), 19,200 (4,700)

4.2.2.3 Epr Spectroelectrochemistry

The solution epr spectra of $[Pt(4\text{-}NO_2\text{-}py)_2Cl_2]^{2-}$, $[Pd(4\text{-}NO_2\text{-}py)_2Cl_2]^{2-}$ and $[Pt(4\text{-}NO_2\text{-}py)_2(ox)]^{2-}$ are all similar, although $[Pt(4\text{-}NO_2\text{-}py)_2Cl_2]^{2-}$ was generated at 233 K in 0.3 M $TBABF_4$/DCM while the other two di-reduced complexes were electrogenerated *in situ* at 273 K in 0.1 M $TBABF_4$/DMF, see Figures 4.37 – 4.39. For clarity only the low field half of each spectrum is shown. The epr activity of these di-anionic species confirms that in all three cases the two reduction electrons are unpaired, *ie* a spin triplet species is generated. This is in line with the redox chemistry of the complexes, see Section 4.2.2.1, which indicates that each 4-NO_2-py ligand is reduced independently of the other, but at very similar potentials. Thus each reduction electron is localised on a 4-NO_2-py ligand and spin pairing of the two reduction electrons does not occur.

Good simulations of the solution epr spectra of $[Pt(4\text{-}NO_2\text{-}py)_2Cl_2]^{2-}$, $[Pd(4\text{-}NO_2\text{-}py)_2Cl_2]^{2-}$ and $[Pt(4\text{-}NO_2\text{-}py)_2(ox)]^{2-}$ can be obtained by coupling the reduction electron to two inequivalent ^{14}N nuclei, an equivalent pair of ^{1}H nuclei and to either the ^{195}Pt nucleus, (natural abundance 34 %, I = ½), or the ^{105}Pd nucleus,

(natural abundance 22 %, I = 5/2), see Table 4.8. In line with the simulation of the solution epr of 4-NO_2-py^{1-}, see Section 4.2.1.3, the two ^{14}N couplings, in each case, could not be assigned with any certainty to either the nitro group nitrogen or nitrogen on the pyridine ring. The ^{1}H pair was assigned as the hydrogens on the meta positions of the pyridine ring, as shown by the CaChe calculations on the free ligand. Thus the epr simulations indicate that in all cases, each reduction electron is localised on a 4-NO_2-py ligand with no communication between the two 4-NO_2-py moieties *ie*, spin pairing of the two reduction electrons does not occur. In the case of $[Pt(4\text{-}NO_2\text{-}py)_2Cl_2]^{2-}$ and $[Pt(4\text{-}NO_2\text{-}py)_2(ox)]^{2-}$ there is significant coupling to the ^{195}Pt nucleus. The small shift in g_{iso} from the free electron value, $g_e = 2.0023$, suggests that there is only a small admixture of metal orbital in the SOMO and that the reduction electron is therefore based on the ligand.

Table 4. 8 Solution epr parameters for $[Pt(4\text{-}NO_2\text{-}py)_2Cl_2]^{2-}$, $[Pt(4\text{-}NO_2\text{-}py)_2(ox)]^{2-}$ and $[Pd(4\text{-}NO_2\text{-}py)_2Cl_2]^{2-}$.

	$[Pt(4\text{-}NO_2\text{-}py)_2Cl_2]^{2-}$ [a]	$[Pt(4\text{-}NO_2\text{-}py)_2(ox)]^{2-}$ [b]	$[Pd(4\text{-}NO_2\text{-}py)_2Cl_2]^{2-}$ [b]
^{195}Pt / G	34.0	39.0	-
^{105}Pd / G	-	-	2.10
^{14}N / G	5.40	4.40	5.41
^{14}N / G	4.10	4.00	3.78
$2 \times {}^{1}H$ / G	2.68	2.68	2.78
g_{iso}	2.0055	2.0071	2.0059
ΔH_{pp} / G	0.70	0.70	0.52
E_{gen} / V	-0.75	-1.00	-0.70

(a) generated *in situ* at 233 K in 0.3 M $TBABF_4$/DCM, (b) generated *in situ* at 273 K in 0.1 M $TBABF_4$/DMF.

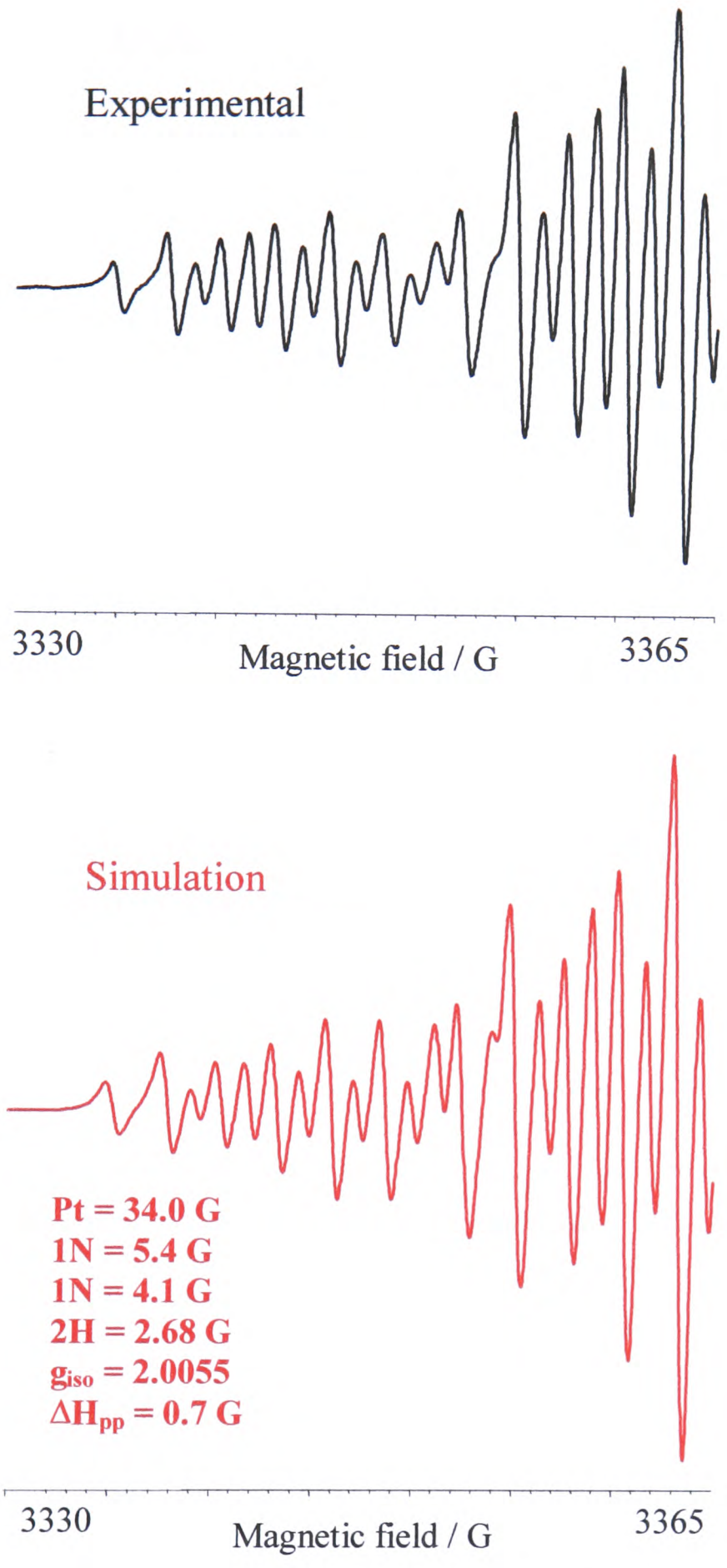

Figure 4. 37 Epr of $[Pt(4\text{-}NO_2\text{-}py)_2Cl_2]^{2-}$ generated *in situ* in 0.3 M $TBABF_4$/DCM at 233 K and E_{gen} = -0.75 V. The black spectrum is the signal obtained experimentally, the red spectrum is the simulation.

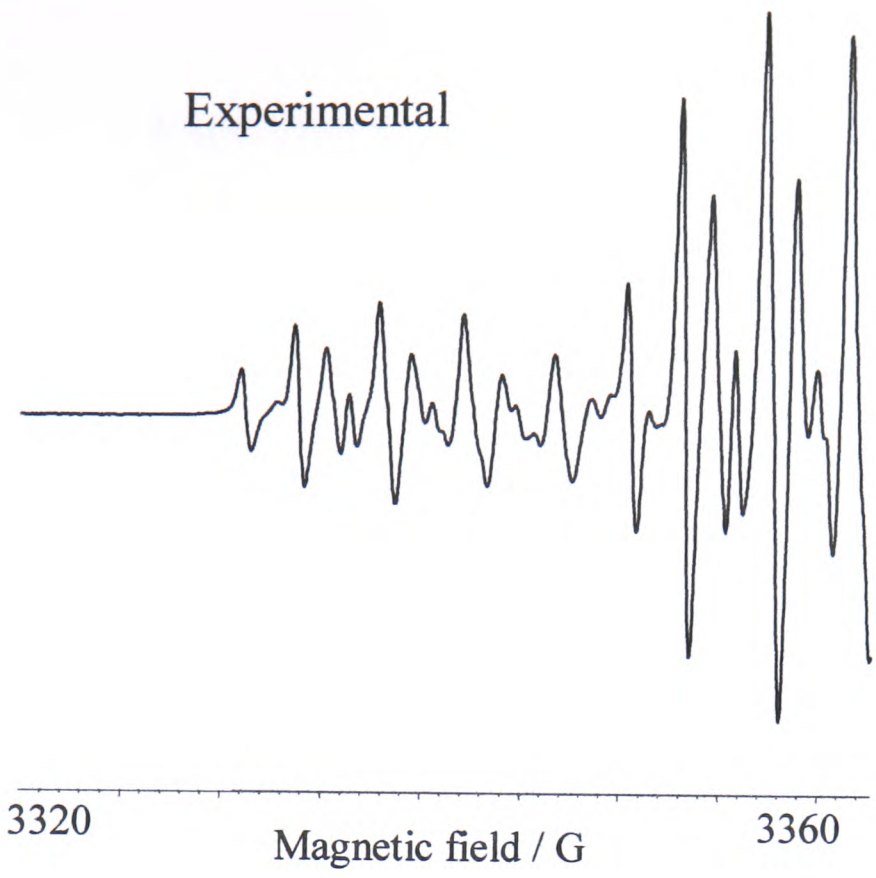

Figure 4. 38 Epr of $[Pt(4\text{-}NO_2\text{-}py)_2(ox)]^{2-}$ generated *in situ* in 0.1 M $TBABF_4$/DMF at 273 K and E_{gen} = -1.0 V. The black spectrum is the signal obtained experimentally, the red spectrum is the simulation.

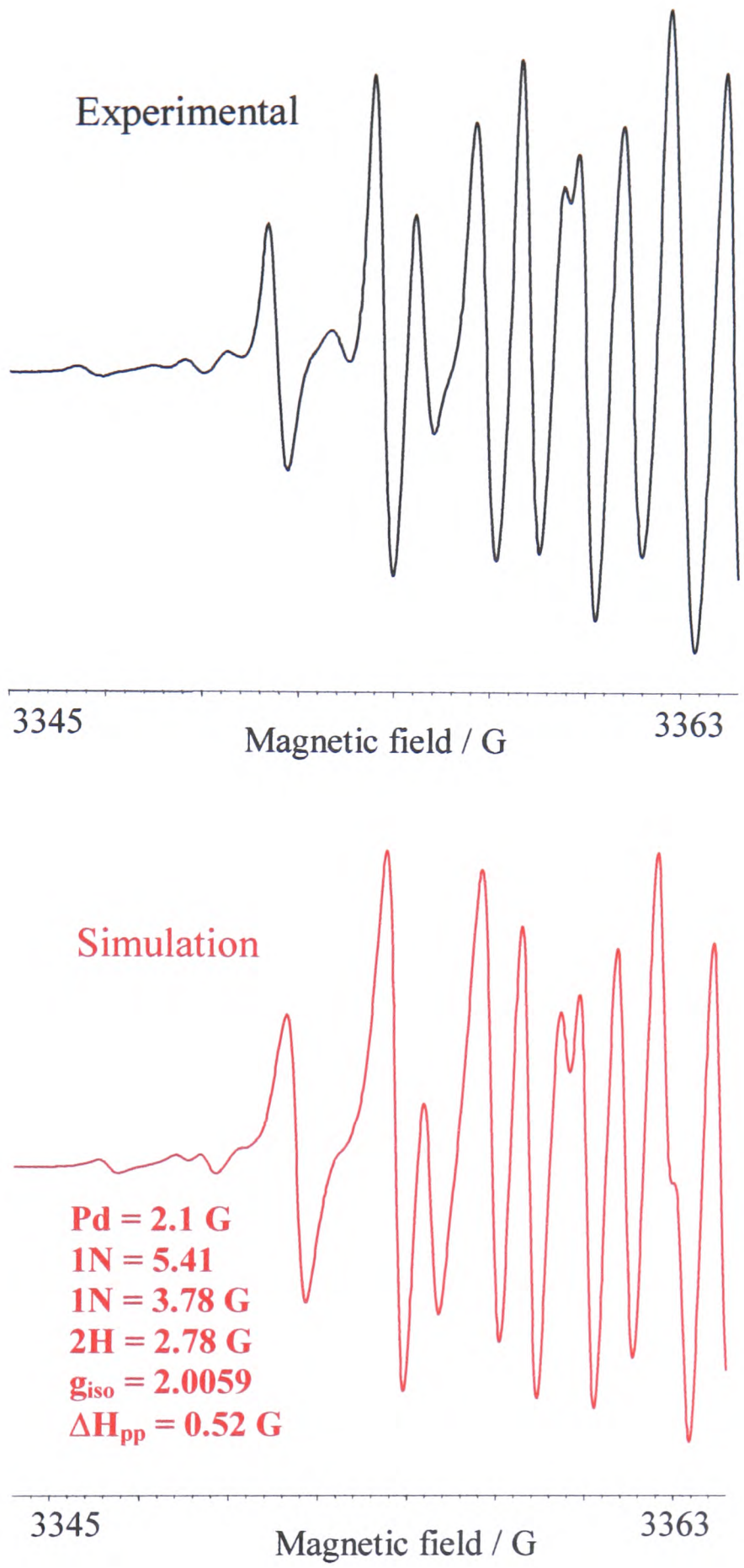

Figure 4. 39 $[Pd(4\text{-}NO_2\text{-}py)_2Cl_2]^{2-}$ generated *in situ* in 0.1 M $TBABF_4$/DMF at 273 K and E_{gen} = -0.7 V. The black spectrum is the signal obtained experimentally, the red spectrum is the simulation.

On cooling to 180 K, a rhombic X-band epr spectrum is obtained for $[Pt(4\text{-}NO_2\text{-}py)_2(ox)]^{2-}$, see Figure 4.40. Although the three g values were measured as $g_1 = 2.0132$, $g_2 = 2.0096$ and $g_3 = 1.9847$ and were in agreement with $g_{iso} = 2.0071$, the ^{195}Pt hyperfine coupling to any of the g values was unresolved. The frozen glass epr of $[Pt(4\text{-}NO_2\text{-}py)_2(ox)]^{2-}$ should be repeated on a spectrometer with a higher field in order to further separate out the signal and obtain a properly resolved rhombic spectrum. At 173 K the spectrum of frozen $[Pd(4\text{-}NO_2\text{-}py)_2Cl_2]^{2-}$ appears to be isotropic, see Figure 4.41, but on closer examination shoulders are visible on both sides of the signal suggesting that the signal may in fact be rhombic. As with the Pt oxalate analogue the frozen epr should be repeated on a Q-band spectrometer to improve the resolution of the spectrum. A frozen epr spectrum of $[Pt(4\text{-}NO_2\text{-}py)_2Cl_2]^{2-}$ could not be obtained, possibly due to the incomplete freezing of the 0.3 M $TBABF_4$/DCM solution.

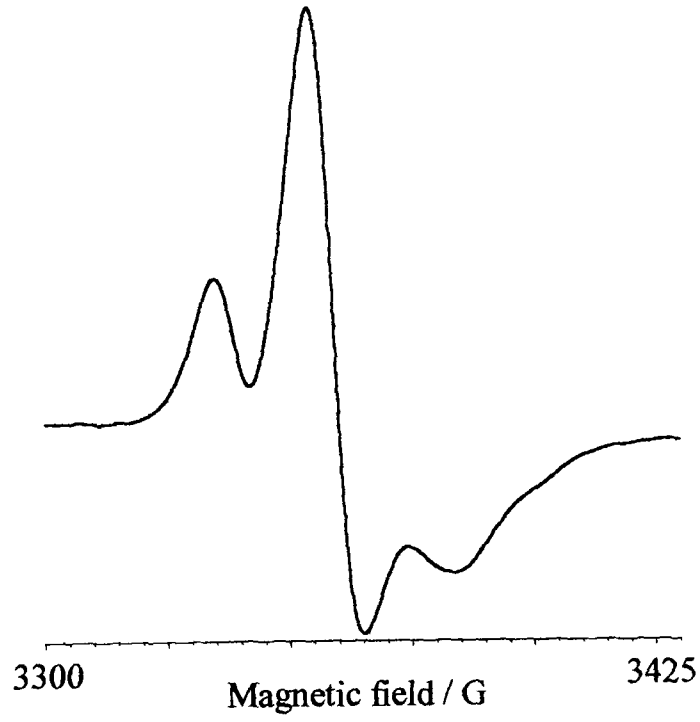

Figure 4. 40 180 K X-band epr spectrum of $[Pt(4\text{-}NO_2\text{-}py)_2(ox)]^{2-}$ in 0.1 M $TBABF_4$/DMF.

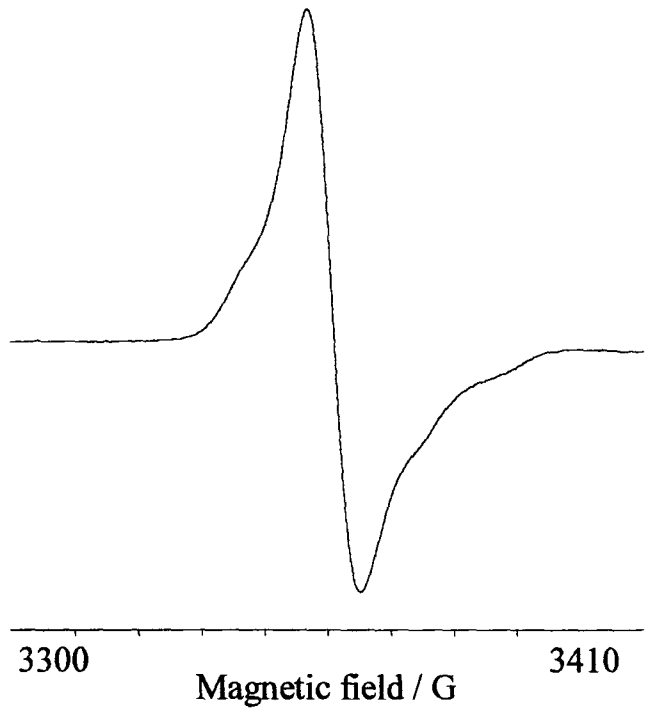

Figure 4. 41 173 K X-band epr spectrum of $[Pd(4\text{-}NO\text{-}py)_2Cl_2]^{2-}$ in 0.1 M $TBABF_4$/DMF.

The *in situ* electrochemical generation of mono-reduced $[Pt(4\text{-}NO_2\text{-}bpy)Cl_2]$ and $[Pd(4\text{-}NO_2\text{-}bpy)Cl_2]$ at 273 K in DMF gives epr active solutions. The simulations of these spectra follow the same basic pattern and assume the reduction electron is localised on the 4-NO_2-py moiety as indicated by the CaChe calculations on the free ligand. The largest ligand coupling is to a ^{14}N nucleus, followed by coupling to an equivalent pair of ^{1}H nuclei and finally to a lone ^{1}H nucleus, see Table 4.9 and Figures 4.42 and 4.43. As for the 4-NO_2-py^{1-} complexes, the ^{14}N coupling could not be accurately assigned to either the nitro group or py ring nitrogen with any certainty. The pair of equivalent hydrogens were assigned to the hydrogens on the meta positions of the nitro substituted pyridine ring and the lone ^{1}H was assigned as the hydrogen in the ortho position of the nitro substituted pyridine ring. Although the CaChe calculations on the free ligand indicate that the second ^{14}N makes a larger contribution to the LUMO than the lone proton, a better simulation is obtained if the ^{1}H nuclei is used instead of a second ^{14}N nuclei. The appearance of the two spectra differs due to the size of the coupling between the reduction electron and the metal centre. For $[Pd(4\text{-}NO_2\text{-}bpy)Cl_2]^{1-}$ coupling to the ^{105}Pd nucleus (natural abundance 22 %, I = 5/2) is not observed and consequently the spectrum is relatively simple. In contrast, for $[Pt(4\text{-}NO_2\text{-}bpy)Cl_2]^{1-}$ there is a large coupling of 35 G to the ^{195}Pt nucleus (natural abundance 34 %, I = ½), leading to a broadening of the epr signal

and a slight loss of resolution for the spectrum. The coupling constants to the 4-NO_2-bpy ligand nuclei are very similar in both cases.

Table 4. 9 Solution epr parameters for $[Pt(4\text{-}NO_2\text{-}bpy)Cl_2]^{1-}$ (in 0.1 M $TBABF_4$/DMF) and $[Pd(4\text{-}NO_2\text{-}bpy)Cl_2]^{1-}$ (in 0.5 M $TBABF_4$/DMF) generated *in situ* at 273 K.

	$[Pt(4\text{-}NO_2\text{-}bpy)Cl_2]^{1-}$	$[Pd(4\text{-}NO_2\text{-}bpy)Cl_2]^{1-}$
^{195}Pt / G	35.0	-
^{105}Pd / G	-	-
^{14}N / G	5.05	6.10
$2 \times {}^{1}H$ / G	3.50	3.15
^{1}H / G	1.80	1.7
g_{iso}	2.0054	2.0046
ΔH_{pp} / G	1.75	1.70
E_{gen} / V	-0.6	-0.7

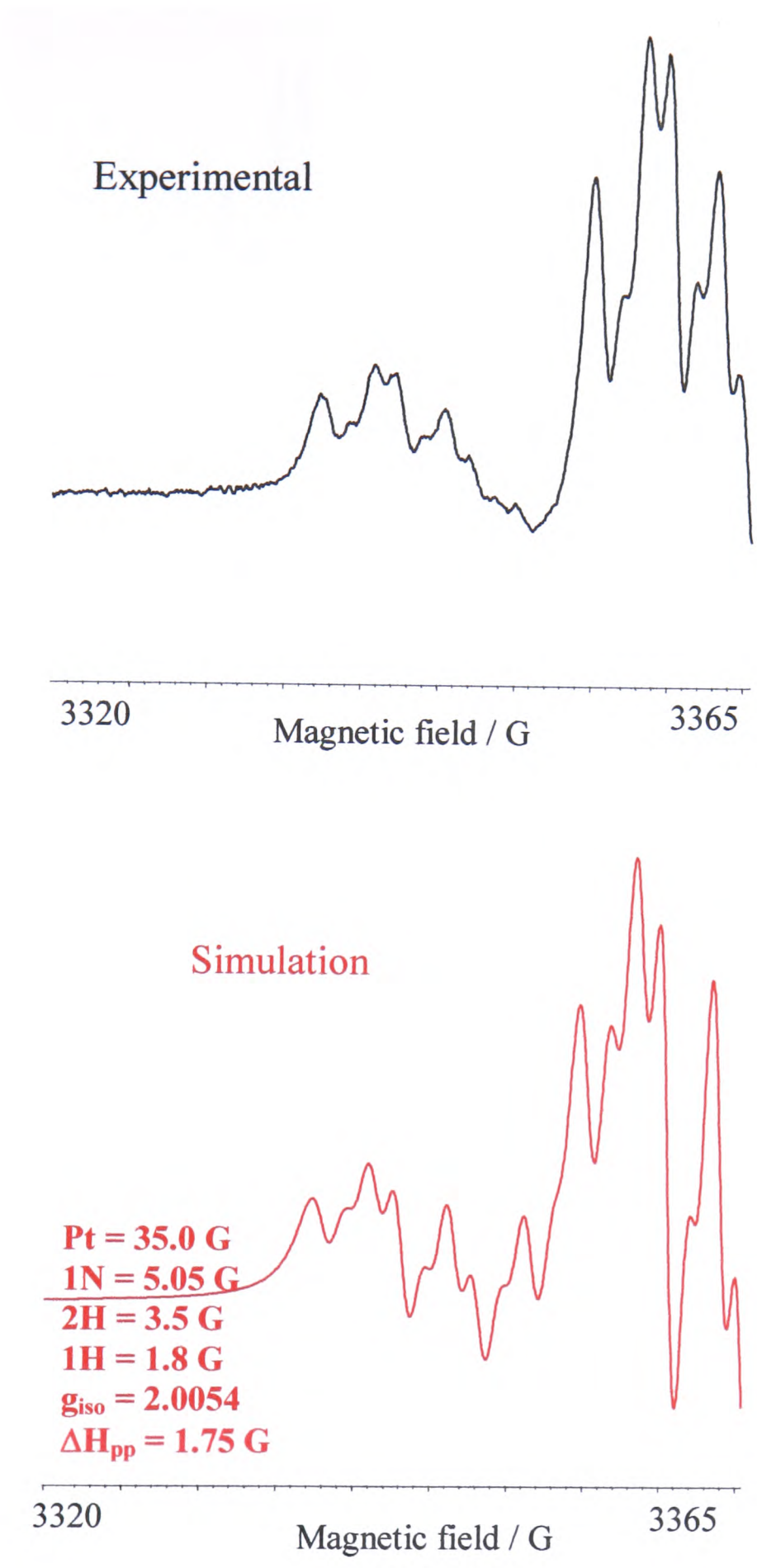

Figure 4. 42 Epr of $[Pt(4\text{-}NO_2\text{-}bpy)Cl_2]^{1-}$ generated *in situ* in 0.1 M $TBABF_4$/DMF at 273 K and E_{gen} = -0.60 V. The black spectrum is the signal obtained experimentally, the red spectrum is the simulation.

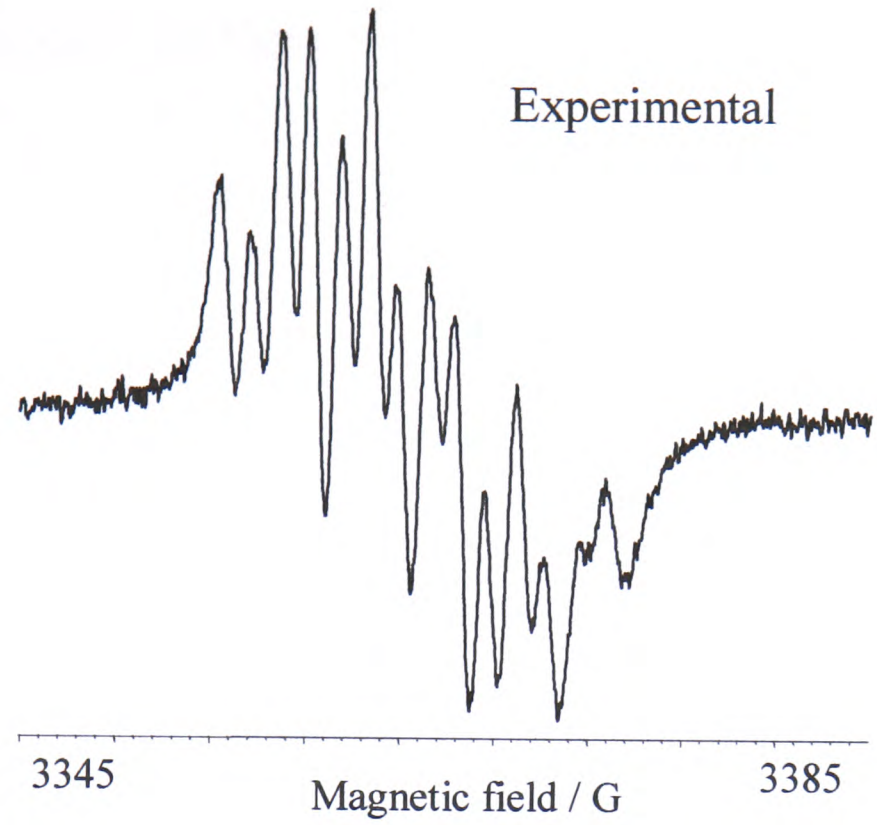

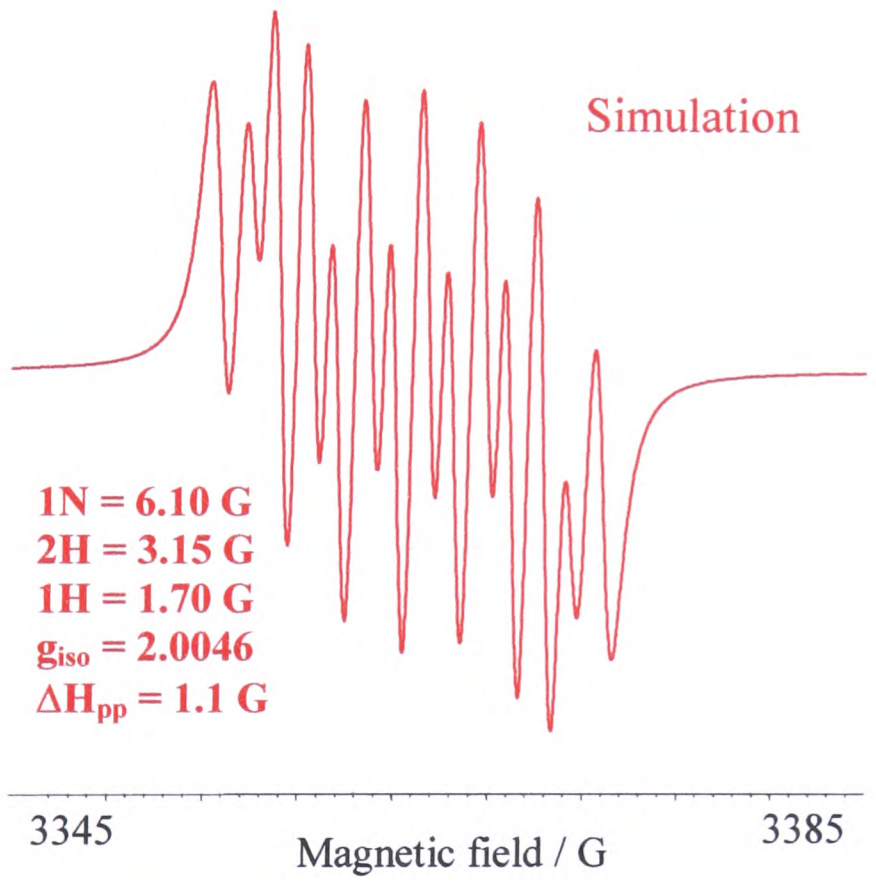

Figure 4. 43 Epr of $[Pd(4\text{-}NO_2\text{-}bpy)Cl_2]^{1-}$ generated *in situ* in 0.1 M $TBABF_4$/DMF at 273 K and E_{gen} = -0.70 V. The black spectrum is the signal obtained experimentally, the red spectrum is the simulation.

On cooling to 176 K, a rhombic X-band epr spectrum is obtained for $[Pt(4\text{-}NO_2\text{-}bpy)Cl_2]^{1-}$, see Figure 4.44. Rhombic g and ^{195}Pt hyperfine tensors are observed with $g_1 = 2.0271$, $g_2 = 2.0093$, $g_3 = 1.9852$, $A_1 = -31$ G and $A_2 = -56$ G. The average of $g_1 + g_2 + g_3$ is in good agreement with g_{iso}. Although the hyperfine splitting of the high field g_3 component (A_3), is unresolved it was estimated to be −18 G from the magnitudes of A_{iso}, A_1 and A_2 using Equation 3.2. Table 4.10 gives details of the epr parameters of $[Pt(4\text{-}NO_2\text{-}bpy)Cl_2]^{1-}$ as a frozen glass.

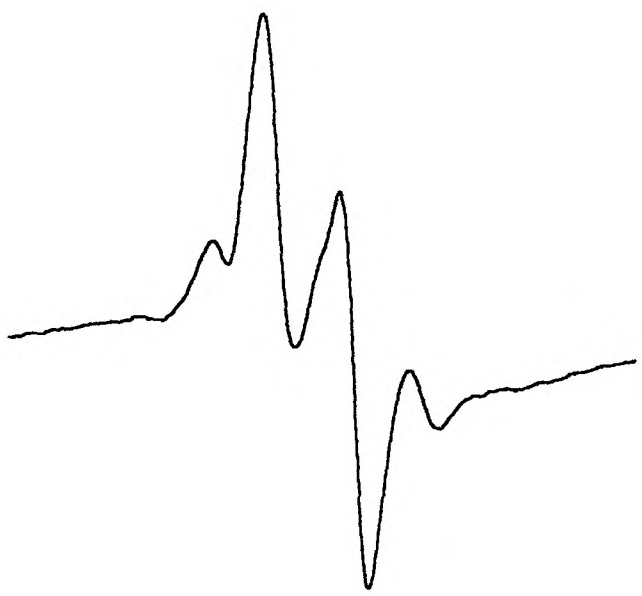

Figure 4. 44 176 K X-band epr spectrum of $[Pt(4\text{-}NO_2\text{-}bpy)Cl_2]^{1-}$ in 0.1 M $TBABF_4$/DMF.

Table 4.10 Epr parameters of $[Pt(4\text{-}NO_2\text{-}bpy)Cl_2]^{1-}$ in 0.1 M $TBABF_4$/DMF at 176 K.

	g_{iso}	g_1	g_2	g_3	A_{iso} / G	A_1 / G	A_2 / G	A_3 / G
$[Pt(4\text{-}NO_2\text{-}bpy)Cl_2]^{1-}$	2.0054	2.0271	2.0093	1.9852	-35 (-33)	-31 (-29)	-56 (-53)	-18 (-17)

(values in parentheses are A / 10^{-4} cm^{-1}).

Using equations 3.3 – 3.5 the contribution of Pt $5d_{yz}$ and $6p_z$ orbitals to the SOMO can be calculated as 5.1 % and 2.5 % respectively. The total contribution of the Pt based orbitals to the SOMO of $[Pt(4\text{-}NO_2\text{-}bpy)Cl_2]^{1-}$ is *ca.* 8 %, confirming that the reduction electron enters an orbital that is predominantly ligand based. This is due to the strong π-accepting influence of the nitro substituent.

In contrast to $[Pt(4\text{-}NO_2\text{-}bpy)Cl_2]^{1-}$, on cooling to 173 K an apparently isotropic X-band epr spectrum is observed for $[Pd(4\text{-}NO_2\text{-}bpy)Cl_2]^{1-}$, see Figure 4.45. Closer inspection reveals structure on the signal from which g tensors are measured at $g_1 = 2.0090$, $g_2 = 2.0062$ and $g_3 = 1.9901$ which average well to g_{iso}. No ^{105}Pd hyperfine splitting is observed, but this is not unexpected given that no coupling to ^{105}Pd was observed in the solution epr spectrum, see Figure 4.43. However, coupling to the nitrogen nucleus is clearly visible on the high field of the signal and was measured as $A^N = 12$ G. The assignment of this high field structure as coupling to ^{14}N rather than ^{105}Pd is in line with the frozen eprs of the related complexes $[Pd(4,4\text{-}(NO_2)_2\text{-}bpy)Cl_2]^{1-}$ and $[Rh(4,4'\text{-}(NO_2)_2\text{-}bpy)(cod)]^{0}$.[25] The frozen epr spectra of both complexes show a very similar pattern to that of $[Pd(4\text{-}NO_2\text{-}bpy)Cl_2]^{1-}$ and given that the structure is present in a complex that does not contain Pd McInnes assigns this high field structure to ^{14}N coupling.[25] Thus, while the frozen epr of $[Pd(4\text{-}NO_2\text{-}bpy)Cl_2]^{1-}$ may look like an isotropic signal, it may in fact be a rhombic signal. The frozen epr should be repeated on a Q-band spectrometer to split the signal and resolve any ^{105}Pd hyperfine coupling.

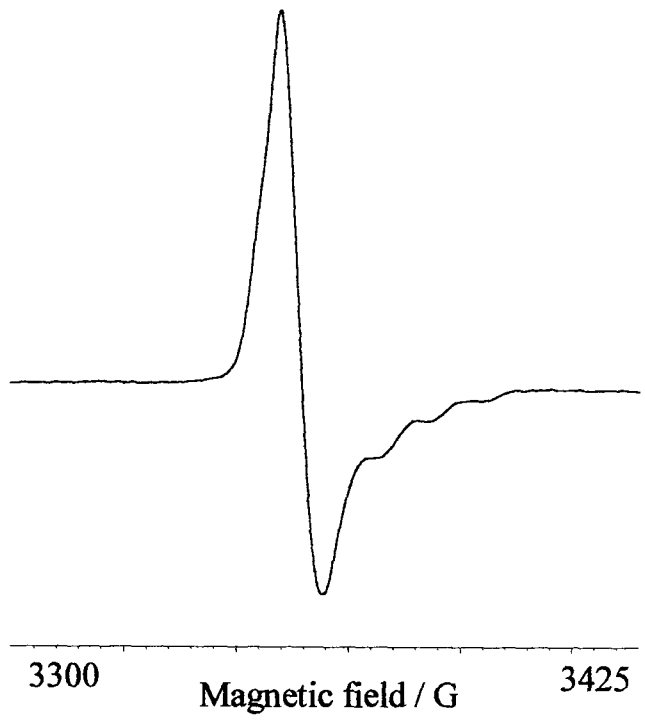

Figure 4. 45 173 K X-band epr spectrum of $[Pd(4\text{-}NO_2\text{-}bpy)Cl_2]^{1-}$ in 0.1 M $TBABF_4$/DMF.

The solution epr spectrum of $[Pt(4,4'\text{-}(NO_2)_2\text{-}bpy)Cl_2]^{1-}$ shows coupling of the reduction electron to the ^{195}Pt nucleus, with any hyperfine coupling to the ligand nuclei unresolved. An isotropic ^{195}Pt hyperfine coupling constant of A_{iso} = 40 G centred at g_{iso} = 2.0018 is observed in 0.1 M $TBABF_4$/DMF solution at room temperature, see Figure 4.46. On freezing to 173 K a rhombic X-band epr signal is observed, see Figure 4.47. Rhombic g and ^{195}Pt hyperfine tensors are measured with g_1 = 2.0325, g_2 = 2.0055, g_3 = 1.9679, A_1 = -32 G and A_2 = -76 G. Although the hyperfine ^{195}Pt coupling to the high field g_3 tensor is unresolved, it can be estimated from the values of A_1 and A_2 along with A_{iso}, using Equation 3.2. A_3 was calculated to be -12 G. Full details of the frozen epr of $[Pt(4,4'\text{-}(NO_2)_2\text{-}bpy)Cl_2]^{1-}$ are given in Table 4.11.

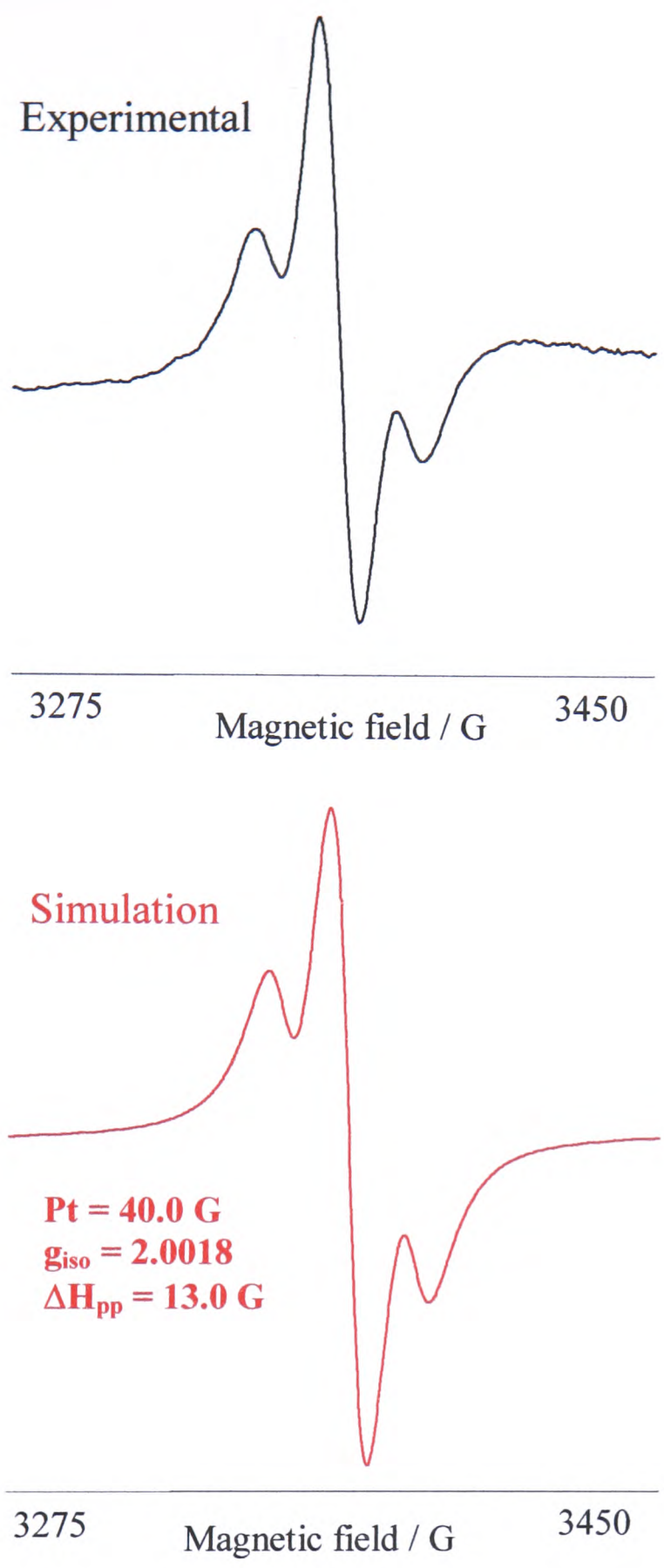

Figure 4. 46 Epr of $[Pt(4,4'\text{-}(NO_2)_2\text{-bpy})Cl_2]^{1-}$ generated *in situ* in 0.1 M $TBABF_4$/DMF at 273 K and E_{gen} = -0.42 V. The black spectrum is the signal obtained experimentally, the red spectrum is the simulation.

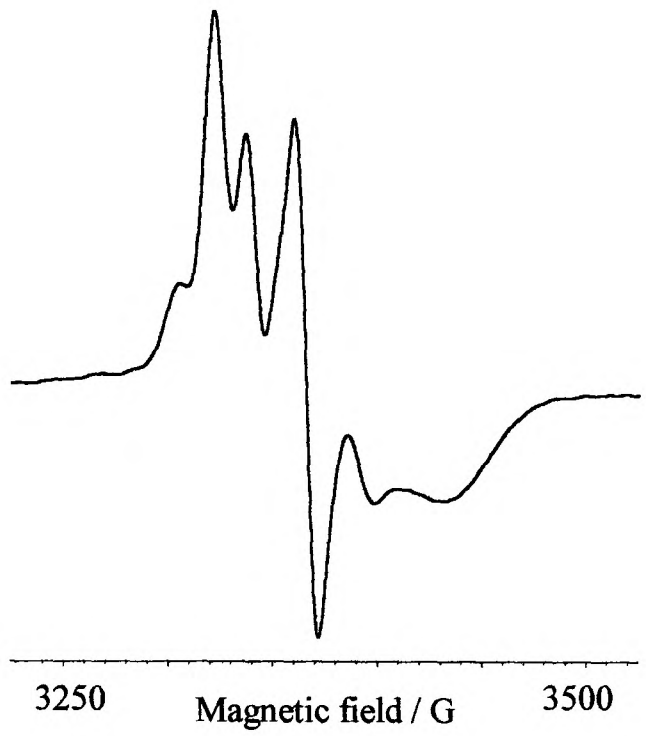

Figure 4. 47 173 K X-band epr spectrum of $[Pt(4,4'\text{-}(NO_2)_2\text{-}bpy)Cl_2]^{1-}$ in 0.5 M $TBABF_4$/DMF.

Table 4. 11 Epr parameters of $[Pt(4,4'\text{-}(NO_2)_2\text{-}bpy)Cl_2]^{1-}$ at 173 K in 0.1 M $TBABF_4$/DMF, E_{gen} –0.9 V.

	g_{iso}	g_1	g_2	g_3	A_{iso} / G	A_1 / G	A_2 / G	A_3 / G
$[Pt(4,4'\text{-}(NO_2)_2\text{-}bpy)Cl_2]^{1-}$	2.0018	2.0325	2.0055	1.9679	-40 (-33)	-32 (-31)	-76 (-72)	-12 (-11)

(values in parentheses are A / 10^{-4} cm^{-1}).

Using Equations 3.3 – 3.5 and assuming the largest A value (A_2) is A_{xx}, the contribution of Pt $5d_{yz}$ and $6p_z$ orbitals to the SOMO is calculated as 8.7 % and 3.9 % respectively. Thus the total contribution of the Pt orbitals to the SOMO is *ca.* 12.6 %. This is in agreement with previous studies by McInnes who calculated the contribution of the Pt $5d_{yz}$ orbital to the SOMO of $[Pt(4,4'\text{-}(NO_2)_2\text{-}bpy)Cl_2]^{1-}$ as 7 %.[25] This indicates that the SOMO is mainly ligand based and can be explained by the influence of the nitro groups which are strongly electron withdrawing.

On generating $[Pt(4,4'\text{-}(NO_2)_2\text{-bpy})Cl_2]^{2-}$ *in situ* the mono-anion is generated first. As the electrogeneration proceeds the signal shifts to lower field and the g_{iso} value changes from $g_{iso} = 2.0018$ for $[Pt(4,4'\text{-}(NO_2)_2\text{-bpy})Cl_2]^{1-}$ to $g_{iso} = 2.0096$ for $[Pt(4,4'\text{-}(NO_2)_2\text{-bpy})Cl_2]^{2-}$. Figure 4.48 shows the changes in the spectrum during the conversion between the mono-anion and the di-anion.

Both $[Pt(4,4'\text{-}(NO_2)_2\text{-bpy})Cl_2]^{2-}$ and $[Pd(4,4'\text{-}(NO_2)_2\text{-bpy})Cl_2]^{2-}$ can be generated *in situ* in 0.1 M $TBABF_4$/DMF at 293 K to give epr active solutions. This indicates that the two reduction electrons are unpaired *ie* a spin triplet species is generated. The best simulations are obtained by assuming coupling to two equivalent ^{14}N nuclei and to two equivalent ^{1}H nuclei as well as the relevant metal centre, see Table 4.12 and Figures 4.49 and 4.50. In the case of $[Pt(4,4'\text{-}(NO_2)_2\text{-bpy})Cl_2]^{2-}$ the spectrum can be successfully simulated by assuming coupling to ^{195}Pt (30.0 G), to a pair of equivalent ^{14}N nuclei (4.25 G) and to a pair of ^{1}H nuclei (2.55 G) with a Lorentzian line width of 0.65 G, see Figure 4.49. This is in good agreement with previous epr simulations of the complex.[25] McInnes assigned the ^{14}N coupling to the nitro group nitrogens on the basis of EHMO calculations which suggested that after the N2 and N2' superhyperfine coupling the next largest in magnitude should be N1 and N1'. However, a better simulation of the experimental spectrum was achieved using coupling to an equivalent pair of ^{14}N nuclei and an equivalent pair of ^{1}H nuclei. On the basis of this argument the ^{14}N coupling was assigned as the nitro group nitrogens. Here, as in the earlier work by McInnes, no attempt was made to assign the position of the ^{1}H nuclei.[25]

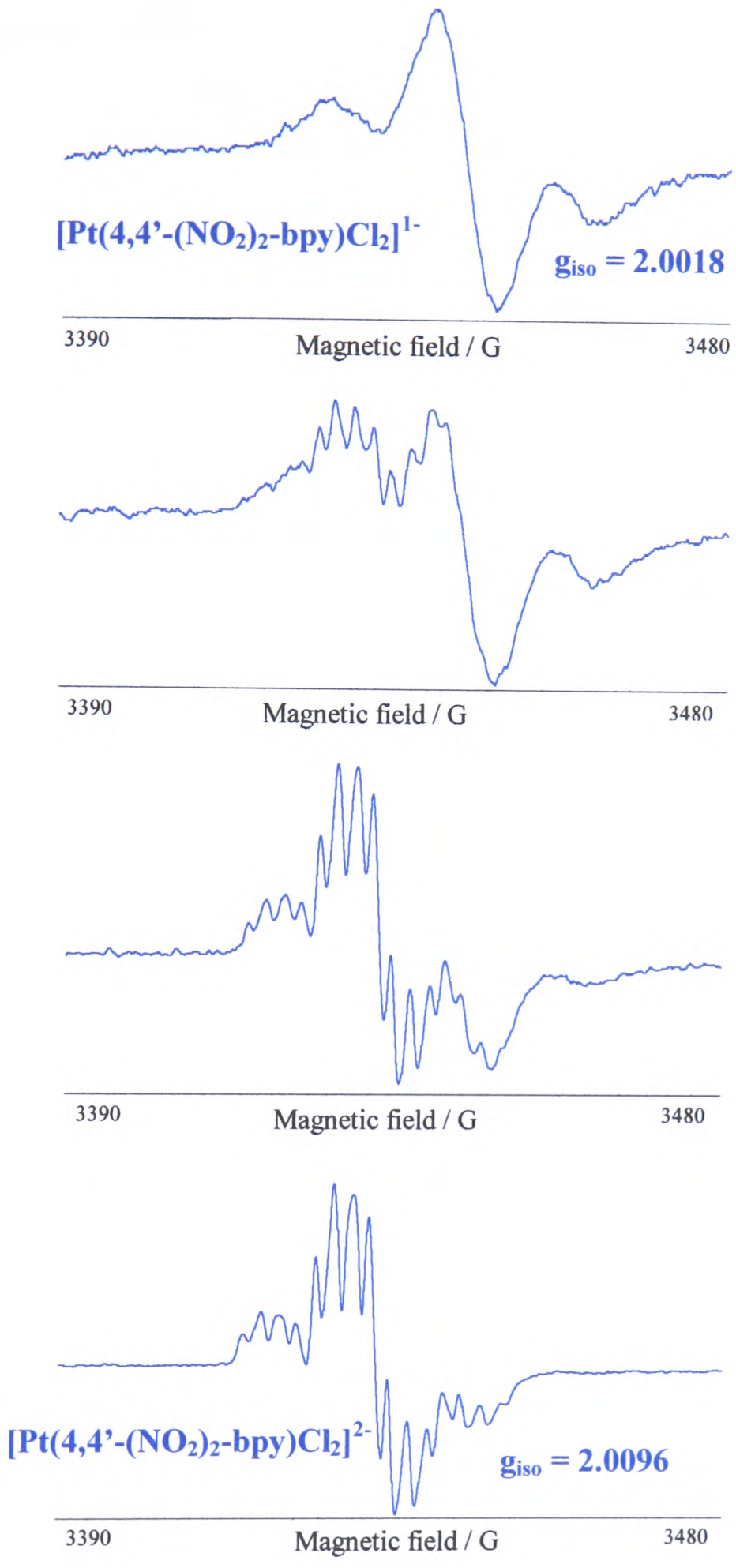

Figure 4. 48 Changes in the epr spectra as $[Pt(4,4'\text{-}(NO_2)_2\text{-}bpy)Cl_2]^{1-}$ changes to $[Pt(4,4'\text{-}(NO_2)_2\text{-}bpy)Cl_2]^{2-}$, E_{gen} = -0.9 V at 293 K in 0.1 M $TBABF_4$/DMF.

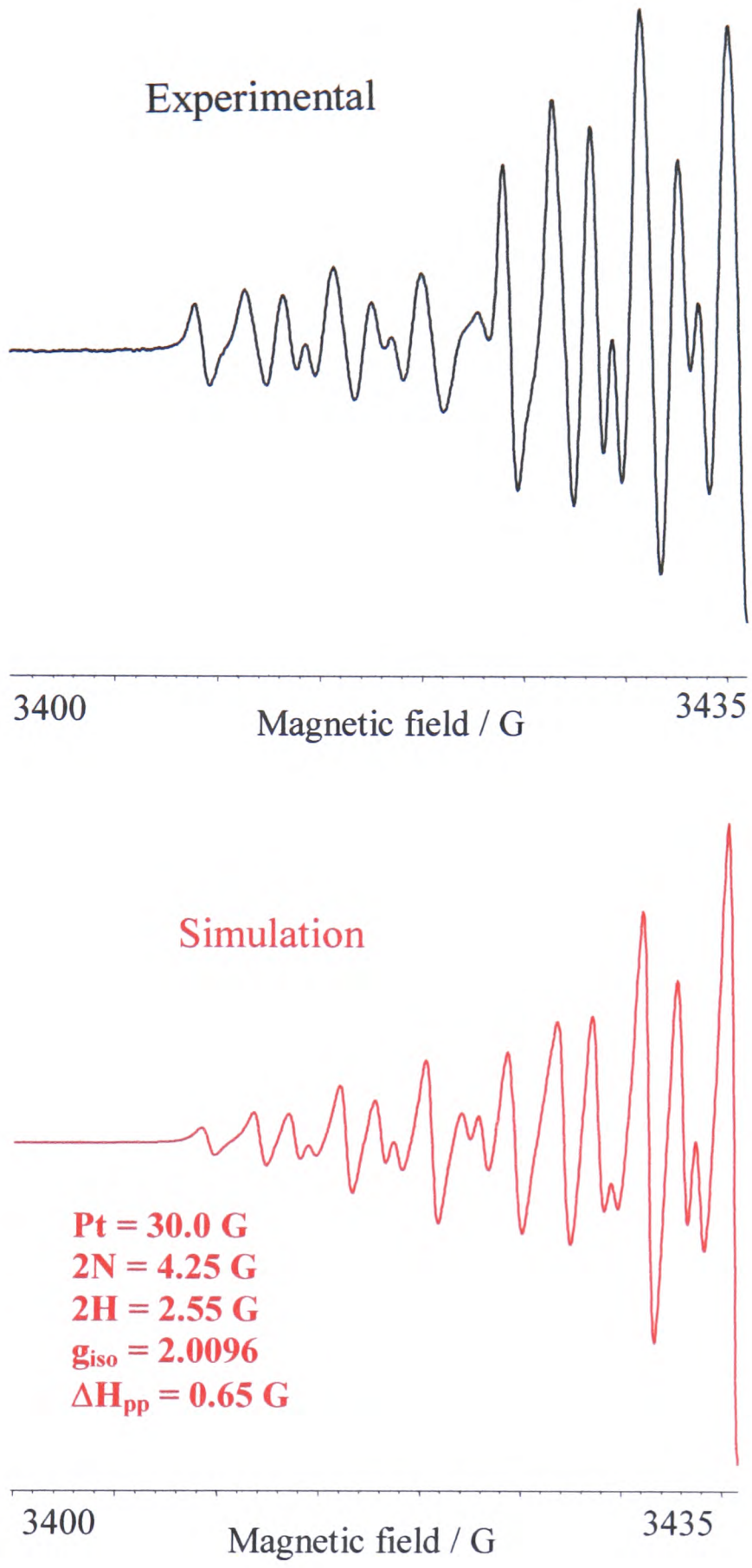

Figure 4. 49 Epr of $[Pt(4,4'\text{-}(NO_2)_2\text{-bpy})Cl_2]^{2-}$ generated *in situ* at 293 K and E_{gen} –0.9 V. The black spectrum is the simulation, the red spectrum is the simulation.

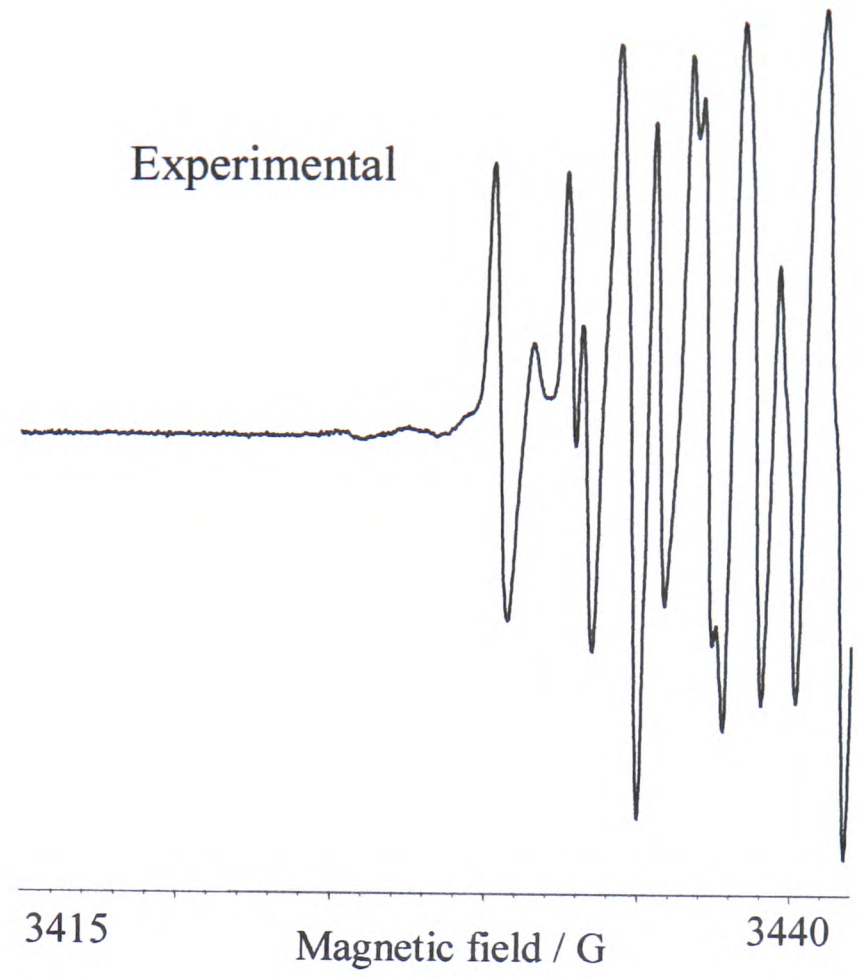

Figure 4. 50 Epr of $[Pd(4,4'\text{-}(NO_2)_2\text{-bpy})Cl_2]^{2-}$ generated *in situ* in 0.1 M $TBABF_4$/DMF at 273 K and E_{gen} = -0.65 V. The black spectrum is the signal obtained experimentally, the red spectrum is the simulation.

Table 4. 12 Epr simulation parameters of $[Pt(4,4'\text{-}(NO_2)_2\text{-}bpy)Cl_2]^{2-}$ and $[Pd(4,4'\text{-}(NO_2)_2\text{-}bpy)Cl_2]^{2-}$, generated *in situ* in 0.1 M $TBABF_4$/DMF at 293K.

	$[Pt(4,4'\text{-}(NO_2)_2\text{-}bpy)Cl_2]^{2-}$	$[Pd(4,4'\text{-}(NO_2)_2\text{-}bpy)Cl_2]^{2-}$
^{195}Pt / G	30.00	-
^{105}Pd / G	-	2.00
$2 \times {}^{14}N$ / G	4.25	4.20
$2 \times {}^{1}H$ / G	2.55	2.55
g_{iso}	2.0096	2.0069
ΔH_{pp} / G	0.65	0.45
E_{gen} / V	-0.90	-0.65

The large difference in linewidth of the solution spectra of the mono-reduced (13.0 G) and di-reduced (0.65 G) $[Pt(4,4'\text{-}(NO_2)_2\text{-}bpy)Cl_2]$ may be attributed to an "electron hopping" mechanism. In the mono-anion the reduction electron can be thermally excited to the low lying excited state (the LUMO-1 of the neutral molecule). This hopping mechanism cannot occur in the di-anion as this low-lying excited state is now occupied. Motten *et al.* proposed this mechanism to explain the difference in the observed linewidths of the solution epr spectra of $[Ru(bpy)_3]^{1+}$ and $[Ru(bpy)_3]^{1-}$.[76] Thus it would be expected that the linewidth of $[Pt(4,4'\text{-}(NO_2)_2\text{-}bpy)Cl_2]^{1-}$ is temperature dependent while that of $[Pt(4,4'\text{-}(NO_2)_2\text{-}bpy)Cl_2]^{2-}$ is not. In agreement with this theory $[Pt(4,4'\text{-}(NO_2)_2\text{-}bpy)Cl_2]^{2-}$ shows no significant variation in linewidth over the temperature range 313 K - 233 K in DMF solution. However, the effect of temperature on the linewidth of $[Pt(4,4'\text{-}(NO_2)_2\text{-}bpy)Cl_2]^{1-}$ was not studied. McInnes found no significant change in the linewidths of $[Pt(4,4'\text{-}(NO_2)_2\text{-}bpy)Cl_2]^{1-}$ or the

di-anionic species over the temperature range 293 – 213 K and attributed this to the energy gap between the orbitals being too small for the electron hopping process to be significantly retarded over the temperature range studied.[25]

On freezing to 150 K the frozen glass epr spectrum of $[Pt(4,4'\text{-}(NO_2)_2\text{-}bpy)Cl_2]^{2-}$ is a broad line showing some coupling to ^{195}Pt, see Figure 4.51. However, any hyperfine interactions were not well resolved and the spectrum should be run on a Q-band spectrometer to split the signal so that the ^{195}Pt coupling can be resolved.

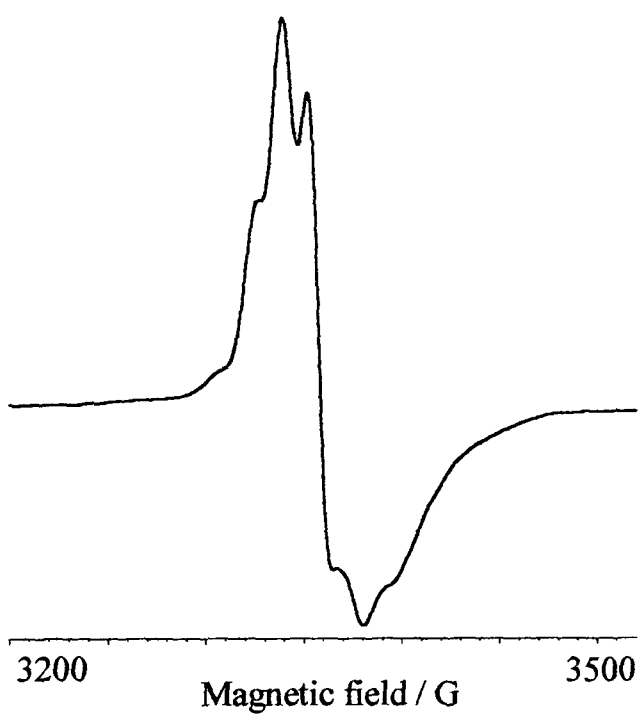

Figure 4. 51 150 K X-band epr of $[Pt(4,4'\text{-}(NO_2)_2\text{-}bpy)Cl_2]^{2-}$ in 0.5 M $TBABF_4$/DMF.

The solution epr spectrum of $[Pd(4,4'\text{-}(NO_2)_2\text{-}bpy)Cl_2]^{1-}$ at room temperature shows a broad single line at $g_{iso} = 2.0003$ (linewidth 10.6 G) with no observable ^{105}Pd hyperfine coupling (22% natural abundance, I = 5/2), see Figure 4.52. At 173 K the epr spectrum shows a broad asymmetric signal with some structure visible as a shoulder on the low field as well as some structure on the high field which may be due to coupling to ^{14}N rather than ^{105}Pd, see discussion on $[Pd(4\text{-}NO_2\text{-}bpy)Cl_2]^{1-}$ at 173 K. The spectrum should be re-run on a Q-band spectrometer to split the signal get and a more resolved spectrum.

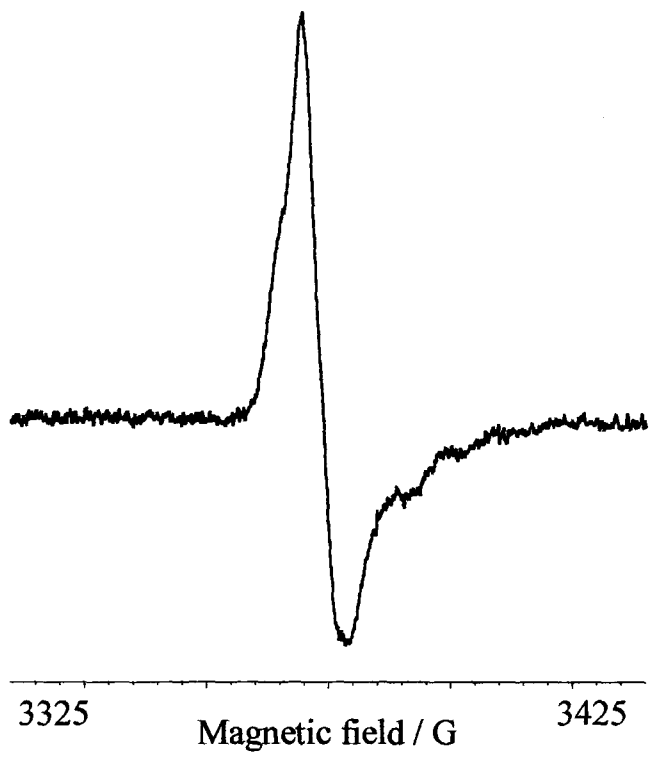

Figure 4. 52 173 K X-band epr spectrum of $[Pd(4,4'\text{-}(NO_2)_2\text{-}bpy)Cl_2]^{1-}$ in 0.5 M $TBABF_4$/DMF.

As for the Pt analogues $[Pd(4,4'\text{-}(NO_2)_2\text{-}bpy)Cl_2]^{2-}$ (0.45 G) has a much smaller intrinsic linewidth than $[Pd(4,4'\text{-}(NO_2)_2\text{-}bpy)Cl_2]^{1-}$ (~10.6 G). Again this was attributed to the electron hopping mechanism in the mono-reduced complex causing line broadening in the epr spectrum. The solution epr of $[Pd(4,4'\text{-}(NO_2)_2\text{-}bpy)Cl_2]^{2-}$ can be simulated following the same pattern as the Pt analogue by assuming coupling to two equivalent ^{14}N nuclei (4.2 G) and to two equivalent ^{1}H nuclei (2.55 G) as well as to ^{105}Pd (2.0 G) , see Figure 4.50. Although the peaks are all in the correct positions the peak intensities of the simulation differ from those in the experimental spectrum. However, $[Pd(4,4'\text{-}(NO_2)_2\text{-}bpy)Cl_2]^{2-}$ is known to decompose and the mismatch between the simulated and experimental peak intensities can be attributed to the instability of the di-reduced species. Figure 4.53 shows how the epr spectrum of $[Pd(4,4'\text{-}(NO_2)_2\text{-}bpy)Cl_2]^{2-}$ changes over time due to decomposition of $[Pd(4,4'\text{-}(NO_2)_2\text{-}bpy)Cl_2]^{2-}$. The initial spectrum a) has a basic structure consisting of 8 lines, the second of which is split into a triplet and the fifth peak also shows some splitting. After 7 hours spectrum d) is notably different. Not only has the signal

collapsed and is therefore more noisy, but the spectrum now consists of 14 lines because almost all of the original 8 lines have split. The clearest example of decomposition is the central peak, which shows no splitting in a), but has split into a triplet in d). Thus the best simulation of $[Pd(4,4'\text{-}(NO_2)_2\text{-}bpy)Cl_2]^{2-}$ is achieved using the model above *ie*. an equivalent pair of ^{14}N nuclei and an equivalent pair of ^{1}H nuclei even although this does not give a particularly good simulation of the peak intensities.

On freezing to 150 K the frozen glass epr spectrum of $[Pd(4,4'\text{-}(NO_2)_2\text{-}bpy)Cl_2]^{2-}$ is a broad asymmetric line with some fine structure on the high field, see Figure 4.54. This may be due to coupling to ^{14}N nuclei rather than to ^{105}Pd, as is the case for the frozen epr of $[Pd(4\text{-}NO_2\text{-}bpy)Cl_2]^{1-}$. Although the signal may look isotropic, it may, like $[Pd(4\text{-}NO_2\text{-}bpy)Cl_2]^{1-}$, be a rhombic signal. The frozen epr should be repeated on a Q-band spectrometer to further split the signal and resolve the ^{105}Pd hyperfine coupling.

The distribution of the LUMO in $[Pd(4,4'\text{-}(NO_2)_2\text{-}bpy)Cl_2]^{2-}$ and $[Pt(4,4'\text{-}(NO_2)_2\text{-}bpy)Cl_2]^{2-}$ is completely different to the LUMO of the free ligand. For $4,4'\text{-}(NO_2)_2\text{-}bpy^{2-}$ the two $4\text{-}NO_2$-py rings are free to rotate around the C2-C2' bond allowing the steric and electronic repulsion between the protons in the 3 and 3' positions to be minimised. Thus the CaChe calculations show that the LUMO is localised on one $4\text{-}NO_2$-py moiety and the LUMO-1 is localised on the other $4\text{-}NO_2$-py moiety. The energy gap between the LUMO and LUMO-1 is smaller than the spin pairing energy of the two reduction electrons, hence each reduction electron is confined to a separate $4\text{-}NO_2$-py half of the ligand. However, on complexation the two $4\text{-}NO_2$-py rings are forced into a planar configuration and as the two halves of the ligand are no longer orthogonal, the LUMO is delocalised over the whole $4,4'\text{-}(NO_2)_2$-bpy ligand. This is reflected in the epr simulation of $[M(4,4'\text{-}NO_2\text{-}bpy)Cl_2]^{2-}$ (M = Pt or Pd), where coupling is shown to two equivalent ^{14}N nuclei and two equivalent ^{1}H nuclei.

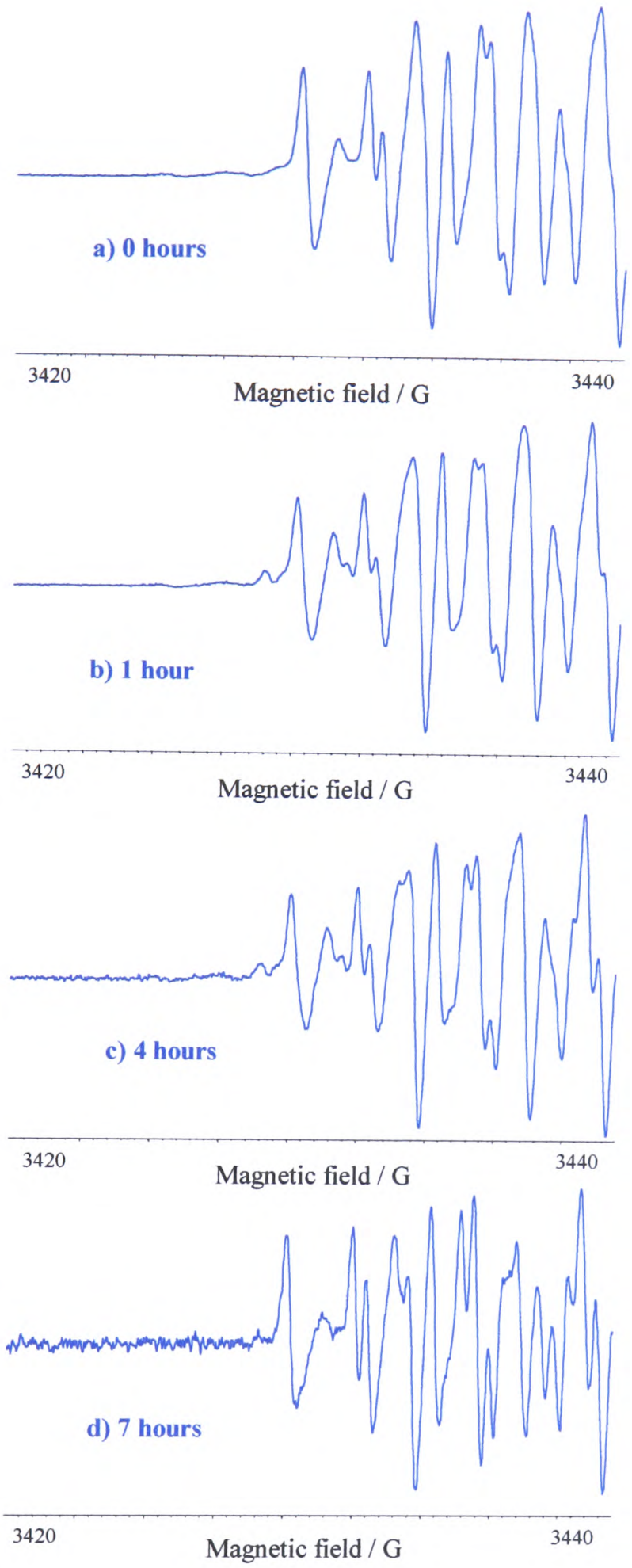

Figure 4. 53 Diagram showing how the epr signal of $[Pd(4,4'\text{-}(NO_2)_2\text{-by})Cl_2]^{2-}$ at 293 K in 0.1 M $TBABF_4$/DMF changes as it decomposes over time. Spectra a) – d) were taken at the times shown, after the initial generation of the epr active species.

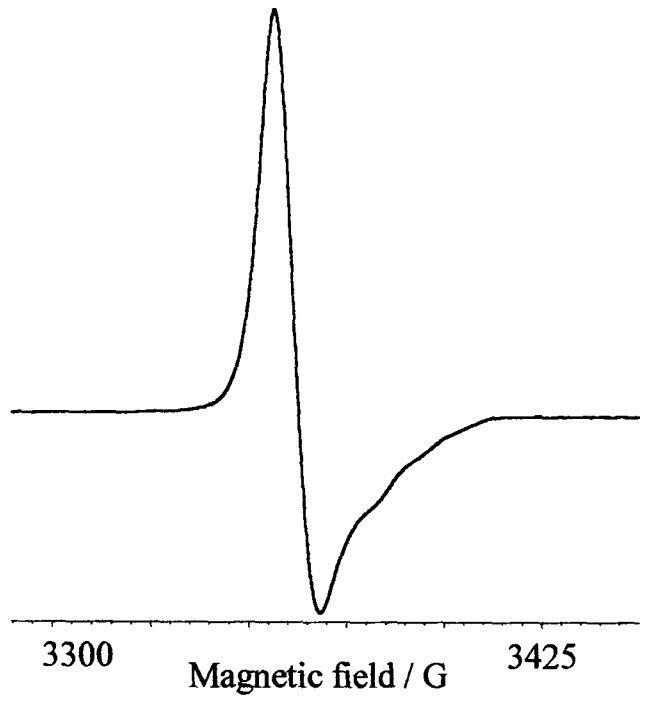

Figure 4. 54 150 K X-band per spectrum of $[Pd(4,4'\text{-}(NO_2)_2\text{-}bpy)Cl_2]^{2-}$ in 0.1 M $TBABF_4$/DMF.

4.3 Conclusions

The electrochemical behaviour of 4,4'-$(NO_2)_2$-bpy, [Pt(4,4'-$(NO_2)_2$-bpy)Cl_2] and [Pd(4,4'-$(NO_2)_2$-bpy)Cl_2] can be fully explained in terms of a molecular orbital scheme with a low lying LUMO and a small LUMO- LUMO-1 energy gap. In the free ligand the two reduction electrons are localised on the 4-NO_2-py moieties because the two 4-NO_2-py parts of the ligand are orthogonal. On complexation the 4,4'-$(NO_2)_2$-bpy ligand is forced to become planar and the reduction electrons are localised over the whole ligand. The LUMO-LUMO-1 energy gap is still smaller than the spin pairing energy. Thus the di-reduction of 4,4'-$(NO_2)_2$-bpy and the Pt and Pd complexes leads to the spin triplet species 4,4'-$(NO_2)_2$-bpy^{2-}, $[Pt(4,4'\text{-}(NO_2)_2\text{-bpy})Cl_2]^{2-}$ and $[Pd(4,4'\text{-}(NO_2)_2\text{-bpy})Cl_2]^{2-}$. A spin triplet system is predicted to have a signal at a lower magnetic field that that of the main signal ($\Delta m_s = \pm 2$). In no case was such a signal observed. The epr signal of the di-reduced species could be well simulated using a spin ½ system and therefore it may be concluded that the zero-field splitting energy must be very small for these systems.

In the case of 4-NO_2-bpy^{1-} and its complexes $[Pt(4\text{-}NO_2\text{-bpy})Cl_2]^{1-}$ and $[Pd(4\text{-}NO_2\text{-bpy})Cl_2]^{1-}$ the reduction electron is localised on the 4-NO_2-py moiety rather than delocalised over the whole ligand.

The redox chemistry of [Pt(4-NO_2-py)$_2Cl_2$], [Pd(4-NO_2-py)$_2Cl_2$] and [Pt(4-NO_2-py)$_2$(ox)] can be explained by the 4-NO_2-py ligands being reduced a very similar potentials with no communication between the ligands.

4.4 Experimental

In the synthesis of the ligands and complexes detailed below, all reagents were commercially available and used as bought unless otherwise stated.

4.4.1 Ligand Syntheses

4.4.1.1 Synthesis of 4,4'-$(NO_2)_2$-bpy

Synthesis of 2,2'-bipyridyl-N,N'-dioxide. 2,2'-bpy (10.01 g, 6.4×10^{-2} moles), hydrogen peroxide (30 %, 13 ml) and glacial acetic acid (75 ml) were heated at 70-80 °C for 3 hours.[77] Further hydrogen peroxide (30 %, 9 ml) was added and the heating continued for 15 hours. After cooling the solution to room temperature, acetone (800 ml) was slowly added, precipitating a white solid of 2,2'-bpy-N,N'-dioxide (6.185 g, 3.29×10^{-2} moles percentage yield 53.98 %). This was collected by filtration and dried under vacuum. CHN analysis of $C_{10}H_8N_2O_2$: calculated 69.75 % C, 4.68 % H, 16.27 % N; found 69.51 % C, 4.81 % H, 16.23 % N.

Synthesis of 4,4'-$(NO_2)_2$-bpy N,N'-dioxide. Nitric acid (fuming, 10 ml) was slowly added to a mixture of 2,2,'-bpy N,N' dioxide (5.007 g, 2.66×10^{-2} moles) and oleum sulfuric acid (1;2 v/v, 15 ml) in an ice bath.[77] The mixture was heated to reflux for 4 hours with the condenser fitted with a calcium chloride tube. Once cooled to room temperature the orange mixture was cautiously poured onto crushed ice to give yellow solid. This was collected, washed with water and air dried to give 4,4'-$(NO_2)_2$-bpy N,N'-dioxide (3.103 g, 1.11×10^{-2} moles, percentage yield 41.73 %).

Synthesis of 4,4'-$(NO_2)_2$-bpy. 4,4'-$(NO_2)_2$-bpy N,N'-dioxide (3.033 g , 1.082×10^{-2} moles) was heated to reflux in PCl_3 (25 ml) for 24 hours.[42] Once cooled the reaction mixture was poured into ice water. This was then basified to pH 13 with concentrated NaOH and extracted exhaustively with $CHCl_3$. The combined organic layers were dried ($NaCO_3$), filtered and evaporated to give a fine golden brown solid. After two

recrystallisations from DCM : hexane, yellow needle-like crystals of 4,4'-$(NO_2)_2$-bpy (1.007 g, 4.06×10^{-3} moles, percentage yield 37.50 %) were isolated. CHN analysis of $C_{10}H_6N_4O_4$: calculated 48.78 % C, 2.46 % H, 22.76 % N; found 48.58 % C, 2.20 % H, 23.15 % N.

4.4.1.2 Synthesis of 4-NO_2-bpy

Synthesis of 2,2'-bpy N-oxide. A solution of 2,2'-bpy (12.012 g, 7.69×10^{-2} moles) in $CHCl_3$ (43 ml) was stirred at 0 °C for 35 minutes.[42] A solution of m-chloroperbenzoic acid (15.450 g, 9×10^{-2} moles) in $CHCl_3$ (150 ml) was then added dropwise over 80 minutes. The mixture was stirred at room temperature for 13.5 hours, then washed three times with 200 ml portions of 5 % Na_2CO_3, dried ($MgSO_4$) and evaporated. To remove the unreacted 2,2'-bpy, the residual oil was extracted with boiling hexane. The extract was evaporated and the residue kept under vacuum, giving the hygroscopic solid 2,2'-bpy N-oxide (3.650 g, 2.12×10^{-2} moles, percentage yield 27.57 %)

Synthesis of 4-NO_2-bpy N-oxide. A stirred solution of 2,2'-bpy N-oxide (3.341 g, 1.94×10^{-2} moles), potassium nitrate (10.409 g, 0.1 moles) and concentrated sulfuric acid (26 ml) was heated to reflux for 23 hours.[42] The reaction was poured onto ice (50 g) and neutralised with cooling to pH 8.5 using 38.5% NaOH. The pale yellow precipitate was filtered and washed with ice water. The filtered precipitate was taken up into $CHCl_3$ (100 ml) and shaken with water. The aqueous layer was extracted exhaustively with $CHCl_3$. The combined $CHCl_3$ layers were dried ($MgSO_4$) and evaporated to yield 4-NO_2-bpy N-oxide (1.631 g, 7.51×10^{-3} moles, percentage yield 38.71 %). CHN analysis of $C_{10}H_7N_3O_3$: calculated 55.31 % C, 3.25 % H, 19.34 % N; found 56.20 % C, 3.40 % H, 19.43 % N.

Synthesis of 4-NO_2-bpy. 4-NO_2-bpy N-oxide (1.55 g, 7.14×10^{-3} moles) and PCl_3 (25 ml) were refluxed together for 21 hours.[42] The reaction was thrown into ice water (200 ml) and then worked up as described for 4,4'-$(NO_2)_2$-bpy (see 4.3.1.1). The

orange/brown crystals obtained were recrystallised from DCM: hexane to yield 4-NO_2-bpy (0.127 g, 6.31×10^{-4} moles, percentage yield 8.84 %). CHN analysis of $C_{10}H_7N_3O_2$: calculated 59.70 % C, 3.51 % H, 20.89 % N; found 59.38 % C, 3.43 % H, 20.66 % N.

4.4.1.3 Synthesis of 4-NO_2-py

The method followed was as given by Dr G. Tennant. A solution of 4-nitropyridine N-oxide (0.420 g, 3×10^{-3} moles) in anhydrous DCM (25 ml) was treated with a catalytic amount of PCl_3 (4×10^{-3} moles, 0.35 ml) and heated under reflux for 1 hour. The DCM was then evaporated off and the resulting yellow residue was treated with water (10 ml). The yellow solution was extracted exhaustively with $CHCl_3$. The combined $CHCl_3$ portions were dried ($MgSO_4$). The $CHCl_3$ was removed under vacuum, giving crude 4-NO_2-py as a yellow solid. The crude product was recrystallised from a 1:3 $CHCl_3$: hexane mixture. The resulting yellow crystals were collected by filtration, washed with hexane and dried under vacuum to give 4-NO_2-py (0.201 g, 1.62×10^{-3} moles, percentage yield 54.0 %). CHN analysis of $C_5H_4N_2O_2$: calculated 48.39 % C, 3.25 % H, 22.57 % N; found 46.96 % C, 3.04 % H, 20.78 % N.

4.4.2 Syntheses of Complexes

4.4.2.1 Synthesis of 4,4'-$(NO_2)_2$-bpy and 4-NO_2-bpy Complexes

The complexes [Pt(4,4'-$(NO_2)_2$-bpy)Cl_2], [Pd(4,4'-$(NO_2)_2$-bpy)Cl_2], [Pt(4-NO_2-bpy)Cl_2] and [Pd(4-NO_2-bpy)Cl_2] were all prepared by the following general procedure. A suspension of the appropriate ligand (1.1 equivalents) was heated under reflux, with stirring, in an aqueous solution of $K_2[PtCl_4]$ or $K_2[PdCl_4]$ (1 equivalent). The resultant precipitate was collected by filtration, washed with water, dried under vacuum and recrystallised from a saturated hot N,N'-

dimethylformamide (DMF, hplc grade) solution. Reflux times, percentage yields and analyses are given in Table 4.13 below.

Table 4. 13 Synthesis details and analyses of the Pt(II) and Pd(II) complexes of 4,4'-$(NO_2)_2$-bpy and 4-NO_2-bpy.

Complex	Reflux time / hrs	Colour	Yield / %	C / %[a] (calc)	H / %[a] (calc)	N/ %[a] (calc)
[Pt(4,4'-$(NO_2)_2$-bpy)Cl_2]	21	dark green	59.9	23.04 (23.45)	0.91 (1.18)	10.35 (10.94)
[Pd(4,4'-$(NO_2)_2$-bpy)Cl_2]	15	yellow	74.2	29.90 (33.41)	2.31 (1.68)	13.25 (15.59)
[Pt(4-NO_2-bpy)Cl_2]	5	green / brown	64.5	25.95 (25.71)	1.52 (1.51)	8.76 (9.00)
[Pd(4-NO_2-bpy)Cl_2]	5	yellow	44.2	35.59 (31.73)	2.16 (1.86)	8.70 (11.10)

a) found

4.4.2.2 Synthesis of Complexes of 4-NO_2-py

The complexes [Pt(4-NO_2-py)$_2Cl_2$] and [Pd(4-NO_2-py)$_2Cl_2$] were synthesised by the same general method. An aqueous solution of 4-NO_2-py (2.2 equivalents) was added, with stirring to an aqueous solution of either $K_2[PtCl_4]$ or $K_2[PdCl_4]$ (1 equivalent). Although a precipitate formed immediately, the reaction mixture was left to stir for 2-3 hours before the bright yellow solid was collected. The precipitate was washed with water and dried under vacuum. The complexes were not recrystallised before analysis.

The complex [Pt(4-NO_2-py)$_2$(ox)] was prepared as follows. An aqueous solution of 4-NO_2-py (2.2 equivalents) was added to an aqueous suspension of $K_2[Pt(ox)_2].2H_2O$ (1 equivalent) and heated to reflux for 5 hours. The yellow precipitate was collected by filtration, washed with water and dried under vacuum. The complex was not

recrystallised before analysis. The percentage yields and analyses obtained for the three complexes of 4-NO_2-py are given below in Table 4.14.

Synthesis of $K_2[Pt(C_2O_4)_2].2H_2O$. $K_2(C_2O_4).2H_2O$ (1.1 equivalents) was added to an aqueous solution of $K_2[PtCl_4]$ (1 equivalent) and the solution heated to 60°C for 1 hour after which another 2.5 equivalents of $K_2(C_2O_4).2H_2O$ was added. The solution was kept at 60°C for a further 24 hours. The dark green precipitate was collected by filtration and recrystallised from hot water. The solution was hot filtered and after one week fine yellow, needle like crystals were collected by filtration, washed with water and dried under vacuum to yield $K_2[Pt(C_2O_4)_2].2H_2O$ (0.046 g, 9.48×10^{-5} moles, percentage yield 19.67 %). CHN analysis of $PtK_2C_4H_4O_{10}$: calculated 9.90 % C, 0.83 % H, 0 % O; found 9.45 % C, 0.93 % H, 0 % O.

Table 4. 14 Synthesis details and analyses of the complexes [Pt(4-NO_2-py)$_2Cl_2$] and [Pd(4-NO_2-py)$_2Cl_2$] and [Pt(4-NO_2-py)$_2$(ox)].

Complex	Colour	Yield / %	C / %[a] (calc)	H / %[a] (calc)	N / %[a] (calc)
[Pt(4-NO_2-py)$_2Cl_2$]	yellow	62.21	23.56 (23.36)	1.49 (1.57)	10.52 (10.90)
[Pd(4-NO_2-py)$_2Cl_2$]	yellow	94.7	28.37 (28.23)	1.84 (1.89)	12.71 (13.17)
[Pt(4-NO_2-py)$_2$(ox)]	yellow	42.84	27.20 (27.13)	0.51 (1.52)	6.54 (10.55)

a) found

CHAPTER 5:

Pt(II) and Pd(II) Complexes of Di-2-pyridyls

Chapter 5 Pt(II) and Pd(II) Complexes of Di-2-pyridyls

Reported here is an electrochemical and spectroelectrochemical investigation of the ligands di-2-pyridyl ketone (dpk) and di-2-pyridyl amine (Hdpa). Their complexes with Pt (II) and Pd (II) were also studied.

5.1 Introduction

5.1.1 Di-2-pyridyl amine (Hdpa)

Di –2-pyridyl amine (Hdpa), first prepared by Tschitschibabin and Zeide[78] from 2-chloropyridine and 2-aminopyridine, is of considerable interest as a ligand for transition metal complexes.[79-82] The molecule shows great flexibility at the amine N atom, (the relative orientations vary over 70 °) and is able to stabilise five co-ordinate copper (II) complexes without formation of a macrocycle.[83, 84]

Di-2-pyridyl amine has a range of chemical and biochemical applications. Boron chelates of Hdpa possess antiviral activity, displaying a marked inhibitory effect on both DNA and RNA containing viruses.[85] Ni-Hdpa complexes have been shown to be efficient catalysts for achieving the electroreductive dimerisation of aromatic halides or arylation of activated olefins in pure ethanol.[86]

Hdpa is known to exhibit trimorphism. The crystal and molecular structure of the low melting polymorph (mp 357 K) was first characterised in 1973 by Johnson and Jacobson.[84] The crystals are orthorhombic and consist of pairs of molecules hydrogen bonded to one another, the dimeric unit possessing twofold crystallographic symmetry, see Figure 5.1. The geometry about the amine nitrogen is planar, the sum of the three angles about it being 359.1 °. Steric hindrance within the ligand is relieved by a twist of the two rings giving rise to a 23 ° dihedral angle between them. The hydrogen bond between the bridging N-H and the pyridine nitrogen, N(3')···H(5)-N(2), joining the two molecules is nearly linear (172 °). The distance

between the H and the receptor atom is 2.18 Å while the N3')···N(2) distance is 3.02 Å.

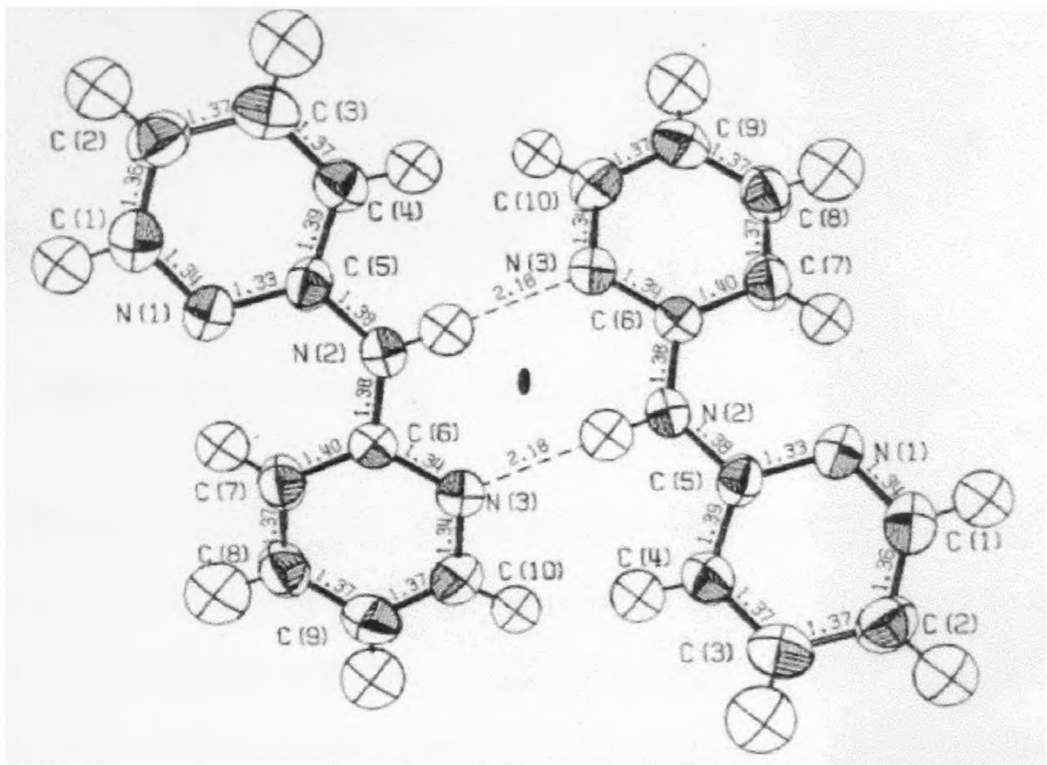

Figure 5. 1 A dimeric unit of the low melting polymorph of Hdpa, showing two-fold symmetry.[84]

These dimeric units are layered approximately perpendicular to the z direction and the distance between the layers is nearly 3.7 Å, a value typical of layered aromatic structures. Distances between dimeric units in the same layer approximate to those values expected for Van der Waals contacts.[84]

In contrast, the crystals of the high melting point polymorph (mp 372 K) are triclinic.[87] The structure consists of an asymmetric dimer of hydrogen bonded Hdpa molecules. The bond distances and angles in the individual molecules are similar to those observed in the low melting point polymorph. However, the asymmetry in the dimer is shown by the difference in the dihedral angles between the pyridyl rings (7.0 ° and 28.8 °) respectively, compared to 23 ° for the low melting polymorph. Despite the large variation in dihedral angle, all bonds to the planar bridging N atoms are short. This implies that the π orbital overlap is insensitive to the dihedral angle.[87]

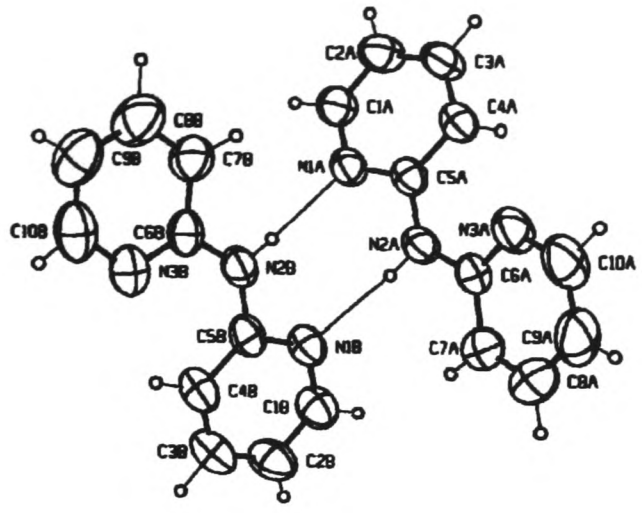

Figure 5. 2 A dimeric unit of the high melting polymorph of Hdpa.[87]

The second difference between the two structures of Hdpa lies in the arrangement of individual molecules within the hydrogen bonded dimers. Whereas the low melting polymorph is a much flatter molecule, which packs into layers of "planar" dimers, the packing in the high melting point structure is less efficient as the dimers are no longer flat enough to form layers and now form a three dimensionally interlocking structure. The dimers of the low and high temperature melting point polymorphs of Hdpa are shown in Figure 5.3 below.

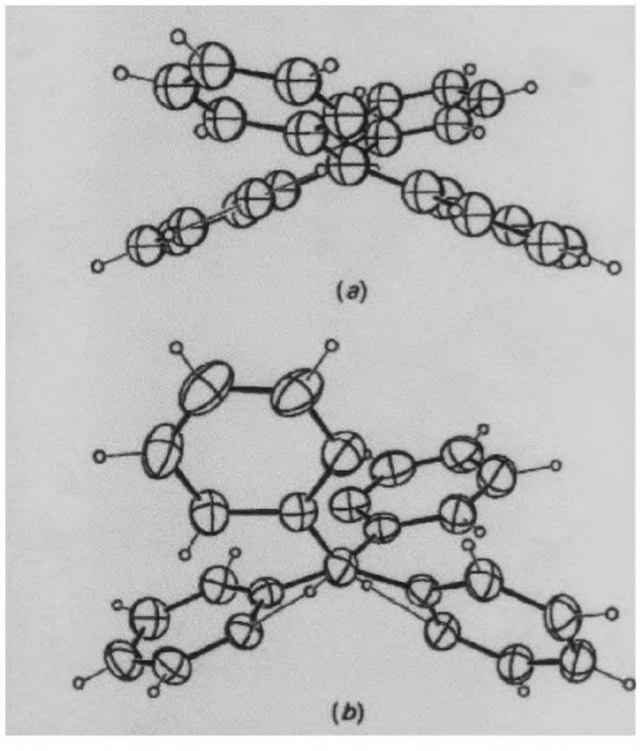

Figure 5. 3 Diagram of the a) low temperature melting point polymorph and b) the high temperature melting polymorph of Hdpa viewed down the direction of the bridge N atoms.[87]

The third polymorph of Hdpa was characterised by Schödel and co-workers.[88] In contrast to the known orthorhombic and triclinic forms, which contain hydrogen bound dimers, the molecules of the monoclinic polymorph are arranged in H-bonded tetramers with eight molecules in the unit cell, space group $P2_{1/c}$. In the structure, the planes of the central C-N(H)-C units of the hydrogen bonded dimers have a centre of inversion and are not twisted relative to each other. The N-H···N hydrogen bonds from both the additional dipyridyl amines expand the central dimer motif to a tetrameric one. The idealised molecular planes of the dipyridyl rings are oriented with angles of 80 ° close to the perpendicular with respect to the central dimer. This arrangement allows for a hydrogen bond between the central dimer and the additional Hdpa molecule, see Figure 5.4. This orientation prevents layer formation and an interlocking crystal structure results.

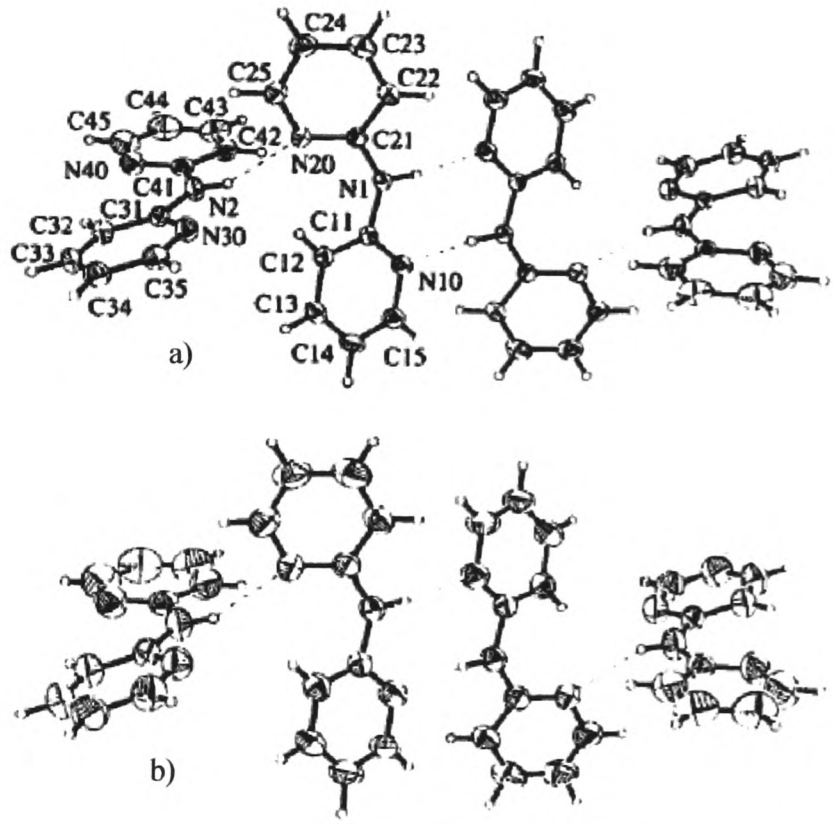

Figure 5. 4 Crystal structure of monoclinic Hpda a) at 150 K b) at room temperature.[88]

Independent of the solvent chosen, the orthorhombic form is the most stable polymorph below 270 K. The monoclinic form appears to be thermodynamically favourable in the range 270 – 310 K and above that temperature the triclinic polymorph is favoured.[88]

5.1.2 Complexes with Hdpa

Di-2-pyridyl amine is known to act as a monodentate or a chelating bidentate ligand.[79-81] The molecule can be deprotonated and the corresponding anion, $[dpa]^{1-}$, can be a chelating bidentate ligand or a bridging chain to three metal atoms, see Scheme 5.1. Under acidic conditions the ligand can form the corresponding H_2dpa^+ cation.[81]

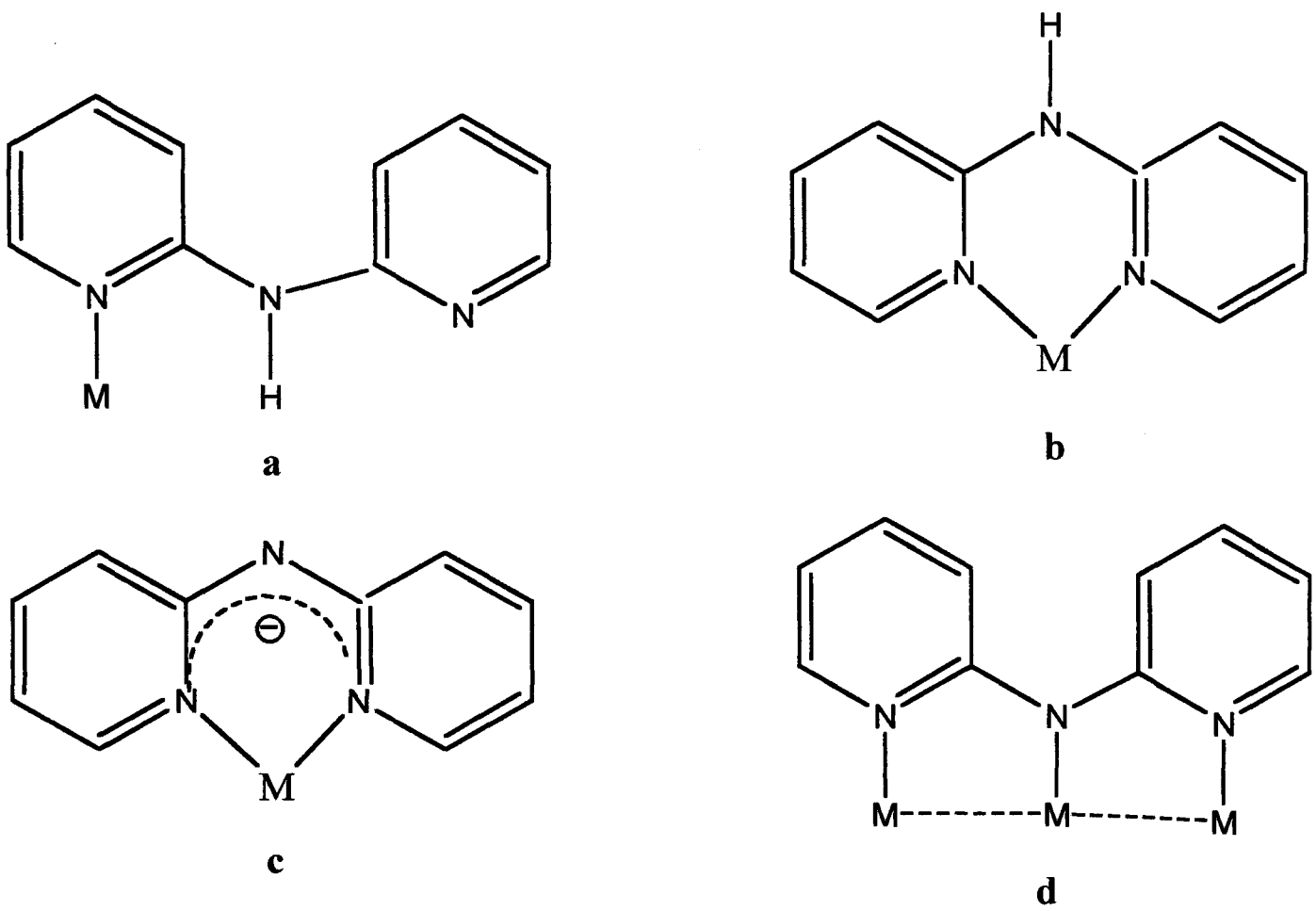

Scheme 5. 1 Representation of the binding modes of Hdpa and $[dpa]^{1-}$ to metal centres from work by Cotton *et al.*.[81]

Kumar and Tuck studied the direct electrochemical synthesis of metal complexes of di-2-pyridyl amine.[80] The electrochemical oxidation of a sacrificial metal anode in a nonaqueous solution of Hdpa under N_2 gives $M(dpa)_n$ complexes in high yield. The electrochemical process is shown below in Scheme 5.2.

$$\text{Cathode} \qquad Hdpa + e^- \rightarrow \tfrac{1}{2} H_2\,(g) + dpa^{1-}$$

$$\text{Anode} \qquad n\,dpa^{1-} + M \rightarrow M(dpa)_n + n\,e^-$$

Scheme 5. 2 Electrode processes that occur during the direct electrochemical synthesis of metal dpa complexes. Where M is Cu, Ag, Tl n = 1, where M is Zn or Cd n = 2.[80]

The compounds formed by this method have a homopolymeric structure where the amine N bonds directly to the metal centre and the N atoms of the pendant pyridyl groups form crosslinkages to other metal centres.

Very little work has been carried out on the complexes formed between Hdpa and the platinum group metals. Morris and co-workers studied the electrochemical behaviour of Ru(bpy) complexes with either Hdpa or $[dpa]^{1-}$.[79] The protonated complexes show electrochemical behaviour typifying the essentially independent functional groups of Hdpa, with an irreversible reduction at very negative potentials associated with the pyridyl π system. The oxidation of the amine function is shifted to more positive potentials on complexation due to stabilisation in the metal heterocycle. The difference observed in the protonated and deprotonated complexes indicates that deprotonation of Hdpa results in substantial changes in both structure and energy.[79]

Although the neutral complexes of $[Pt(Hdpa)Cl_2]$ and $[Pd(Hdpa)Cl_2]$[89]and $[Pd(dpa)_2]$[90] are known, only one study into the electrochemical and spectroelectrochemical behaviour of $[Pt(Hdpa)Cl_2]$ could be found.[91] Anbalagan and co-workers assign the irreversible oxidation at 1.7 V to oxidation of the NH proton and the irreversible reduction at –0.9 V as being metal centred.[91]

5.1.3 Di-2-pyridyl ketone (dpk)

Dpk is used as a complexing ligand for spectrophotomeric determination of numerous metal cations.[92-93] Cu(I) complexes of dpk are efficient photocatalysts for the conversion of norbornadiene to quadricyclane,[94] the reaction being of considerable interest as a solar energy storage process.

Free dpk is twisted due to the lone pairs on nitrogen and oxygen and exhibits tremendous structural differences on single and double protonation.[95] In aqueous solution, dpk remains unprotonated above pH = 5, provided no metal cations are present. The ligand is singly protonated only when pH = 0 and diprotonated, *ie* in the geminal diol form (dpk.H_2O), below pH = -5, see Scheme 5.3 below.

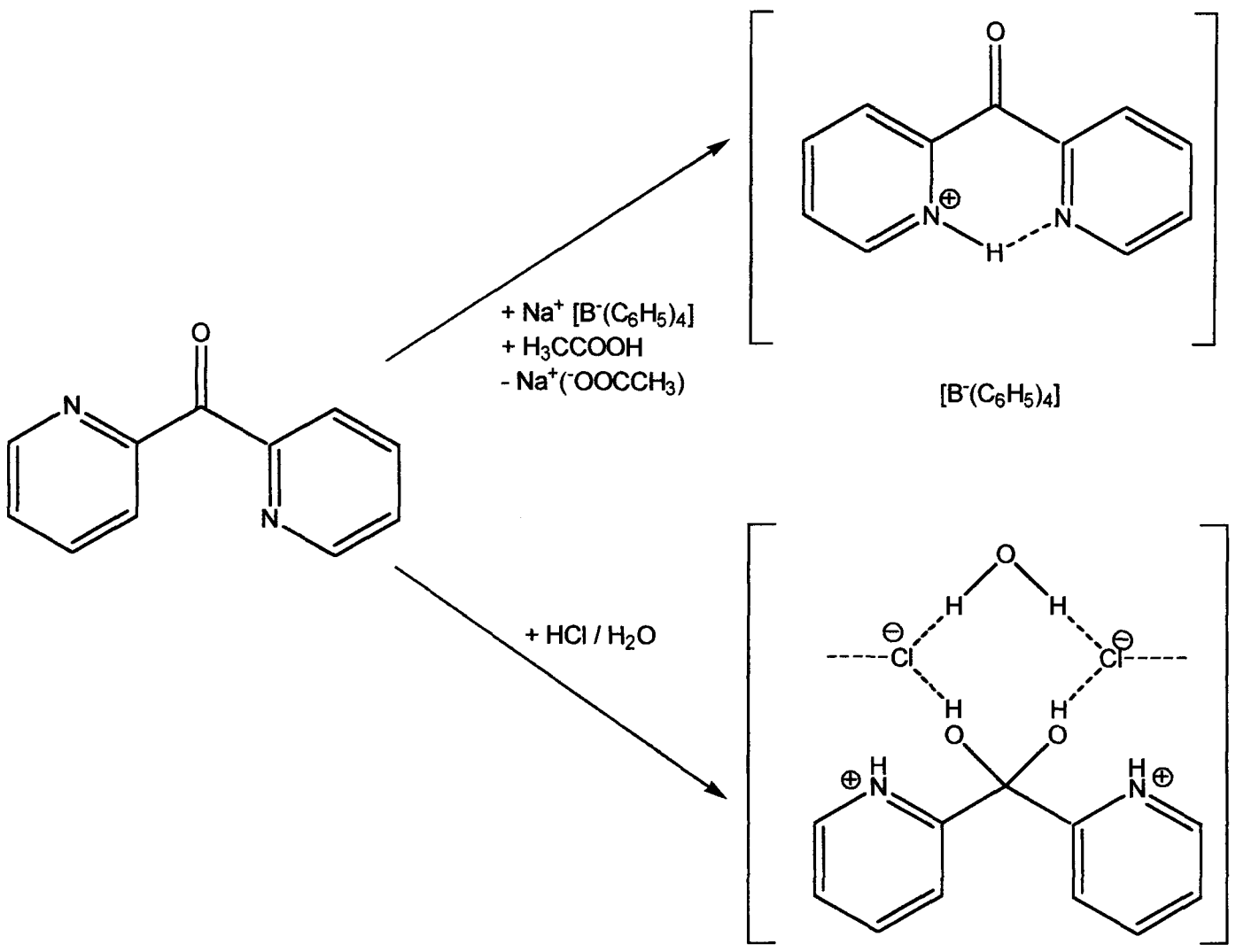

Scheme 5. 3 Reactions of dpk from Bock *et al.*.[95]

The molecular structure lacks any symmetry, the planar pyridine rings are twisted differently round the planar ketone subunit C-C(O)-C by torsional angles of 41 ° for ring I and –163 ° for ring II. The planes of rings I and II are twisted relative to each other by 56 ° and their N centres approach an *anti* configuration which avoids repulsive interaction between the N electron pair on ring II and the in-plane electron density around the centre O.[95]

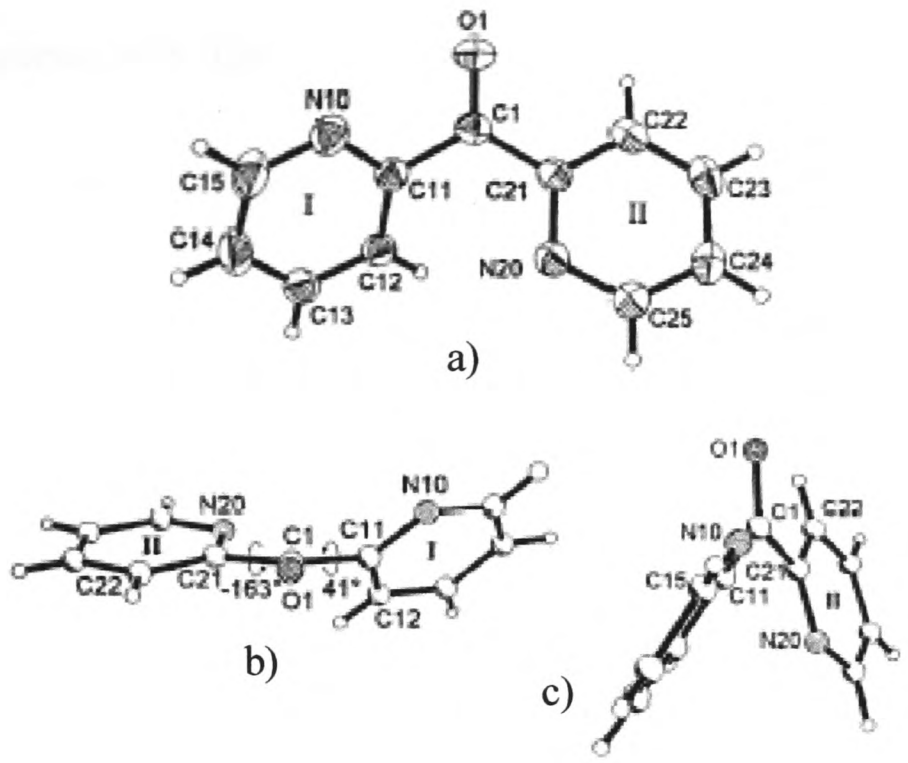

Figure 5. 5 Structures of dpk a) molecular structure (50% thermal ellipsoids) and numbering. b) showing the torsional angles. c) the planes of the rings are twisted relative to each other by 56°.[95]

Dpk crystallises from benzene solutions in the monoclinic form, space group $P2_{1/n}$, with the molecules being arranged in a herringbone pattern in the crystallographic *x*, *y* plane. There are 4 molecules per unit cell. The packing does not reveal significant intermolecular interactions.[95]

In the mono-cation, generated in acetic acid by the addition of sodium tetraphenylborate, an intramolecular hydrogen bond forms between one protonated N and the other pyridine ring N, causing the pyridine rings to become planar. In contrast, aqueous HCl produces a di-cation with both N centres protonated and the geminal diol is formed, see Scheme 5.3. The resulting hydrate is embedded in a complex hydrogen-bonded network. The central C is almost tetrahedral and the pyridine rings are each twisted by 85 ° relative to the angle halving line O-C-O.[95]

5.1.4 Complexes with dpk

Unlike Hdpa a number of studies have been carried out on dpk complexes with platinum group metals.[89-90, 92] Sommerer and Abboud report the unusual structure of [Pt(dpk.H_2O)$_2$] dichloride tetrahydrate.[96] The Pt(II) hydrate is co-ordinated by four N-atoms from the two (dpk.H_2O) ligands and two additional long range O-atom interactions resulting in pseudo-octahedral geometry instead of the more usual square planar geometry observed for Pt(II) complexes. This formation of a six-membered chelate in a boat-like conformation, together with the long range off-axial interactions between Pt and O in the apical positions of the complex contribute to the stability of the hydrated species.[96]

A study by Annibale and co-workers on the chemical behaviour of dpk on interaction with Pt(II), Pd(II) and Au(III) further confirms the stability of Pt(II) dpk complexes.[97] When co-ordinated to metal ions, dpk easily undergoes addition of various nucleophiles (HX), including water, at the carbon atom of the carbonyl group to produce the corresponding condensation product $(C_5H_4N)_2C(OH)X$. In solution, all species undergo either addition or release of protic molecules depending on HX (X = OH, OMe, OEt) concentration. The rates of reversible hydrolysis and the stability of the hydrated species increase going from Pt(II) > Pd(II) > Au(III), thus paralleling both the electron withdrawing properties of the metal cation and their ability to fill the apical position of a tetragonal-pyramidal co-ordination shell.[97]

Only [Pt(dpk)Cl_2] could be isolated in the solid state with the ligand still in its original keto form. However, different absorption spectra are obtained depending on whether the compound is dissolved in an aprotic, (eg MeCN etc), or a protic, (H_2O, MeOH, etc) solvent. This is a clear indication that the reversible uptake of a protic molecule is occurring. In the case of platinum the equilibrium is shifted in favour of the keto form. Even in a 50 % v/v water acetone mixture both species are present in comparable concentration.

For gold complexes the equilibrium between the keto and hydrated form of dpk (dpk.H_2O), lies well in favour of the hydrated form. A 0.1 % v/v of water in acetonitrile is enough to move the equilibrium completely in favour of the hydrated form.[97]

Pd(II) complexes occupy the middle ground between Pt(II) and Au(III) as both [Pd(dpk.H_2O)Cl_2] and [Pd(dpk)Cl_2] are readily isolated in the solid state depending on whether synthesis was carried out in protic or aprotic solvent. Both [Pd(dpk.H_2O)Cl_2] and [Pd(dpk)Cl_2] give similar absorption spectra in protic solvents. Their spectra in aprotic solvents are also similar but different from the spectra in protic solvents. Small amounts of water added to the complex in the aprotic solvent give intermediate spectra between [Pd(dpk)Cl_2] and [Pd(dpk.H_2O)Cl_2] indicating that a reversible uptake of a protic molecule HX occurs in solution.[97] Conversion of the hydrated Pd complex into the keto complex is described in Section 5.3.1.2. Spectrophotomeric experiments show that dpk always reacts with the metal ion to give the complex in its keto form which then reacts with HX to give the hydrated species.[97]

Such addition products of ketones are generally unstable and exist only when the carbonyl group is flanked by strong electron-withdrawing groups.[97] The unusual behaviour of Pt(II), Pd(II) and Au(III) complexes of dpk is explained by the formation of a 6-membered chelate in the boat conformation which destroys the co-planarity of the ligand and the conjugation over the carbonyl group, facilitating the hydration of the keto group. An additional driving force for the metal-promoted hydration may arise from the interaction of the hydroxy or the X group of C(OH)X with the central metal ion.[97]

5.2 Results and Discussion

5.2.1 Di-2-pyridyl ketone (dpk)

The cyclic voltammogram of dpk in 0.1 M $TBABF_4$/DMF at 293 K is shown in Figure 5.6 and indicates a reversible reduction at -1.37 V, (0.086). The reduction is electrochemically reversible as indicated by the linear i_p versus $\nu_{1/2}$ response. At 86 mV the separation between E_{pc} and E_{pa} is slightly larger than the 59 mV expected and may indicate there is a change in the geometry of the ligand as it undergoes reduction. The number of electrons involved in the reduction process could not be accurately determined using bulk electrolysis. This may be due to the conversion of the dpk into an intermediate that does not display redox activity. There are many examples in the literature of ketones being chemically reduced by reaction with sodium borohydride.[98-100] Dpk is known to undergo structural changes on single and double protonation.[95] In the mono-cation, the pyridine rings of dpk are planarized due to protonation between the two pyridine ring nitrogen atoms, see Scheme 5.3. In aqueous hydrogen chloride, a di-cation with both pyridine nitrogens protonated is produced. The ligand is now in its geminal diol form.[95]

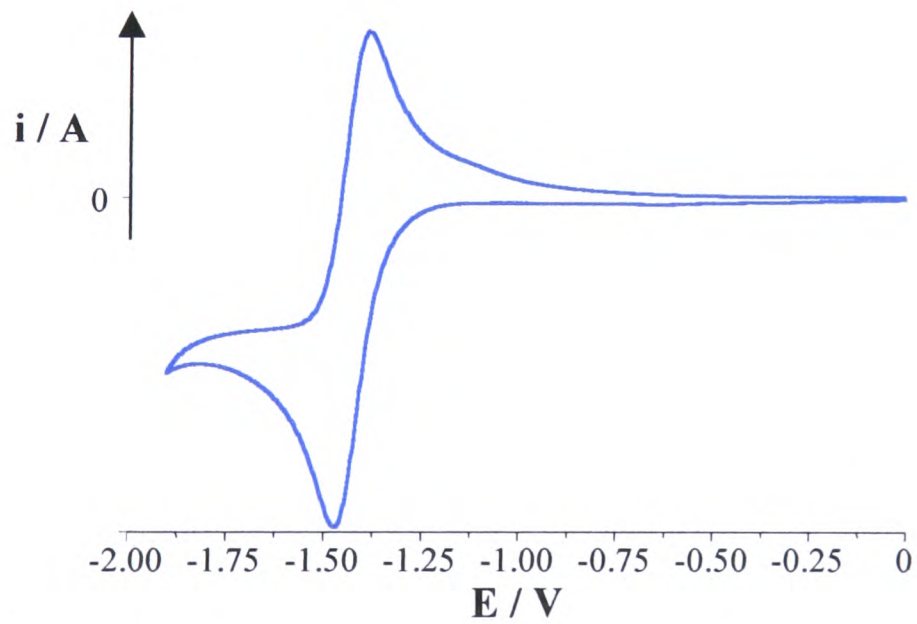

Figure 5. 6 Cyclic voltammogram of dpk in 0.1 M $TBABF_4$/DMF at 293 K, scan rate 0.1 V/s.

Thus the change in geometry of dpk indicated in the cyclic voltammogram was tentatively attributed to reduction of the ketone promoting protonation of the carbonyl group and the formation of the geminal diol or an intermediate. This may also explain the inconclusive coulometry results. The effect of reducing dpk will be more fully investigated in the rest of this chapter.

In situ electrochemical reduction of dpk carried out at 298 K in 0.01 M $TBABF_4$/DMF gave the epr active species dpk^{1-}, which was dark blue in colour. The room temperature solution epr spectrum of dpk^{1-} is a complex spectrum with 110 lines with a g_{iso} of 2.006. As the spectrum is symmetrical only the low field half is shown for clarity, Figure 5.7. A satisfactory simulation of this epr spectrum could not be obtained. This was attributed to the epr active solution containing a mixture of dpk^{1-} and $dpk.H_2O^{1-}$ as well as an intermediate. Despite being unable to simulate this spectrum it is a good example of the high resolution spectra that can be obtained using *in situ* epr techniques.

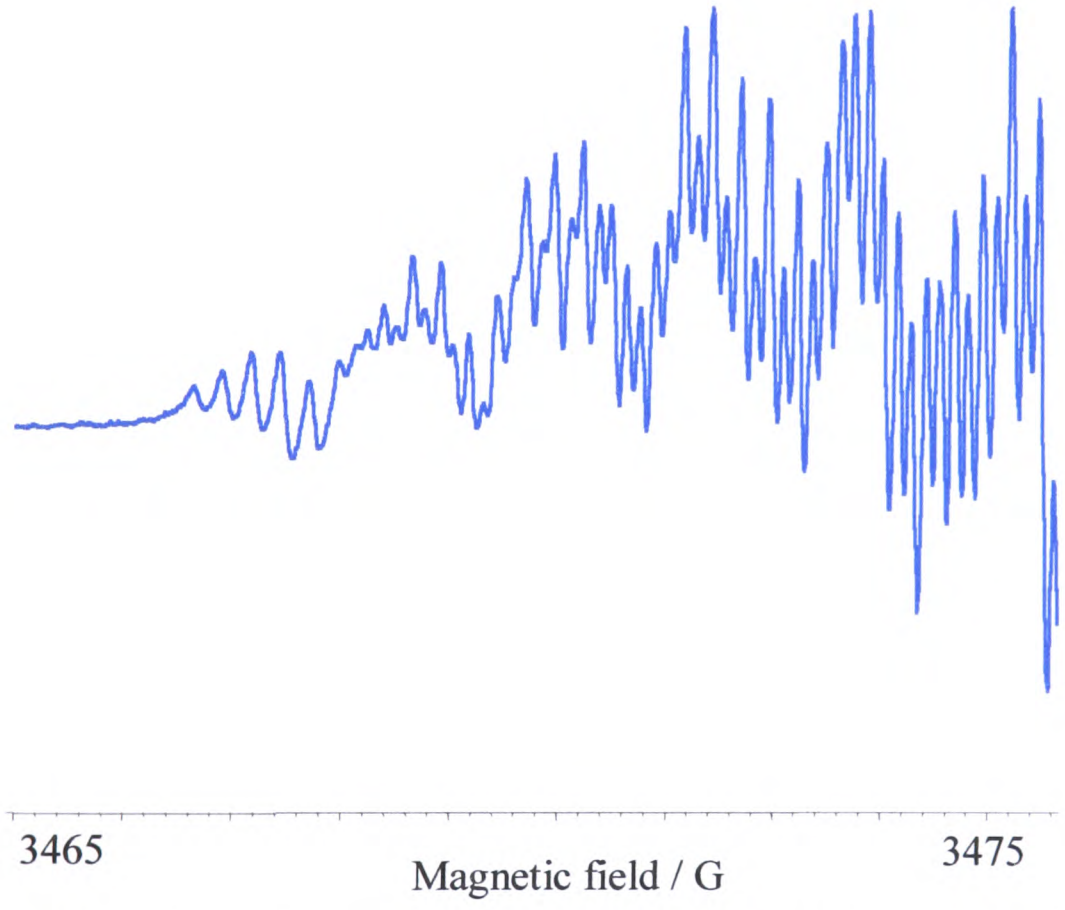

Figure 5. 7 Epr spectrum obtained on mono-reduction of dpk in 0.01 M $TBABF_4$/DMF at 298 K, E_{gen} –1.8 V.

The UV/vis/nir spectrum of dpk, run in MeOH, shows three peaks at 41,500 cm^{-1} (ε = 5,200 M^{-1} cm^{-1}), 37,200 cm^{-1} (ε = 6,400 M^{-1} cm^{-1}) and a much less intense peak at 28,300 cm^{-1} (ε = 100 M^{-1} cm^{-1}). These results compare well with those of Bock *et al.* who found that in aqueous solution, dipyridyl ketone remains unprotonated provided the pH >5 and no metal cations are present,[95] see Table 5.1.

Table 5. 1 UV/vis spectra for dpk in MeOH and in aqueous solution at pH > 5.

Dpk in MeOH (pH = 7)		**Dpk (pH > 5) in aqueous solution [a]**	
Peak position / cm^{-1}	**ε / M^{-1} cm^{-1}**	**Peak position / cm^{-1}**	**ε / M^{-1} cm^{-1}**
41,500	5,200	41,300	8,500
37,200	6,400	37,600	10,000
28,300	100	29,400	200

(a) from the work of Bock *et al.*.[95]

In line with previous studies of the absorption spectra of dpk, the two higher energy peaks are assigned as $\pi \rightarrow \pi^*$ intraligand transitions, with the peak at 37,200 cm^{-1} attributed to the $\pi \rightarrow \pi^*$ transitions of the HOMO-LUMO level, and the higher energy peak at 41,500 cm^{-1} assigned as $\pi \rightarrow \pi^*$ transitions of the HOMO-LUMO-1.[102] The difference in peak position of the two peaks gives the energy difference between the LUMO and LUMO-1 levels of the ligand, see Table 5.2.

Table 5. 2 Energy differences between LUMO and LUMO-1 levels of the dpk in MeOH.

	$\pi \rightarrow \pi^*$ HOMO-LUMO / cm^{-1}	$\pi \rightarrow \pi^*$ HOMO-LUMO-1 / cm^{-1}	ΔE / cm^{-1}
Dpk	37,200	41,500	4,300

Favaro and co-workers assigned the lowest energy transition to be of $n \rightarrow \pi^*$ character, due to the small absorption coefficient and the hypsochromic shift the peak undergoes on increasing the solvent polarity.[101] The ligand was investigated by spectroelectrochemistry in 0.1 M $TBABF_4$/DMF at 228 K. The spectrum of the neutral species shows a single high energy band at 36,900 cm^{-1} (ε = 8,100 M^{-1} cm^{-1}), see Figure 5.8, which was assigned as a $\pi \rightarrow \pi^*$ intraligand transition. The two other bands observed in the UV/vis/nir spectrum in MeOH are not observed here because the higher energy band lies out with the absorption range for UV/vis spectra in DMF and the weak band at 28,300cm^{-1} is masked by its more intense neighbour.

Close inspection of the UV/vis/nir spectra recorded during the reduction of dpk in 0.1 M $TBABF_4$/DMF at 228 K revealed three phases in the reduction process, see Figures 5.8 - 5.10. Such divisions in the spectra are to be expected if the dpk is undergoing a chemical reaction on reduction. Initially, in Phase I, the $\pi \rightarrow \pi^*$ transition band at 36,900 cm^{-1} collapses. Phase I was assigned as the initial reduction of the dpk before further reaction at the carbonyl group occurred. Molecular Orbital calculations using CaChe software (using PM3 calculation and wavefunction) indicate that the LUMO is based on the C=O part of the molecule. The additional negative charge is based mainly on the carbonyl O atom, although it is stabilised by delocalisation over the whole ligand. The $\pi \rightarrow \pi^*$ transition collapses as the LUMO π^*

orbital becomes semi-occupied. An isosbestic point is observed at 33,100 cm^{-1} indicating that dpk is reduced with no decomposition. However, even at 228 K dpk^{1-} is not stable and reacts. During Phase I dpk is reduced to dpk^{1-}, however, not all the dpk is reduced before significant reaction occurs and hence the $\pi \rightarrow \pi^*$ transition of dpk does not completely collapse.

The reaction of dpk^{1-} then enters a second phase as bands at 30,900 cm^{-1} (ε = 5,700 M^{-1} cm^{-1}), 27,000 cm^{-1} (ε = 1,700 M^{-1} cm^{-1}), 22,100 cm^{-1} (ε = 1,900 M^{-1} cm^{-1}) and 14,900 cm^{-1} (ε = 3,100 M^{-1} cm^{-1}) grow in, see Figure 5.9 and Scheme 5.4. Phase II was attributed to the initial reduction induced reaction where the negatively charged carbonyl O atom attacks a water molecule to give the singly protonated intermediate $dpk.H^0$. These bands were assigned as $\pi \rightarrow \pi^*$ transitions of $dpk.H^0$.

A third and final phase is then observed in the UV/vis/nir spectra. Phase III was assigned as the second stage in the formation of the geminal diol as ^-OH attacks the carbonyl C atom and the addition of water to the carbonyl C=O group is completed to give $dpk.H_2O^{1-}$. The bands at 30,900 cm^{-1}, 27,000 cm^{-1} and 14,900 cm^{-1} all collapse but the band at 22,100 cm^{-1} (ε = 2,900 M^{-1} cm^{-1}) continues to grow. On collapsing, the band at 14,900 cm^{-1} becomes broader and is slightly blue shifted, see Figure 5.10. These bands were assigned as $\pi \rightarrow \pi^*$ transitions of $dpk.H_2O^{1-}$. This final spectrum is characteristic of $dpk.H_2O^{1-}$.

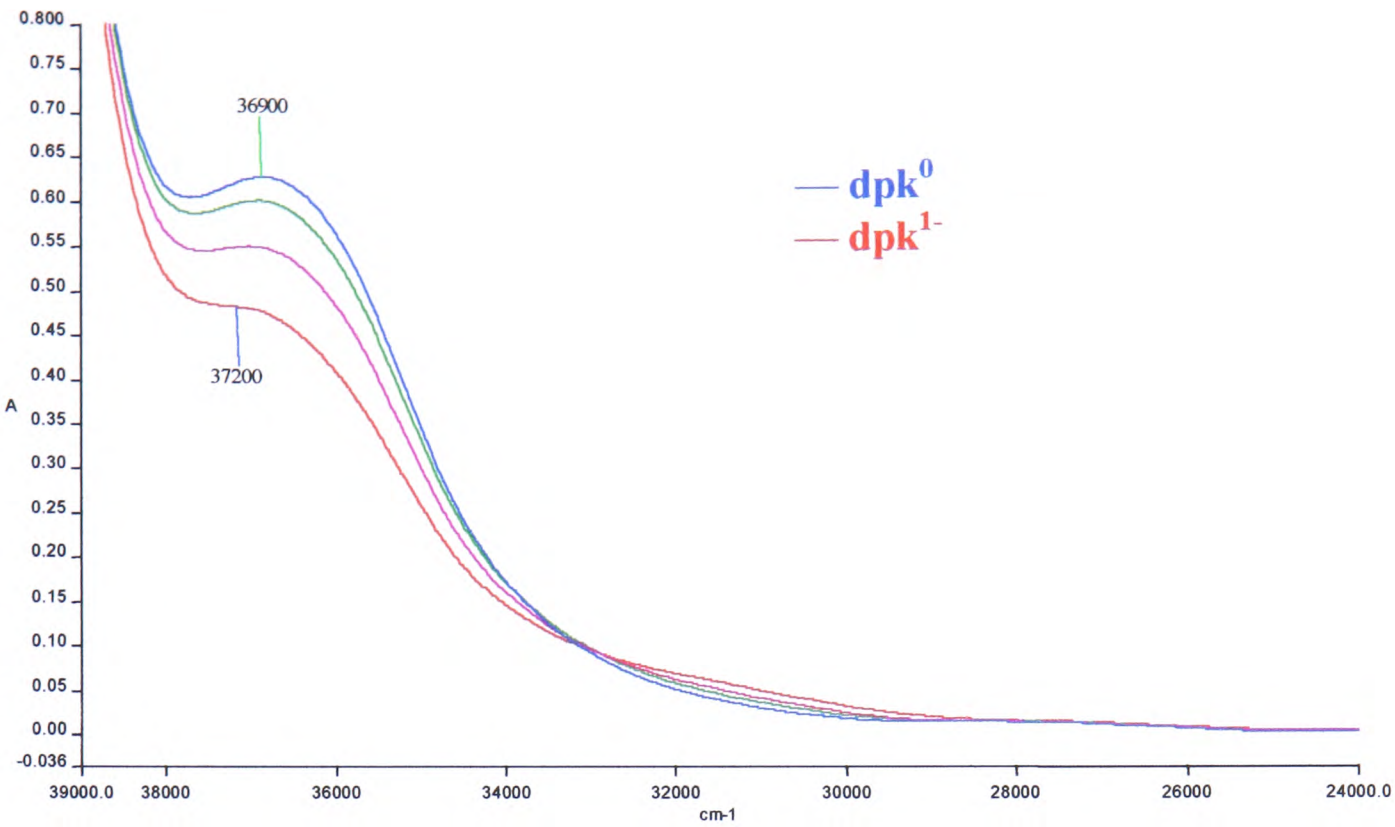

Figure 5. 8 UV/vis/nir of Phase I, $dpk^{0/1-}$ in 0.1 M $TBABF_4$/DMF at 228 K, E_{gen} –1.8 V.

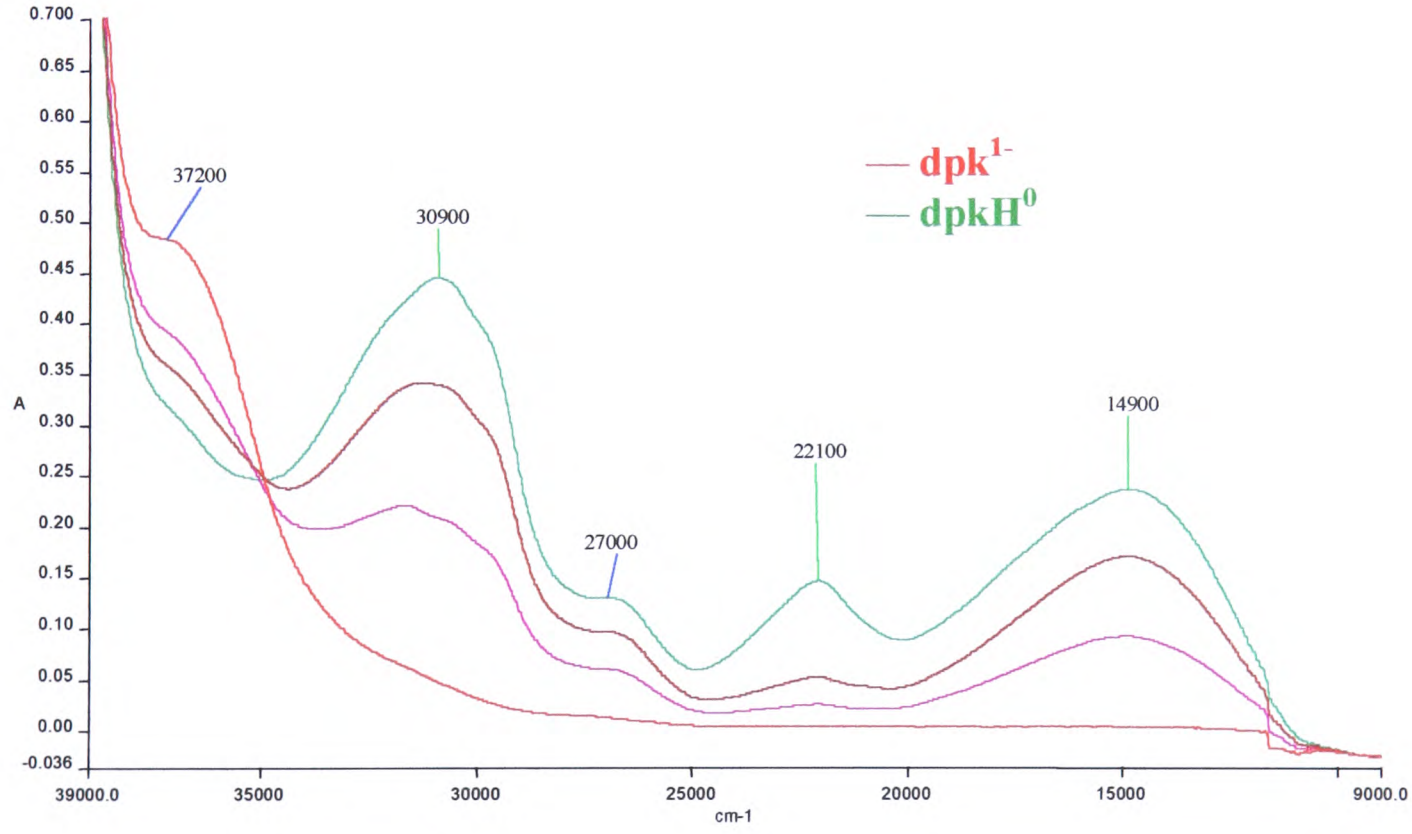

Figure 5. 9 UV/vis/nir of Phase II showing dpk^{1-}/$dpkH^0$ in 0.1 M $TBABF_4$/DMF at 228 K, E_{gen} –1.8 V.

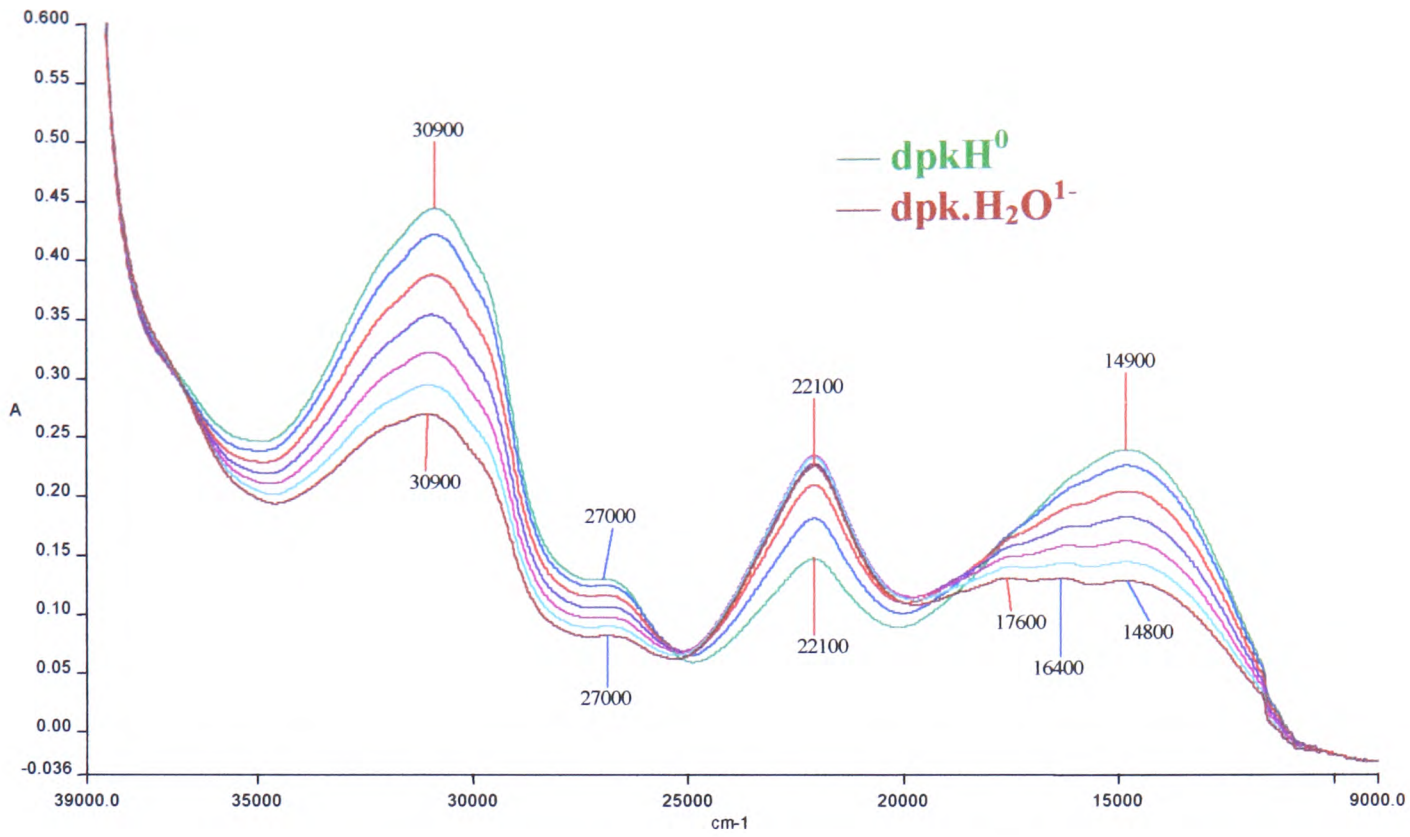

Figure 5. 10 UV/vis/nir of Phase III showing $dpkH^0$/$dpk.H_2O^{1-}$ in 0.1 M $TBABF_4$/DMF at 228 K, E_{gen} = -1.8 V.

The peaks in this OTTLE experiment are difficult to assign unambiguously as the reduction of dpk is closely followed by a chemical reaction and an equilibrium is established between dpk^{1-}, $dpkH^0$ and $dpk.H_2O^{1-}$. Consequently, the peak at 22,100cm^{-1} in Phase II, see Figure 5.9 may be due to $dpk.H_2O^{1-}$ and the isosbestic point at 18.5-20 kcm^{-1} in Phase III is broader that would be expected for a reaction where no chemical reaction follows the redox process. Thus the discontinuity of the OTTLE spectra can be attributed to the reduction of dpk promoting conversion of dpk^{1-} to its geminal diol form $dpk.H_2O^{1-}$, via the intermediate $dpk.H^0$, see Scheme 5.4. Phases II and III are reversible as taking the generation potential back to 0 V causes all the bands below 31,000 cm^{-1} to collapse. However, the spectrum for the neutral species is not fully regenerated.

Table 5. 3 Peak positions and molar extinction coefficients, ε, for the 3 phases observed during the reduction of dpk^0 to $dpk.H_2O^{1-}$ in 0.1 M $TBABF_4$/DMF at 228 K, E_{gen} = -1.80 V.

Dpk	Phase I	Phase II	Phase III
Peak position / cm^{-1} (ε / M^{-1} cm^{-1})	36,900 (8,100)	30,900 (5,700)	30,900 (3,500)
		27,000 (1,700)	sh 27,000 (1,100)
		22,100 (1,900)	22,100 (2,900)
		14,900 (3,100)	18-14,000 (*ca* 1,600)

To confirm that dpk is being reduced to $dpk.H_2O^{1-}$ an *in situ* IR electrogeneration of the reduced species should be carried out. If the C=O band at 1690 cm^{-1} collapsed on reduction to be replaced by an O-H band at *ca.* 3400 cm^{-1} and the IR spectrum could be returned to its original state on regeneration of the neutral species, this would prove that reduction of dpk leads to the formation of $dpk.H_2O^{1-}$ via a reversible reduction/chemical reaction. To carry out such an experiment a solvent that will show the relevant IR bands at 1690 cm^{-1} and *ca.* 3400 cm^{-1} and allow electrogeneration of the reduced species at –1.8 V is required. DMF allows generation of the reduced species but absorptions do not permit observation of IR bands below 1800 cm^{-1}. DCM is a suitable IR solvent but decomposes rapidly at potentials below –1.6 V. The experiment was attempted using acetonitrile, MeCN, but the electrochemistry and IR data indicated decomposition of the redox species before reduction was complete. However, a combined IR/coulometry experiment was carried out on the first reduction of $[Pt(dpk)Cl_2]$, see Section 5.2.1.2, as complexation of dpk shifts the first reduction potential to –0.65 V allowing the electrochemistry and IR to be carried out in DCM.

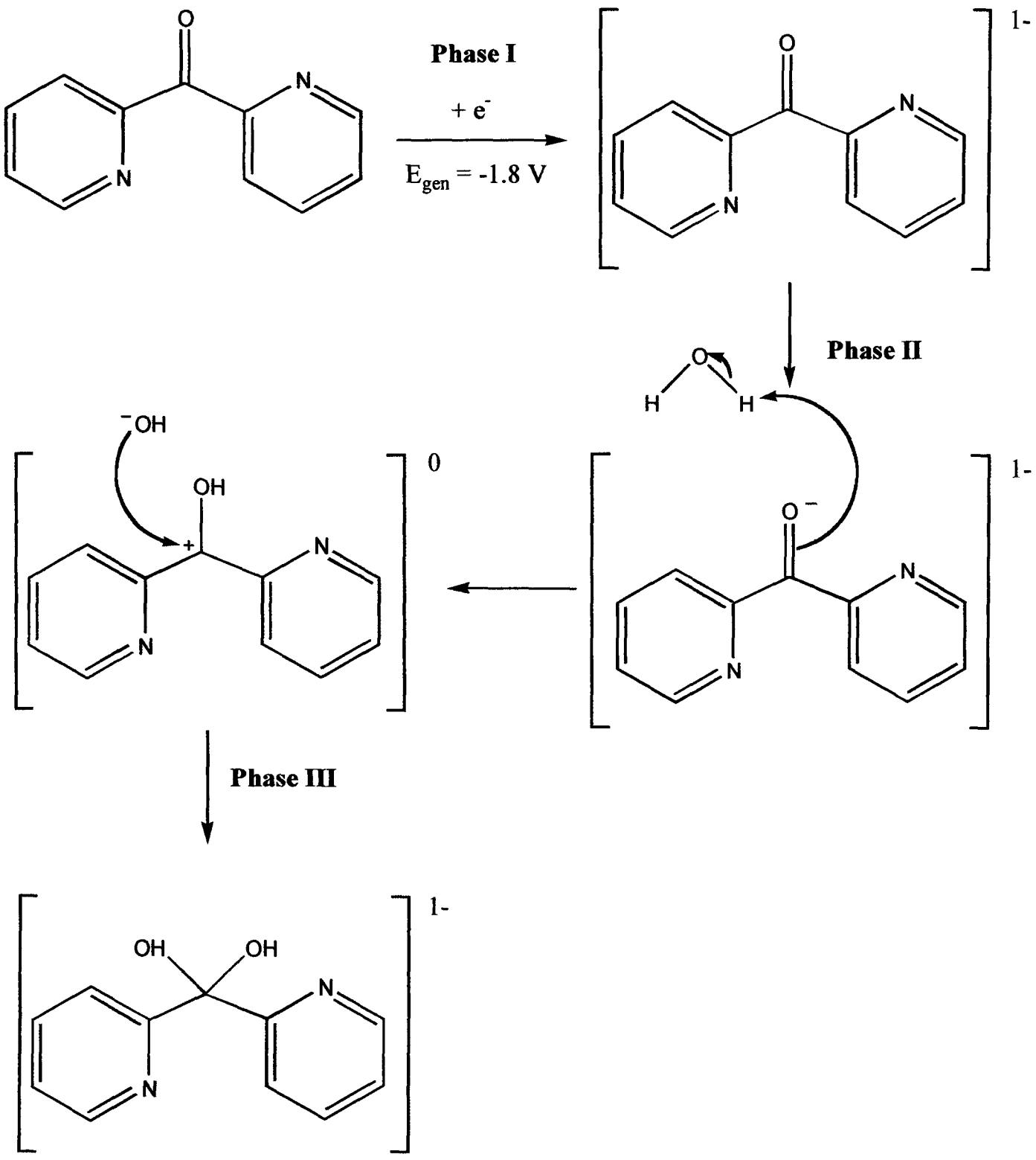

Scheme 5. 4 Reduction and subsequent chemical reaction of dpk/dpk^{1-} to give $dpkH^{0}$ and $dpk.H_2O^{1-}$ as illustrated by the UV/vis/nir spectra shown in Figures 5.8 – 5.10.

5.2.1.2 [Pt(dpk)Cl_2]

The cyclic voltammogram of [Pt(dpk)Cl_2] in 0.1 M $TBABF_4$/DMF at 293 K shows two reductions, the first is a fully reversible, one electron reduction at -0.65 V, (0.083), see Figure 5.11. The number of electrons involved in this reduction process was confirmed by coulometry. Neutral [Pt(dpk)Cl_2] is yellow when dissolved in DMF, the mono-reduced species is bright pinky purple and remains stable at room temperature for *ca.* one hour. The reduction is electrochemically reversible as indicated by the linear i_p versus $\nu^{1/2}$ response. The second reduction is also a reversible one electron process occurring at -1.36 V, (0.096).

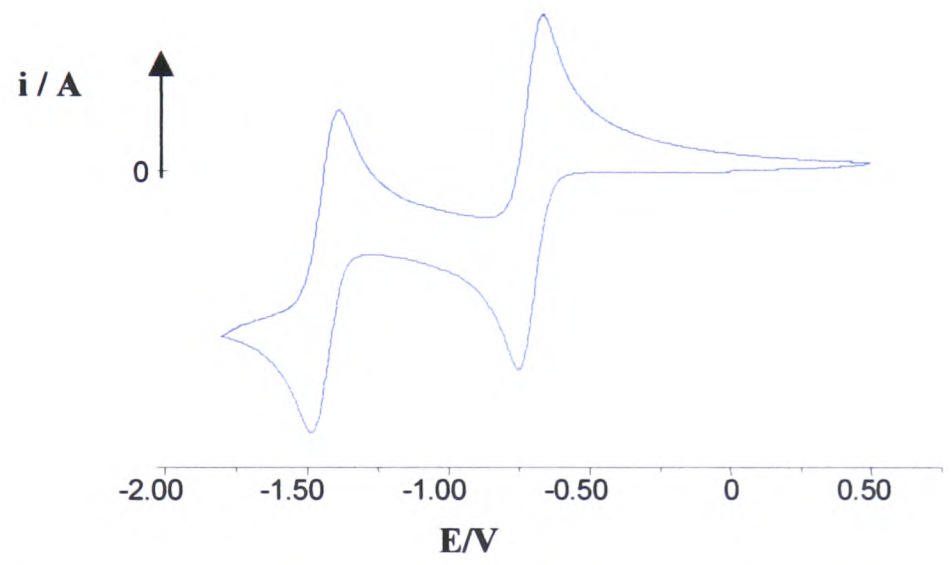

Figure 5. 11 Cyclic voltammogram of [Pt(dpk)Cl_2] in 0.1 M $TBABF_4$/DMF at 293 K, scan rate 0.1 V/s.

Previous work by Annibale *et al.* has established that [Pt(dpk)Cl_2] undergoes reversible uptake of a protic molecule, HX, as the absorption spectrum for [Pt(dpk)Cl_2] in water, (the complex is the geminal diol form [Pt(dpk.H_2O)Cl_2]), differs from that of [Pt(dpk)Cl_2] in acetonitrile (MeCN), (the complex is in the keto form [Pt(dpk)Cl_2]). However, for the Pt complex the equilibrium lies in favour of the keto form.[97] A combined coulometry/IR experiment was carried out to investigate whether reduction of [Pt(dpk)Cl_2] results in conversion of the dpk ligand from its keto form to its geminal diol form. The mono-reduced species was generated by

coulometry at room temperature under N_2 in 0.3 M $TBABF_4$/DCM. IR and UV/vis spectra were recorded before reduction, after reduction to the mono-reduced species and again after re-oxidation to the neutral complex. The initial IR spectrum (blue), see Figure 5.12, shows a ν C=O band at 1697 cm^{-1}, in line with literature values.[97] The band collapses upon reduction to the mono-reduced species (red), E_{gen} = -1.0 V. Molecular Orbital calculations using CaChe software (with a PM3 calculation and wavefunction) on free dpk indicate that the LUMO is based on the C=O part of the molecule. Hence, in the first reduction of $[Pt(dpk)Cl_2]$ the extra negative charge will be based on the C=O bond, causing collapse of the IR band at 1697 cm^{-1}. Once the neutral species is regenerated, the solution IR shows partial re-growth of the C=O band, (green line), indicating only partial re-generation of the complex in its keto form. Thus we propose that reduction of $[Pt(dpk)Cl_2]$ facilitates addition of H_2O at the carbon atom of the carbonyl group producing the corresponding addition product $[Pt(dpkH_2O)Cl_2]$ in agreement with the findings of Annibale and co-workers.[97] A more accurate assignment of the IR will be made later in the chapter.

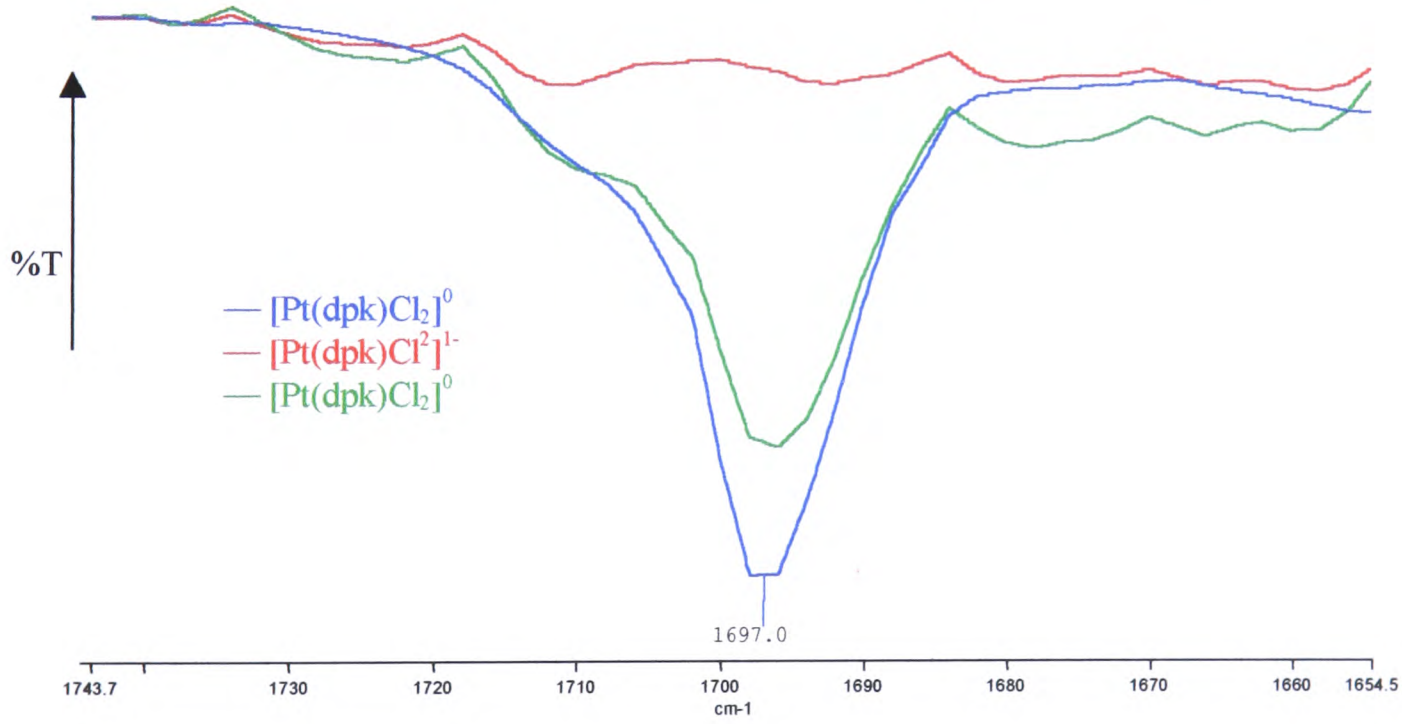

Figure 5. 12 IR spectra showing changes in C=O band during conversion $[Pt(dpk)Cl_2]^0$ to $[Pt(dpk)Cl_2]^{1-}$ in 0.3 M $TBABF_4$/DCM at 293 K, E_{gen} = -1.0 V.

An experiment using the OTTLE cell was performed on the two reversible reductions of $[Pt(dpk)Cl_2]$ at 228 K in 0.1 M $TBABF_4$/DMF. The results are shown below in Figures 5.13 and 5.14. The spectrum of the neutral species is dominated by an intense band at 36,500 cm^{-1} (ε = 17,100 M^{-1} cm^{-1}), assigned as an intraligand $\pi \rightarrow \pi^*$ transition, which collapses on reduction. Co-ordination of dpk stabilises the LUMO as demonstrated by the positive shift in the redox potential of the first reduction, Figure 5.11, compared to that of the free ligand, see Figure 5.6. In accordance with the stabilisation of the LUMO, the intraligand $\pi \rightarrow \pi^*$ transition of $[Pt(dpk)Cl_2]$ is expected to shift to lower energy compared to that of the free ligand. A similar band is present in the spectrum of neutral dpk, although shifted to higher energy at 36,900 cm^{-1} (ε = 8,100 M^{-1} cm^{-1}), see Figure 5.8. The broad band at 31,000 – 24,000 cm^{-1} (ε = 1,700 M^{-1} cm^{-1}) is most likely a mixture of CT transitions and spin forbidden transitions.

On reduction to $[Pt(dpk)Cl_2]^{1-}$ the intense $\pi \rightarrow \pi^*$ intraligand transition at 36,500 cm^{-1} and the broad band at 24-31 kcm^{-1} collapse to be replaced by a band at 32,200 cm^{-1} (ε = 4,800 M^{-1} cm^{-1}), see Figure 5.13. Note the isosbestic points at 32,500 cm^{-1} and 29,900 cm^{-1} indicating the clean conversion between $[Pt(dpk)Cl_2]^0$ and $[Pt(dpk)Cl_2]^{1-}$. On reduction to $[Pt(dpk)Cl_2]^{1-}$ some of the compound will immediately start to react with a proton source, probably H_2O, to form $[Pt(dpkH)Cl_2]^0$. These reactions are discussed further below. This spectrum was attributed to the generation of $[Pt(dpk)Cl_2]^{1-}$.

The UV/vis/nir spectra recorded during the reduction of $[Pt(dpk)Cl_2]^{1-}$ to $[Pt(dpk.H_2O)Cl_2]^{2-}$ is shown in Figure 5.14. Bands at 36,700 cm^{-1} (ε = 10,200 M^{-1} cm^{-1}), 32,000 cm^{-1} (ε = 7,500 M^{-1} cm^{-1}), 23,400 cm^{-1} (ε = 1,300 M^{-1} cm^{-1}), 18,600 cm^{-1} (ε = 1,800 M^{-1} cm^{-1}) and 12,200 cm^{-1} (ε = 1,800 M^{-1} cm^{-1}) are all observed to grow in. This spectrum is similar to those obtained during the reduction and subsequent chemical reaction of dpk^{1-} to $dpk.H_2O^{1-}$ via $dpkH^0$, see Figures 5.9 and 5.10, as all of the bands observed in that spectrum are visible here, although shifted to slightly lower energy. The final spectrum in Figure

5.14 is similar to that of dpk.H_2O^{1-} and dpkH^0 therefore, as for the unbound dpk, it is difficult to assign the peaks unambiguously as the reduction is followed by a chemical reaction. Consequently, this spectrum was tentatively assigned as $[Pt(dpk.H_2O)Cl_2]^{2-}$ as the peaks were similar to those characteristic of unbound dpk.H_2O^{1-}.

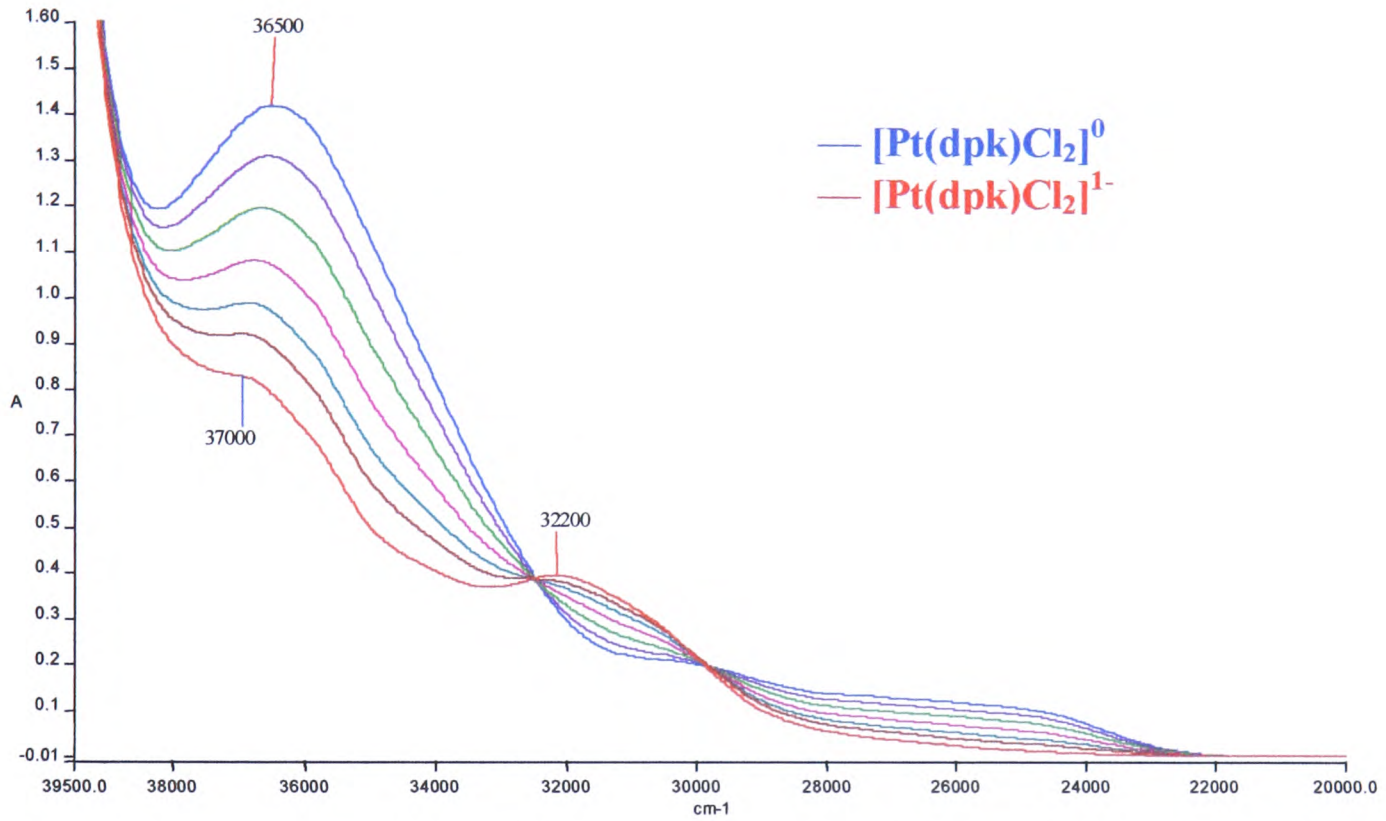

Figure 5. 13 UV/vis of $[Pt(dpk)Cl_2]^{0/1-}$ in 0.1 M $TBABF_4$/DMF at 228 K, E_{gen} = -1.0 V.

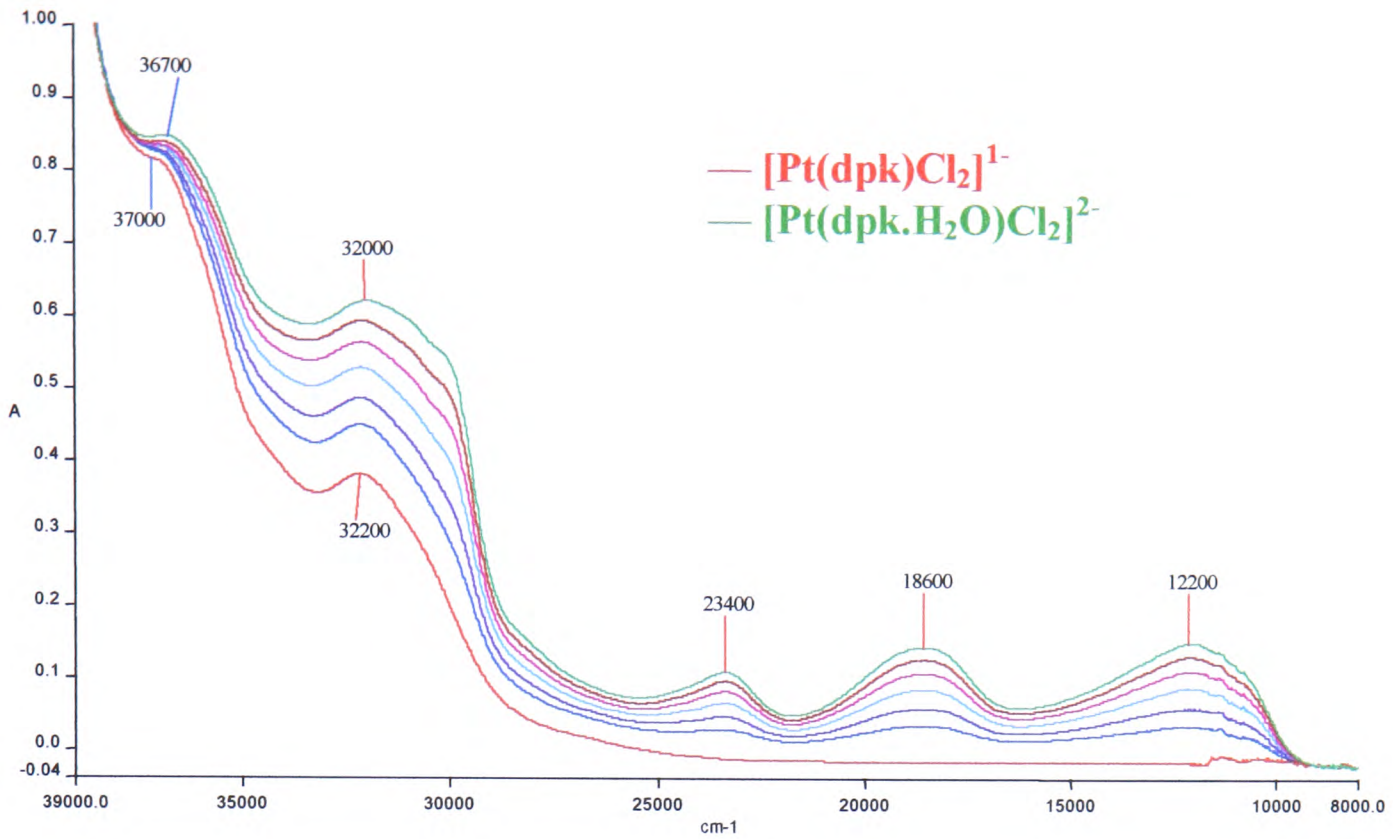

Figure 5. 14 UV/vis showing conversion of $[Pt(dpk)Cl_2]^{1-}$ to $[Pt(dpk.H_2O)Cl_2]^{2-}$ in 0.1 M $TBABF_4$/DMF at 228 K, E_{gen} = -1.8 V.

Table 5. 4 Peak positions and molar extinction coefficients, ε, of $[Pt(dpk)Cl_2]$ / $[Pt(dpk)Cl_2]^{1-}$ / $[Pt(dpk.H_2O)Cl_2]^{2-}$ in 0.1 M $TBABF_4$/DMF at 228 K.

Oxidation state	Peak position/cm^{-1}, (ε / M^{-1} cm^{-1})
0	36,500 (17,100) 31,000-24,000 (1,700)
1^-	37,000 (10,000) 32,200 (4,800)
2^-	36,700 (10,200) 32,000 (7,500) 23,400 (1,300) 18,600 (1,800) 12,200 (1,800)

The behaviour of $[Pt(dpk)Cl_2]$ on reduction can be explained in relation to the reduction and subsequent chemical reaction of the free ligand. At –1.0 V $[Pt(dpk)Cl_2]$ undergoes reduction to $[Pt(dpk)Cl_2]^{1-}$. Molecular Orbital calculations using CaChe software (PM3 calculation with PM3 wavefunction) on dpk indicated that the LUMO is based on the C=O. Thus the first reduction on the free ligand and on $[Pt(dpk)Cl_2]$ is based on the C=O. Such an increase in the electron density on the C=O would account for the collapse of the C=O band at 1697 cm^{-1} in the IR spectrum of $[Pt(dpk)Cl_2]^{1-}$. The negative charge on the carbonyl group leads to some of the $[Pt(dpk)Cl_2]^{1-}$ reacting with a proton source, probably water, to give $[Pt(dpkH)Cl_2]^0$ and $[Pt(dpk.H_2O)Cl_2]^{1-}$. Addition of a second reduction electron to $[Pt(dpk)Cl_2]^{1-}$ further builds up the charge on the C=O part of the molecule. Thus dpk is now doubly reduced and is unstable even when bound to Pt^{2+}. The $[Pt(dpk)Cl_2]^{2-}$ goes on to react with a proton source, again H_2O to yield either complexed $(dpkH)^0$ or $(dpk.H_2O)^{1-}$. The new spectrum is very similar to either $dpkH^0$ or $[dpk.H_2O]^{1-}$, see Figures 5.9 and 5.10 and Table 5.3. For this to occur it must be inferred that the potential needed to reduce $[Pt(dpk)Cl_2]^{1-}$ to $[Pt(dpk)Cl_2]^{2-}$ is not sufficient to reduce $[Pt(dpkH)Cl_2]^0$ or $[Pt(dpk.H_2O)Cl_2]^{1-}$ to the di-reduced species and hence the new product species are immediately oxidised to $[Pt(dpkH)Cl_2]^0$ or $[Pt(dpk.H_2O)Cl_2]^{1-}$ at the electrode surface, see Scheme 5.5. This is a reasonable hypothesis as protonated or hydrated dpk^{1-} is more like pyridine and pyridine is very difficult to reduce. This re-oxidation process is accelerated when the E_{gen} is switched back to –1.0 V.

In situ electrochemical reduction of $[Pt(dpk)Cl_2]$ in 0.3 M $TBABF_4$/DCM at 273 K gives a pinky purple epr active species. The epr signal of this paramagnetic species is a broad central line with ^{195}Pt satellites indicating coupling of the unpaired electron to the Pt nucleus, $A^{Pt} = 39.0$ G, $g_{iso} = 2.0018$. Any superhyperfine coupling to the ligand nuclei was unresolved, see Figure 5.15.

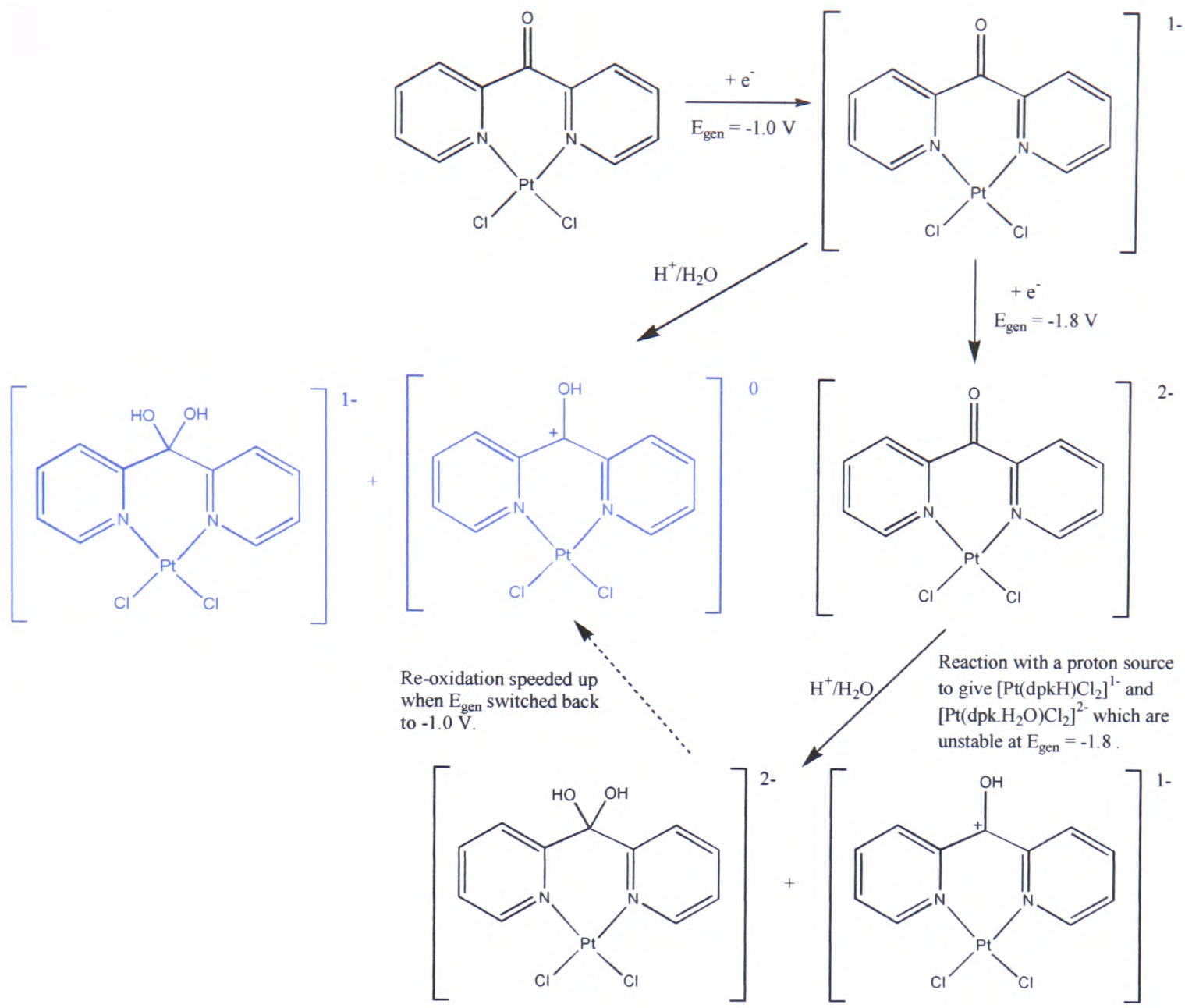

Scheme 5. 5 Chemical reactions of $[Pt(dpk)Cl_2]$ after reduction to –1.0 V and –1.8 V, showing the routes to the formation of $[Pt(dpkH)Cl_2]^0$ and $[Pt(dpk.H_2O)Cl_2]^{1-}$, shown in blue, in 0.1 M $TBABF_4$/DMF at 228 K.

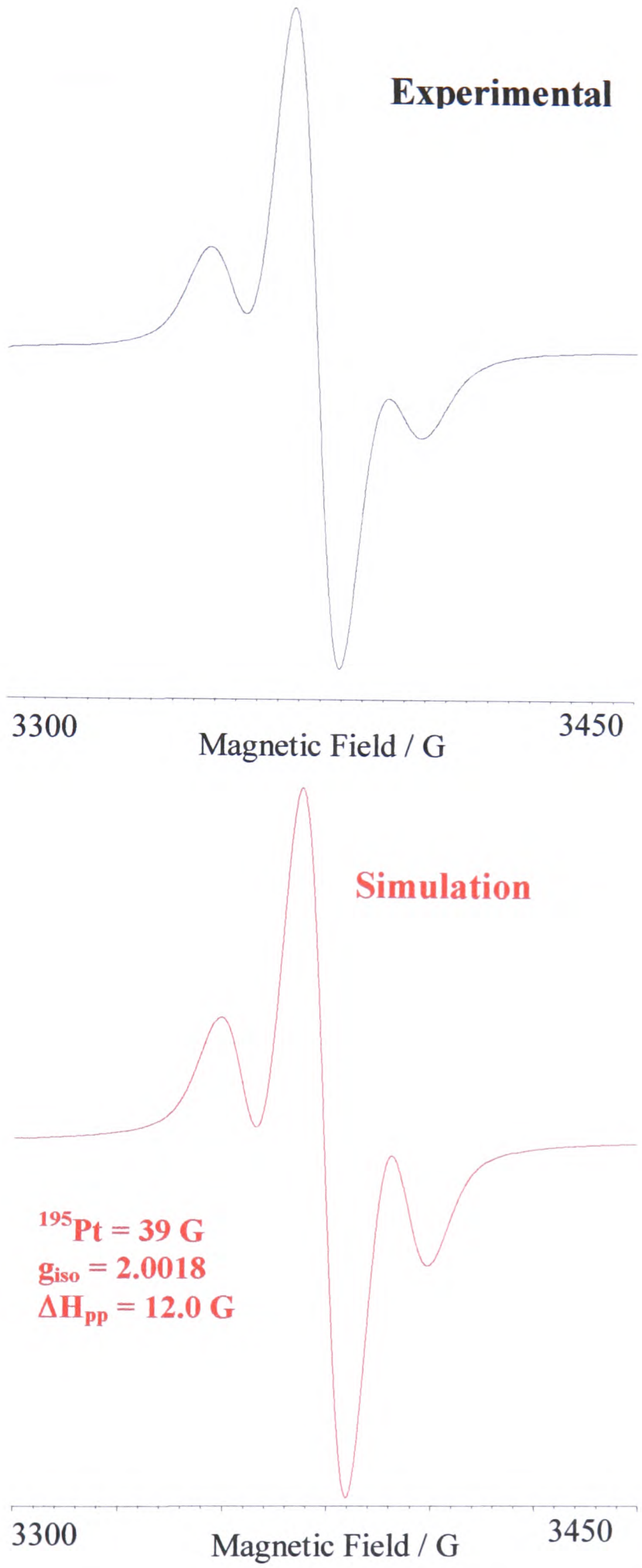

Figure 5. 15 Epr of $[Pt(dpk)Cl_2]^{1-}$ generated *in situ* in 0.3 M $TBABF_4$/DCM at 273 K and E_{gen} = -1.0 V. The black spectrum is the signal obtained experimentally, the red spectrum is the simulation.

5.2.1.3 [Pd(dpk)Cl_2]

Figure 5.16, below, shows the cyclic voltammogram obtained for [Pd(dpk)Cl_2], in 0.1 M $TBABF_4$/DMF at 293 K. Two reductions are evident, E_1 = -0.59 V and E_2 = -0.81 V, both are irreversible and do not become any more reversible with increasing scan rate or decreasing temperature. These reductions were assigned as being Pd based, the Pd-based molecular orbitals being lower in energy than the π^* orbitals of the ligand. The irreversible nature of the reduction process resulted in no further study of [Pd(dpk)Cl_2].

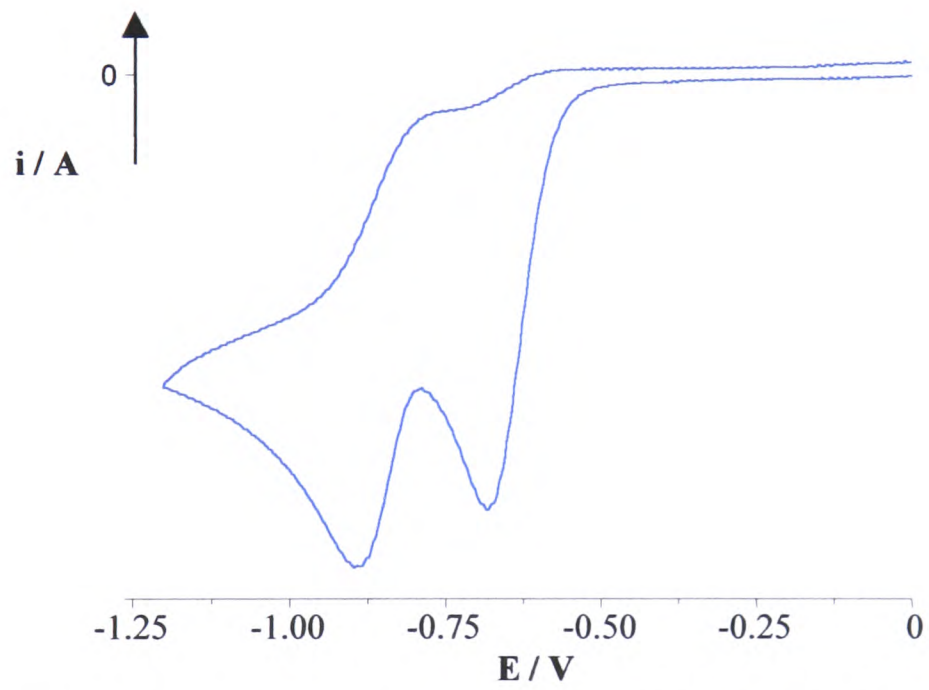

Figure 5. 16 Cyclic voltammogram of [Pd(dpk)Cl_2] in 0.1 M $TBABF_4$/DMF at 293 K, scan rate 0.1 V/s.

5.2.2 Di-2-pyridyl amine (Hdpa)

The cyclic voltammogram of Hdpa in 0.1 M $TBABF_4$/DMF at 293 K, see Figure 5.17, revealed a reversible reduction at –0.84 V, (0.320) and an irreversible oxidation at +1.32 V. The reduction is electrochemically reversible as indicated by the linear i_p versus $\nu^{1/2}$ response. The large separation between E_{pc} and E_{pa} indicates there is a change in the geometry of the ligand as it undergoes reduction.[81] Previous electrochemical studies on Hdpa attribute the irreversible oxidation to the oxidation of the amine portion of the ligand.[79, 91] The number of electrons involved in the reduction could not be determined, as coulometric studies of the reduction at 233 K were inconclusive. Bulk electrogeneration of the reduced species at 293 K was not successful, indicating that the mono-reduced species is unstable at room temperature. Given the nature of the reduction at –0.84 V, it may be due to a breakdown product of Hdpa or an impurity. Consequently, the epr spectrum of the $Hdpa^{1-}$ could not be studied.

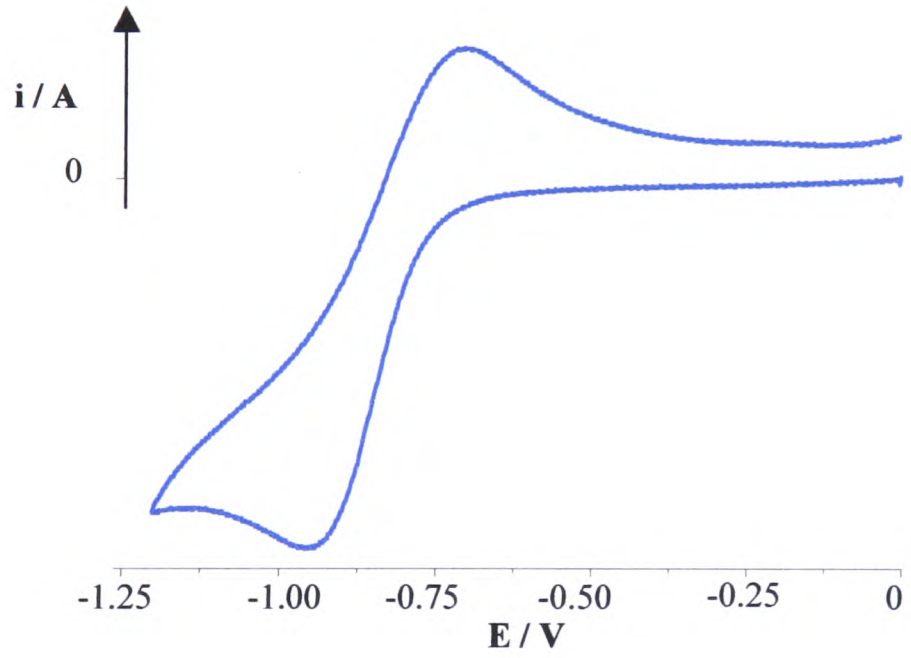

Figure 5. 17 Cyclic voltammogram of Hdpa in 0.1 M $TBABF_4$/DMF at 293 K, scan rate 0.1 V/s.

The UV/vis spectrum of Hdpa, in MeOH shows four peaks at 32,200 cm^{-1} (ε = 16,200 M^{-1} cm^{-1}), 37,900 cm^{-1} (ε = 24,200 M^{-1} cm^{-1}), 45,600 cm^{-1} (ε = 4,900 M^{-1} cm^{-1}) and 52,400 cm^{-1} (ε = 35,400 M^{-1} cm^{-1}).

UV/vis/nir spectroelectrochemistry of Hdpa was carried out in 0.1 M $TBABF_4$/DMF at 233 K. In the spectrum taken before reduction, the neutral species shows two peaks at 31,600 cm^{-1} (ε = 15,300 M^{-1} cm^{-1}) and 37,000 cm^{-1} (ε = 12,700 M^{-1} cm^{-1}), see Figure 5.18. This compares well with the spectrum of Hdpa in MeCN obtained by Morris *et al.* where the peaks appeared at 32,300 cm^{-1} (ε = 11,000 M^{-1} cm^{-1}) and 37,700 cm^{-1} (ε = 19,000 M^{-1} cm^{-1}).[79] Both the peak at 37,000 cm^{-1} and the peak at 31,600cm^{-1} were assigned as being due to intraligand transitions. On reduction, the peak at 37,000 cm^{-1} collapses and the peak at 31,600 cm^{-1} grows and is slightly red shifted to 31,100 cm^{-1} (ε = 15,300 M^{-1} cm^{-1}). A broad band at 27,200 cm^{-1} (ε = 6,500 M^{-1} cm^{-1}) also grows in. In previous work Morris *et al.* noted that uncomplexed dpa^{1-} has an intraligand charge transfer at 27,400 cm^{-1}.[79] The bands were assigned as intraligand transitions. The slight discontinuity in the UV/vis/nir spectra may be due to a geometrical change in the ligand as it undergoes reduction. On taking the generation potential back to 0 V, the original spectrum is regenerated with no loss of intensity for any of the peaks, indicating that this reduction is fully chemically reversible.

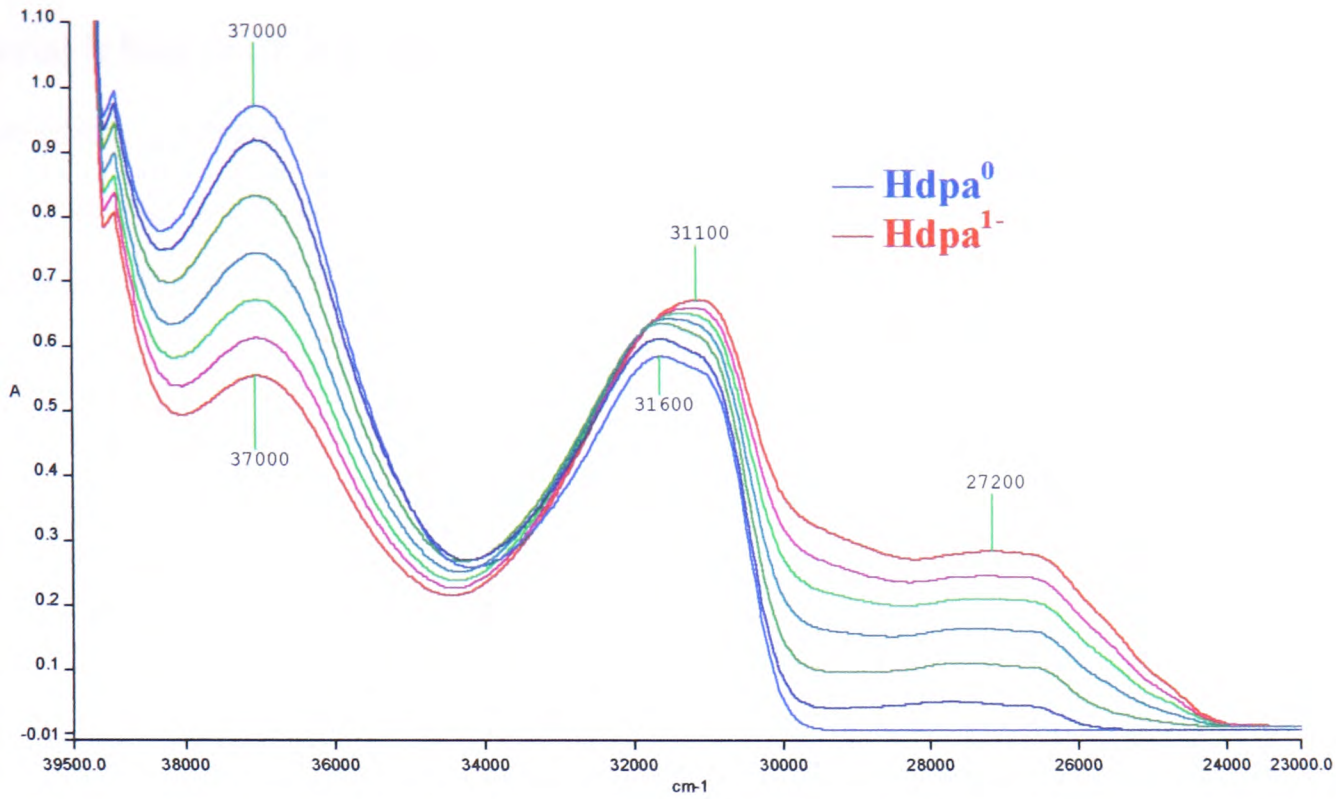

Figure 5. 18 UV/vis/nir spectra for $Hdpa^{0/1-}$ in 0.1 M $TBABF_4$/DMF at 233 K, E_{gen} = -1.25 V.

Table 5. 5 Peak positions and molar extinction coefficients, ε, for $Hdpa^{0/1-}$ at 233 K in 0.1 M $TBABF_4$/DMF, E_{gen} = -1.25 V.

Oxidation state	Peak position / cm^{-1} (ε / M^{-1} cm^{-1})
0	37,000 (22,200) 31,600 (13,400)
1^-	37,000 (12,700) 31,100 (15,300) 27,200 (6,500)

5.2.2.1 [Pt(Hdpa)Cl_2]

The cyclic voltammogram of [Pt(Hdpa)Cl_2] in 0.1 M $TBABF_4$/DMF at 293 K shows three irreversible oxidations at E_1 = 1.04 V, E_2 = 0.90 V and E_3 = 0.77 V and a distended reduction E_{pc} = -1.30 V, E_{pa} = -0.59 V, ($E_{1/2}$ = -0.98 V), see Figure 5.19. The return peak is not due to impurities or decomposition products because it is not

present when the potential is only taken to –1.0 V and does not get any bigger if the potential is held at –1.7 V. The reduction is electrochemically reversible as indicated by the linear i_p versus $\nu^{1/2}$ response. In line with previous electrochemical studies of the free ligand, see Section 5.2.2, the oxidations were attributed to the amine moiety and the reduction was attributed to the pyridyl moieties. The electrochemistry of the complex was studied at a range of temperatures, on cooling the reduction gradually became more distended, while warming the solution caused a decrease in peak-to-peak separation. Such behaviour indicates the complex is undergoing a geometrical change on reduction. Changes in temperature had no effect on the irreversible oxidations. Bulk generation of the reduced species at –1.7 V at room temperature lead to decomposition of the complex. Coulometric studies of the reduction at 233 K were inconclusive due to the instability of the reduced compound. Consequently an epr spectrum of $[Pt(Hdpa)Cl_2]^{1-}$ could not be obtained.

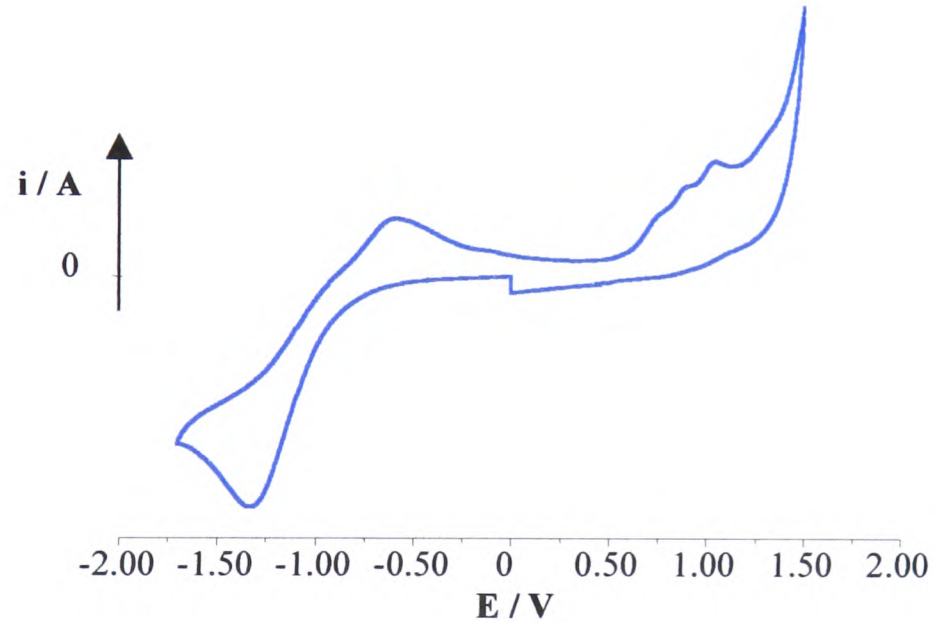

Figure 5. 19 Cyclic voltammogram of $[Pt(Hdpa)Cl_2]$ at 293 K in 0.1 M $TBABF_4$/DMF, scan rate 0.1 V/s.

To confirm that the Hdpa was still in its neutral form after complexation, an IR study of the $[Pt(Hdpa)Cl_2]$ was carried out. The IR spectrum showed the intense ν (C-N) band at 1436 cm^{-1}, the same position it appeared for the free ligand and three ν (N-H)

bands at 3194 cm^{-1}, 3231 cm^{-1} and 3276 cm^{-1} which Cotton *et al.* assigned as the **b** binding mode of Hdpa, see Scheme 5.1.[81] This, along with the results of the CHN analysis, see Section 5.3.1.3, confirms that $[Pt(Hdpa)Cl_2]$ has been synthesised.

UV/vis/nir studies of the reduction of $[Pt(Hdpa)Cl_2]^0$ to the mono-reduced species E_{gen} = -1.7 V, were carried out in 0.1 M $TBABF_4$/DMF at 231 K. Before reduction, the neutral complex shows four bands/shoulders at 34,100 cm^{-1} (ε = 9,400 M^{-1} cm^{-1}), 32,200 cm^{-1} (ε = 6,500 M^{-1} cm^{-1}), 29,400 cm^{-1} (ε = 3,700 M^{-1} cm^{-1}) and 24,400 cm^{-1} (ε = 800 M^{-1} cm^{-1}), see Figure 5.20. In line with the previous studies by Anbalagan and co-workers, the bands at 34.1 kcm^{-1} and 32.2 kcm^{-1} were assigned as a $\pi \rightarrow \pi^*$ transition of Hdpa, and an $n \rightarrow \pi^*$ transition of Hdpa, respectively. The band at 29.4 kcm^{-1} was assigned as at MLCT transition and the weak band at 24.4 kcm^{-1} was attributed to Pt d-d transitions.[91]

On reduction, the bands at 34.2 kcm^{-1} and 32.2 kcm^{-1}, assigned as intraligand transitions of Hdpa grew and became more defined, giving bands at 34,300 cm^{-1}, (ε = 12,700 M^{-1} cm^{-1}) and 32,200cm^{-1} (ε = 6,600 M^{-1} cm^{-1}), see Figure 5.20. The bands attributed to the Pt metal centre at 29.4 kcm^{-1} and 24.4 kcm^{-1} were replaced by three bands in the visible region at 28,100 cm^{-1} (ε = 5,700 M^{-1} cm^{-1}), 27,200 cm^{-1} (ε = 5,900 M^{-1} cm^{-1}) and 23,100 cm^{-1} (ε = 6,200 M^{-1} cm^{-1}) see Table 5.6 and Figure 5.20. These bands could not be accurately assigned as being characteristic of $[Pt(Hdpa)Cl_2]^{1-}$ as previous attempts to generate $[Pt(Hdpa)Cl_2]^{1-}$ in bulk at 233 K had failed due to the apparent instability of the reduced species. On switching the generation potential back to 0 V, the original spectrum was not regenerated.

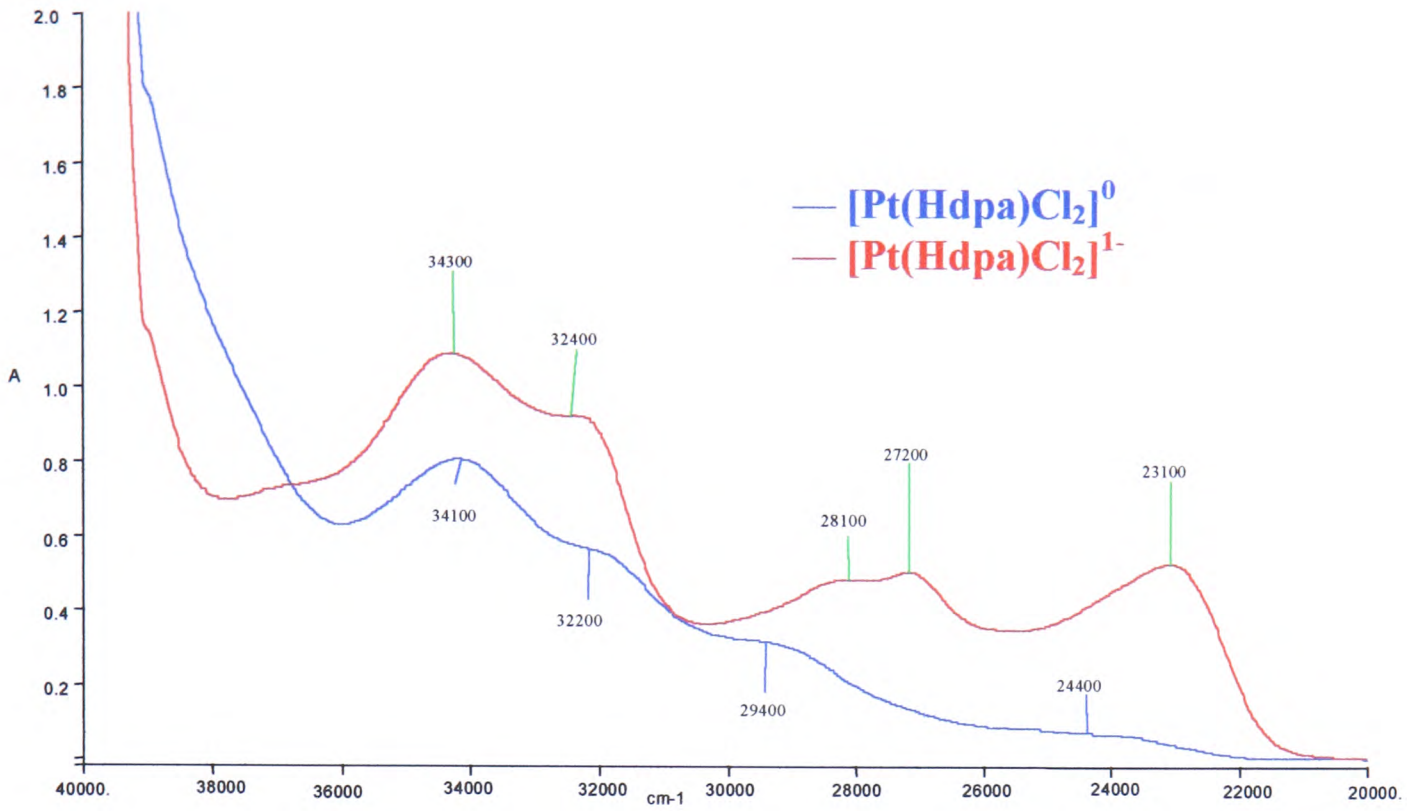

Figure 5. 20 UV/vis spectra of $[Pt(Hdpa)Cl_2]^{0/1-}$ in 0.1 M $TBABF_4$/DMF at 231 K, E_{gen} = -1.7 V.

Table 5. 6 Peak position and molar extinction coefficient, ε, for $[Pt(Hdpa)Cl_2]^{0/1-}$, in 0.1 M $TBABF_4$/DMF at 231 K.

Oxidation state	Peak position / cm^{-1} (ε / M^{-1} cm^{-1})
0	34,100 (9,400) 32,200 (6,500) 29,400 (3,700) 24,400 (800)
1^-	34,300 (12,700) 32,400 (6,600) 28,100 (5,700) 27,200 (5,900) 23,100 (6,200)

5.3 Conclusions

The redox behaviour of dpk and $[Pt(dpk)Cl_2]$ can be explained in terms of the reduction electron entering the lowest energy unoccupied π^* orbital of the dpk ligand. The reduction of the ligand is closely followed by a chemical reaction. Although after reduction the negative charge is partially delocalised over the pyridyl ring π systems, it is based mainly on the carbonyl group. This promotes the addition of water to the carbonyl group giving dpk in its geminal diol form, $dpk.H_2O^{1-}$ via the intermediate $dpkH^0$. As chelation of dpk to a metal cation promotes formation of the geminal diol the conversion of $[Pt(dpk)Cl_2]^{1-}$ to $[Pt(dpk.H_2O)Cl_2]^{1-}$ occurs more quickly than for the free ligand. From the results of *in situ* UV/vis/nir experiments $[Pt(dpkH)Cl_2]^0$ would appear to be the most stable species in this series of reactions.

$[Pt(Hdpa)Cl_2]$ undergoes a distended reduction at –0.98 V. The reduced species is unstable, as indicated by *in situ* UV/vis/nir experiments. Consequently the UV/vis spectra could not be accurately assigned and an epr spectrum of $[Pt(Hdpa)Cl_2]^{1-}$ could not be obtained.

5.4 Experimental

The ligands di-2-pyridyl ketone (dpk) and di-2-pyridyl amine (Hdpa) were commercially available from Aldrich and used as bought.

5.4.1 Synthesis of Complexes

5.4.1.1 Synthesis of $[Pt(dpk)Cl_2]$.

A solution of $K_2[PtCl_4]$ (0.208 g, 5.01×10^{-4} moles) in water (5 ml) was added dropwise, with stirring to a solution of dpk (0.092 g, 4.99×10^{-4} moles) in water (5 ml).[89] A yellow solid slowly formed and precipitated out of solution. After 8 hours stirring at room temperature the yellow solid was collected by filtration, washed with water and dried under vacuum to give $[Pt(dpk)Cl_2]$ (0.149 g, 3.31×10^{-4} moles, percentage yield 66.33 %). CHN analysis of $PtC_{11}H_8N_2OCl_2$: calculated 29.35 % C, 1.79 % H, 6.22 % N; found 29.12 % C, 1.81 % H, 5.99 % N.

5.4.1.2 Synthesis of $[Pd(dpk)Cl_2]$.

An aqueous solution of dpk (0.203 g, 1.1×10^{-3} moles) was added, with stirring, to a solution of $K_2[PdCl_4]$ (0.359 g, 1.1×10^{-3} moles) in water (5 ml) containing a slight excess of LiCl (0.055 g, 1.3×10^{-3} moles).[89] The solution was stirred overnight. A pinky brown precipitate formed and was collected by filtration, washed with water and dried to give $[Pd(dpk.H_2O)Cl_2]$ (0.381 g, 1×10^{-3} moles, percentage yield 90.9 %). CHN analysis for $PdC_{11}H_{10}N_2O_2C_{l2}$: calculated 34.81 % C, 2.66 % H, 7.38 % N; found 34.58 % C, 2.42 % H, 7.07 % N.

$[Pd(dpk.H_2O)Cl_2]$ (0.370 g, 9.75×10^{-4} moles) was refluxed in water (37 ml) for 2 hours. The yellow precipitate was collected by filtration and dried under vacuum to give $[Pd(dpk)Cl_2]$ (0.310 g, 8.6×10^{-4} moles, percentage yield 78.18 %). CHN

analysis for $PdC_{11}H_8N_2OCl_2$: calculated 36.55 % C, 2.23 % H, 7.75 % N; found 36.02 % C, 2.07 % H, 7.47 % N.

5.4.1.3 Synthesis of [Pt(Hdpa)Cl_2]

A solution of Hdpa (0.082 g, 4.82×10^{-4} moles) and $K_2[PtCl_4]$ (0.200 g, 4.8×10^{-4} moles) in water (20 ml) were refluxed overnight. The yellow/brown precipitate was collected by filtration, washed with water and dried under vacuum to give [Pt(Hdpa)Cl_2] (0.204 g, 4.67×10^{-4} moles, percentage yield 97.14 %). CHN analysis for $PtC_{10}H_9N_3Cl_2$: calculated 27.47 % C, 2.07 % H, 10.23 % N; found 26.56 % C, 2.03 % H, 10.23 % N.

CHAPTER 6:

Studies on the complexes [Pt(5,5'-$(Me)_2$-bpy)(mnt)] and [Pt(5,5'-$(CO_2Et)_2$-bpy)(mnt)].

Chapter 6 Studies on the Complexes [Pt(5,5'-(Me)$_2$-bpy)(mnt)] and Pt(5,5'-(CO$_2$Et)$_2$-bpy)(mnt)]

Reported in this chapter are the synthesis, redox chemistry, spectroelectrochemistry (UV/vis/nir, epr) and emission spectra (both fluid and frozen solution) of the complexes [Pt(5,5'-(Me)$_2$-bpy)(mnt)] and [Pt(5,5'-(CO$_2$Et)$_2$-bpy)(mnt)] , (mnt = maleonitriledithiolate). In this chapter evidence is presented that the electronic character of the redox active orbital is similar in each case, *ie* it is the lowest unoccupied π^* orbital of the (X)$_2$-bpy ligand. For both complexes the HOMO is of mixed Pt/mnt character. These complexes luminesce in both fluid solution and at 77 K. Both complexes have a ^{3}{d(Pt)/p(S)$\rightarrow\pi^*$(bpy)} emitting state although if the excitation energy is >20,000 cm^{-1} [Pt(5,5'-(Me)$_2$-bpy)(mnt)] shows both ^{3}{d(Pt)/p(S)$\rightarrow\pi^*$(bpy)} and ^{3}{d(Pt)/p(S)$\rightarrow\pi^*$(mnt)} emitting states.

6.1 Introduction

Research involving the excited state processes of transition metal diimine complexes has played a major part in the development of inorganic photochemistry over the last thirty years.[102-104] Much of the early work such as that by Webb *et al.* involved complexes such as PtX_4^{2-} (X = halide), $Pt(CN)_4^{2-}$ and Pt(diimine)X$_2$, for which emission was observed at 77 K either in the solid state or in frozen glasses.[102] In 1983 Johnson and co-workers reported the synthesis and characterisation of a series of luminescent square planar complexes of the general formula $[M(L)(L')(mnt)]^{n-}$ (n = 1, M = Rh, Ir; n = 0, M = Pt; L = L' = CO, P(OR)$_3$).[104] Emission from these complexes was observed at room temperature in the solid state and at 77 K in frozen solution. Both the emission spectra and the excitation spectra are highly structured. The similarity of these spectra, including the vibrational structure associated with the metal-mnt moiety, indicated that the complexes possessed a common emitting state. This, along with the decrease in energy of the emission and absorption maxima with

increasing electron donor ability of the L and L' ligand set, supported the assignment of the emitting state as MLCT involving the dithiolate ligand.[104]

Until the work by Zuleta and co-workers in 1990, luminescence from d^8 complexes in fluid solution had been a relative rarity.[105] A series of platinum (diimine) (dithiolate) complexes having the general formula Pt(N-N)(S-S) were prepared. Prior to this only a few complexes of this type had been reported.[106] All solution luminescent complexes of Pt(II) found to date contain a diimine or related hetero aromatic chelating ligand. These systems exhibited a broad, intense absorption band in the visible region of the spectrum that was highly solvatochromic. Luminescence was detected in both the solid state and fluid solution at room temperature.[105]

Zuleta noted that for a given dithiolate, changing the diimine ligand gave a small shift in the energy and a small change in the intensity of the emission.[105] In contrast, changing the dithiolate gave completely different emissive behaviour. The difference was particularly noticeable on changing from a 1,2-dithiolate such as mnt, to a 1,1-dithiolate such as ecda, (ethyl-2-cyano-3,3-dithioacrylate). All Pt(diimine)(mnt) complexes showed weak but structured luminescence at 298 K. As the temperature decreased to 77 K there was a corresponding increase in intensity and a sharpening of the structure. Zuleta noted that for mnt complexes the intensity of the luminescence and emission maxima varied with the N donor, being weakest for [Pt(bpy)(mnt)] and strongest for [Pt(4,4'-$(Me)_2$-bpy)(mnt)].[105] At room temperature in the solid state, the i-mnt (2,2-dicyano-1,1-ethylene dithiolate) and ecda compounds showed a more intense but unstructured luminescence than the mnt compounds and indeed no structure was discernible at 77 K. On cooling from 298 K to 196 K the emission maxima of the i-mnt and ecda complexes shift to lower energy by 10-30 nm, followed by a further 10-30 nm shift upon cooling to 77 K. This behaviour is known as a rigidochromic shift and is commonly observed in emission spectra of Pt(diimine)(dithiolate) complexes on cooling.[105, 107, 108]

Many studies have been undertaken over the years to elucidate the origins of the emitting state in Pt(diimine)(dithiolate) complexes.[34, 107-109] The low energy band in the absorption spectra exhibits solvent dependence and the energy of the band increases with increasing solvent polarity. Zuleta *et al.* probed the basis of this solvatochromism by systematic ligand variation of the complexes of the general structure Pt(N-N)(S-S).[108] It was noted that the solvatochromic band is present in diimine complexes containing unsaturated or saturated dithiolates, but absent in complexes containing a saturated diamine and an unsaturated dithiolate, indicating that for the solvent dependent transition a π system on the N donor is needed but not necessarily on the dithiolate. Hence the LUMO in such complexes is mainly of π^* diimine character. [Pt(4,4'-$(Me)_2$-bpy)Cl_2] does not show intense solvatochromism whereas [Pt(4,4'-$(Me)_2$-bpy)(edt)], with a saturated sulfur chelating ligand does, suggesting that the HOMO has significant sulfur character. Given that the solvatochromism is of the negative type, *ie* the transition shifts to higher energy with increasing solvent polarity, Zuleta *et al.* postulated that the ground state is highly polar and that upon excitation the dipole moment is greatly reduced, or even reversed.[34] Extended Hückel Molecular Orbital (EHMO) calculations were carried out for model diimine dithiolate and bis(thiolate) complexes.[34, 108] The LUMO was found to be almost exclusively π^* diimine in character whereas the HOMO is a combination of Pt(d) and S(p) atomic orbitals. Zuleta *et al.* thus ascribed the solvatochromic absorption as a Pt(d)/S(p)$\rightarrow\pi^*$diimine transition in all cases.[34]

For all of the Pt diimine complexes, except those of mnt, the broad asymmetric emission was assigned as having the same orbital parentage as the solvatochromic absorption, but arising from a state of different multiplicity *ie* ^{3}{d(Pt)/p(S)$\rightarrow\pi^*$(diimine)}. All of the mnt complexes had emission spectra with similar types and degrees of structuring indicating that they possessed a common emitting state. On the basis of systematic ligand variation and molecular orbital calculations Zuleta assigned this state as ^{3}{d(Pt)/p(S)$\rightarrow\pi^*$(mnt)}.[34, 108]

The interest in Pt(diimine)(dithiolate) complexes has been fuelled by their potential use as dye sensitizers in the conversion of solar energy to electricity.[2, 109, 110] Large-band-gap semiconductors such as titanium dioxide (TiO_2) are used to absorb solar light. Although they are more stable against photocorrosion that small-band-gap semiconductors such as Si or GaAs, their large band gap greatly reduces the fraction of solar energy that can be harvested. The efficiency of these solar cells can be greatly improved by using a high concentration of dopants or electronically excited states of molecules (dye sensitizers) where the electronically excited adsorbed dye injects an electron into the conduction band of the TiO_2 semiconductor.

The schematic shown below shows a model for dye sensitisation in a regenerative photoelectrochemical cell.[2] The cell consists of a molecular sensitizer (*eg* Pt(diimine)(dithiolate)) anchored to the semiconductor surface, a solution containing relay electrolyte and a counter electrode. Light promotes the sensitizer to its excited electronic state and the excited dye injects an electron into the conduction band of the

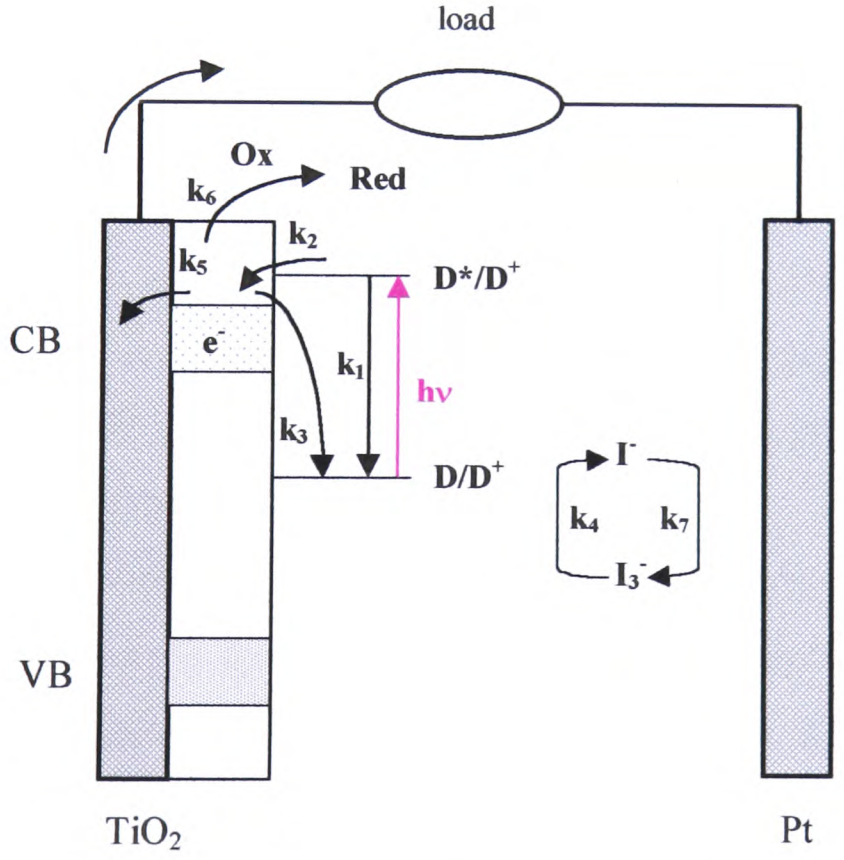

Figure 6. 1 Schematic representation of the elementary steps involved in a regenerative photochemical cell for light conversion based on dye sensitization of semiconductors.

semiconductor (at a rate k_2). The dye itself is oxidised. The injected electron then flows at a rate k_5 through an external circuit to do useful work. The oxidised dye is reduced to its initial state by an electron donor, I^- (k_4), acting as a relay electrolyte. The oxidised electrolyte (I_3^-) is reduced at the counter electrode (k_7) and the solar cell is therefore regenerative. Loss mechanisms, which will affect the efficiency of the cell, include radiative and non-radiative decay of the excited dye molecule (k_1), recombination of the photoinjected electron with the oxidised dye (k_3) and recombination of the conduction band electrons with the oxidised electron donor (k_6).[2]

For an efficient sensitizer the dye absorption must overlap the solar emission spectrum so as to allow maximum power conversion. The Pt(d)/S(p)→π^*diimine charge transfer transitions of Pt(diimine)(dithiolate) can be tuned in two ways:

i) Introducing a diimine ligand with a low-lying π^* molecular orbital (LUMO).

ii) Destabilising the HOMO by increasing the donor properties of the dithiolate ligand.

Using the second approach and varying the dithiolate ligands, Islam and co-workers were able to tune the excited state by *ca.* 4000 cm^{-1}.[110] Cummings *et al.* used both approaches to carry out a study on two series of Pt(diimine)(dithiolates). The first series comprised of Pt(dbbpy)(dithiolate) where dbbpy = 4,4'-*tert*-butyl-2,2'-bipyridine and the dithiolates are tbcda, cpdt, dmqdt, mnt and tdt.[111] The structures and full names of this series are shown below in Figure 6.2. The second series was of Pt(diimine)(tdt) complexes where tdt = toluene-3,4-dithiolate and the diimines are 3,4,7,8-tetramethyl-1,10-phenanthroline (tmphen), 4,4'-(t-Bu)$_2$-bpy (dbbpy), 4,4'-(Me)$_2$-bpy (dmbpy), phenanthroline (phen), 5-chloro-1,10-phenanthroline (Cl-phen) and 4,4'-(CO_2Et)$_2$-bpy (EC-bpy).

All compounds displayed solvatochromic absorption bands and solution luminescence which were attributed to a common charge-transfer-to-diimine excited state.[111] As with earlier work by Zuleta, the spin character of the emissive state was assigned to be different from that of the ground state, making the photoluminescence a formally spin-forbidden process.[111] The purity of the spin states and the selection rules are substantially reduced in heavy metal complexes such as those of Pt(II). Cummings *et al.* found that changing the substituents on the bpy or phen affected the energy of the LUMO, which is based on the diimine.[111] Electron donating groups increase the energy of the LUMO and the consequent energy gap while electron withdrawing groups have the opposite effect.

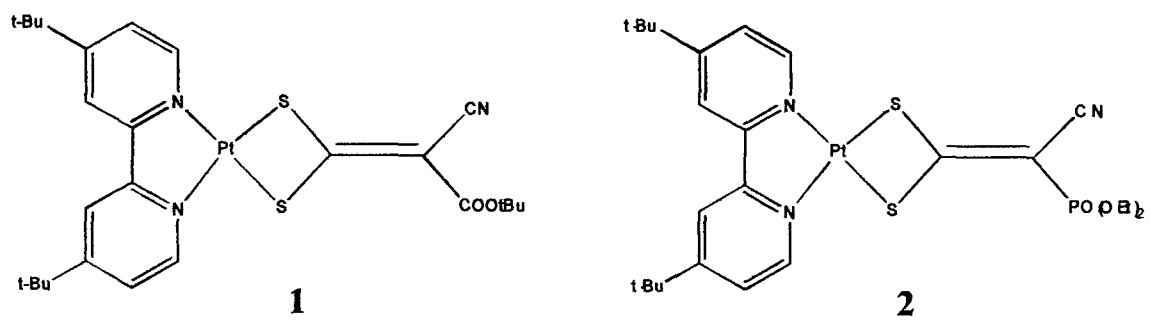

Figure 6. 2 [Pt(4,4'-(*t*-Bu)$_2$-bpy)(dithiolates)] studied by Cummings *et al.*.[111] **1** = tbcda (1-(tert-butylcarboxy)-1-cyanoethylene-2,2-dithiolate), **2** = cpdt (1-diethylphosphonate-1-cyanoethylene-2,2-dithiolate), **3** = edt (1,2-ethanedithiolate), **4** = dmqdt (6,7-dimethyl-quinoxaline-2,3-dithiolate), **5** = mnt (maleonitriledithiolate), **6** = tdt (toluene-3,4-dithiolate).

The energy of the HOMO is affected by the nature of the dithiolate, with the charge transfer absorption band energy increasing along the series tdt<mnt<dmqdt~edt<tbcda~cpdt. Cummings noted that the complexes with 1,1-dithiolates had larger charge transfer energies than those complexes with 1,2-dithiolates, consistent with HOMOs that are lower in energy.[111]

Although Pt(diimine)(dithiolate) complexes are clearly of use in solar energy conversion cells, the use of these complexes would be limited to systems that operate anaerobically as these complexes are known to undergo photo-oxidation under aerobic conditions.[112, 113]

The complexes [Pt(5,5'-$(Me)_2$-bpy)(mnt)] and [Pt(5,5'-$(CO_2Et)_2$-bpy)(mnt)] will be studied in this chapter to investigate whether changing the bpy substituent from an electron-donor (Me) to an electron-acceptor (CO_2Et) will allow tuning of the mixed ligand-to-diimine charge transfer transition. The reasoning behind this work lies in the results of Chapter 3 where the comparison of $E_{½}$ values for [Pt(5,5'-$(X)_2$-bpy)Cl_2] and the Hammett parameter σ_m with the corresponding values for the 4,4' analogue indicate that the 5,5' position is electronically the most important site of substitution. By this argument, changing the substituents at the 5,5' position should allow the excited state to be tuned to a greater degree. Work reported here indicates that the LUMO is primarily based on the diimine ligand while the HOMO is based on the mnt. The solvatochromic absorption band was attributed to a Pt(d)/S(p)→π^*diimine charge transfer transition. Excitation/emission studies indicated that the emitting state was a different multiplicity to the solvatochromic absorption *ie* it is a triplet state, and the emitting state of [Pt(5,5'-$(CO_2Et)_2$-bpy)(mnt)] is assigned as ^{3}{d(Pt)/p(S)→π^*(bpy)}. [Pt(5,5'-$(Me)_2$-bpy)(mnt)] has two emitting states ^{3}{d(Pt)/p(S)→π^*(bpy)} and ^{3}{d(Pt)/p(S)→π^*mnt}. When the excitation energy is <20,000 cm^{-1} there is insufficient energy to populate the mnt excited state and only emission from ^{3}{d(Pt)/p(S) →π^*(bpy)} is observed.

6.2 Results and Discussion

The appearance of the [Pt(5,5'-$(X)_2$-bpy)(mnt)] complexes differ from those of their Cl analogues. [Pt(5,5'-$(Me)_2$-bpy)(mnt)] is a bright orange powder, whereas the Cl analogue is a pale yellow green crystalline substance. [Pt(5,5'-$(CO_2Et)_2$-bpy)(mnt)] is a deep purple powder; the Cl analogue is a dark red powder.

6.2.1 Redox Chemistry of [Pt(5,5'-$(X)_2$-bpy)(mnt)]

Cyclic voltammetric studies of [Pt(5,5'-$(Me)_2$-bpy)(mnt)] and [Pt(5,5'-$(CO_2Et)_2$-bpy)(mnt)] were carried out at 293 K in 0.1 M $TBABF_4$/DMF and both revealed a fully reversible, one electron reduction in the range –0.51—1.12 V, see Figures 6.3 and 6.4 and Table 6.1. A second reduction process is observed at potentials 460-690 mV more negative than the first. As with the Cl analogues, the potential separation between the reduction processes is associated with the spin pairing energy of the two added electrons in the redox-active orbital. The second reduction is fully reversible for [Pt(5,5'-$(CO_2Et)_2$-bpy)(mnt)] and quasi-reversible for [Pt(5,5'-$(Me)_2$-bpy)(mnt)]. [Pt(5,5'-$(Me)_2$-bpy)(mnt)] shows an irreversible oxidation attributed to the mnt ligand while the oxidation attributed to the mnt ligand in [Pt(5,5'-$(CO_2Et)_2$-bpy)(mnt)] is quasi-reversible.

Table 6.1 shows the redox properties of [Pt(5,5'-$(Me)_2$-bpy)(mnt)] and [Pt(5,5'-$(CO_2Et)_2$-bpy)(mnt)] along with those of their Cl analogues. The redox potentials of the two reductions are in good agreement, indicating that it is the nature of the diimine ligand that influences the reduction potentials rather than the other ligands attached to the Pt(II) centre.

Upon reduction of [Pt(5,5'-$(Me)_2$-bpy)(mnt)] to the mono-reduced species in 0.1 M $TBABF_4$/DMF, the solution changes colour from orange to olive green. [Pt(5,5'-$(CO_2Et)_2$-bpy)(mnt)] is yellow in solution while the mono-reduced species is green.

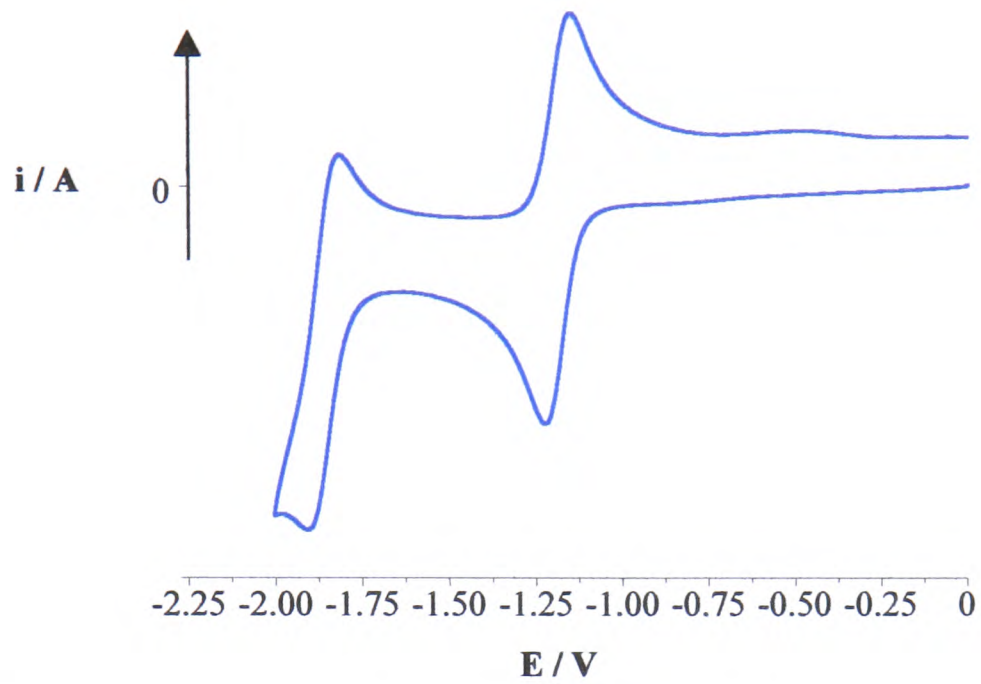

Figure 6. 3 Cyclic voltammogram of [Pt(5,5'-$(Me)_2$-bpy)(mnt)] at 298 K in 0.1 M $TBABF_4$/DMF, scan rate 0.2 V/s.

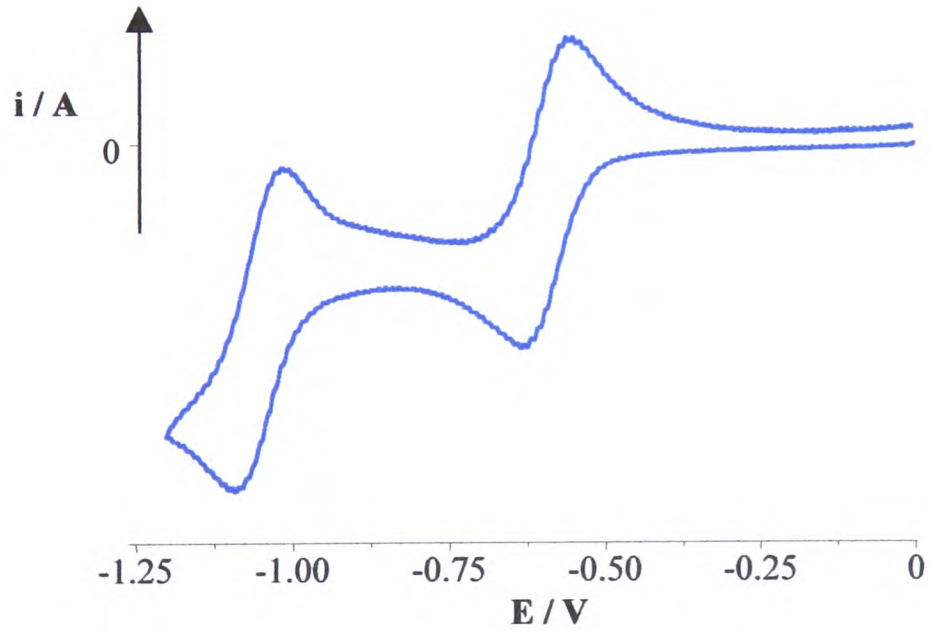

Figure 6. 4 Cyclic voltammogram of [Pt(5,5'-$(CO_2Et)_2$-bpy)(mnt)] in 0.1 M $TBABF_4$/DMF at 298 K, scan rate 0.1 V/s.

Table 6. 1 Redox potentials of complexes [Pt(5,5'-$(X)_2$-bpy)L] where X = Me or CO_2Et and L = mnt or Cl_2, at 293 K in 0.1 M $TBABF_4$/DMF.

Complex	E_1 / V	E_2 / V	E_3 / V	$E_1 - E_2$ / V
[Pt(5,5'-$(Me)_2$-bpy)(mnt)]	-1.12 (0.073)[a]	-1.81 (0.151)[a]	1.18[b]	0.69
[Pt(5,5'-$(CO_2Et)_2$-bpy)(mnt)]	-0.51 (0.063)	-0.97 (0.061)	1.24[c]	0.46
[Pt(5,5'-$(Me)_2$-bpy)Cl_2]	-1.17 (0.081)	-1.82 (0.156)	-	0.65
[Pt(5,5'-$(CO_2Et)_2$-bpy)Cl_2]	-0.53 (0.074)	-1.03 (0.071)	-	0.50

a) the values in parentheses are $E_{pa} - E_{pc}$. b) irreversible, anodic peak potential quoted. c) quasi-reversible.

6.2.2 UV/vis/nir Spectroelectrochemistry

The UV/vis/nir spectroelectrochemistry of [Pt(5,5'-$(Me)_2$-bpy)(mnt)] and [Pt(5,5'-$(CO_2Et)_2$-bpy)(mnt)] was carried out at approximately 233 K in 0.1 M $TBABF_4$/DMF. The spectrum of [Pt(5,5'-$(Me)_2$-bpy)(mnt)] shows an intense high energy band at 36,000 cm^{-1} (ε = 18,600 M^{-1} cm^{-1}), a second intense band at 31,700 cm^{-1} (ε = 22,300 M^{-1} cm^{-1}), a band in the near UV at 25,100 cm^{-1} (ε = 4,700 M^{-1} cm^{-1}) and a broad band in the visible region at 21,500 cm^{-1} (ε = 4,700 M^{-1} cm^{-1}), see Figure 6.5. The bands at 36,000 cm^{-1} and 31,700 cm^{-1} were assigned as bpy $\pi \rightarrow \pi^*$ intraligand transitions and the band at 25,100 cm^{-1} was assigned as an mnt $\pi \rightarrow \pi^*$ intraligand transition in line with the UV/vis spectrum of

Na_2(mnt) which shows mnt intraligand transitions at 25.1 kcm^{-1} and 35.3 kcm^{-1}. One of the chief characteristics of Pt(diimine)(dithiolates) is the strong negative solvatochromism exhibited by the lowest energy absorption band *ie* the energy of the lowest energy absorption increases with increasing solvent polarity. Numerous papers have studied this negative solvatochromism.[34, 105-107] Zuleta and co-workers observed that the intense solvatochromic transition occurs only in complexes containing an unsaturated diimine ligand and S (or Se) donor atoms, indicating that the solvatochromic transition is from a filled orbital having significant sulfur p character to an unoccupied level which is a π^* diimine orbital.[108] The basis of solvent dependence of the transition is rationalised in terms of a large dipole moment change between the ground and excited states. The low solubility of mnt complexes has been noted and indeed the complexes studied here were insoluble in all but the most polar solvents (DMF, DMSO, benzonitrile and propionitrile), making a comprehensive study of solvatochromism difficult.[108] From the limited results obtained it would appear that the lowest energy band decreases in energy with increasing solvent polarity. However, this result was treated with caution given the small range of solvent polarities studied and the large experimental errors involved. On the basis of the solvatochromism, rather than its nature, the lowest energy band at 21,500 cm^{-1} (ε = 4,700 M^{-1} cm^{-1}) was attributed to a mixed Pt(d)/S(p)-π^*diimine (*ie.* bpy) charge transfer transition in line with work by Zuleta.[34, 108] Mixing of the Pt(d) and S(p) orbitals in the HOMO has resulted in a smaller HOMO-LUMO gap in [Pt(diimine)(dithiolate)] compared to [Pt(diimine)Cl_2] and hence a shift of the low energy band to decreased wavenumber.

As previously discussed in Section 3.2.1.2, the UV/vis/nir spectrum of $Na^+(bpy^{1-})$ has three characteristic features diagnostic for the presence of co-ordinated bpy^{1-}. These are an nir band at *ca.* 10 kcm^{-1}, comprising of three peaks or shoulders, a doublet in the visible region at *ca.* 20 kcm^{-1} and an intense band in the near UV at *ca.* 25 kcm^{-1}.[29] On reduction of [Pt(5,5'-$(Me)_2$-bpy)(mnt)] to its mono-reduced form, see Figure 6.5 and Table 6.2, the spectrum obtained is similar to that obtained for $Na^+(bpy^{1-})$ (and indeed for $[Pt(5,5'\text{-}(Me)_2\text{-}bpy)Cl_2]^{1-}$, see Figure 3.12), with a broad band in the near ir

and several peaks in the 20-25 kcm^{-1} region. The band growth is characteristic of this type of species with the bpy^{1-} internal transitions increasing while the corresponding bpy $\pi \rightarrow \pi^*$ intraligand transitions at 36,000 cm^{-1} and 31,700 cm^{-1} collapse. The band at 24,000 cm^{-1} probably includes a contribution from the mnt $\pi \rightarrow \pi^*$ transition as it is unaffected by the reduction of the bpy ligand and should remain at 25,100 cm^{-1}. The isosbestic points at 30 kcm^{-1}, 33.5 kcm^{-1}, 35.6 kcm^{-1} and 36.5 kcm^{-1} indicate a clean conversion from the neutral complex to the mono-reduced anion. On resetting the potential back to 0 V, the original spectrum is regenerated indicating the electron transfer is fully chemically reversible.

On generation of the di-reduced species an intense band at 35,700 cm^{-1} (ε = 21,200 M^{-1} cm^{-1}) grows in, along with a broad, intense band with shoulders in the 22-29 kcm^{-1} region, see Figure 6.6 and Table 6.2. The band at 10.9 kcm^{-1} (ε = 1,700 M^{-1} cm^{-1}) has collapsed and blue shifted. This new band covers the region 10-18 kcm^{-1} with shoulders at 13,700 cm^{-1} (ε = 2,100 M^{-1} cm^{-1}) and 15,000 cm^{-1} (ε = 2,300 M^{-1} cm^{-1}), see Figure 6.6. The bands attributed to bpy^{1-} have collapsed. König and Kremer have previously assigned the electronic spectrum of bpy^{2-} as consisting of a peak at *ca.* 16.4 kcm^{-1} and a second very intense band at *ca.* 26.8 kcm^{-1}.[29] This doublet would be expected to move to higher energy than is observed for bpy^{2-} because of the effects of complexation and of the electron donating Me substituents. Assigning UV/vis/nir bands is notoriously difficult and in this case is made more difficult as the absorption spectra of 5,5'-$(Me)_2$-bpy^{2-} could not be obtained as the second reduction process occurred at potentials more negative than the solvent breakdown. No absorption spectra for $[Pt(5,5'\text{-}(Me)_2\text{-}bpy)Cl_2]^{2-}$ could be obtained as the di-reduced species is unstable. Despite this the broad band with shoulders at 25,600 cm^{-1} (ε = 13,600 M^{-1} cm^{-1}) and 26,700 cm^{-1} (13,400 M^{-1} cm^{-1}) is assigned to bpy^{2-} with the now doubly occupied LUMO involved in transitions to higher energy empty π^* antibonding orbitals. This is in agreement with the results of cyclic voltammetry on [Pt(5,5'-$(Me)_2$-bpy)(mnt)], see Section 6.2.1 that indicates the spin pairing of the reduction electrons does occur.

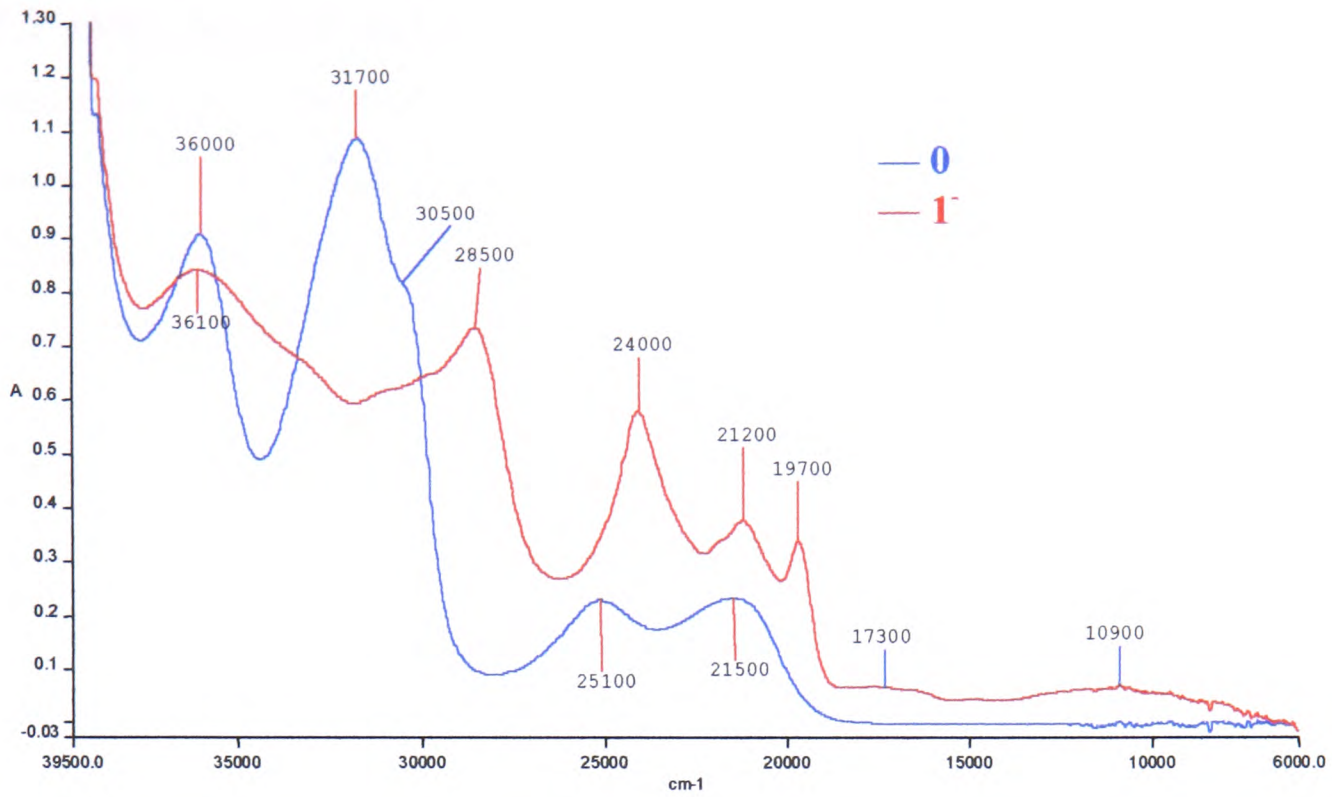

Figure 6. 5 UV/vis/nir spectra of $[Pt(5,5'\text{-}(Me)_2\text{-}bpy)(mnt)]^{0/1-}$ at 231 K in 0.1 M $TBABF_4$/DMF, E_{gen} = -1.5 V.

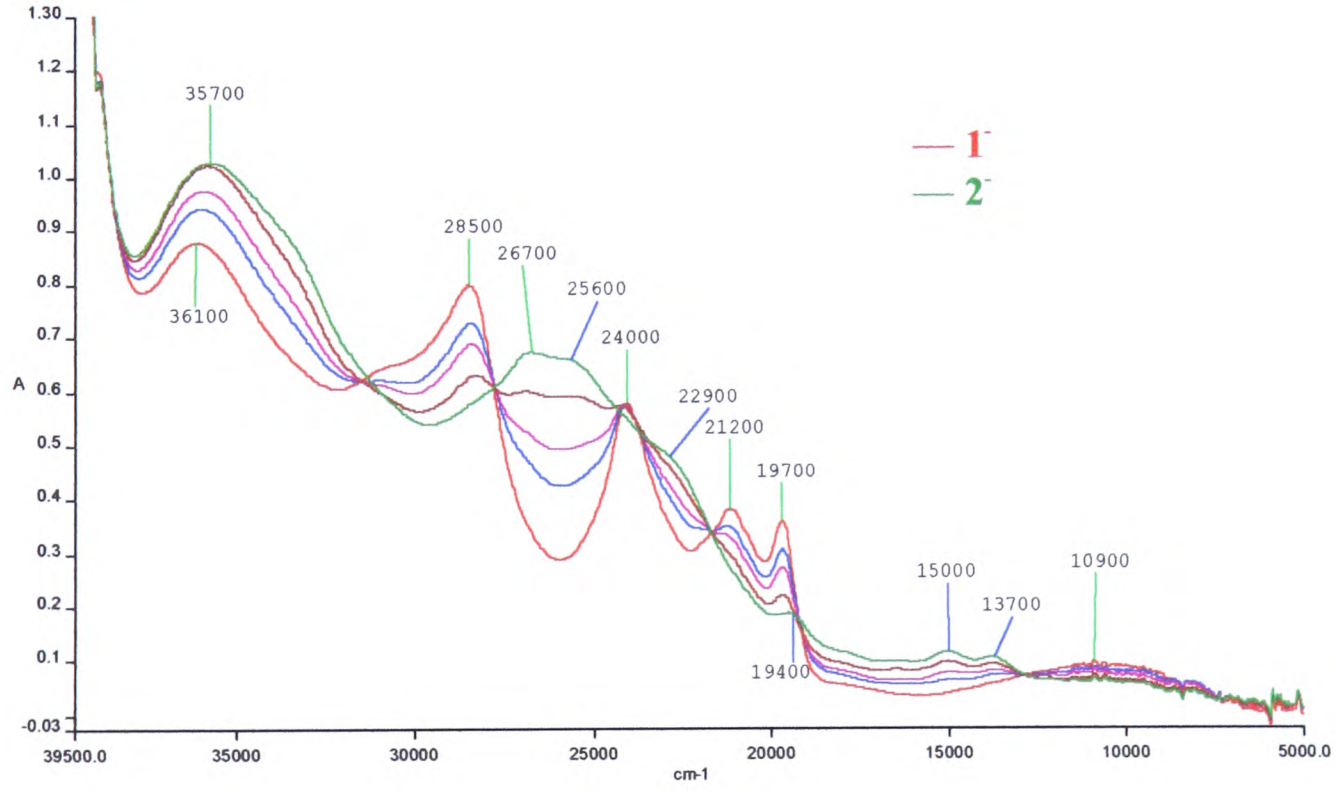

Figure 6. 6 UV/vis/nir spectra of $[Pt(5,5'\text{-}(Me)_2\text{-}bpy)(mnt)]^{1-/2-}$ at 231 K in 0.1 M $TBABF_4$/DMF, E_{gen} = -2.0 V.

The resemblance between the UV/vis/nir spectra of $Na^{+}(bpy^{1-})$, $[Pt(5,5'\text{-}(Me)_2\text{-}bpy)Cl_2]^{1-}$ and $[Pt(5,5'\text{-}(Me)_2\text{-}bpy)(mnt)]^{1-}$ indicates that the reduction electron enters an orbital that is primarily based on the $(Me)_2$-bpy ligand and more precisely on the bpy part of the ligand. Thus the one electron reduction product can be formulated as $[Pt(II)(5,5'\text{-}(Me)_2\text{-}bpy)^{1-}(mnt)]^{1-}$. The same assignment for the reduction product of $[Pt(5,5'\text{-}(Me)_2\text{-}bpy)Cl_2]$ was made in Chapter 3.

On generation of the mono-oxidised species $[Pt(5,5'\text{-}(Me)_2\text{-}bpy)(mnt)]^{1+}$ the peaks attributed to the bpy $\pi \rightarrow \pi^*$ intraligand transitions partially collapse as do the peaks at 25,100 cm^{-1} and 21,500 cm^{-1}. However, the spectrum showed signs of decomposition at this point and the generation potential was switched back to 0 V. On resetting the generation potential back to 0 V the spectrum of the neutral species was not regenerated, indicating that the electron transfer is not chemically reversible. This is in line with cyclic voltammetric studies on the complex.

The UV/vis/nir spectrum of $[Pt(5,5'\text{-}(CO_2Et)_2\text{-}bpy)(mnt)]$ shows an intense peak at 33,900 cm^{-1} (ε = 14,100 M^{-1} cm^{-1}) with lower energy shoulders at 31,800 cm^{-1} (ε = 11,400 M^{-1} cm^{-1}) and 30,000 cm^{-1} (ε = 12,300 M^{-1} cm^{-1}) as well as bands at 25,700 cm^{-1} (ε = 1,900 M^{-1} cm^{-1}) and 18,400 cm^{-1} (ε = 2,000 M^{-1} cm^{-1}), see Figure 6.7 and Table 6.2. The bands at >29 kcm^{-1} were assigned as having bpy $\pi \rightarrow \pi^*$ intraligand transition character and the band at 25,700 cm^{-1} was assigned as a mnt $\pi \rightarrow \pi^*$ intraligand transition in line with the assignment made for the spectrum of $[Pt(5,5'\text{-}(Me)_2\text{-}bpy)(mnt)]$. As for the Me analogue, $[Pt(5,5'\text{-}(CO_2Et)_2\text{-}bpy)(mnt)]$ shows poor solubility in all but the most polar of solvents. The band at 18,400 cm^{-1} showed solvatochromism (band energy decreasing with increasing solvent polarity) but the nature of the solvatochromism was ignored on the basis of experimental error. The band at 18,400 cm^{-1} was assigned as the Pt(d)/S(p)$\rightarrow\pi^*$diimine charge transfer transition.

The UV/vis/nir spectrum of $[Pt(5,5'\text{-}(CO_2Et)_2\text{-}bpy)(mnt)]^{1-}$ differs from that obtained for $[Pt(5,5'\text{-}(Me)_2\text{-}bpy)(mnt)]^{1-}$, although it does bear similarities to the UV/vis/nir

spectra of $[Pt(5,5'\text{-}(CO_2Et)_2\text{-}bpy)Cl_2]^{1-}$ and $5,5'\text{-}(CO_2Et)_2\text{-}bpy^{1-}$. The broad nir band at 10-15 kcm^{-1} for $5,5'\text{-}(CO_2Et)_2\text{-}bpy^{1-}$, see Section 3.2.2.2, shifts to higher energy on complexation and for $[Pt(5,5'\text{-}(CO_2Et)_2\text{-}bpy)(mnt)]^{1-}$ appears at 16,900 cm^{-1} (ε = 3,700 M^{-1} cm^{-1}), see Figure 6.7. This shift to higher energy arises because on complexation the LUMO is stabilised, increasing the energy gap between the LUMO and LUMO-1. Thus all the transitions associated with co-ordinated bpy^{1-} shift to higher energy. Consequently the band at 22,000 cm^{-1} (ε = 5,300 M^{-1} cm^{-1}) was assigned to a co-ordinated bpy^{1-} transition. The band at 25,700 cm^{-1} (ε = 7,100 M^{-1} cm^{-1}) was also assigned to a co-ordinated bpy^{1-} transition although it will have some mnt $\pi \rightarrow \pi^*$ character in line with the assignments made for $[Pt(5,5'\text{-}(Me)_2\text{-}bpy)(mnt)]^{1-}$. The resemblance between the UV/vis/nir absorption spectra of $[Pt(5,5'\text{-}(CO_2Et)_2\text{-}bpy)(mnt)]^{1-}$ and $5,5'\text{-}(CO_2Et)_2\text{-}bpy^{1-}$, see Section 3.2.1.2, indicates that the reduction electron enters an orbital that is localised on the $5,5'\text{-}(CO_2Et)_2$-bpy ligand. Consequently the one electron reduction product can be formulated as $[Pt(II)(5,5'\text{-}(CO_2Et)_2\text{-}bpy)^{1-}(mnt)]^{1-}$ in the same way that the one electron reduction product of the Me analogue can be formulated as $[Pt(II)(5,5'\text{-}(Me)_2\text{-}bpy)^{1-}(mnt)]^{1-}$.

Upon conversion of $[Pt(5,5'\text{-}(CO_2Et)_2\text{-}bpy)(mnt)]^{1-}$ to $[Pt(5,5'\text{-}(CO_2Et)_2\text{-}bpy)(mnt)]^{2-}$ the bands associated with bpy^{1-} at 16.9 kcm^{-1}, 22.0 kcm^{-1} and 25.7 kcm^{-1} collapse, to be replaced by an intense doublet with peaks at 20,700 cm^{-1} (ε = 55,500 M^{-1} cm^{-1}) and 22,300 cm^{-1} (ε = 25,500 M^{-1} cm^{-1}), see Figure 6.8. This doublet grows in at 19-21 kcm^{-1} on reduction of the free ligand, see Section 3.2.1.2 and 20-23 kcm^{-1} on di-reduction of $[Pt(5,5'\text{-}(CO_2Et)_2\text{-}bpy)Cl_2]$, see Section 3.2.2.2, the shift to higher energy again being brought about by complexation. Electrochemical data, see Section 6.2.1, suggest that spin pairing of the two reduction electrons occurs as it does with the Cl analogue and the free ligand, see Chapter 3. Thus these intense peaks are assigned as intraligand transitions from the now doubly occupied LUMO to higher energy, empty π^* antibonding orbitals. The isosbestic points at 18.6 kcm^{-1}, 24.8 kcm^{-1},

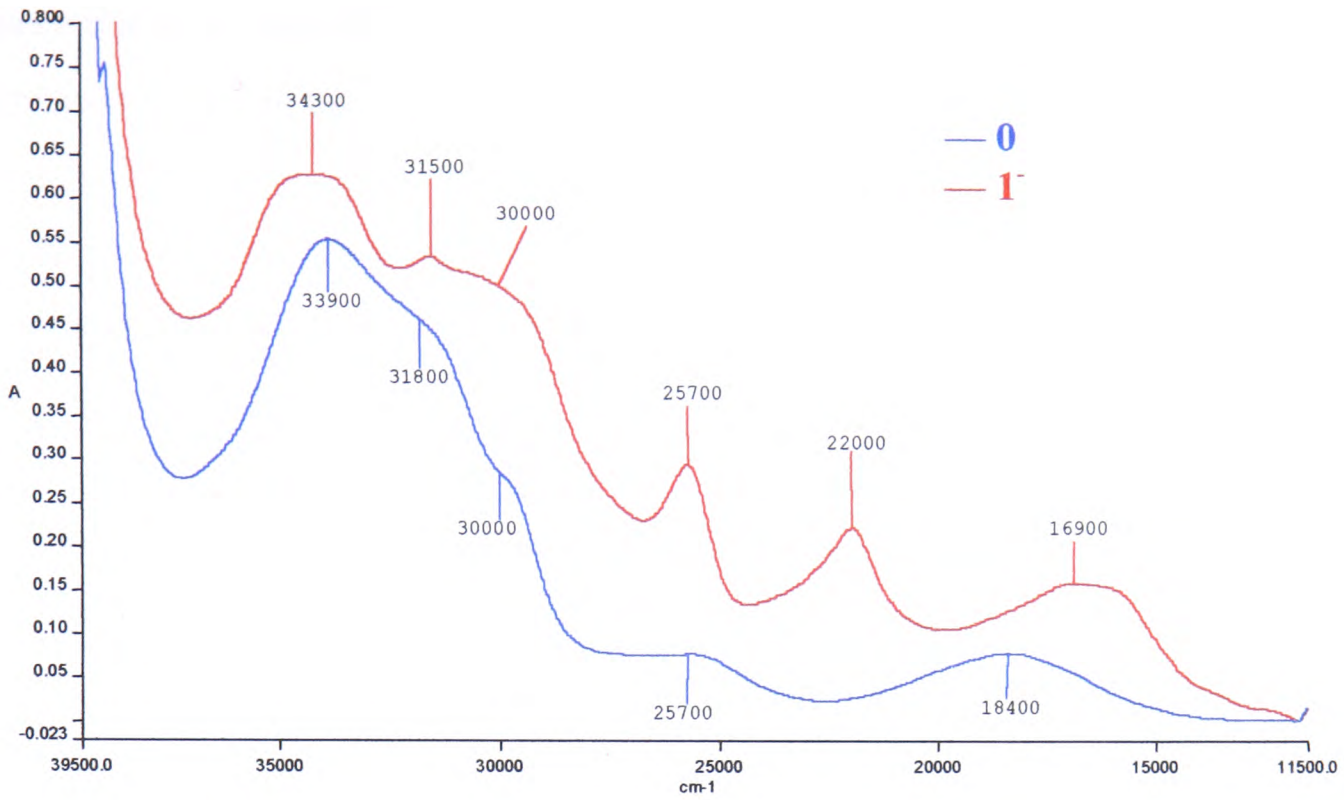

Figure 6.7 UV/vis/nir spectra of $[Pt(5,5'\text{-}(CO_2Et)_2\text{-}bpy)(mnt)]^{0/1-}$ in 0.1 M $TBABF_4$/DMF at 228 K, E_{gen} = -0.80 V.

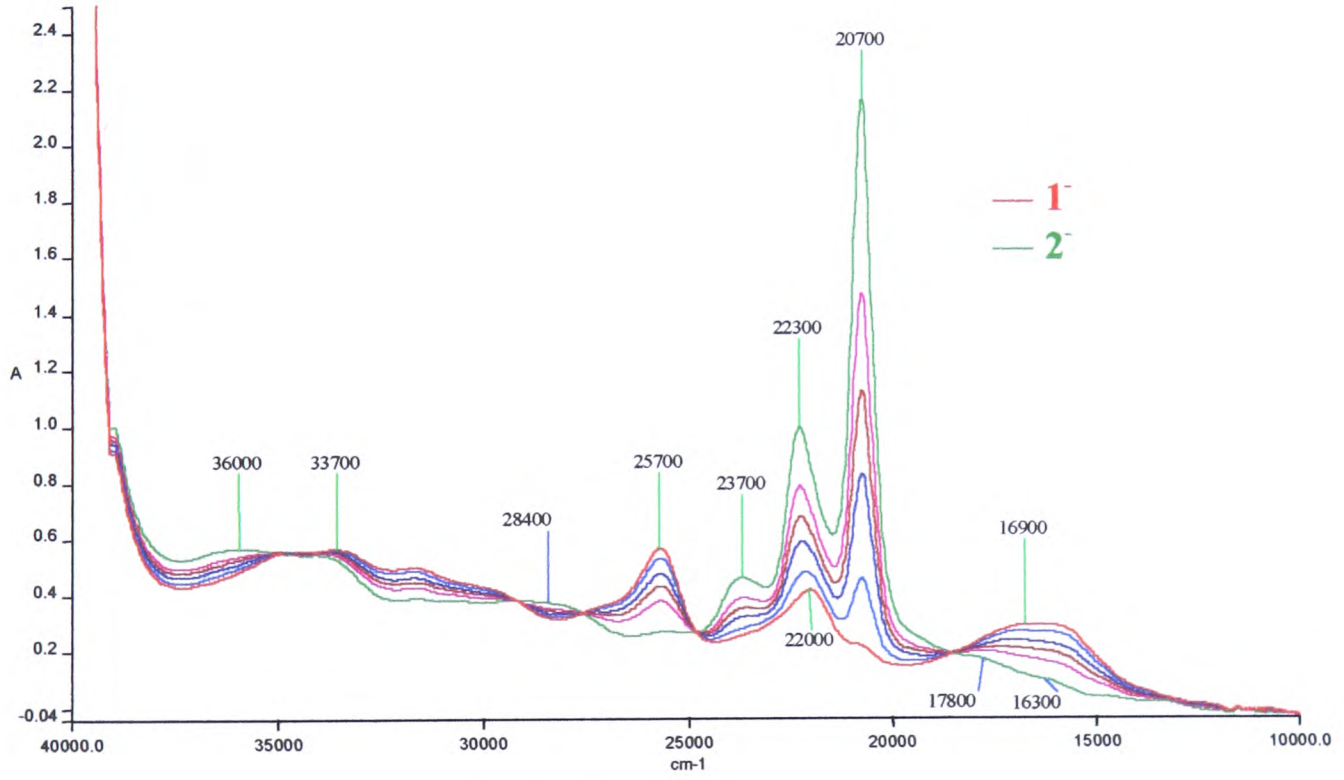

Figure 6. 8 UV/vis/nir spectra of $[Pt(5,5'\text{-}(CO_2Et)_2\text{-}bpy)(mnt)]^{1-/2-}$ in 0.1 M $TBABF_4$/DMF at 228 K, Egen = -1.30 V.

27.6 kcm^{-1}, 29.2 kcm^{-1} and 34.8 kcm^{-1} indicate that there is a clean conversion between the mono and di-reduced species with no decomposition. The strong resemblance between the UV/vis/nir spectra of $[Pt(5,5'(CO_2Et)_2\text{-bpy})(mnt)]^{1-/2-}$ and $[Pt(5,5'(CO_2Et)_2\text{-bpy})Cl_2]^{1-/2-}$, see Figure 3.15, justifies the assignment of the MO of the complex as being based on the bpy moiety with little contribution from the Pt or mnt MOs. Thus the two electron reduction product can be formulated as $[Pt(5,5'\text{-}(CO_2Et)_2\text{-bpy})^{2-}(mnt)]^{2-}$.

On resetting the generation potential back to 0 V after generating $[Pt(5,5'\text{-}(CO_2Et)_2\text{-bpy})(mnt)]^{2-}$ the UV/vis/nir of the neutral $[Pt(5,5'\text{-}(CO_2Et)_2\text{-bpy})(mnt)]$ is regenerated indicating that both the reductions of $[Pt(5,5'\text{-}(CO_2Et)_2\text{-bpy})(mnt)]$ are fully chemically reversible.

On the generation of $[Pt(5,5'\text{-}(CO_2Et)_2\text{-bpy})(mnt)]^{1+}$ from $[Pt(5,5'\text{-}(CO_2Et)_2\text{-bpy})(mnt)]^{0}$ the bands associated with the bpy $\pi \rightarrow \pi^*$ intraligand transitions shift to lower energy at 30,400 cm^{-1} (ε = 12,100 M^{-1} cm^{-1}), see Figure 6.9. Studies on the series $[Ru(bpy)_3]^{3+/2+}$ and $[Ir(bpy)_3]^{3+}$ indicate that the $\pi \rightarrow \pi^*$ intraligand transitions associated with co-ordinated bpy commonly shift to lower energy as the positive charge on the complex is increased.[28, 52] The bands at 25,700 cm^{-1} and 18,400 cm^{-1} which have been assigned to transitions involving the mnt part of the compound both collapse indicating that the site of oxidation is based, at least in part, on the mnt ligand.

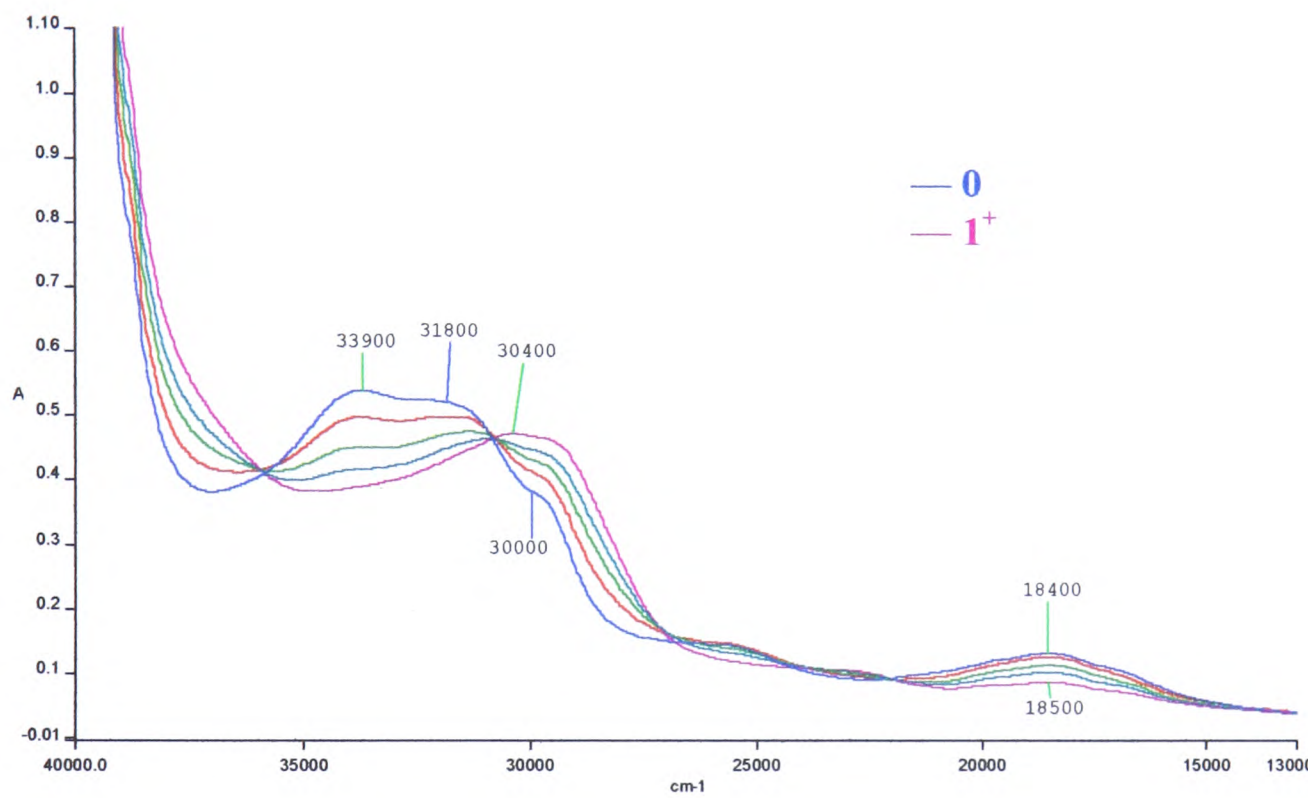

Figure 6. 9 UV/vis/nir of $[Pt(5,5'\text{-}(CO_2Et)_2\text{-}bpy)(mnt)]^{0/1+}$ in 0.1 M $TBABF_4$/DMF at 228 K, E_{gen} = 1.37 V.

Table 6. 2 Peak positions and molar extinction coefficients, ε, for $[Pt(5,5'\text{-}(Me)_2\text{-}bpy)(mnt)]^{1+/0/1-/2-}$ and $[Pt(5,5'\text{-}(CO_2Et)_2\text{-}bpy)(mnt)]^{1+/0/1-/2-}$ in 0.1 M $TBABF_4$/DMF.

Oxidation state	$[Pt(5,5'\text{-}(Me)_2\text{-}bpy)(mnt)]$[a] Peak position / cm^{-1} ( ) ε / M^{-1} cm^{-1}	$[Pt(5,5'\text{-}(CO_2Et)_2\text{-}bpy)(mnt)]$[b] Peak position / cm^{-1} ( ) ε / M^{-1} cm^{-1}
0	36,000 (18,600), 31,700 (22,000), sh 30,500 (16,700), 25,100 (4,700), 21,500 (4,700)	33,900 (14,100), sh 31,800 (11,400), sh 30,000 (12,300), 25,700 (1,900), 18,400 (2,000)
1^-	36,100 (17,700), sh 33,400 (14,000), sh 30,800 (13,000), 28,500 (16,000), 24,000 (11,800), 21,200 (7,800), 19,700 (7,300), 17,300 (1,400), 10,900 (1,700)	34,300 (15,600), 31,500 (13,200), sh 30,000 (12,300), 25,700 (7,100), 22,000 (5,300), 16,900 (3,700)
2^-	35,700 (21,200), sh 33,500 (18,000), sh 28,000 (12,300), 26,700 (13,400), 25,600 (13,600), 22,900 (9,800), 19,400 (2,100), 15, 000 (2,300), 13,700 (2,100)	36,000 (14,400), 28,400 (9,600), 23,700 (11,700), 22,300 (25,500), 20,700 (55,500), 17,800 (4,400), 16,300 (2,500)
1^+	Sh 36,800 (17,200), 31,500 (14,600), 30,300 (12,900), 28,000-18,000 (3,200)	30,400 (12,100), 23,200 (2,700), 18,400 (2,200)

a) at 231 K, b) at 228 K.

6.2.3 Epr Spectroelectrochemistry

Reduction of [Pt(5,5'-$(Me)_2$-bpy)(mnt)] and [Pt(5,5'-$(CO_2Et)_2$-bpy)(mnt)] to their mono-reduced species gives epr active solutions. The solution epr spectra of $[Pt(5,5'\text{-}(Me)_2\text{-bpy})(mnt)]^{1-}$ and $[Pt(5,5'\text{-}(CO_2Et)_2\text{-bpy})(mnt)]^{1-}$ are similar, showing coupling of the reduction electron to the ^{195}Pt nucleus (natural abundance 34 %, I = ½), see Table 6.3. Any superhyperfine coupling of the reduction electron to ligand nuclei is unresolved, see Figure 6.10.

Table 6. 3 Epr parameters of $[Pt(5,5'\text{-}(X)_2\text{-bpy})(mnt)]^{1-}$ in 0.1 M $TBABF_4$/DMF.

$[Pt(5,5'\text{-}(X)_2\text{-bpy})(mnt)]^{1-}$ X =	^{195}Pt coupling / G	g_{iso}	ΔH_{pp} / G	E_{app} / V
Me[a]	53	1.9991	15	-1.5
CO_2Et[b]	36	1.9954	10	-0.8

a) Generated by coulometry at 233 K. Epr spectrum collected at 293 K. b) Generated *in situ* at 273 K.

The small shift in g_{iso} from the free electron value, g_e, of 2.0023, suggests that there is only a small admixture of metal orbitals in the SOMO and therefore the reduction electron is based mainly on the bpy ligand. This is in agreement with the results UV/vis/nir studies and the results of the solution epr of the Cl analogues, see Section 3.2.2.3. Due to the poor solubility of the mnt complexes and the difficulty in obtaining the mono-reduced epr spectra, the epr spectra of the di-reduced complexes could not be obtained. However, given the similarity between the electrochemistry and the UV/vis/nir spectra of the mnt and Cl analogues it is expected that the di-reduction of the [Pt(5,5'-$(X)_2$-bpy)(mnt)] complexes would lead to collapse of the epr spectrum as it does for the Cl analogues, providing further evidence that spin pairing of the two reduction electrons occurs with both electrons occupying an orbital based on the bpy moiety.

Frozen epr spectra of $[Pt(5,5'\text{-}(Me)_2\text{-}bpy)(mnt)]^{1-}$ and $[Pt(5,5'\text{-}(CO_2Et)_2\text{-}bpy)(mnt)]^{1-}$ could not be obtained due to the poor solubility of the complexes in any epr solvents, (including DMF).

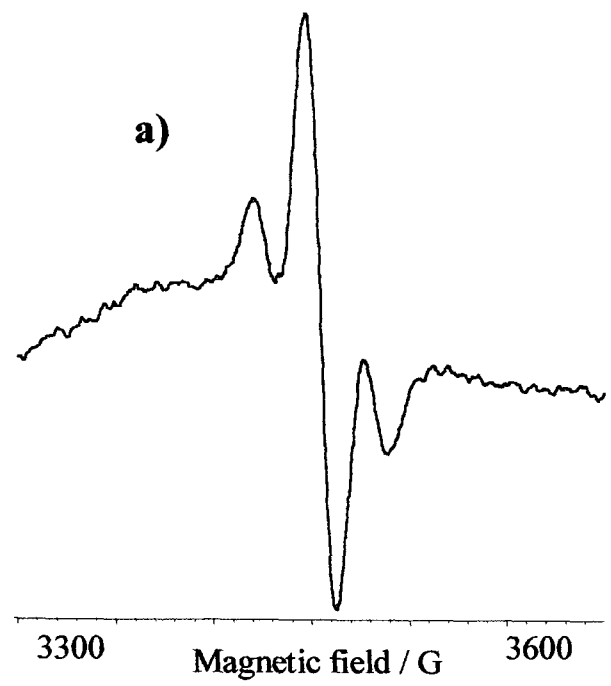

Figure 6. 10 Solution epr of **a)** $[Pt(5,5'\text{-}(Me)_2\text{-}bpy)(mnt)]^{1-}$ in 0.1 M $TBABF_4$/DMF, generated by coulometry at 233 K, E_{gen} –1.5 V, epr spectrum collected at 298 K. **b)** $[Pt(5,5'\text{-}(CO_2Et)_2\text{-}bpy)(mnt)]^{1-}$ in 0.1 M $TBABF_4$/DMF, generated *in situ* at 273 K, E_{gen} –0.8 V.

6.2.4 Emission studies

Both [Pt(5,5'-$(Me)_2$-bpy)(mnt)] and [Pt(5,5'-$(CO_2Et)_2$-bpy)(mnt)] luminesce at room temperature in fluid solution and at 77 K as a frozen glass. Due to the poor solubility of the complexes the effect of solvent polarity on the energy and intensity of the emission bands could not be studied. All emission spectra were studied in a DMSO/EtOH solvent mixture.

For both [Pt(5,5'-$(Me)_2$-bpy)(mnt)] and [Pt(5,5'-$(CO_2Et)_2$-bpy)(mnt)] in fluid solution at 298 K, the emission spectra is broad and asymmetric with no discernible structure. Excitation at 525 nm for [Pt(5,5'-$(Me)_2$-bpy)(mnt)] gives rise to an emission at 650 nm, see Figure 6.11. The excitation spectrum of [Pt(5,5'-$(CO_2Et)_2$-bpy)(mnt)] shows two peaks at 525 nm and 585 nm. Excitation at 525 nm gives an emission band at 660 nm, see Figure 6.12. Excitation at 585 nm also gives an emission band at 660 nm but, it is weaker than that observed for the 525 nm excitation.

At 77 K there is an increase in intensity of the emission and excitation spectra along with a sharpening of the structure. The position of the emission maxima shifts 10-15 nm to lower energy. Different excitation spectra are obtained for [Pt(5,5'-$(Me)_2$-bpy)(mnt)] depending on the chosen λ_{em}. Collection at 660 nm yields a structured excitation spectrum with the lowest energy peak at 520 nm, the other peaks being at approximately 485 nm and 395 nm. In contrast, collection at 610 nm yields a similar excitation spectrum, with bands at approximately 485 nm, 458 nm and 395 nm, but the band at 520 nm is not observed, see Figure 6.13. Thus, if excitation occurs at 485 nm the bands at 610 nm and 660 nm are both observed but, if the complex is excited at 525 nm, only the band at 660 nm is observed.

Further excitation/emission studies were carried out in an attempt to clarify the origins of this phenomenon. The results were reproducible and excitation at higher energy (395 nm and 455 nm) gave emission spectra showing the two bands at 610 nm and

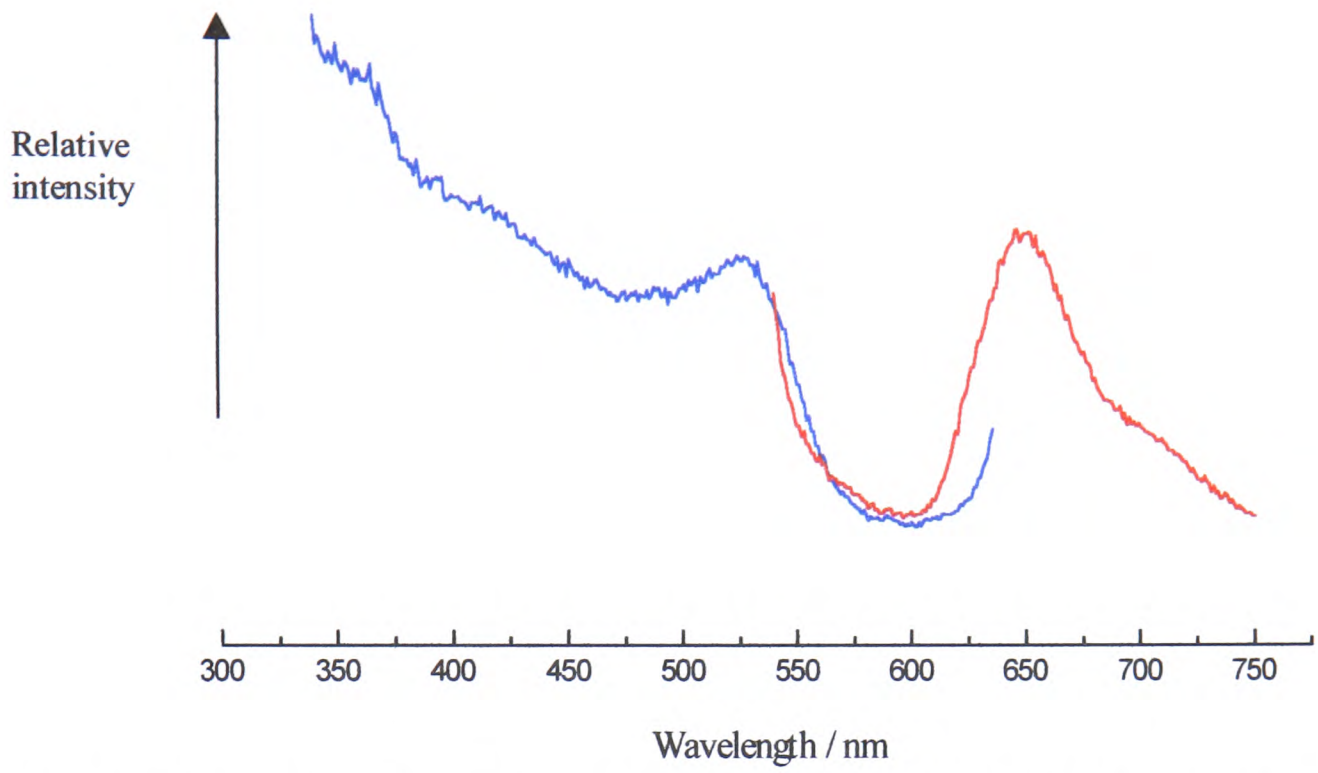

Figure 6. 11 Emission/excitation spectra obtained for [Pt(5,5'-$(Me)_2$-bpy)(mnt)] in fluid solution, EtOH/DMSO at 298 K. Blue is the excitation spectrum, red is the emission spectrum obtained on excitation at 525 nm.

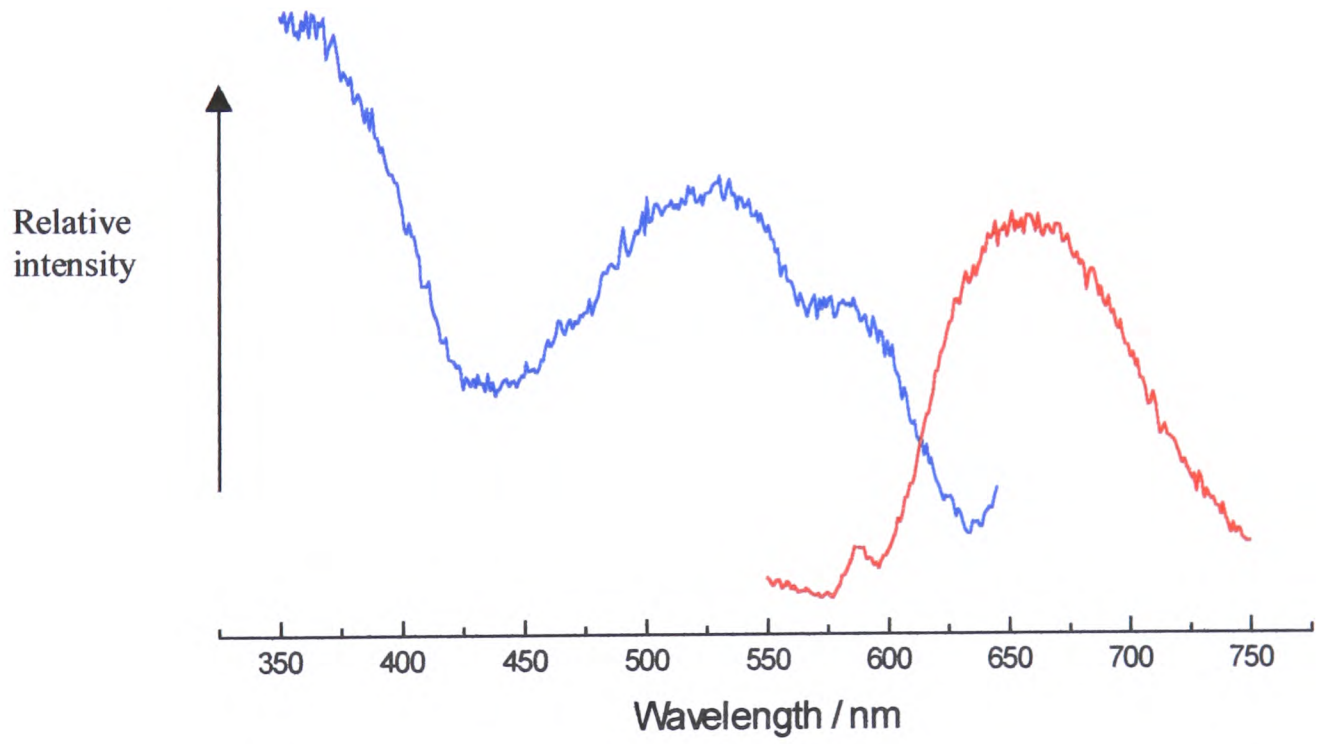

Figure 6. 12 Emission/excitation spectra obtained for [Pt(5,5'-$(CO_2Et)_2$-bpy)(mnt)] in fluid solution, EtOH/DMSO at 298 K. Blue is the excitation spectrum, red is the emission spectrum obtained on excitation at 500 nm.

660 nm as expected. The sample was systematically excited at 5 nm intervals between 485 nm and 525 nm. When excited at higher energy (shorter wavelength), both the peaks are clearly visible. However as the excitation energy decreases the peak at 610 nm begins to shrink and becomes a shoulder (excitation at 505 –510 nm) until excitation at 515 nm where only the peak at 660 nm is visible. This abrupt change in the emission spectra with changing excitation energy indicates that it is not a vibrational progression that is being observed, rather two different excited states are being populated depending on the excitation energy.

On comparing the excitation spectra with the corresponding absorption spectrum of [Pt(5,5'-$(Me)_2$-bpy)(mnt)] it is apparent that the features of the excitation spectra at 395 nm and 455-485 nm correspond to the absorption peaks at 398 nm (25,100 cm^{-1}) and 466 nm (21,500 cm^{-1}) which were assigned to an mnt $\pi \rightarrow \pi^*$ intraligand transition and a Pt(d)/S(p)$\rightarrow\pi^*$bpy charge transfer transition respectively, see Section 6.2.2. Hence, exciting the molecule at energies >20,000 cm^{-1} (wavelengths <500 nm) would appear to excite both the bpy and mnt ligands, leading to population of both of their excited states. However, exciting the molecule at energies <19,400 cm^{-1} (wavelengths >515 nm), which corresponds to the low energy tail of the Pt(d)/S(p)$\rightarrow\pi^*$bpy charge transfer transition, gives only sufficient energy to excite electronic transitions within the bpy ligand. Consequently only the bpy emission band at 660 nm is observed. Such an assignment is in line with the EHMO calculations on [Pt(bpy)Cl_2] carried out by Zuleta and co-workers who calculated that the bpy-based LUMO and the mnt-based LUMO-1 lie very close in energy (0.13 eV, 1,050 cm^{-1}) whereas the energy difference between the bpy-based LUMO and the next highest bpy-based π^* antibonding orbital is approximately 0.91 eV, (7,340 cm^{-1}).[34] From this argument it follows that the energy at which the excitation spectra changes from giving an emission spectrum with a lone peak at 660 nm, (bpy-based LUMO), to two bands at 610 nm, (mnt-based LUMO-1), and 660 nm must be the energy difference between the LUMO and LUMO-1. From the results obtained here the energy difference between the bpy-based LUMO and the mnt-based LUMO-1 is estimated to

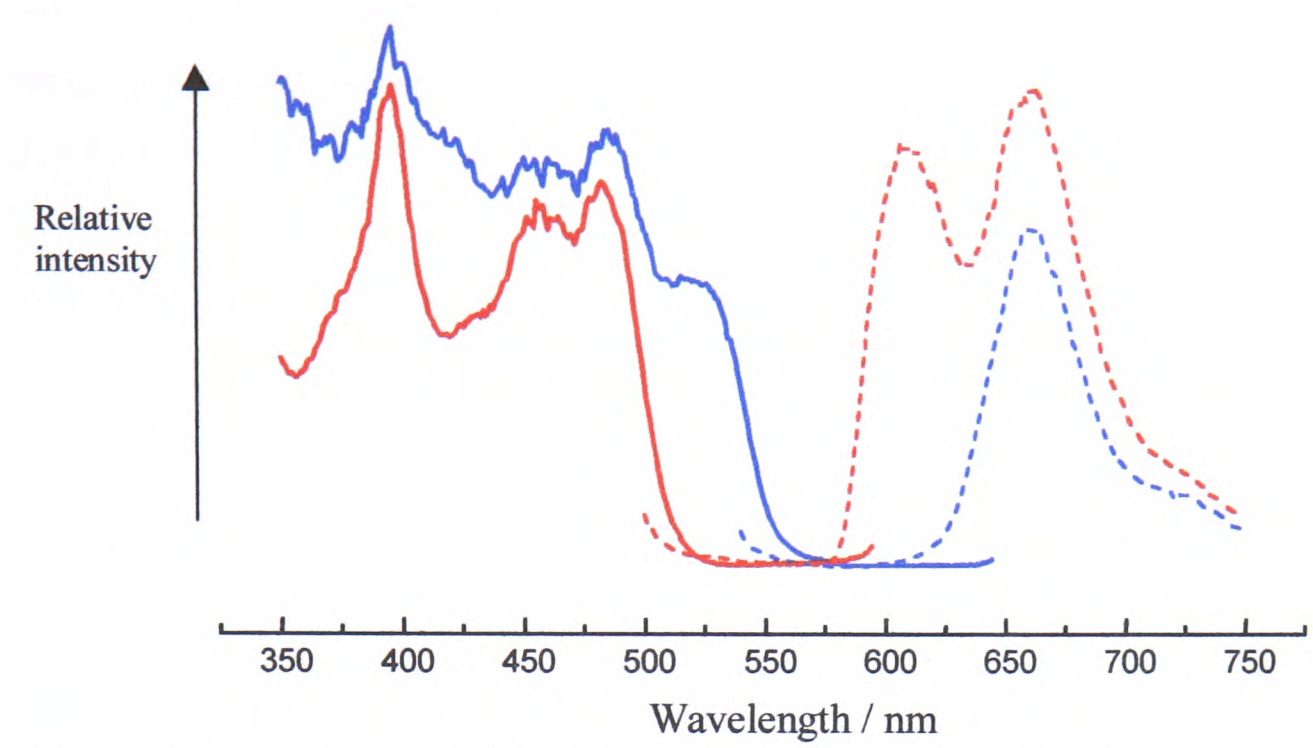

Figure 6. 13 Dependence of emission spectra on excitation energy for [Pt(5,5'-$(Me)_2$-bpy)(mnt)] in EtOH/DMSO at 77 K. Blue line is the excitation spectrum obtained on collection at 660 nm, blue dashes is the emission spectrum obtained on excitation at 525 nm. The red line is the excitation spectrum obtained on collection at 610 nm, red dashes is the emission spectrum obtained on excitation at 485 nm.

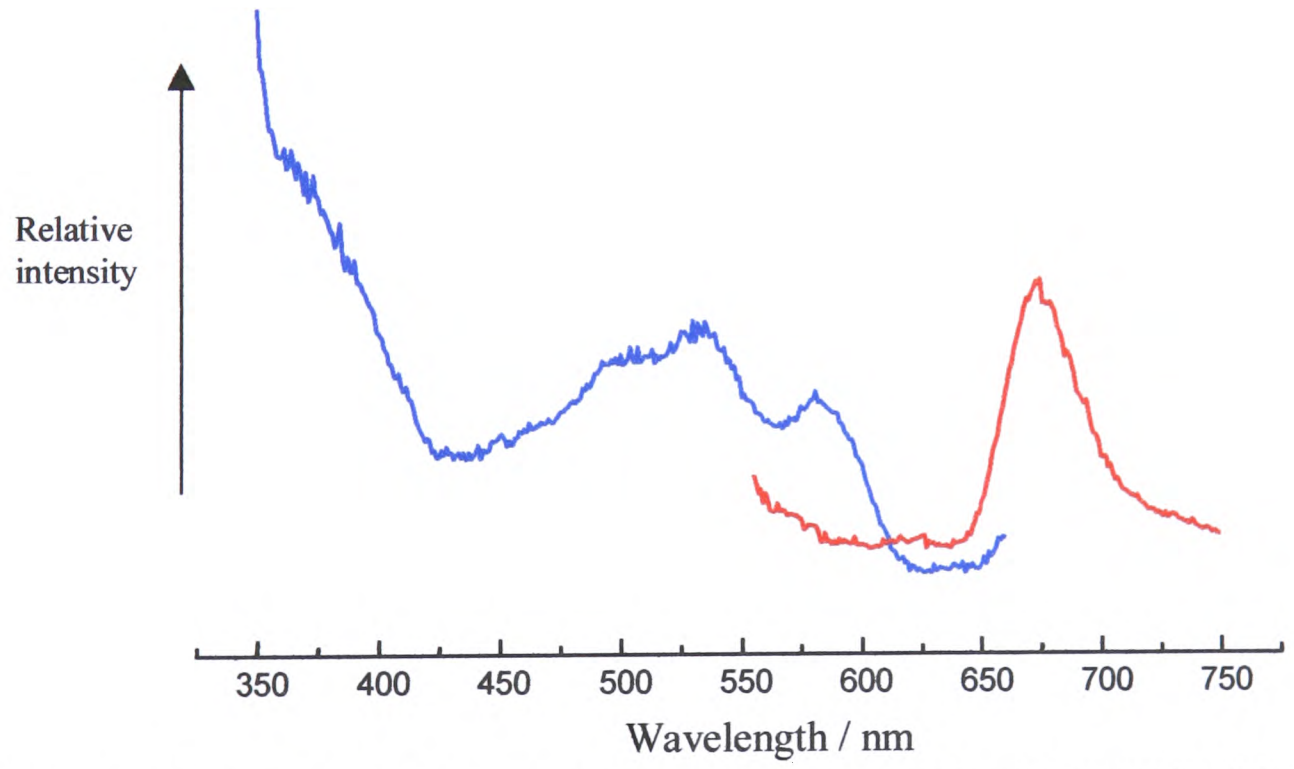

Figure 6. 14 Emission/excitation spectra for [Pt(5,5'-$(CO_2Et)_2$-bpy)(mnt)] in EtOH/DMSO at 77 K. Blue line is excitation spectrum obtained on collection at 675 nm, red line is the emission spectrum obtained on excitation at 525 nm.

be *ca.* 400 cm^{-1}. This is in good agreement with the EHMO calculations on [Pt(bpy)Cl_2] as electron donating substituents such as Me are known to destabilise the LUMO thus raising the energy of any $\pi \rightarrow \pi^*$ intraligand transitions, see Chapter 3 and decreasing the energy gap between the bpy-based LUMO and the mnt-based LUMO-1.

In contrast, only one emission at 675 nm is observed regardless of whether the [Pt(5,5'-$(CO_2Et)_2$-bpy)(mnt)] frozen glass is excited at 525 nm or 585 nm, see Figure 6.14. This may be due to the fact that electron withdrawing substituents on bpy, such as CO_2Et, stabilise the LUMO thus increasing the energy gap between the bpy-based LUMO and the mnt-based LUMO-1. The corresponding $\pi \rightarrow \pi^*$ intraligand transitions are shifted to lower energy, the Pt(d)/S(p)$\rightarrow\pi^*$bpy charge transfer transition is a wide band at 15-22 kcm^{-1}, centred on 18,400 cm^{-1}, see Figure 6.7. The excitation spectrum shows three shoulders at 580 nm, 530 nm and 505 nm, all of which are within the lowest energy absorption band. The mnt-based $\pi \rightarrow \pi^*$ intraligand transition appears at 25,700 cm^{-1}, see Figure 6.7.

Table 6.4, below, lists the energy of the lowest energy absorption bands, the emission maxima and the excitation bands for [Pt(4,4'-$(Me)_2$-bpy)(mnt)], [Pt(5,5'-$(Me)_2$-bpy)(mnt)] and [Pt(5,5'-$(CO_2Et)_2$-bpy)(mnt)] and demonstrates that the emission band shifts to lower energy with increasing acceptor strength of the diimine. This is in agreement with the findings of Cummings and co-workers who interpreted this trend as evidence to support the assignment of the charge-transfer-to-diimine emitting state for all of the Pt(diimine)(dithiolate) complexes studied.[111] The large separation and red shift between the lowest energy excitation band and the highest energy emission band for both complexes at 77 K is commonly observed for Pt(diimine)(mnt) complexes.[105] Such a shift is indicative of intersystem crossing *ie* there is a singlet-triplet transition in the excited state and the emitting state is of a different multiplicity to the ground state.[41, 105] Thus all of the observed emitting states for both [Pt(5,5'-$(Me)_2$-bpy)(mnt)] and [Pt(5,5'-$(CO_2Et)_2$-bpy)(mnt)] were assigned as triplet-singlet emissions. However, the emitting state(s) of

[Pt(5,5'-$(Me)_2$-bpy)(mnt)] depend on the excitation energy. If excitation occurs at 20,000 cm^{-1} or above, then both the ^{3}{d(Pt)/p(S)→π^*(bpy)} and ^{3}{d(Pt)/p(S)→π^*(mnt)}emitting states are observed. If excitation occurs at ~19,400 cm^{-1} or below then only the ^{3}{d(Pt)/p(S)→π^*bpy} emitting state is observed. Regardless of excitation energy, the emitting state of [Pt(5,5'-$(CO_2Et)_2$-bpy(mnt)] is assigned to a ^{3}{d(Pt)/p(S)→π^*(bpy)} emitting state.

This preliminary work suggests that [Pt(5,5'-$(X)_2$-bpy)(mnt)] complexes make suitable luminescent chromophores for solar energy conversion cells and that altering the substituents on the bpy ligand allows tuning of the excited state. The difference in energy of the emission bands of [Pt(5,5'-$(Me)_2$-bpy)(mnt)] and the 4,4' analogue indicates that changing the substituent at the 5,5' position allows the excited state to be tuned to a greater degree than if the substituents at the 4,4' position were altered. This is in agreement with the findings of Chapter 3.

Table 6. 4 Energies of the absorption, emission and excitation maxima for the Pt(diimine)(dithiolate) complexes.

	E_{abs} / kcm^{-1}	E_{em} / kcm^{-1}	E_{exc} / kcm^{-1}
[Pt(4,4'-$(Me)_2$-bpy)(mnt)][a]	21.19[b]	16.26[c,f]	20.08[c]
[Pt(5,5'-$(Me)_2$-bpy)(mnt)]	21.46[d]	16.39[e, f] & 15.15[e, g]	20.62[e]
[Pt(5,5'-$(CO_2Et)_2$-bpy)(mnt)]	18.38[d]	14.81[e, g]	19.05[e]

All absorption spectra were measured at 298 K. Emission and excitation values are from data at 77 K. a) from the values given by Cummings *et al.*,[111] b) in benzonitrile, c) in DCM, d) in DMF, e) DMSO/EtOH, f) mnt emitting state, g) bpy emitting state.

6.3 Conclusions

The redox chemistry of [Pt(5,5'-$(Me)_2$-bpy)(mnt)] and [Pt(5,5'-$(CO_2Et)_2$-bpy)(mnt)] can be explained in terms of the two reduction electrons entering the same orbital, in this case the lowest unoccupied π^* orbital of the $(X)_2$-bpy ligand. These complexes either undergo an irreversible oxidation, ([Pt(5,5'-$(Me)_2$-bpy)(mnt)]), or a quasi-reversible oxidation, ([Pt(5,5'-$(CO_2Et)_2$-bpy)(mnt)]), based on the mnt ligand. Comparison of the electrochemistry of the complexes with their Cl analogues indicates that the LUMO is not affected by the introduction of the mnt ligand. Thus the HOMO is based on the mnt ligand and the LUMO is based on the bpy ligand. The lowest energy absorption band for both complexes is assigned as a mixed Pt(d)/S(p)$\rightarrow\pi^*$bpy charge transfer transition. Both complexes luminesce in solution at room temperature and at 77 K. Varying X allows control of the energy of the π^* LUMO and hence the energy of the emission. For [Pt(5,5'-$(CO_2Et)_2$-bpy)(mnt)] the emitting state was assigned as ^{3}{(Pt)d/(S)p$\rightarrow\pi^*$(bpy)}. In the case of [Pt(5,5'-$(Me)_2$-bpy)(mnt)] the emitting state is dependent on the excitation energy. On excitation above 20,000 cm^{-1} two emitting states assigned to ^{3}{(Pt)d/(S)p$\rightarrow\pi^*$(bpy)} and ^{3}{(Pt)d/(S)p$\rightarrow\pi^*$(mnt)} were observed. Below 20,000 cm^{-1} only the ^{3}{(Pt)d/(S)p$\rightarrow\pi^*$(bpy)} emission is observed. Electron donating substituents destabilise the LUMO and allow both the mnt and bpy excited states to be populated. Electron withdrawing substituents have the opposite effect and result in population of only the bpy excited state.

6.4 Experimental

The Na_2(mnt) used was supplied by Mr Donald Robertson, the platinum salts used were synthesised by the methods given in Chapter 3. The solvents used were commercially available (Aldrich) and used as bought.

6.4.1 Synthesis of [Pt(5,5'-$(Me)_2$-bpy)(mnt)]

[Pt(5,5'-$(Me)_2$-bpy)Cl_2] (0.040 g, 8.88×10^{-5} moles) was dissolved in DMSO (10 ml). Na_2mnt (0.330 g, 1.78×10^{-4} moles) was dissolved in methanol (5 ml). The two solutions were mixed together with stirring.[105] A bright red precipitate formed immediately. After 1 hour, the precipitate was collected by filtration, washed with water, ethanol then ether and dried under vacuum. [Pt(5,5'-$(Me)_2$-bpy)(mnt)] was obtained as a bright orange powder (0.041 g, 8.05×10^{-5} moles, percentage yield 90.65 %). CHN analysis for $PtC_{16}H_{12}N_4S_2$: calculated 37.72 % C, 2.37 % H, 11.00 % N; found 38.39 % C, 1.71 % H, 11.77 % N.

6.4.2 Synthesis of [Pt(5,5'-$(CO_2Et)_2$-bpy)(mnt)]

Na_2mnt (0.012 g, 6.62×10^{-5} moles) dissolved in methanol (2 ml) was added, with stirring, to a solution of [Pt(5,5'-$(CO_2Et)_2$-bpy)Cl_2] (0.025 g, 4.41×10^{-5} moles) in DMSO (10 ml). The solution immediately turned dark pink. After stirring for 48 hours the solid was collected by filtration, washed with water, ethanol, then ether and dried under vacuum. [Pt(5,5'-$(CO_2Et)_2$-bpy)(mnt)] was obtained as a dark pink solid (0.013 g, 2.04×10^{-5} moles, percentage yield 46.26 %). CHN analysis for $PtC_{20}H_{16}N_4O_4S_2$: calculated 37.73 % C, 2.53 % H, 8.80 % N; found 39.07 % C, 2.61 % H, 8.70 % N.

Conclusions and Further Work

Cyclic voltammetric studies on 5,5'-$(X)_2$-bpy and [Pt(5,5'-$(X)_2$-bpy)Cl_2], (where X = Me, H, CO_2Me and CO_2Et), showed two reversible one electron reductions. The redox chemistry, as investigated using UV/vis and epr techniques indicates that both of the reduction electrons enter the same orbital, in this case the empty π^* orbital of the $(X)_2$-bpy ligand. Systematic variation of X allows us to control the energy of the π^* LUMO. Electron withdrawing substituents stabilise the LUMO, electron donating substituents have the opposite effect. Plotting the Hammett parameters σ_m and σ_p against the first reduction potentials of [Pt(5,5'-$(X)_2$-bpy)Cl_2] and [Pt(4,4'-$(X)_2$-bpy)Cl_2] indicates that 5,5' position is electronically the most important site of substitution.

The electrochemical behaviour of 4,4'-$(NO_2)_2$-bpy and its complexes with Pt(II) and Pd(II) can be explained in terms of a molecular orbital scheme with a low lying LUMO and a very small LUMO and LUMO-1 energy gap. In the free ligand the 4-NO_2-py rings are orthogonal and so each reduction electron is localised on a 4-NO_2-py moiety of the ligand. On complexation the ligand is forced to become planar and the reduction electrons are localised over the whole ligand. The LUMO-LUMO-1 energy gap is still smaller than the spin pairing energy consequently, di-reduction of the ligand and the complexes leads to the spin triplet species 4,4'-$(NO_2)_2$-bpy^{2-}, [Pt(4,4'-($NO_2)_2$-bpy)Cl_2]$^{2-}$ and [Pd(4,4'-$(NO_2)_2$-bpy)Cl_2]$^{2-}$. As the epr signals of such species could be well simulated using a spin ½ system it may be concluded that the zero-field splitting is very small for these systems.

In the case of 4-NO_2-bpy^{1-} and its complexes [Pt(4-NO_2-bpy)Cl_2]$^{1-}$ and [Pd(4-NO_2-bpy)Cl_2]$^{1-}$ the reduction electron is localised on the 4-NO_2-py moiety. The redox chemistry of [Pt(4-NO_2-py)$_2Cl_2$], [Pd(4-NO_2-py)$_2Cl_2$] and [Pt(4-NO_2-py)$_2$(ox)] can be explained by the 4-NO_2-py ligands being reduced a very similar potentials with no communication between the ligands.

The redox behaviour of dpk and $[Pt(dpk)Cl_2]$ indicates that the reduction electron enters the lowest energy unoccupied π^* orbital of the dpk ligand. Reduction of the ligand is closely followed by chemical reaction as the additional negative charge on the carbonyl group promotes the addition of water to the C=O group giving dpk in its geminal diol form ($dpk.H_2O^{1-}$), via the intermediate $dpk.H^0$. Conversion of $[Pt(dpk)Cl_2]$ to $[Pt(dpk.H_2O)Cl_2]^{1-}$ via the intermediate $[Pt(dpk.H)Cl_2]^{1-}$ occurs more quickly than for the free ligand as chelation of dpk to a metal cation promotes formation of the geminal diol.

The redox chemistry of $[Pt(5,5'\text{-}(Me)_2\text{-bpy})(mnt)]$ and $[Pt(5,5'\text{-}(CO_2Et)_2\text{-bpy})(mnt)]$ can be attributed to the two reduction electrons entering the same orbital *ie* the lowest unoccupied π^* orbital of the $(X)_2$-bpy ligand, in line with the results of the studies on the chloride analogues. The electrochemistry of $[Pt(5,5'\text{-}(Me)_2\text{-bpy})(mnt)]$ shows an irreversible oxidation while $[Pt(5,5'\text{-}(CO_2Et)_2\text{-bpy})(mnt)]$ undergoes a quasi-reversible oxidation. Thus the HOMO is based on the mnt ligand and the LUMO on the bpy ligand. The lowest energy absorption band for both complexes is assigned as a mixed Pt(d)/S(p)$\rightarrow\pi^*$bpy charge transfer transition. Both complexes luminesce in solution at room temperature and at 77 K. Varying X allows control of the energy of the π^* LUMO and hence the energy of the emission. For $[Pt(5,5'\text{-}(CO_2Et)_2\text{-bpy})(mnt)]$ the emitting state was assigned as $^3\{(Pt)d/(S)p\rightarrow\pi^*(bpy)\}$. For $[Pt(5,5'\text{-}(Me)_2\text{-bpy})(mnt)]$ the emitting state is dependent on the excitation energy. On excitation above 20,000 cm^{-1} two emitting states assigned to $^3\{(Pt)d/(S)p\rightarrow\pi^*(bpy)\}$ and $^3\{(Pt)d/(S)p\rightarrow\pi^*(mnt)\}$ were observed. Below 20,000 cm^{-1} only the $^3\{(Pt)d/(S)p\rightarrow\pi^*(bpy)\}$ emission is observed. Electron donating substituents destabilise the LUMO and allow both the mnt and bpy excited states to be populated. Electron withdrawing substituents have the opposite effect and result in population of the bpy excited state only.

A number of frozen epr spectra from Chapter 4 including $[Pt(4\text{-}NO_2\text{-}py)_2Cl_2]^{2-}$, $[Pd(4\text{-}NO_2\text{-}py)_2Cl_2]^{2-}$, $[Pt(4\text{-}NO_2\text{-}py)_2(ox)]^{2-}$, $[Pd(4\text{-}NO_2\text{-}bpy)Cl_2]^{1-}$, $[Pt(4,4'(NO_2)\text{-bpy})Cl_2]^{2-}$, $[Pd(4,4'(NO_2)\text{-bpy})Cl_2]^{2-}$ and $[Pt(4,4'(NO_2)\text{-bpy})Cl_2]^{1-}$,

should all be repeated on a Q-band spectrometer to improve the resolution of the spectra and allow the measurement of the g_{xx}, g_{yy} and g_{zz} values and any associated hyperfine splitting values of ^{195}Pt and ^{105}Pd.

More 5,5'-$(X)_2$-bpy ligands should be synthesised with a greater variation in the electron withdrawing and donating abilities of X. With the recent publication of a simpler and more convenient synthetic route to 5,5'-$(X)_2$-bpy using an alternative of the Ullman reaction, this task should allow the synthesis of a greater number of 5,5' disubstituted bpys than was possible during the course of this work.[114] More [Pt(5,5'-$(X)_2$-bpy)Cl_2] complexes eg X = Cl, Ph, OEt should be synthesised and studied to see if they fit the 5,5' gradient on the Hammett plot.

5,5'-$(NO_2)_2$-bpy and 5-NO_2-bpy should be synthesised and studied by electrochemical and spectroelectrochemical techniques to further investigate the interesting redox chemistry of NO_2-substituted bpy derivatives and the effect of substitution at the 5,5' position.

The electrochemical and luminescent properties of [Pt(5,5'-$(X)_2$-bpy)(mnt)] complexes have only been studied very briefly here and a great deal of work remains to be done on this particular class of compound. Further studies on the lifetimes and quantum yields of the emissive states of [Pt(5,5'-$(Me)_2$-bpy)(mnt)] and [Pt(5,5'-$(CO_2Et)_2$-bpy)(mnt)] should be undertaken. The frozen epr spectra of these complexes in the mono-reduced form should also be obtained. Having shown that altering the substituents at the 5,5' positions allows tuning of the redox orbitals and hence the emissive states to a greater degree than altering the substituents at the 4,4' positions, a greater number of complexes of the type [Pt(5,5'-$(X)_2$-bpy)(mnt)] should be synthesised. The effect of altering the electron withdrawing and electron donating strengths of the substituent on the emissive states should be fully investigated. Complexes of [Pt(5,5'-$(X)_2$-bpy)L], where L = diimine, using an alternative to mnt should also be investigated.

References

1 F.P. Rotzinger, S. Munavalli, P. Comte, J.K. Hurst, M. Gratzel, F-J. Pern and A.J. Frank; J. Am. Chem. Soc., 1987, 6619-626.

2 C.A. Bignozzi, R. Argazzi and C.J. Kleverlaan; Chem. Soc. Rev., 2000, **29**, 87-96.

3 H.F.M. Nelissen, A.F.J. Schut, F. Venema, M.C. Feiters and R.J.M. Nolte; J.Chem. Soc., Chem. Commun., 2000, 577-578.

4 V.W-W. Yam and A.S-F. Kai; Inorganica Chimica Acta, 2000, **300-302**, 82-90.

5 N.N. Greenwood and A. Earnshaw; "Chemistry of the Elements", Pergamon Press, 1989.

6 F. Vögtle; "Supramolecular Chemistry", John Wiley and Sons, 1993.

7 F.W. Cagle; Acta. Cryst., 1948, **1**, 58-59.

8 L.L. Merritt and E.D. Schroeder; Acta Cryst., 1956, **9**, 801-804.

9 R. Tsuchida and Y. Shimura; Bull. Chem. Soc. Japan; 1956, **29**, 311-316.

10 D.F. Schriver, P.W. Atkins and C.H. Langford; "Inorganic Chemistry", 2nd Edition, Oxford University Press, 1994.

11 G.L. Geoffroy, H. Isci, J. Litrenti and W.R. Mason; Inorg. Chem., 1977, **16(8)**, 4950-1955.

12 W.B. Connick and H.B. Gray; Acta Cryst., 1994, **C50**, 1040-1042.

13 A.J. Canty, N.J. Minchin, B.W. Skelton and A.H. White; Aust. J. Chem., 1992, **45**, 423-427.

14 E.J.L. McInnes, A.J. Welch and L.J. Yellowlees; Acta Cryst., 1995, **C51**, 2023-2025.

15 B. Rosenberg, L. van Camp, J.E. Trasko and V.H Mansour; Nature, 1969, **222**, 385-386.

16 G.T. Morgan and F.H. Burstall; J. Chem. Soc., 1934, 965-971.

17 R.S. Osborn and D. Rogers; J. Chem. Soc. Dalton, 1974, 1002-1004.

18 C-M. Che, L-Y. He, C-K. Poon and T.C.W. Mak; Inorg. Chem., 1989, **28**, 3081-3083.

19 P.M. Gidney, R.D. Gillard and B.T. Heaton; J. Chem. Soc. Dalton; 1973, 132-134.

20 E. Bielli, P.M. Gidney, R.D. Gillard and B.T. Heaton; J. Chem. Soc. Dalton, 1974, 2133-2139.

21 V.M. Miskowski and V.H. Houlding; Inorg. Chem., 1989, **28**, 1529-1533.

22 V.M. Miskowski and V.H. Houlding; Inorg. Chem., 1991, **30**, 4446-4452.

23 P.S. Braterman, J-I. Song, C. Vogler and W. Kaim; Inorg. Chem., 1992, **31**, 222-224.

24 P.S. Braterman, J-I. Song, F.M. Wimmer, S. Wimmer, W. Kaim, A. Klein and R.D. Peacock, Inorg. Chem., 1992, **31**, 5084-5088.

25 E.J.L. McInnes; PhD Thesis, University of Edinburgh, 1995.

26 R.H. Herber, M. Croft, M.J. Coyer, B. Bilash and A. Sahiner; Inorg. Chem., 1994, **33**, 2422-2426.

27 D. Collison, F.E. Mabbs, E.J.L. McInnes, K.J. Taylor, A.J. Welch and L.J. Yellowlees; J.Chem. Soc., Dalton Trans., 1996, 329-334.

28 V.T. Coombe, G.A. Heath, A.J. Mackenzie and L.J. Yellowlees; J. Chem. Soc., Chem.. Commun., 1984, **23**, 3423-3425.

29 E. König and S. Kremer; Chem. Phys. Lett., 1970, **5**, 87-90.

30 P.S. Braterman and J-I. Song; Inorganica Chimica Acta, 1991, **183**, 131-132.

31 L. Yang, F.L. Wimmer, S. Wimmer, J. Zhao and P.S. Braterman; J. Organomet. Chem., 1996, **525**, 1-8.

32 E.J.L McInnes, R.D. Farley, C.C. Rowlands, A.J. Welch, L. Rovatti and L.J. Yellowlees;, J. Chem. Soc., Dalton Trans., 1999, 4203-4208.

33 E.J.L. McInnes, R.D. Farley, S.A. Macgregor, K.J. Taylor, L.J. Yellowlees and C.C. Rowlands; J. Chem. Soc., Faraday Trans., 1998, **94**, 2985-2991.

34 J.A. Zuleta, J.M. Bevilacqua, D.M. Prosperio, P.D. Harvey and R. Eisenberg; Inorg. Chem., 1992, **31**, 2396-2404

35 A.J.Baird and L.R. Faulkner; "Electrochemical Methods Fundamentals and Application", John Wiley and Sons, 1980.

36 C.P. Poole; "Electron Spin Resonance", Dover Publications, 1996.

37 E.A.V. Ebsworth, D.W.H. Rankin and S. Cradock; "Structural Methods in Inorganic Chemistry", Blackwell Scientific Publications, 1991.

38 F.E. Mabbs and D. Collison; "Studies in Inorganic Chemistry, Vol 16, Electron Paramagnetic Resonance of d Transition Metal Compounds", Elsevier, 1992.

39 I.B. Goldberg, A. J. Baird, S. W. Feldberg; J. Phys. Chem. 1972, **79** 2550.

40 D.A. Skoog and J.J. Leary, "Principles of Instrumental Analysis", 4th Edn., Saunders College Publishing, 1992.

41 P.W. Atkins; "Physical Chemistry", 5th Edn., Oxford University Press, 1994.

42 D. Wenkert and R.B. Woodward; J. Org. Chem., 1983, **48**, 283.

43 W.H.F. Sasse and C.P. Whittle; J. Chem. Soc. Trans., 1961, 1347

44 C.P. Whittle; J. Heterocyclic Chem., 1977, **14**, 191-194.

45 G.R. Newkome, J. Gross and A.K. Patri; J. Org. Chem., 1997, **62**, 3013-3014.

46 U.S. Schubert, C. Eschbaumer and G. Hochwimmer; Tett. Lett., 1998, **39**, 8643-8644.

47 F.Pichot, J.H. Beck and C. M. Elliott; J. Phys. Chem. A, 1999, **103**, 6263-6267.

48 P.D. Beer, O. Kocian, R.J. Mortimer and C. Ridgway; J. Chem. Soc. Dalton Trans., 1993, 2629-2638.

49 T.J. Meyer: Acc. Chem. Res., 1978, **11**, 94.

50 D.G. Whitten; Acc. Chem. Res., 1980, **13**, 83 – 90.

51 C.M. Elliott and E.J. Hershenhart; J. Am. Chem. Soc., 1982, **104**, 7519-7526.

52 G.A. Heath, L.J. Yellowlees and P.S. Braterman; Chem. Commun., 1981, 287-289.

53 K. Kurita and R.L. Williams; J.Polym. Sci., Polm. Chem. Ed., 1973, **11**, 3125-3150.

54 P.N.W. Baxter and J.A. Connor; J. Organomet. Chem., 1988, **355**, 189-196.

55 J. March; "Advanced Organic Chemistry", 3rd edition, Wiley Scientific Publications, 1985.

56 J.A. Connor and C. Overton; J.Organomet. Chem., 1984, 277 – 284.

57 J. Yoo, J. Kim, Y.S. Sohn and Y. Do; Inorganic Chimica Acta, 1997, **263**, 53-60.

58 K. Shih and R.H. Herber; Inorg. Chem., 1992, **31**, 5444-5449.

59 C. Che, K. Wan, L. He, C.Poon and V.W. Yam; Chem. Commun., 1989, 943-944.

60 C. Hansch, A. Leo and R.W. Taft; Chem. Rev., 1991, **91**, 165-195.

61 N.G. Connelly, W.E. Geiger, G.A. Lane, S.J. Raven and P.H. Rieger; J. Am. Chem. Soc., 1986, 6219-6224.

62 P.H. Rieger; J. Mag. Res., 1997, **124**, 140-146.

63 G.M. Badger and W.H.F. Sasse; J. Chem. Soc. Trans., 1956, 616.

64 F.H.J. Case; J. Am. Chem. Soc., 1946, **68**, 2574.

65 G. Maerker and F.H. Case; J. Am. Chem. Soc., 1958, **80**, 2745-2748.

66 S. Anderson, E.C. Constable, K.R. Seddon, J.E. Turp, J.E. Baggot and M.J. Pilling; J. Chem. Soc., Dalton Trans., 1985, 2247-2261.

67 M.A. Weiner and A. Basu; Inorg. Chem., 1980, **19**, 2797-2800.

68 M. Pilkington, S.J. Hauser, C. Hoffman and H.B. Bürgi; Acta Cryst., 1997, **C53**, 1719-1721.

69 A. Basu, M. Weiner; T.C. Strekas and H.D. Gafney; Inorg. Chem., 1982, **21**, 1085-1092.

70 A. Basu, H.D. Gafney and T.C. Strekas; Inorg. Chem., 1982, **21**, 2231-2235.

71 M.J. Cook, A.P. Lewis, G.S.G. McAuliffe, V. Skarda, A.J. Thomson, J.L. Glaser and D.J. Robbin; J. Chem. Soc. Perkin Trans. II, 1984, 1293-1301.

72 M.J. Cook, A.P. Lewis, G.S.G. McAuliffe, V. Skarda, A.J. Thomson, J.L. Glaser and D.J. Robbin; J. Chem. Soc. Perkin Trans. II, 1984, 1303-1307.

73 T-J. Kinnunen, M. Haukka, M. Nousiainen, A. Patrikka and T.A. Pakanen; J. Chem. Soc., Dalton Trans., 2001, 2649-2654.

74 E.J.L. McInnes, A.J. Welch and L.J. Yellowlees; Chem. Commun., 1996, 2393-2394.

75 K.J. Taylor; PhD thesis, The University of Edinburgh, 1990.

76 A.G. Motten, K. Hanck and M.K. De Armond, Che. Phys. Lett., 1981, **79(3)**, 541-546.

77 P.G. Simpson, A. Vinguerra and J.V. Quaglino; Inorg. Chem., 1963, **2**, 282.

78 A.E. Tschitschibabin and O.A. Zeide, Zh. Russ. Khim. Ova.; 1914, **46**, 1216 –1224.

79 D.E. Morris, Y. Ohsawa; D.P. Segers, M.K. DeArmond and K.W. Hanck; Inorg. Chem., 1984, **23**, 3010 – 3017.

80 R. Kumar and D. G. Tuck, Inorg. Chim. Acta., 1989, **157**, 51 – 56.

81 F.A. Cotton; L.M. Daniels, G.T. Jordan and C.A. Murillo; Polyhedron, 1998, **17(4)**, 589-597.

82 M. Ishaq; Jour. Chem. Soc. Pak., 1993, **15(1)**, 36-38.

83 J.E Johnson and R.A. Jacobson, T.A. Beineke; J. Chem. Soc. (A), 1971, 1371-1374.

84 J.E. Johnson and R.A. Jacobson; Acta Cryst., 1973, **B29 (3)**, 1669.

85 N.A. Lagutkin, N.I. Mitin, M.M. Zubairov, V.A. Dorokhov and B.A. Mikhailov; Pharm. Chem. J., 1982, 464 – 467.

86 V. Courtois, R. Barhdadi, S. Condon and M. Troupel; Tett. Lett. 1999, **40**, 5993 – 5996.

87 G.J. Pyrka and A.A. Pinkerton; Acta Cryst., 1992, **C48**, 91-94.

88 H. Schödel, C. Näther, H. Bock and F. Butenschön; Acta Cryst., 1996, **B52**, 842-853.

89 V.N. Joshi and A.S. Gijare; J. Indian Chem. Soc., 1989, **66**, 474-475.

90 J.F. Geldard and F. Lions; J. Am. Chem. Soc., 1962, **84**, 2262-2263.

91 V. Anbalagan and T.S. Srivastava; J. Photochem. Photobiol. A: Chem., 1994, **77**, 141-148.

92 S.L. Wang, J.W. Richardson, S.J. Briggs, R.A. Jacobson and W.P. Jensen; Inorg. Chim. Acta, 1986, **111**, 67-72.

93 S.O. Sommerer, J.D. Baker, W.P. Jensen A. Hamza and R.A. Jacobson; Inorg. Chim. Acta, 1993, **210**, 173-176.

94 A. Basu, A.R. Saple and N.Y. Sapre; J. Chem. Soc. Dalton Trans.; 1987, 1797-1799.

95 H. Bock, T.T.H. Van, H. Schödel and R. Dienelt; Eur. J. Org. Chem., 1998, 585-592.

96 S.O. Sommerer, K.A. Abboud; Acta Cryst., 1993, **C49**, 1152-1154.

97 Annibale, G., Canovese, L., Cattalini, L., Natile, G., Biagini-Cingi, M., Manotti-Lanfredi, A. and Tiripicchio, A. J. Chem. Soc. Dalton Trans.; 1981, **12**, 2280.

98 S.F. Sun and P.R. Neidig; J. Org. Chem., 1969, **34**, 1854-1856.

99 B. Rickborn and M.T. Wuesthoff; J. Am. Chem. Soc., 1970, **92**, 6894-6904.

100 H.C. Brown and K. Ichikawa; J. Am. Chem. Soc., 1962, **84(1)**, 373-376.

101 G. Favaro, A. Romani and G. Poggi; Spectrochimica Acta, 1990, **46A**, 3, 425-427.

102 D.L. Webb and L.A. Rossiello; Inorg. Chem., 1971, **10(10)**, 2213-2218.

103 W.H. Elfring and G.A. Crosby; J. Am. Chem. Soc., 1981, **103**, 2683-2687.

104 C.E. Johnson, R. Eisenberg, T.R. Evans and M.S. Burberry; J. Am. Chem. Soc., 1983, **105**, 1795-1802.

105 J. Zuleta, M.S. Burberry and R. Eisenberg; Coord. Chem. Rev., 1990, 47-64.

106 A. Vogler, H. Kunkely, J. Hlavatsch and A. Merz; Inorg. Chem., 1984, **23**, 506-509.

107 J.A Zuleta, J.M. Bevilacqua, J.M. Rehm and R.D. Eisenberg; Inorg. Chem., 1992, **31**, 1332-1337.

108 J.A. Zuleta, J.M. Bevilacqua and R.D. Eisenberg; Coord. Chem. Rev., 1991, **111**, 237-248.

109 M. Hissler, J.E. McGarrah, W.B. Connick, D.K. Geiger, S.D. Cummings and R. Eisenberg; Coord. Chem. Rev., 2000, **208**, 115-137.

110 A. Islam, H. Sugihara, K. Hara, L.P. Singh, R. Katoh, M. Yanagida, Y. Takahashi, S. Murata and H. Arakawa; Inorg. Chem., 2001, **40**, 5371-5380.

111 S.D. Cummings and R. Eisenberg; J. Am. Chem. Soc., 1997, **118**, 1949-1960.

112 W.B. Connick and H.B. Gray; J. Am. Chem. Soc., 1997, **119**, 11620-11627.

113 Y. Zhang, K.D. Ley and K.S. Schanze; Inorg. Chem., 1996, **35**, 7102-7110.

114 J. Hassan, V. Penalva, L. Lavenot, C. Gozzi and M. Lamaire; Tetrahedron, 1998, **54**, 13793-13804.

Appendices

Crystal Structure of trans-[Pt(4-NO_2-py)$_2$$Cl_2$]

Table 1. Crystal data and structure refinement for lj76ac.

Contact	Simon Parsons, S.Parsons@ed.ac.uk
A. CRYSTAL DATA	
Empirical formula	C10 H8 Cl2 N4 O4 Pt Trans-[Pt2Cl2(4nitro-pyr)2]
Formula weight	514.19
Wavelength	0.71073 A
Temperature	150(2) K
Crystal system	Monoclinic
Space group	P2(1)/n
Unit cell dimensions	a = 7.456(3) A alpha = 90°. b = 24.561(10) A beta = 105.891(5)° c = 7.811(3) A gamma = 90°.
Volume	1375.7(10) A^3
Number of reflections for cell	2659 (2.5 < theta < 26.5°.)
Z	4
Density (calculated)	2.483 Mg/m^3
Absorption coefficient	10.608 mm^-1
F(000)	960
B. DATA COLLECTION	
Crystal description	Yellow plate
Crystal size	0.75 x 0.45 x 0.11 mm
Instrument	CCD area detector
Theta range for data collection	2.84 to 26.42°.
Index ranges	-9<=h<=8, -30<=k<=23, -9<=l<=9

Reflections collected	6511
Independent reflections	2740 [R(int) = 0.0319]
Scan type	phi and omega scans
Absorption correction	Sadabs (Tmin= 0.400, Tmax=1)

C. SOLUTION AND REFINEMENT.

Solution	Patterson (DIRDIF)
Refinement type	Full-matrix least-squares on F^2
Program used for refinement	SHELXL-97
Hydrogen atom placement	geometric
Hydrogen atom treatment	riding
Data / restraints / parameters	2740/0/190
Goodness-of-fit on F^2	1.103
Conventional R [F>4sigma(F)]	R1 = 0.0352 [2344 data]
Weighted R (F^2 and all data)	wR2 = 0.0848
Final maximum delta/sigma	0.001
Weighting scheme	calc w=1/[\s^2^(Fo^2^)+(0.0240P)^2^+3.2138P] where P=(Fo^2^+2Fc^2^)/3
Largest diff. peak and hole	2.360 and -1.193 e.A^-3

Table 2. Atomic coordinates (x 10^4) and equivalent isotropic displacement parameters (A^2 x 10^3) for lj76ac. U(eq) is defined as one third of the trace of the orthogonalized Uij tensor.

	x	y	z	U(eq)
Pt(1)	-107(1)	44(1)	2467(1)	15(1)
Cl(1)	-2574(2)	-435(1)	2958(2)	20(1)
Cl(2)	2397(2)	512(1)	2011(2)	19(1)
O(1A)	4227(7)	-2426(2)	2648(6)	38(1)
N(1A)	1412(7)	-642(2)	2872(6)	16(1)
O(2A)	5529(7)	-2157(2)	5328(6)	36(1)
C(2A)	759(9)	-1095(3)	1979(8)	19(1)
N(2A)	4483(8)	-2093(2)	3843(8)	27(1)
C(3A)	1728(9)	-1576(3)	2204(8)	19(1)
C(4A)	3434(8)	-1581(2)	3490(8)	18(1)
C(5A)	4141(8)	-1124(3)	4437(8)	18(1)
C(6A)	3094(8)	-655(3)	4096(7)	19(1)
O(1B)	-6535(7)	2113(2)	204(7)	43(1)
N(1B)	-1650(7)	724(2)	2030(6)	16(1)
N(2B)	-4869(8)	2156(3)	991(7)	28(1)
O(2B)	-4082(8)	2589(2)	1478(6)	42(1)
C(2B)	-3335(8)	728(3)	841(8)	20(1)
C(3B)	-4456(8)	1182(3)	485(8)	20(1)
C(4B)	-3753(9)	1652(2)	1372(8)	17(1)
C(5B)	-2029(9)	1664(3)	2600(8)	20(1)
C(6B)	-1016(9)	1190(3)	2887(8)	19(1)

Table 3. Bond lengths [A] and angles [deg] for lj76ac.

Pt(1)-N(1B)	2.005(5)
Pt(1)-N(1A)	2.006(5)
Pt(1)-Cl(2)	2.3019(16)
Pt(1)-Cl(1)	2.3027(16)
O(1A)-N(2A)	1.215(7)
N(1A)-C(2A)	1.331(7)
N(1A)-C(6A)	1.353(7)
O(2A)-N(2A)	1.218(7)
C(2A)-C(3A)	1.372(8)
N(2A)-C(4A)	1.467(8)
C(3A)-C(4A)	1.389(8)
C(4A)-C(5A)	1.368(8)
C(5A)-C(6A)	1.376(8)
O(1B)-N(2B)	1.230(7)
N(1B)-C(2B)	1.343(7)
N(1B)-C(6B)	1.344(7)
N(2B)-O(2B)	1.223(8)
N(2B)-C(4B)	1.476(8)
C(2B)-C(3B)	1.377(9)
C(3B)-C(4B)	1.374(9)
C(4B)-C(5B)	1.378(9)
C(5B)-C(6B)	1.372(9)

N(1B)-Pt(1)-N(1A)	179.17(17)
N(1B)-Pt(1)-Cl(2)	90.54(14)
N(1A)-Pt(1)-Cl(2)	89.84(14)
N(1B)-Pt(1)-Cl(1)	90.37(14)
N(1A)-Pt(1)-Cl(1)	89.26(14)
Cl(2)-Pt(1)-Cl(1)	178.95(5)
C(2A)-N(1A)-C(6A)	119.1(5)
C(2A)-N(1A)-Pt(1)	120.6(4)
C(6A)-N(1A)-Pt(1)	120.3(4)
N(1A)-C(2A)-C(3A)	123.3(6)
O(1A)-N(2A)-O(2A)	124.7(6)
O(1A)-N(2A)-C(4A)	118.0(5)
O(2A)-N(2A)-C(4A)	117.3(5)
C(2A)-C(3A)-C(4A)	116.4(6)
C(5A)-C(4A)-C(3A)	121.7(6)
C(5A)-C(4A)-N(2A)	119.7(6)
C(3A)-C(4A)-N(2A)	118.5(6)
C(4A)-C(5A)-C(6A)	117.9(6)
N(1A)-C(6A)-C(5A)	121.5(6)
C(2B)-N(1B)-C(6B)	118.3(5)
C(2B)-N(1B)-Pt(1)	120.5(4)
C(6B)-N(1B)-Pt(1)	121.2(4)
O(2B)-N(2B)-O(1B)	124.3(6)
O(2B)-N(2B)-C(4B)	118.1(6)
O(1B)-N(2B)-C(4B)	117.6(6)
N(1B)-C(2B)-C(3B)	123.1(6)
C(4B)-C(3B)-C(2B)	116.9(6)
C(3B)-C(4B)-C(5B)	121.5(6)
C(3B)-C(4B)-N(2B)	119.1(6)
C(5B)-C(4B)-N(2B)	119.4(6)
C(6B)-C(5B)-C(4B)	117.6(6)
N(1B)-C(6B)-C(5B)	122.5(6)

Symmetry transformations used to generate equivalent atoms:

Table 4. Anisotropic displacement parameters (A^2 x 10^3) for 1j76ac. The anisotropic displacement factor exponent takes the form: -2 pi^2 [h^2 a*^2 U11 + ... + 2 h k a* b* U12]

	U11	U22	U33	U23	U13	U12
Pt(1)	16(1)	15(1)	15(1)	-1(1)	5(1)	-2(1)
Cl(1)	19(1)	22(1)	20(1)	-2(1)	10(1)	-5(1)
Cl(2)	18(1)	22(1)	20(1)	0(1)	8(1)	-5(1)
O(1A)	40(3)	30(3)	42(3)	-15(2)	9(2)	11(2)
N(1A)	16(3)	17(3)	16(2)	1(2)	6(2)	-3(2)
O(2A)	43(3)	36(3)	26(3)	8(2)	2(2)	12(2)
C(2A)	24(4)	20(4)	13(3)	-1(3)	2(2)	-4(2)
N(2A)	29(3)	26(3)	30(3)	2(3)	14(3)	2(2)
C(3A)	23(3)	22(4)	19(3)	4(3)	16(3)	-3(2)
C(4A)	21(3)	19(3)	16(3)	1(3)	11(2)	1(2)
C(5A)	17(3)	23(4)	15(3)	3(3)	6(3)	2(2)
C(6A)	25(3)	20(4)	13(3)	-2(2)	9(2)	-3(2)
O(1B)	38(3)	47(4)	42(3)	10(3)	9(3)	18(2)
N(1B)	20(3)	13(3)	19(3)	-1(2)	11(2)	-2(2)
N(2B)	32(4)	31(4)	24(3)	5(3)	16(3)	11(3)
O(2B)	64(4)	25(3)	37(3)	-3(2)	14(3)	7(3)
C(2B)	20(3)	23(4)	16(3)	-1(3)	6(3)	-6(2)
C(3B)	11(3)	34(4)	19(3)	4(3)	9(2)	1(2)
C(4B)	26(3)	14(3)	17(3)	6(2)	15(3)	3(2)
C(5B)	28(4)	19(3)	16(3)	0(2)	12(3)	-5(2)
C(6B)	26(3)	16(3)	15(3)	1(2)	7(3)	-1(2)

Table 5. Hydrogen coordinates (x 10^4) and isotropic displacement parameters (A^2 x 10^3) for lj76ac.

	x	y	z	U(eq)
H(2A)	-437	-1084	1145	23
H(3A)	1256	-1890	1516	23
H(5A)	5318	-1130	5303	22
H(6A)	3562	-332	4735	22
H(2B)	-3775	401	215	24
H(3B)	-5660	1172	-335	24
H(5B)	-1557	1988	3225	24
H(6B)	179	1191	3725	23

Courses and Conferences Attended

Inorganic Seminar and Colloquia

ICCC, University of Edinburgh, July 2000.

1st Chianti Electrochemisty Meeting, Certosa di Pontignano, Siena, July 2000.

Introduction to Electrochemistry Course, Siena, July 2000.

Introduction to Epr Spectroscopy, February 2001.

USIC, University of Edinburgh, September 2002.